

THE UNIVERSITY OF OKLAHOMA
GRADUATE COLLEGE

SYNTHESIS, STRUCTURE, AND SOLUTION PROPERTIES OF
BENZOANNELATED CRYPTANDS

A Dissertation

SUBMITTED TO THE GRADUATE FACULTY

in partial fulfillment of the requirements for the

degree of

Doctor of Philosophy

By

GARY LEE NUNNERY SMITH

Norman, Oklahoma

2006

UMI Number: 3206115

Copyright 2006 by
Smith, Gary Lee Nunnery

All rights reserved.

UMI[®]

UMI Microform 3206115

Copyright 2006 by ProQuest Information and Learning Company.
All rights reserved. This microform edition is protected against
unauthorized copying under Title 17, United States Code.

ProQuest Information and Learning Company
300 North Zeeb Road
P.O. Box 1346
Ann Arbor, MI 48106-1346

SYNTHESIS, STRUCTURE, AND SOLUTION PROPERTIES OF
BENZOANNELATED CRYPTANDS

A Dissertation APPROVED FOR THE
DEPARTMENT OF CHEMISTRY AND BIOCHEMISTRY

BY

Richard W. Taylor

C. LeRoy Blank

Robert L. White

Kenneth M. Nicholas

John F. Scamehorn

© Copyright by GARY LEE NUNNERY SMITH 2006
All Rights Reserved.

ACKNOWLEDGEMENTS

The journey of this project was accomplished by a multitude of individuals who graciously blessed me with their financial support, direction, encouragement, friendship, patience, and love. I would like to thank Dr. Richard W. Taylor for sharing with me his time, wisdom, and passion for chemistry. I am grateful for your patience, support, and encouragement through this long journey. The direction you gave me in this project and in my career choices has been invaluable. I am thankful to my graduate committee: Professors C. LeRoy Blank, Robert L. White, Kenneth M. Nicholas, and John F. Scamehorn. Furthermore, the skills and services offered from Drs. Susan S. Alguindigue, Masood A. Khan, Douglas R. Powell, Larry Russon, Li Zhang and fellow graduate students Nathalie Rocher, Lei Yang, and Ge Zu contributed immensely to this project and I am extremely grateful. This project was supported by grants from the Oklahoma Center for the Advancement of Science and Technology, the National Institutes of Health, and through teaching assistantships from the University of Oklahoma Department of Chemistry and Biochemistry. I have had the benefit of sharing lab space for the last 5+ years with many amazing people. It was a joy to share everyday for many years with my friends Bo Tan and Kendra Cox. They have contributed to my chemistry knowledge and impacted my view on life. I have been blessed by the many conversations and laughs we have shared in together. I am also grateful for the time shared in the lab with Jumoke Olowu, Rebecca Craig-Schapiro, Shaun Grewal, Tam Nguyen, and Baige Bian. The friendships developed in the Chemistry Department, especially Whitney Smith, Shawn Carter, Adam Hixson, Huaxing Pei, Peter Nagy, Alex Xulu, Karen Johnson, Jamie Huntley, Steven Foster, Russell Franks, Gwen Giffin, and Rachel Mason, have made my

time here very special. I also spent my time at O.U. out of the lab and I am thankful for the friendships that were developed at Norman First Church of the Nazarene, the O. U. Nazarene Student Center, and St. Paul's Episcopal Church. Throughout my life, I have always been supported, encouraged, and loved by my precious family. Thank you Mom for your unconditional love, support, and encouragement, even though you don't know what I do. Thank you Kathy, Chris, Katelyn, and Cody for all the great times we have shared in during my time at O.U., the home projects completed, and the many other ways you have supported me. Richard and Chantal, thank you for the computer that I used to complete this project, and for your constant love and support. Heather, my amazing and true wife, I am grateful for how you have found the balance in responding to my constant fluctuation of emotions with compassion, encouragement, and challenge. You continually motivate me to be a better person in all that I do and I am blessed to share life with you everyday. This work is in memory of my dad, Garland Lee Smith, who passed away during my time at O.U. He modeled to me the importance of hard work, but never at the sacrifice of time with your family. I miss you greatly. Lastly, I am overwhelmed and grateful by the goodness of God the Creator who blessed us with this creation so we could study it and share in it together.

TABLE OF CONTENTS

	Page
LIST OF TABLES.....	viii
LIST OF FIGURES.....	x
LIST OF SCHEMES.....	xx
CHAPTER ONE. INTRODUCTION.....	1
I. Cryptands.....	1
II. Metal Toxicity.....	13
III. Objective.....	15
References.....	17
CHAPTER TWO. SYNTHESIS OF STARTING MATERIALS, MONOCYCLIC AND BICYCLIC DIAMIDES AND DIAMINES.....	19
I. Introduction.....	19
II. Summaries of Synthetic Methods.....	23
A. Synthesis of Acyclic Diamines and Starting Materials.....	23
B. Synthesis of Monocyclic Diamides and Diamines.....	26
C. Synthesis of Bicyclic Diamines (Cryptands).....	30
III. Experimental.....	38
A. General Methods.....	38
B. Reagents.....	39
C. Synthesis of Acyclic Diamines and Starting Materials.....	42

D. Synthesis of Monocyclic Diamides and Diamines.....	53
E. Synthesis of Bicyclic Diamines (Cryptands).....	78
References.....	102
CHAPTER THREE. SPECTROSCOPIC STUDIES OF AN2.2.1 AND AN2.2.2.....	103
I. Introduction.....	103
II. Experimental.....	106
A. Reagents.....	106
B. pH Measurements.....	108
C. Standardization of Ligand Solutions.....	109
D. Spectrophotometric Analysis of An2.2.1 and An2.2.2.....	111
E. Determination of Ligand Protonation Constants (K_H).....	117
F. Determination of Metal Binding Constants (K_{ML}).....	119
References.....	124
CHAPTER FOUR. RESULTS AND DISCUSSION.....	125
I. Structures and NMR Assignments of Monocyclic Ligands.....	125
II. Structures and NMR Assignments of Bicyclic and Tricyclic Compounds....	148
III. Structures of Cryptate Complexes.....	165
IV. Protonation and Metal Binding Constants for An2.2.1 and An2.2.2.....	182
V. Summary.....	225
References.....	227

LIST OF TABLES

		Page
Table 1-1	Formation constants ($\log K_{ML}$) for cryptands 2.2.1 and 2.2.2 in H ₂ O at 25°C.....	5
Table 1-2	Structural parameters for 2.2.2 and 2.2 _B .2 _B	9
Table 1-3	Formation constants ($\log K_{ML}$) for 2.2.2 and 2.2 _B .2 _B in H ₂ O at 25 °C.....	9
Table 1-4	Formation constants ($\log K_{ML}$) for EGTA and BAPTA in H ₂ O at 25°C...	11
Table 4-1	Hydrogen bond parameters for 2.2*, (7).....	130
Table 4-2	Hydrogen bond parameters for An2.2*, (11).....	132
Table 4-3	Hydrogen bond parameters for 2.2 _S *, (8).....	134
Table 4-4	¹ H and ¹³ C NMR data for An2.1*, (9).....	138
Table 4-5	H-H and C-H correlation NMR data for An2.1*, (9).....	139
Table 4-6	¹ H and ¹³ C NMR data for An2.2*, (11).....	140
Table 4-7	H-H and C-H correlation NMR data for An2.2*, (11).....	141
Table 4-8	¹ H and ¹³ C NMR data for An3.1*, (13).....	143
Table 4-9	H-H and C-H correlation NMR data for An3.1*, (13).....	143
Table 4-10	Hydrogen bond parameters for An3.1*, (13).....	145
Table 4-11	NMR peak assignments for An3.1.1*, (22) at 58 °C in CDCl ₃	164
Table 4-12	Relative abundance of the elemental isotopes of potassium.....	170
Table 4-13	Relative abundance of the elemental isotopes of lead.....	173
Table 4-14	Average lead-donor distances and N...N non-bonding distances for lead cryptates.....	181
Table 4-15	Protonation constants ($\log K_{Hi}$) for An2.2.2, (19) in H ₂ O.....	185
Table 4-16	Protonation constants ($\log K_{Hi}$) for An2.2.1, (16) in H ₂ O.....	188

Table 4-17	Formation constants ($\log K_{ML}$) for An2.2.2, (19) with barium in H ₂ O at 25°C.....	198
Table 4-18	Formation constants ($\log K_{ML}$) for An2.2.2, (19) with strontium in H ₂ O at 25°C.....	199
Table 4-19	Formation constants ($\log K_{ML}$) for An2.2.2, (19) with lead in H ₂ O at 25°C.....	202
Table 4-20	Formation constants ($\log K_{ML}$) for An2.2.2, (19) in H ₂ O at 25°C.....	209
Table 4-21	Formation constants ($\log K_{ML}$) for 2.2.2, 2.2 _B .2 _B , and An2.2.2, (19) in H ₂ O at 25°C.....	209
Table 4-22	Formation constants ($\log K_{ML}$) for An2.2.1, (16) in H ₂ O at 25°C.....	216
Table 4-23	Formation constants ($\log K_{ML}$) for An2.2.1, (16) in H ₂ O at 25°C.....	222
Table 4-24	Formation constants ($\log K$) for 2.1.1, 2.2.1, An2.2.2, (19), and An2.2.1, (16) in H ₂ O at 25°C.....	223

LIST OF FIGURES

	Page
Figure 1-1	General cryptand structure and naming scheme.....2
Figure 1-2	Species distribution of 2.2.2.....3
Figure 1-3	X-ray crystal structure of unprotonated cryptand 2.2.2.....4
Figure 1-4	X-ray crystal structure of diprotonated cryptand $H_2 2.2.2^{2+}$4
Figure 1-5	Complexation selectivity patterns of 2.2.1 and 2.2.2.....5
Figure 1-6	X-ray crystal structure of $2.2.2 \cdot K^+$6
Figure 1-7	X-ray crystal structure of $2.2.2 \cdot Pb^{2+} \cdot NCS^- \cdot SCN^-$7
Figure 1-8	Cryptand 2.2 _B .2 _B8
Figure 1-9	Complexation selectivity patterns of 2.2.2, 2.2 _B .2 _B , and 2.2.1.....10
Figure 1-10	Structures of EGTA and BAPTA.....11
Figure 1-11	Benzoannelated cryptands.....12
Figure 1-12	Benzoannelated cryptands An2.2.1, An2.2.2, An3.1.1, and An3.1.1.3.....15
Figure 2-1	General synthetic scheme for the synthesis of cryptands.....19
Figure 2-2	Balanced reaction between a diamine and diacid chloride with a scavenger base present.....19
Figure 2-3	1H NMR of 2,2'-[ethane-1,2-diylbis(oxy)]diacetyl chloride, (1) in $CDCl_3$44
Figure 2-4	^{13}C NMR of 2,2'-[ethane-1,2-diylbis(oxy)]diacetyl chloride, (1) in $CDCl_3$44
Figure 2-5	1H NMR of 1,1'-[ethane-1,2-diylbis(oxy)]bis(2-nitrobenzene), (3) in DMSO.....46
Figure 2-6	ESI-MS ⁺ of 1,1'-[ethane-1,2-diylbis(oxy)]bis(2-nitrobenzene), (3) in MeOH.....47
Figure 2-7	1H NMR of 2,2'-[ethane-1,2-diylbis(oxy)]dianiline, (4) in DMSO.....48

Figure 2-8	ESI-MS ⁺ of 2,2'-[ethane-1,2-diylbis(oxy)]dianiline, (4) in MeOH.....	49
Figure 2-9	¹ H NMR of 1,1'-[oxybis(2,1-ethanediyloxy)]bis[2-nitro-benzene], (5) in CDCl ₃	50
Figure 2-10	ESI-MS ⁺ of 1,1'-[oxybis(2,1-ethanediyloxy)]bis[2-nitro-benzene], (5) in MeOH.....	51
Figure 2-11	¹ H NMR of 2,2'-[oxybis(ethane-2,1-diyloxy)]dianiline, (6) in CDCl ₃	52
Figure 2-12	ESI-MS ⁺ of 2,2'-[oxybis(ethane-2,1-diyloxy)]dianiline, (6) in MeOH.....	53
Figure 2-13	¹ H NMR of 2.2*, (7) in CDCl ₃	55
Figure 2-14	ESI-MS ⁺ of 2.2*, (7) in MeOH.....	55
Figure 2-15	X-ray crystal structure of 2.2*, (7), Molecule A.....	56
Figure 2-16	X-ray crystal structure of 2.2*, (7), Molecule B.....	56
Figure 2-17	¹ H NMR of 2.2 _S *, (8) in CDCl ₃	58
Figure 2-18	ESI-MS ⁺ of 2.2 _S *, (8) in MeOH.....	58
Figure 2-19	X-ray crystal structure of 2.2 _S *, (8).....	59
Figure 2-20	¹ H NMR of An2.1*, (9) in CDCl ₃	60
Figure 2-21	¹³ C NMR of An2.1*, (9) in CDCl ₃	61
Figure 2-22	ESI-MS ⁺ of An2.1*, (9) in MeOH.....	61
Figure 2-23	X-ray crystal structure of An2.1*, (9).....	62
Figure 2-24	¹ H NMR of An2.1, (10) in CDCl ₃	63
Figure 2-25	ESI-MS ⁺ of An2.1, (10) in MeOH.....	64
Figure 2-26	X-ray crystal structure of An2.1, (10).....	64
Figure 2-27	¹ H NMR of An2.2*, (11) in CDCl ₃	66
Figure 2-28	¹³ C NMR of An2.2*, (11) in CDCl ₃	67
Figure 2-29	ESI-MS ⁺ of An2.2*, (11) in MeOH.....	67

Figure 2-30	X-ray crystal structure of An2.2*, (11).....	68
Figure 2-31	¹ H NMR of An2.2, (12) in CDCl ₃	69
Figure 2-32	¹³ C NMR of An2.2, (12) in CDCl ₃	70
Figure 2-33	ESI-MS ⁺ of An2.2, (12) in MeOH.....	70
Figure 2-34	X-ray crystal structure of An2.2, (12).....	71
Figure 2-35	¹ H NMR of An3.1*, (13) in CDCl ₃	73
Figure 2-36	¹³ C NMR of An3.1*, (13) in CDCl ₃	73
Figure 2-37	ESI-MS ⁺ of An3.1*, (13) in MeOH.....	74
Figure 2-38	X-ray crystal structure of An3.1*, (13), Molecule A.....	74
Figure 2-39	X-ray crystal structure of An3.1*, (13), Molecule B.....	75
Figure 2-40	¹ H NMR of An3.1, (14) in CDCl ₃	76
Figure 2-41	¹³ C NMR of An3.1, (14) in CDCl ₃	77
Figure 2-42	ESI-MS ⁺ of An3.1, (14) in MeOH.....	77
Figure 2-43	X-ray crystal structure of An3.1, (14).....	78
Figure 2-44	ESI-MS ⁺ of An2.1.2*, (15) in MeOH.....	79
Figure 2-45	X-ray crystal structure of An2.1.2*, (15).....	80
Figure 2-46	¹ H NMR of An2.2.1, (16) in CDCl ₃	82
Figure 2-47	¹³ C NMR of An2.2.1, (16) in CDCl ₃	82
Figure 2-48	ESI-MS ⁺ of An2.2.1, (16) in MeOH.....	83
Figure 2-49	X-ray crystal structure of An2.2.1, (16).....	83
Figure 2-50	ESI-MS ⁺ of An2.2.1*, (17) in MeOH.....	85
Figure 2-51	X-ray crystal structure of An2.2.1*, (17), Molecule A.....	86
Figure 2-52	X-ray crystal structure of An2.2.1*, (17), Molecule B.....	86

Figure 2-53	ESI-MS ⁺ of An2.2.2*, (18) in MeOH.....	88
Figure 2-54	X-ray crystal structure of An2.2.2*, (18).....	88
Figure 2-55	¹ H NMR of An2.2.2, (19) in CDCl ₃	90
Figure 2-56	¹³ C NMR of An2.2.2, (19) in CDCl ₃	91
Figure 2-57	ESI-MS ⁺ of An2.2.2, (19) in MeOH.....	91
Figure 2-58	X-ray crystal structure of An2.2.2, (19).....	92
Figure 2-59	ESI-MS ⁺ of An3.1.1.3*, (20) in MeOH.....	93
Figure 2-60	¹ H NMR of An3.1.1.3, (21) in CDCl ₃	95
Figure 2-61	¹³ C NMR of An3.1.1.3, (21) in CDCl ₃	95
Figure 2-62	ESI-MS ⁺ of An3.1.1.3, (21) in MeOH.....	96
Figure 2-63	X-ray crystal structure of An3.1.1.3.....	96
Figure 2-64	¹ H NMR of An3.1.1*, (22) at 58°C in CDCl ₃	98
Figure 2-65	¹³ C NMR of An3.1.1*, (22) at 58°C in CDCl ₃	98
Figure 2-66	ESI-MS ⁺ of An3.1.1*, (22) in MeOH.....	99
Figure 2-67	X-ray crystal structure of An3.1.1*, (22).....	99
Figure 2-68	ESI-MS ⁺ of An3.1.1, (23) in MeOH.....	101
Figure 3-1	Structure of bis(<i>o</i> -aminophenoxy)ethane- <i>N,N,N',N'</i> -tetraacetic acid (BAPTA).....	103
Figure 3-2	Plot of absorbance at 274 nm versus [Pb ²⁺] for the standardization of An2.2.2, (19) at pH = 6.6.....	110
Figure 3-3	Absorbance versus wavelength for An2.2.1, (16), from 0.070 mM - 0.025 mM at pH = 2.5-3.1.....	113
Figure 3-4	Absorbance at 272 nm versus concentration for An2.2.1, (16), at pH = 2.5-3.1.....	113
Figure 3-5	Absorbance versus wavelength for An2.2.1, (16), from 0.070 mM - 0.025 mM at pH = 6.0-6.6.....	114

Figure 3-6	Absorbance at 278 nm versus concentration for An2.2.1, (16), at pH = 6.0 - 6.6.....	114
Figure 3-7	Absorbance versus wavelength for An2.2.2, (19), from 0.18 mM - 0.068 mM at pH = 2.4-3.0.....	115
Figure 3-8	Absorbance at 272 nm versus concentration for An2.2.2, (19), at pH = 2.4-3.0.....	115
Figure 3-9	Absorbance versus wavelength for An2.2.2, (19), from 0.18 mM - 0.068 mM at pH = 6.2-6.6.....	116
Figure 3-10	Absorbance at 276 nm versus concentration for An2.2.2, (19) at pH = 6.2-6.6.....	116
Figure 3-11	Metal ion titrations: (1) fully complexed at 1:1 stoichiometry (2) less than 50% complexed.....	120
Figure 4-1	Monocyclic diamides 2.2*, (7), An2.2*, (11), 2.2 _S *, (8), and 8a.....	126
Figure 4-2	X-ray crystal structure of 2.2*, (7), Molecule A.....	127
Figure 4-3	X-ray crystal structure of 2.2*, (7), Molecule B.....	127
Figure 4-4	X-ray crystal structure of 2.2*, (7), showing the formation of hydrogen-bonded chains for molecule A.....	128
Figure 4-5	X-ray crystal structure of 2.2*, (7), showing the formation of hydrogen-bonded chains for molecule B.....	129
Figure 4-6	X-ray crystal structure of An2.2*, (11).....	130
Figure 4-7	X-ray crystal structure of An2.2*, (11), showing the angle between the benzene rings.....	132
Figure 4-8	Monobenzo 18-membered diamide.....	133
Figure 4-9	X-ray crystal structure of 2.2 _S *, (8).....	134
Figure 4-10	X-ray crystal structure of 2.2 _S *, (8), showing the formation of hydrogen-bonded chains.....	135
Figure 4-11	NMR numbering scheme for macrocyclic amides An2.1*, (9), An2.2*, (11), An3.1*, (13).....	137
Figure 4-12	X-ray crystal structure of An2.1*, (9).....	140

Figure 4-13	Lactam (a) and lactim (b) forms of amides.....	141
Figure 4-14	X-ray crystal structure of An3.1*, (13), Molecule A.....	144
Figure 4-15	X-ray crystal structure of An3.1*, (13), Molecule B.....	144
Figure 4-16	X-ray crystal structure of An2.2.1, (16).....	149
Figure 4-17	¹ H NMR peak assignment for An2.2.1, (16), in CDCl ₃	150
Figure 4-18	Methylene protons in cryptands.....	151
Figure 4-19	¹³ C NMR peak assignment for An2.2.1, (16), in CDCl ₃	152
Figure 4-20	HSQC of An2.2.1, (16) in CDCl ₃	153
Figure 4-21	X-ray crystal structure of An2.2.2, (19).....	154
Figure 4-22	¹ H NMR peak assignment for An2.2.2, (19), in CDCl ₃	155
Figure 4-23	¹³ C NMR peak assignment for An2.2.2, (19), in CDCl ₃	155
Figure 4-24	HSQC of An2.2.2, (19), in CDCl ₃	156
Figure 4-25	An3.1.1.3, (21), and other macrotricyclic cryptands.....	157
Figure 4-26	X-ray crystal structure of An3.1.1.3, (21).....	159
Figure 4-27	X-ray crystal structure of An3.1.1.3, (21), viewed along O2-O5 axis.....	160
Figure 4-28	X-ray crystal structure of An3.1.1.3, (21), viewed along N2-N4 axis.....	160
Figure 4-29	ESI ⁺ -MS of An3.1.1.3, (21).....	161
Figure 4-30	X-ray crystal structure of An3.1.1*, (22).....	162
Figure 4-31	NMR numbering scheme for An3.1.1*, (22).....	163
Figure 4-32	Cryptands 2.2.2, 2.2 _B .2 _B , and 2 _N 2 _N 2 _N	165
Figure 4-33	X-ray crystal structure of An2.2.2·K ⁺ ·ClO ₄ ⁻	166
Figure 4-34	X-ray crystal structure of An2.2.2·K ⁺ ·ClO ₄ ⁻ viewed along N1-N2 axis.....	167

Figure 4-35	Metal center and coordination geometry of An2.2.2·K ⁺ ·ClO ₄ ⁻	168
Figure 4-36	Packing diagram of An2.2.2·K ⁺ ·ClO ₄ ⁻	169
Figure 4-37	ESI ⁺ -MS of An2.2.2·K ⁺ ·ClO ₄ ⁻ in MeOH.....	170
Figure 4-38	Calculated isotope distribution (top) and ESI ⁺ -MS of An2.2.2·K ⁺ (bottom).....	171
Figure 4-39	X-ray crystal structure of An2.2.2·Pb ²⁺ ·(NCS ⁻) ₂ viewed along N1-N10 axis.....	172
Figure 4-40	Packing diagram of An2.2.2·Pb ²⁺ ·(NCS ⁻) ₂	172
Figure 4-41	ESI ⁺ -MS of An2.2.2·Pb ²⁺ ·(NCS ⁻) ₂	173
Figure 4-42	Calculated isotope distribution (top) and ESI ⁺ -MS of An2.2.2·Pb ²⁺ (bottom).....	174
Figure 4-43	Calculated isotope distribution (top) and ESI ⁺ -MS of [An2.2.2·Pb ²⁺ ·NCS ⁻] ⁺ (bottom).....	174
Figure 4-44	X-ray crystal structure of 2.2 _B .2 _B ·Pb ²⁺ ·NCS ⁻	175
Figure 4-45	X-ray crystal structure of 2.2 _B .2 _B ·Pb ²⁺ ·NCS ⁻ viewed along N1-N10 axis.....	175
Figure 4-46	Metal center and coordination geometry of 2.2 _B .2 _B ·Pb ²⁺ ·NCS ⁻	176
Figure 4-47	Packing diagram for 2.2 _B .2 _B ·Pb ²⁺ ·NCS ⁻	178
Figure 4-48	ESI ⁺ -MS of 2.2 _B .2 _B ·Pb ²⁺ ·NCS ⁻ complex.....	179
Figure 4-49	Calculated isotope distribution (top) and ESI ⁺ -MS of [2.2 _B .2 _B ·Pb ²⁺ ·I] ⁺ (bottom).....	179
Figure 4-50	Calculated isotope distribution (top) and ESI ⁺ -MS of 2.2 _B .2 _B ·Pb ²⁺ (bottom).....	180
Figure 4-51	Spectra from the titration of 0.13 mM An2.2.2, (19), from pH 2.5-6.5.....	183
Figure 4-52	Isosbestic points for cryptand An2.2.2, (19), at 264 nm and 276 nm.....	183
Figure 4-53	Plot of absorbance at 284 nm versus a _H for the titration of An2.2.2, (19), shown in Figure 4-51.....	184

Figure 4-54	Species distribution for An2.2.2, (19).....	186
Figure 4-55	Spectra from the titration of 0.072 mM An2.2.1, (16), from pH 1.9-6.5.....	187
Figure 4-56	Plot of absorbance at 240 nm versus a_H for the titration of An2.2.1, (16), shown in Figure 4-55.....	187
Figure 4-57	Species distribution of An2.2.1, (16).....	189
Figure 4-58	Spectra from the titration of 0.15 mM An2.2.2, (19), with lead at pH = 7.0.....	192
Figure 4-59	Plot of fraction of the absorbance change versus the ratio of total lead to total An2.2.2, (19), concentrations from the titration shown in Figure 4-58.....	192
Figure 4-60	Spectra from the titration of 0.18 mM An2.2.2, (19), with barium at pH = 8.2.....	193
Figure 4-61	Plot of fraction of the absorbance change versus the ratio of total barium to total An2.2.2, (19), concentrations from the titration shown in Figure 4-60.....	193
Figure 4-62	Spectra from the titration of 0.17 mM An2.2.2, (19), with strontium at pH = 9.5.....	194
Figure 4-63	Plot of fraction of the absorbance change versus the ratio of total strontium to total An2.2.2, (19), concentrations from the titration shown in Figure 4-62.....	194
Figure 4-64	Spectra from the titration of 0.091 mM An2.2.2, (19), with barium at pH = 3.7.....	196
Figure 4-65	Plot of absorbance at 234 nm versus $[Ba^{2+}]$ for the titration of An2.2.2, (19), shown in Figure 4-64.....	196
Figure 4-66	Spectra from the titration of 0.091 mM An2.2.2, (19), with strontium at pH = 4.2. Some spectra have been omitted for clarity.....	197
Figure 4-67	Plot of absorbance at 240 nm versus $[Sr^{2+}]$ for the titration of An2.2.2, (19), shown in Figure 4-66.....	197
Figure 4-68	Plot of K'_{ML} vs. a_H for $BaAn2.2.2^{2+}$ using values from Table 4-15.....	199

Figure 4-69	Spectra from the batch titration of 0.18 mM An2.2.2, (19), with lead at pH = 2.1.....	201
Figure 4-70	Plot of absorbance at 284 nm versus $[Pb^{2+}]$ for the titration of An2.2.2, (19), shown in Figure 4-69.....	201
Figure 4-71	Plot of absorbance at 284 nm versus $[Pb^{2+}] * \alpha$ for a batch titration of An2.2.2, (19), and lead.....	202
Figure 4-72	Spectra from the titration of 0.091 mM An2.2.2, (19), with sodium at pH = 9.0.....	204
Figure 4-73	Plot of absorbance at 240 nm versus $[Na^+]$ for the titration of An2.2.2, (19), shown in Figure 4-72.....	204
Figure 4-74	Spectra from the titration of 0.091 mM An2.2.2, (19), with cadmium at pH = 7.7.....	205
Figure 4-75	Plot of absorbance at 282 nm versus $[Cd^{2+}]$ for the titration of An2.2.2, (19), shown in Figure 4-74.....	205
Figure 4-76	Spectra from the titration of 0.091 mM An2.2.2, (19), with calcium at pH = 9.4.....	206
Figure 4-77	Plot of absorbance at 242 nm versus $[Ca^{2+}]$ for the titration of An2.2.2, (19), shown in Figure 4-76.....	206
Figure 4-78	Spectra from the titration of 0.18 mM An2.2.2, (19), with potassium at pH = 9.0.....	207
Figure 4-79	Plot of absorbance at 260 nm versus $[K^+]$ for the titration of An2.2.2, (19), shown in Figure 4-78.....	207
Figure 4-80	Spectra from the titration of 0.061 mM An2.2.1, (16), with lead at pH = 6.9.....	211
Figure 4-81	Plot of fraction of the absorbance change versus the ratio of total lead to total An2.2.1, (16), concentrations from the titration shown in Figure 4-80.....	211
Figure 4-82	Spectra from the titration of 0.091 mM An2.2.1, (16), with cadmium at pH = 7.0.....	212
Figure 4-83	Plot of fraction of the absorbance change versus the ratio of total cadmium to total An2.2.1, (16), concentrations from the titration shown in Figure 4-82.....	212

Figure 4-84	Spectra from the titration of 0.091 mM An2.2.1, (16), with lead at pH = 3.6.....	214
Figure 4-85	Plot of absorbance at 250 nm versus [Pb ²⁺] for the titration of An2.2.1, (16), shown in Figure 4-84.....	214
Figure 4-86	Spectra from the titration of 0.091 mM An2.2.1, (16), with cadmium at pH = 4.3.....	215
Figure 4-87	Plot of absorbance at 280 nm versus [Cd ²⁺] for the titration of An2.2.1, (16), shown in Figure 4-86.....	215
Figure 4-88	Spectra from the titration of 0.070 mM An2.2.1, (16), with barium at pH = 8.4.....	217
Figure 4-89	Plot of absorbance at 254 nm versus [Ba ²⁺] for the titration of An2.2.1, (16), shown in Figure 4-88.....	217
Figure 4-90	Spectra from the titration of 0.070 mM An2.2.1, (16), with sodium at pH = 8.3.....	218
Figure 4-91	Plot of absorbance at 260 nm versus [Na ⁺] for the titration of An2.2.1, (16), shown in Figure 4-90.....	218
Figure 4-92	Spectra from the titration of 0.070 mM An2.2.1, (16), with strontium at pH = 8.6.....	219
Figure 4-93	Plot of absorbance at 250 nm versus [Sr ²⁺] for the titration of An2.2.1, (16), shown in Figure 4-92.....	219
Figure 4-94	Spectra from the titration of 0.070 mM An2.2.1, (16), with calcium at pH = 8.7.....	220
Figure 4-95	Plot of absorbance at 248 nm versus [Ca ²⁺] for the titration of An2.2.1, (16), shown in Figure 4-94.....	220
Figure 4-96	Spectra from the titration of 0.070 mM An2.2.1, (16), with potassium at pH = 9.1.....	221
Figure 4-97	Plot of absorbance at 264 nm versus [K ⁺] for the titration of An2.2.1, (16), shown in Figure 4-96.....	221
Figure 4-98	Complexation selectivity patterns of An2.2.1, (16), and An2.2.2, (19)...	224

LIST OF SCHEMES

	Page
Scheme 1-1 Stepwise synthesis of cryptands.....	1
Scheme 2-1 Synthesis of An2.2.1 and An2.2.2.....	21
Scheme 2-2 Synthesis of An3.1.1.3 and An3.1.1.....	22
Scheme 2-3 Synthesis of 2,2'-[ethane-1,2-diylbis(oxy)]diacetyl chloride, (1).....	23
Scheme 2-4 Synthesis of 2,2'-[ethane-1,2-diylbis(thio)]diacetyl chloride, (2).....	24
Scheme 2-5 Synthesis of 1,1'-[ethane-1,2-diylbis(oxy)]bis(2-nitrobenzene), (3).....	24
Scheme 2-6 Synthesis of 2,2'-[ethane-1,2-diylbis(oxy)]dianiline, (4).....	25
Scheme 2-7 Synthesis of 1,1'-[oxybis(2,1-ethanedioxy)]bis[2-nitro-benzene], (5).....	25
Scheme 2-8 Synthesis of 2,2'-[oxybis(ethane-2,1-dioxy)]dianiline, (6).....	25
Scheme 2-9 Synthesis of 2.2*, (7).....	26
Scheme 2-10 Synthesis of 2.2 _s *, (8).....	27
Scheme 2-11 Synthesis of An2.1*, (9).....	27
Scheme 2-12 Synthesis of An2.1, (10).....	28
Scheme 2-13 Synthesis of An2.2*, (11).....	28
Scheme 2-14 Synthesis of An2.2, (12).....	29
Scheme 2-15 Synthesis of Synthesis of An3.1*, (13).....	29
Scheme 2-16 Synthesis of An3.1, (14).....	30
Scheme 2-17 Synthesis of An2.1.2*, (15).	31
Scheme 2-18 Synthesis of An2.2.1, (16).....	31
Scheme 2-19 Synthesis of An2.2.1*, (17).....	32
Scheme 2-20 Synthesis of Synthesis of An2.2.1, (16).....	33

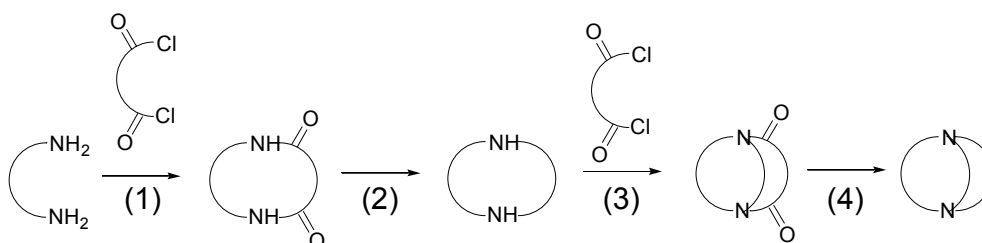
Scheme 2-21	Synthesis of An2.2.2*, (18).....	33
Scheme 2-22	Synthesis of An2.2.2, (19).....	34
Scheme 2-23	Synthesis of An3.1.1.3*, (20).....	35
Scheme 2-24	Synthesis of An3.1.1.3, (21).....	36
Scheme 2-25	Synthesis of An3.1.1*, (22).....	36
Scheme 2-26	Synthesis of An3.1.1, (23).....	37

Chapter One

Introduction

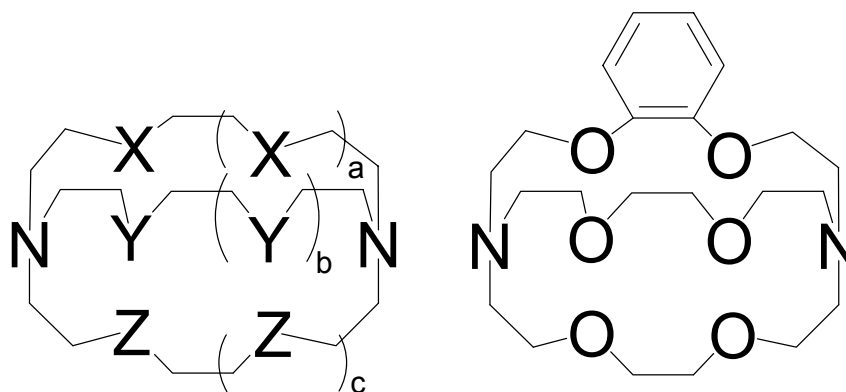
I. Cryptands

In 1969, Lehn and co-workers¹ reported the use of a stepwise addition process utilizing high dilution conditions shown in Scheme 1-1 for the synthesis of the first diazapolyoxa macrobicyclic ligands.²



Scheme 1-1. Stepwise synthesis of cryptands.

These ligands, called cryptands employ a three digit naming system to provide a shorthand alternative to the formal IUPAC names. Each digit corresponds to the number of donor atoms (O, S, N) in each bridge and letters are used as subscripts to designate heteroatoms other than oxygen or the presence of substituents (other than ethylene groups) in the bridging strands.² Figure 1-1 shows examples of the notation used to name these compounds.



$X=Y=Z=O$; $a=b=c=1$ 2.2.2
 $a=b=1, c=0$ 2.2.1
 $a=2, b=c=0$ 3.1.1
 $X=S, Y=Z=O$; $a=b=c=1$ $2_S.2.2$

2.2.2_B

Figure 1-1. General cryptand structure and naming scheme.

The synthesis of cryptands has been accomplished through a variety of methods.² High dilution synthesis is used in order to minimize the production of polymers and promote the formation of the monomeric macrocycle or cryptand. This is accomplished in high dilution because the rate of intermolecular interaction (polymer production) has a second order concentration dependence, while intramolecular interaction (ring closure) is a first order process. The stepwise cyclization method also allows for flexibility in structural alterations. The general step-wise synthesis method (see Scheme 1-1) starts with the high dilution reaction of equimolar solutions of an α,ω -diamine and an α,ω -diacyl chloride (1), followed by purification and reduction of the macrocyclic amide product utilizing diborane or lithium aluminum hydride (2). A second high dilution reaction with another α,ω -diacyl chloride (3), and subsequent reduction of the bicyclic amide with diborane (4) yields the cryptand.

Typical cryptands such as 2.2.1 and 2.2.2 are bis(trialkylamines) that can be protonated at each bridgehead nitrogen. The stepwise protonation constants, in water are

$\log K_{H1} = 10.53$, $\log K_{H2} = 7.50$ for 2.2.1 and $\log K_{H1} = 9.60$, $\log K_{H2} = 7.28$ for 2.2.2.³

Due to the basicity of these compounds, a mixture of the protonated and diprotonated ligands occurs at physiological pH. Figure 1-2 shows the species distribution of cryptand 2.2.2 from pH 5-12.

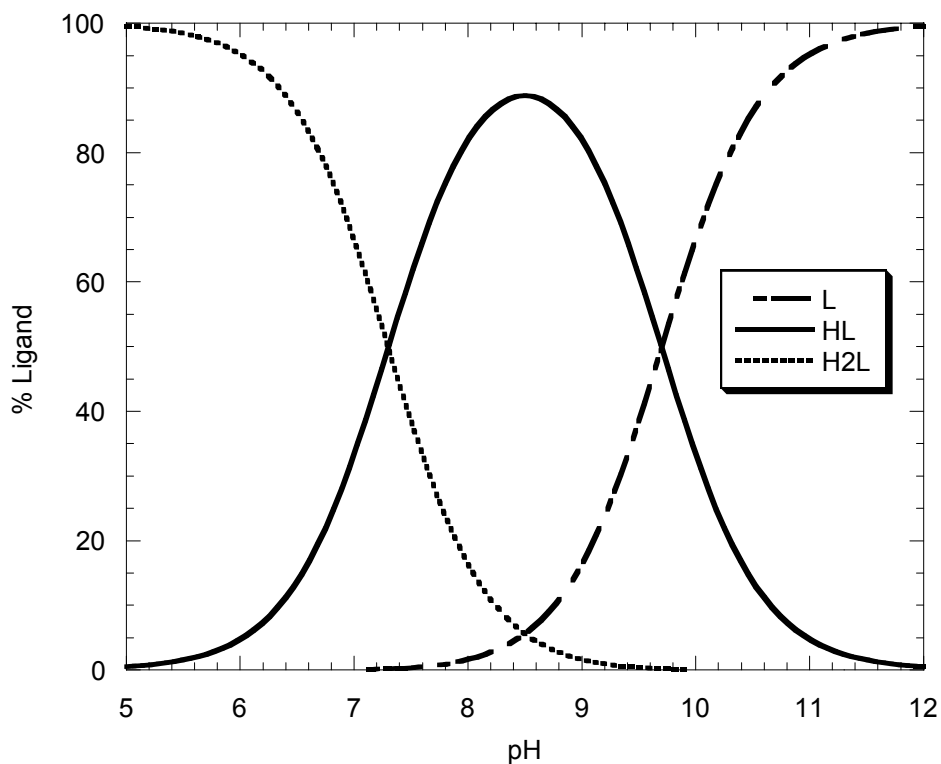


Figure 1-2. Species distribution of 2.2.2.³

The solid-state structures for the unprotonated cryptand 2.2.2 and the diprotonated cryptand $H_2 2.2.2^{2+}$ are shown in Figures 1-3 and 1-4, respectively.^{4,5} The lone-pairs on the nitrogen atoms can exist in three conformations: either facing in (*endo-endo*), facing out (*exo-exo*), or a combination (*endo-exo*).⁶ Cryptand 2.2.2 has a football-like shape with an $N \cdots N$ non-bonding distance of 6.871 Å.⁴ Cryptand 2.2.2 has an *endo-endo* nitrogen conformation, and an arrangement of some oxygen atoms pointed toward the inside of the cavity and others facing away.⁴ In contrast, Cryptand $H_2 2.2.2^{2+}$ has a much shorter $N \cdots N$ non-bonding distance of 5.71 Å and a more spherical shape.⁵ As a result of

protonation the six oxygen atoms are oriented toward the center of the cavity and the hydrogens on the nitrogens are pointing into the cavity.

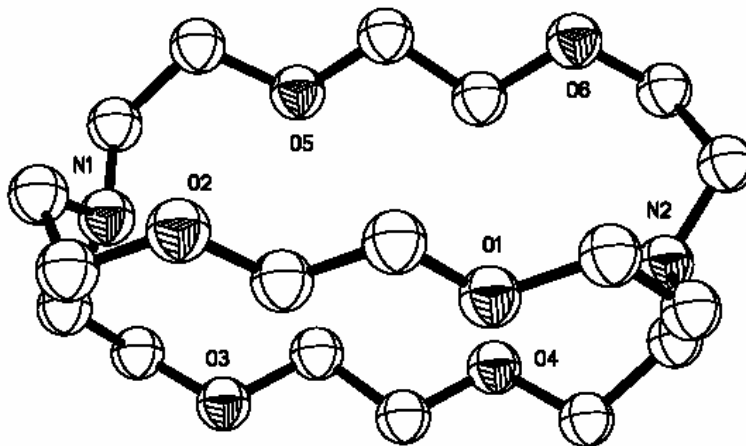


Figure 1-3. X-ray crystal structure of unprotonated cryptand 2.2.2.⁴

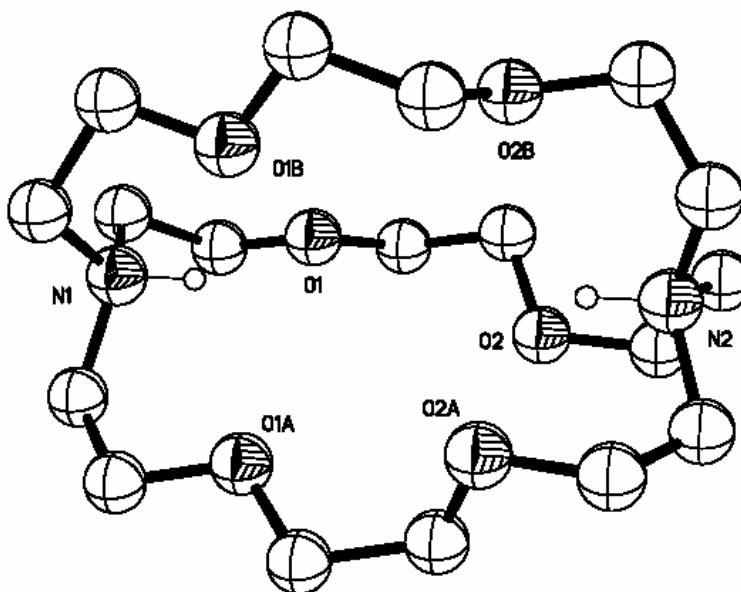


Figure 1-4. X-ray crystal structure of diprotonated cryptand H₂2.2.2.²⁺.⁵

Although these ligands are easily protonated, cryptands form very strong metal complexes. Cryptand refers specifically to the ligand, and the term cryptate is used exclusively to describe a metal-ligand complex. The stability constants in H₂O for lead, cadmium, and other ions of interest for 2.2.1 and 2.2.2 are shown in Table 1-1.²

Table 1-1. Formation constants ($\log K_{ML}$) for cryptands 2.2.1 and 2.2.2 in H_2O at $25^\circ C$.^a

	Na^+	K^+	Ca^{2+}	Sr^{2+}	Ba^{2+}	Cd^{2+}	Pb^{2+}
2.2.1	5.4	3.9	6.9	7.3	6.3	9.5	12.4
2.2.2	4.0	5.5	4.5	8.1	9.6	6.8	12.4

^aRef. ⁷.

The data in Table 1-1 provide evidence for the inherent selectivity of 2.2.1 and 2.2.2 for the toxic heavy metals cadmium and lead over important biological cations such as sodium, potassium, and calcium. Figure 1-5 presents a plot of the $\log K_{ML}$ values versus ionic radius.^{2,8}

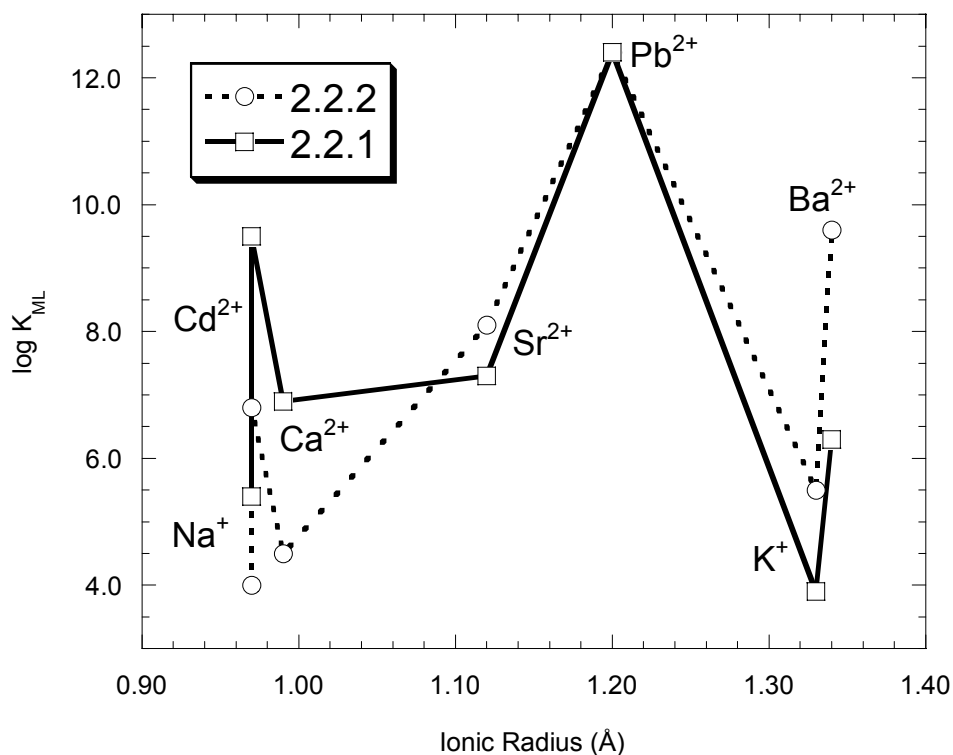


Figure 1-5. Complexation selectivity patterns of 2.2.1 and 2.2.2.^{2,8}

The binding constant selectivity sequences in 2.2.1 and 2.2.2 are $Pb^{2+} > Cd^{2+} > Sr^{2+} > Ca^{2+} > Ba^{2+} > Na^+ > K^+$ and $Pb^{2+} > Ba^{2+} > Sr^{2+} > Cd^{2+} > K^+ > Ca^{2+} > Na^+$, respectively. From this diagram, it is clear that the cryptands are selective with respect to

charge (2.2.1 and 2.2.2: $\text{Pb}^{2+} > \text{K}^+$) and size (2.2.1: $\text{Na}^+ > \text{K}^+$; 2.2.2: $\text{K}^+ > \text{Na}^+$). This figure also demonstrates the correlation between cavity size and cation diameter evident by the preference of smaller cations sodium, cadmium and calcium for the smaller cryptand 2.2.1 in comparison with 2.2.2. The medium-sized cations strontium and lead bind with equal strength for both cryptands and the larger cations potassium and barium prefer the larger cryptand 2.2.2. The solid-state structures for several cryptates have been solved.^{4,9-12} Figures 1-6 and 1-7 show the potassium and lead 2.2.2 cryptates, respectively, in order to compare the complexes in the solid-state. The potassium cryptate is an eight coordinate complex with the metal in the center position of the cavity and bound to all eight donor atoms of the cryptand. The average K-N and K-O distances are 2.87 Å and 2.79 Å.¹⁰ Cryptand 2.2.2 is able to contract around the potassium cation with a geometry that is intermediate between a bicapped trigonal prism and a bicapped trigonal antiprism.¹⁰ The N...N non-bonding distance is 5.75 Å.¹⁰

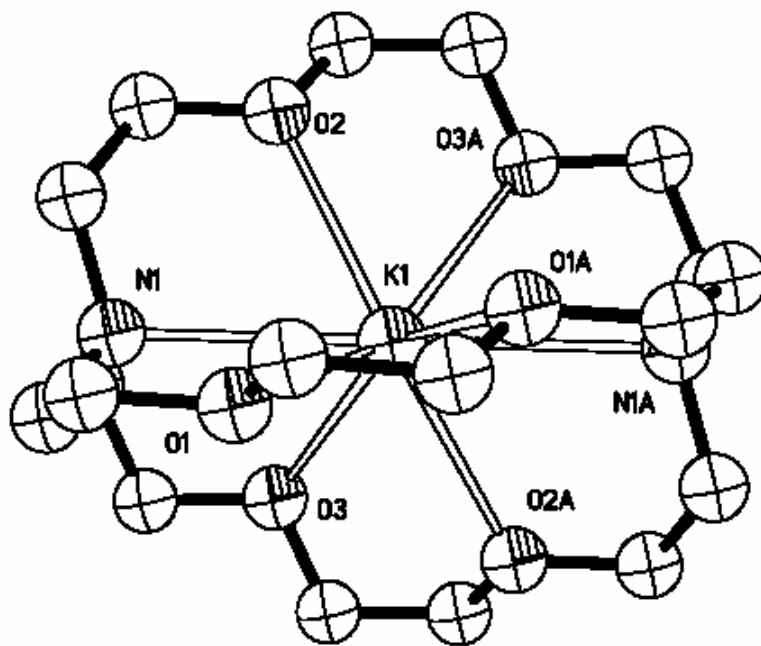


Figure 1-6. X-ray crystal structure of $2.2.2 \cdot \text{K}^+$.¹⁰

Lead forms a ten-coordinate cryptate complex involving all eight donor atoms from cryptand 2.2.2 and a sulfur and nitrogen atom from separate thiocyanate anions. The geometry can be described as a hexagonal pyramid with a trigonally capped base.¹² The Pb-N distances are 2.858 Å and 2.909 Å, Pb-O distances range from 2.729 Å to 2.980 Å, and the thiocyanate distances are 2.642 Å for the nitrogen and 3.121 Å for the sulfur.¹²

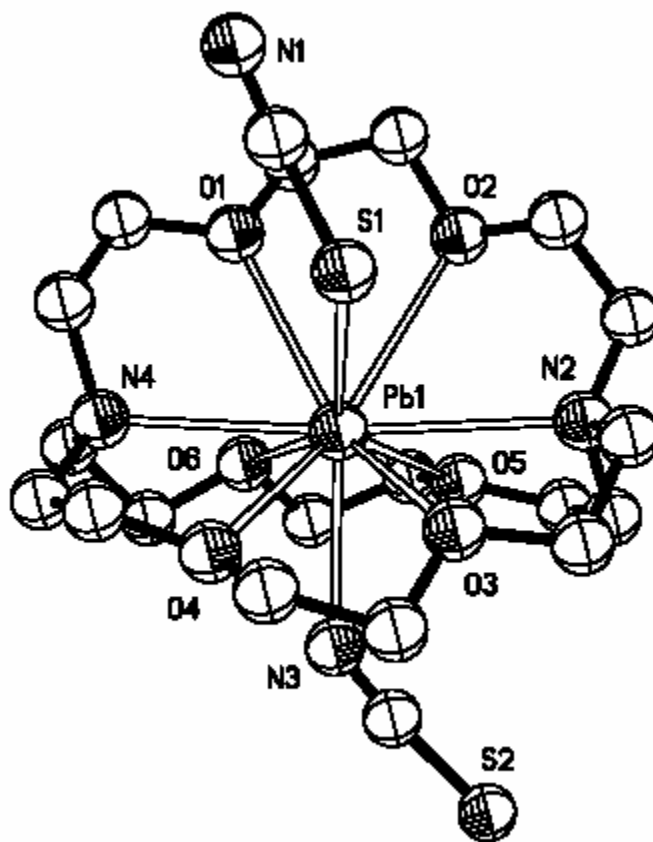


Figure 1-7. X-ray crystal structure of 2.2.2·Pb²⁺·NCS⁻·SCN⁻.¹²

Cryptand 2.2.2 contracts around the lead cation and the N··N non-bonding distance is 5.76 Å. The lead and potassium cryptates in the solid-state differ slightly in coordination number (10 vs. 8) and the lead and potassium cryptates have nearly identical average metal-oxygen (2.80 Å vs. 2.79 Å) and metal-nitrogen distances (2.88 Å vs. 2.87 Å) and

N \cdots N non-bonding distances (5.76 Å vs. 5.75 Å). However, in solution the formation constants ($\log K_{ML}$) differ greatly (12.4 vs. 3.9). Cryptand 2.2.2 is very flexible, evident by the range of N \cdots N non-bonding distances in the solid-state structures of the cations calcium (5.44 Å)⁹, strontium (5.69 Å)¹³, and barium (5.99 Å)¹¹.

The metal complexation properties of cryptands can be altered by variation of several structural factors. These include the number and type of donor atoms (Figure 1-1), the addition of backbone substituents into the bridging chains, and by the type of bridgehead atoms (alkyl N vs. C vs. aryl N). The introduction of one and two benzene rings into the bridging ether strands has been investigated by several groups.¹⁴⁻¹⁸ Cryptand 2.2_B.2_B includes benzene rings in the center of two of the polyether strands and is shown in Figure 1-8. The benzo rings present in 2.2_B.2_B also allow for attachment of other functional groups onto the cryptand.¹⁶

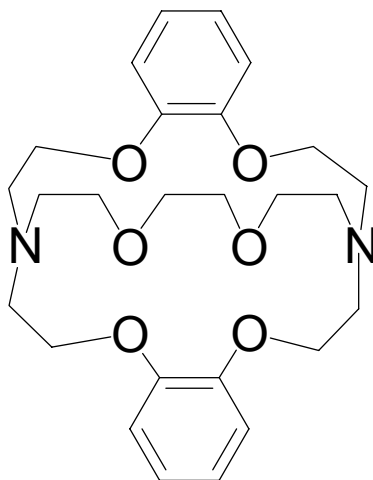


Figure 1-8. Cryptand 2.2_B.2_B.

A comparison of the solid-state structure properties of the parent cryptand 2.2.2 with the benzo-substituted cryptand 2.2_B.2_B is shown in Table 1-2. The benzo-substituted cryptand is distinctly different than the parent compound. Cryptand 2.2_B.2_B has lower

conformational freedom dictated by the eclipsed configuration of the oxygen atom pairs (4, 7), and (13, 16) connected to the benzene rings.¹⁹

Table 1-2. Structural parameters for 2.2.2 and 2.2_B.2_B.

	2.2.2 ⁴	2.2 _B .2 _B ¹⁹
Space Group	P2 ₁ /c	P2 ₁ /c
N;N Conformation	Endo-Endo	Endo-Endo
Donor atom arrangement	Endo: O4, O16, O24 Exo: O7, O13, O21	Endo: O4, O7, O21 Tangential: O13, O16 Exo: O24
N···N Distance (Å)	6.871	5.161
OCCO Torsion Angles (°)	O4-O7: -175 O13-O16: -178 O21-O24: 179	O4-O7: -4.8 O13-O16: -6.1 O21-O24: 71.4

For 2.2_B.2_B, the N···N non-bonding distance is greatly reduced to 5.161 Å and only one oxygen is pointing away from the cavity. These differences in structure indicate that smaller conformational changes will be required during the formation of metal complexes.¹⁹ The formation constants for 2.2_B.2_B for selected metals are shown in Table 1-3.

Table 1-3. Formation constants (log K_{ML}) for 2.2.2 and 2.2_B.2_B in H₂O at 25 °C.

	Na ⁺	K ⁺	Ca ²⁺	Sr ²⁺	Ba ²⁺	Pb ²⁺
2.2.2 ^a	4.0	5.5	4.5	8.1	9.6	12.4
2.2 _B .2 _B	3.4 ^b	4.4 ^b	3.5 ^c	6.4 ^c	5.7 ^c	11.4 ^d

^aRef. 7. ^bRef. 20. ^cRef. 21. ^dRef. 22

The K_{ML} values for cryptand 2.2_B.2_B are all lower in magnitude in comparison to 2.2.2. The basicity of the oxygen atoms next to the benzene rings and the flexibility of

the two bridging strands containing benzene rings are reduced.¹⁴ The selectivity sequence among divalent cations changes from $\text{Pb}^{2+} > \text{Ba}^{2+} > \text{Sr}^{2+} > \text{Ca}^{2+}$ in 2.2.2 to $\text{Pb}^{2+} > \text{Sr}^{2+} > \text{Ba}^{2+} > \text{Ca}^{2+}$ in 2.2_B.2_B.^{7,14,21} Figure 1-9 shows the differences in complex formation constants in solution between cryptand 2.2_B.2_B, the parent compound 2.2.2, and cryptand 2.2.1.^{14,21} Cryptand 2.2_B.2_B shows a more specific size restriction towards the larger cations similar to 2.2.1.

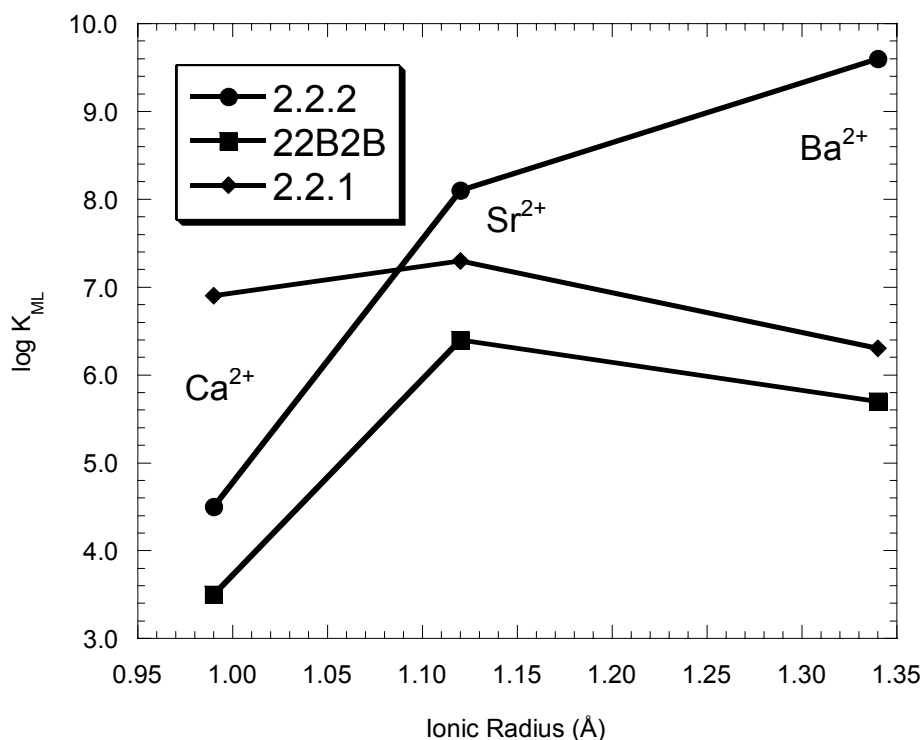


Figure 1-9. Complexation selectivity patterns of 2.2.2, 2.2_B.2_B, and 2.2.1.^{7,21}

The alkyl cryptands 2.2.1, 2.2.2, and 2.2_B.2_B all have high K_{H1} values ($K_{\text{H1}} \sim 9$ -10.5; $K_{\text{H2}} \sim 6$ -7.5). Protonation constants in this range result in the metal formation constants being dependent on pH near physiological pH (~ 7), and also result in the cryptands being present mainly as the mono- and diprotonated forms at physiological pH (Fig. 1-2).²³ The latter results in a slower reaction between the metal ion and protonated cryptand. Tsien overcame both of these problems in designing calcium indicators and

buffers by the addition of benzene rings.²³ Figure 1-10 shows the structural modification of EGTA to obtain BAPTA by the incorporation of benzene rings.

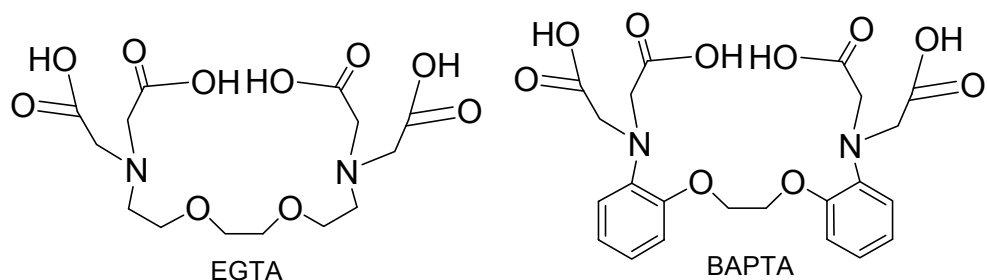


Figure 1-10. Structures of EGTA and BAPTA.

Table 1-4 illustrates the effects of introduction of benzene rings on the highest protonation constants (K_H) and metal formation constants (K_{ML}) at 25°C.⁷ The K_H 's and K_{ML} 's decrease by three orders of magnitude for BAPTA, but the selectivity ($K_S = K_{M^*L}/K_{ML}$) for Pb^{2+} vs. Ca^{2+} actually increases from 5,500 to 33,000.

Table 1-4. Formation constants ($\log K_{ML}$) for EGTA and BAPTA in H_2O at 25°C.⁷

	$H^+(1)$	$H^+(2)$	Ca^{2+}	Pb^{2+}	Cd^{2+}
EGTA	9.52	8.71	10.86	14.6	16.5
BAPTA	6.32	5.45	6.78	11.3	12.2

To employ the strategy of Tsien, the use of polyoxa dianilines as the α,ω -diamine results in cryptands with bridgehead nitrogen atoms that are less basic than the trialkyl amines of the parent cryptands. Several benzoannelated cryptands have been synthesized, but these compounds contained additional substituents (fluorophore).²⁴⁻²⁶ These cryptands were developed as receptors for specific cations, while also reducing the competitive protonation reaction. Protonation constants have not been reported for the bridgehead nitrogens. Crossley and co-workers developed a 2.2.2 benzoannelated cryptand derivative (I) for use as an extracellular fluorescent probe for potassium ion.²⁴

Smith and co-workers have prepared a 2.2.1_N benzoannelated cryptand (II) as a selective indicator for intracellular free sodium ion ($\log K_{ML} = 1.3-1.6$) that utilizes either changes in fluorescence or ¹⁹F-NMR chemical shift²⁷, and Mortellaro et al. proposed the synthesis of a 3.1.1 benzoannelated cryptand derivative (III).²⁸ Crossley et al.²⁴ and Smith and co-workers^{26,27} evaluated complexation for sodium, potassium, and other alkali and alkaline-earth cations. These benzoannelated cryptands are shown in Figure 1-11.

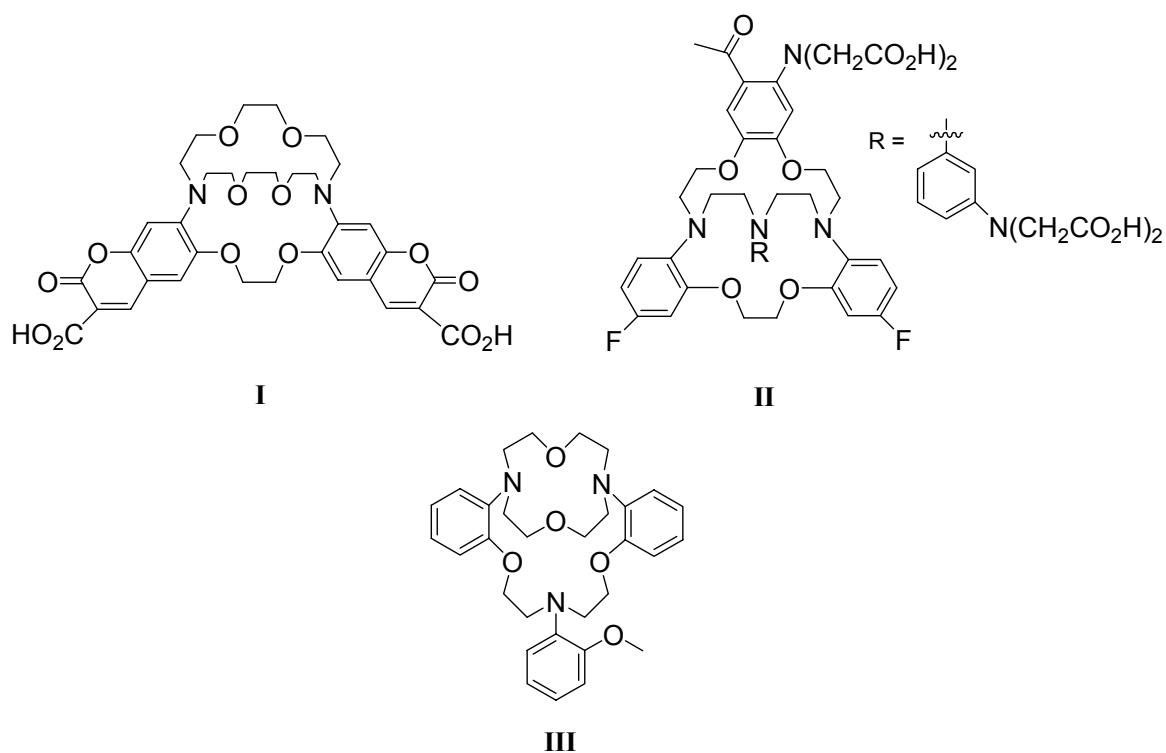


Figure 1-11. Benzoannelated cryptands.

II. Metal Toxicity

Cryptands 2.2.1, 2.2.2, and 2.2_B.2_B have shown favorable selectivity for lead and cadmium versus the biologically important cations Na⁺, K⁺, and Ca²⁺. The large log K_{ML} values (Cd2.2.1 = 9.5; Pb2.2.1, Pb2.2.2, Pb2.2_B.2_B ≥ 11.4) are also sufficient to react with low concentrations of these metals ([M] ≤ 10⁻⁶). The Agency for Toxic Substances and Disease Registry (ATSDR) as well as the Environmental Protection Agency (EPA) rank lead and cadmium as the second and seventh most important substances, respectively, on the list of priority of hazardous substances.²⁹ The internal exposure of lead to the human body can either occur from inhalation or oral consumption. Acute exposure to high levels of lead may result in brain damage, kidney damage, and gastrointestinal distress, while chronic exposure results in effects on the central nervous system, blood pressure, kidneys, and vitamin D metabolism.³⁰ Evidence suggests that lead toxicity may occur at levels as low as 10-15 µg/dL (4.8-7.2 x 10⁻⁷ M).²⁹ The vast dispersion of lead in the environment is primarily due to industrial usage and previous use as an antiknock agent in leaded gasoline.³¹ In 1990, the Clean Air Act Amendments banned the sale of leaded gasoline.²⁹ Lead is the fifth most consumed metal in the United States with 85% being produced domestically.²⁹ Exposure to lead can occur through a variety of avenues including the atmosphere, food, soil, water, and lead-based paint.³⁰ In an aqueous medium, the solubility of lead approaches 110 ppb (5.3 x 10⁻⁷ M) at a pH of 6.5, and above pH 8 it is approximately 10 ppb (4.8 x 10⁻⁸ M).³⁰

Although cadmium toxicity effects have been seen by both inhalation and oral exposure, the greatest concern are long-term oral exposures.³² At acute levels, cadmium potentially causes nausea, vomiting, diarrhea, muscle cramps, salivation, sensory

disturbances, liver injury, convulsions, shock and renal failure. Chronic exposure to cadmium can result in cardiovascular, hematological, neurological, and testicular effects.²⁹ The maximum contaminant level (MCL) for cadmium in drinking water is 0.005 mg/L (4.4×10^{-8} M).³² Distribution of cadmium in the environment is caused by natural occurrences in zinc, lead, and copper ores as well as in coal, fossil fuels, and the release in volcanic action.²⁹ The industrial release of cadmium occurs through many methods, some of which include leaching of landfills, waste streams from smelting and refining of zinc, and the manufacture of nickel-cadmium batteries.²⁹

III. Objective

The purpose of this project is to synthesize "anilino" cryptand derivatives An2.2.1, An2.2.2, and An3.1.1 with the expectation that selectivity for Pb^{2+} and Cd^{2+} will be retained and cryptands will have large $\log K_{\text{ML}}$ values. It will also be expected that the cryptands will have $\log K_{\text{Hi}} < 6.5$ based on the BAPTA/EGTA structural modifications. These compounds would then have minimal protonation side reactions at physiological pH and could have potential uses as components for sensors. The types of modifications investigated in this specific project include the length of bridging chains (cavity size) and the incorporation of benzylic rings (acid-base chemistry, conformation). The benzoannelated cryptands synthesized in this project are shown in Figure 1-12. Cryptands An3.1.1 and An3.1.1.3 are shown in parentheses because they were made but the solution properties were not studied.

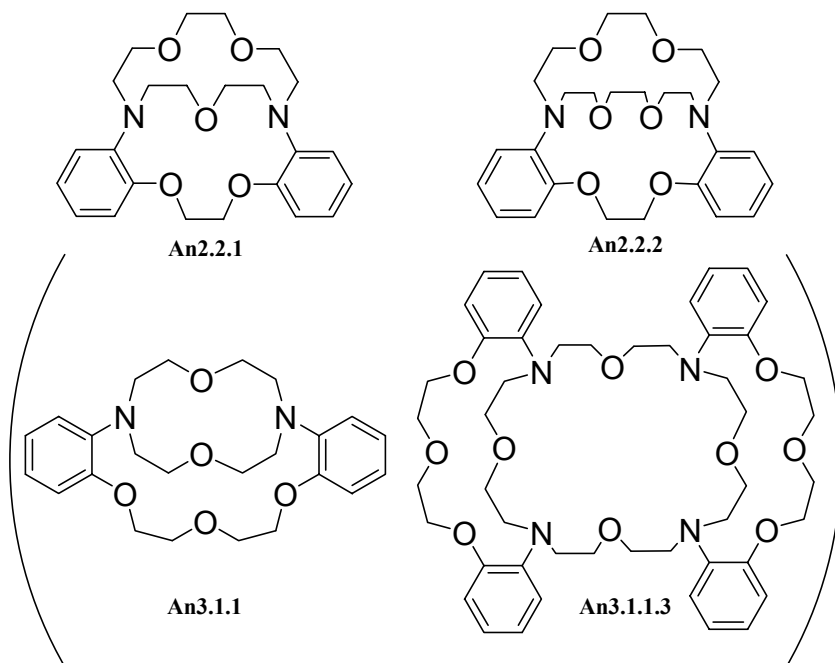


Figure 1-12. Benzoannelated cryptands An2.2.1, An2.2.2, An3.1.1, and An3.1.1.3.

The prefix “An” is used to indicate that the nitrogens are “aniline” type nitrogens because of the presence of the benzene rings. The protonation and metal formation constants of the prepared benzoannelated cryptands An2.2.1 and An2.2.2 will be determined to evaluate the effects of the addition of benzylic rings by comparing with the known values for the parent cryptands 2.2.1, 2.2.2, and 2.2_B.2_B. Comparison of the protonation constants will reveal the effects of aniline (aryl) versus alkyl bridgehead nitrogens. The comparison of the metal formation constants will reveal the effects of the benzene rings that limit conformational freedom and decreases the basicity of the attached donor atoms. Comparison of cryptands 2.2_B.2_B and An2.2.2 will reveal the importance of position of the benzene rings. The benzo rings in cryptand 2.2_B.2_B resulted in a decrease in basicity of the attached oxygen atoms and limited the conformational freedom of these two bridges.¹⁴ Cryptand An2.2.2 will have the conformational freedom limited in one bridge and the benzene rings have the potential to decrease the basicity of one oxygen pair and the bridgehead nitrogens. Comparisons will be made between the benzoannelated cryptands in terms of the effects of the number of donor atoms present (An2.2.1 vs. An2.2.2) and cavity size (An2.2.1 vs. An2.2.2). The metals studied in this project will include the biologically important cations Na⁺, K⁺, and Ca²⁺, alkaline earth cations Sr²⁺ and Ba²⁺, and the toxic heavy metals Cd²⁺ and Pb²⁺.

References

- (1) Dietrich, B.; Lehn, J. M.; Sauvage, J. P. *Tetrahedron Lett.* **1969**, *34*, 2885-2888.
- (2) Dietrich, B. In *Comprehensive Supramolecular Chemistry*; Gokel, G. W., Ed.; Elsevier Science Inc.: New York, 1996; Vol. 1, pp 153-212.
- (3) Lehn, J. M.; Sauvage, J. P. *J. Am. Chem. Soc.* **1975**, *97*, 6700-6707.
- (4) Metz, B.; Moras, D.; Weiss, R. *J. Chem. Soc. Perkin Trans. 2* **1976**, 423-429.
- (5) Atwood, J. L.; MacGillivray, L. R. *J. Org. Chem.* **1995**, *60*, 4972-4973.
- (6) Lehn, J. M. *Struct. Bonding* **1973**, *16*, 1-69.
- (7) Smith, R. M.; Martell, A. E., 6.0 ed., 2001.
- (8) *CRC Handbook of Chemistry and Physics*, 71st ed.; CRC Press inc.: Boca Raton, 1990-1991.
- (9) Metz, B.; Moras, D. *Acta Cryst. B.* **1973**, *29*, 1377.
- (10) Metz, B.; Moras, D.; Weiss, R. *Chem. Commun.* **1971**, 444-445.
- (11) Metz, B.; Moras, D.; Weiss, R. *J. Am. Chem. Soc.* **1971**, *93*, 1806-1808.
- (12) Weiss, R.; Metz, B. *Inorg. Chem.* **1974**, *13*, 2094-2098.
- (13) Chekhlov, A. N. *Koord. Khim.* **2004**, *30*, 410.
- (14) Buschmann, H.-J.; Dantz, D. A.; Schollmeyer, E. *Polyhedron* **1998**, *17*, 1891-1895.
- (15) Taylor, R. W.; Bemtgen, J. M.; Springer, M. E.; Loyola, V. M.; Wilkins, R. G. *Inorg. Chem.* **1984**, *23*, 3348-3353.
- (16) Gansow, O. A.; Kausar, A. R.; Triplett, K. B. *J. Heterocyclic Chem.* **1981**, *18*, 297-302.
- (17) Cox, B. G.; Firman, P.; Schneider, H.; Schneider, I. *Inorg. Chim. Acta* **1981**, *49*, 153-158.
- (18) Lehn, J. M.; Dietrich, B.; Sauvage, J. P. *J. Chem. Soc., Chem. Commun.* **1973**, 15-16.
- (19) Taylor, R. W.; Ott, N. L.; Barnes, C. L.; Van Der Helm, D. *Acta Cryst.* **1982**, *B38*, 2277-2280.
- (20) Chantooni, M. K. J.; Kolthoff, I. M. *Proc. Natl. Acad. Sci.* **1981**, *78*, 7245-7247.
- (21) Cox, B. G.; Schneider, H.; Truong, N. v. *J. Am. Chem. Soc.* **1984**, *106*, 1273-1280.
- (22) Craig, M. E. Ph. D. Thesis. University of Oklahoma, Norman, OK, 1990.
- (23) Tsien, R. Y. *Biochemistry* **1980**, *19*, 2396-2404.
- (24) Crossley, R.; Goolamali, Z.; Sammes, P. G. *J. Chem. Soc., Perkin Trans. 2* **1994**, 1615-1623.
- (25) Prasanna de Silva, A.; Nimal Gunaratne, H. Q.; Samankumara Sarchanayake, K. R. A. *Tetrahedron Lett.* **1990**, *31*, 5193-5196.
- (26) Smith, G. A.; Kirschenlohr, H. L.; Metcalfe, J. C.; Clarke, S. D. *J. Chem. Soc. Perkin Trans. 2* **1993**, 1205-1209.
- (27) Smith, G. A.; Hesketh, T. R.; Metcalfe, J. C. *Biochem. J.* **1988**, *250*, 227-232.
- (28) He, H.; Mortellaro, M. A.; Leiner, M. J. P. In *European Patent Application: Europe*, 2001, pp 1-47.
- (29) U.S. Agency for Toxic Substances and Disease Registry Home Page. www.atsdr.cdc.gov/tfacts13 (accessed Feb. 2002).

- (30) U.S. Agency for Toxic Substances and Disease Registry Home Page.
www.atsdr.cdc.gov/interactionprofiles/ip04 (accessed Nov. 2003).
- (31) U. S. Environmental Protection Agency. *Lead Poisoning and Your Children*.
Government Pamphlet. 2000.
- (32) U. S. Environmental Protection Agency Home Page.
www.epa.gov/OGWDW/dwh/t-ioc/cadmium (accessed Nov. 2003).

Chapter Two

Synthesis of starting materials, monocyclic and bicyclic diamides and diamines

I. Introduction

The syntheses described in this work are accomplished using the stepwise cyclization method. This allows for flexibility in structure alterations and also provides multiple synthetic routes for a given product. The general step-wise synthesis method for cryptands is shown in Figure 2-1.

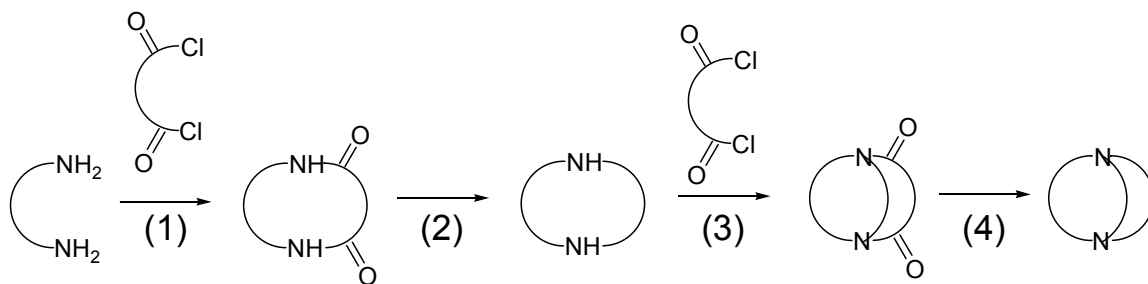


Figure 2-1. General synthetic scheme for the synthesis of cryptands.

Synthesis of the acyclic diamines and, in some cases, the diacid chlorides are necessary before the first cyclization step. Synthesis of the monocyclic diamides is accomplished in a high-dilution reaction between the diamine and diacyl chloride (1). A scavenger base is added for the cyclization steps to react with HCl formed and promote the formation of the ammonium chloride salt as shown in Figure 2-2.

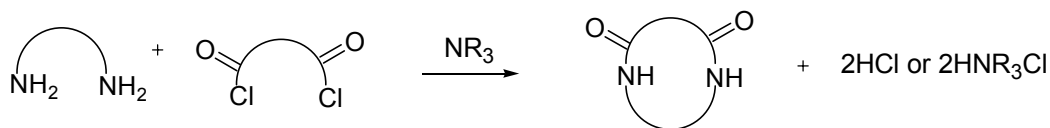
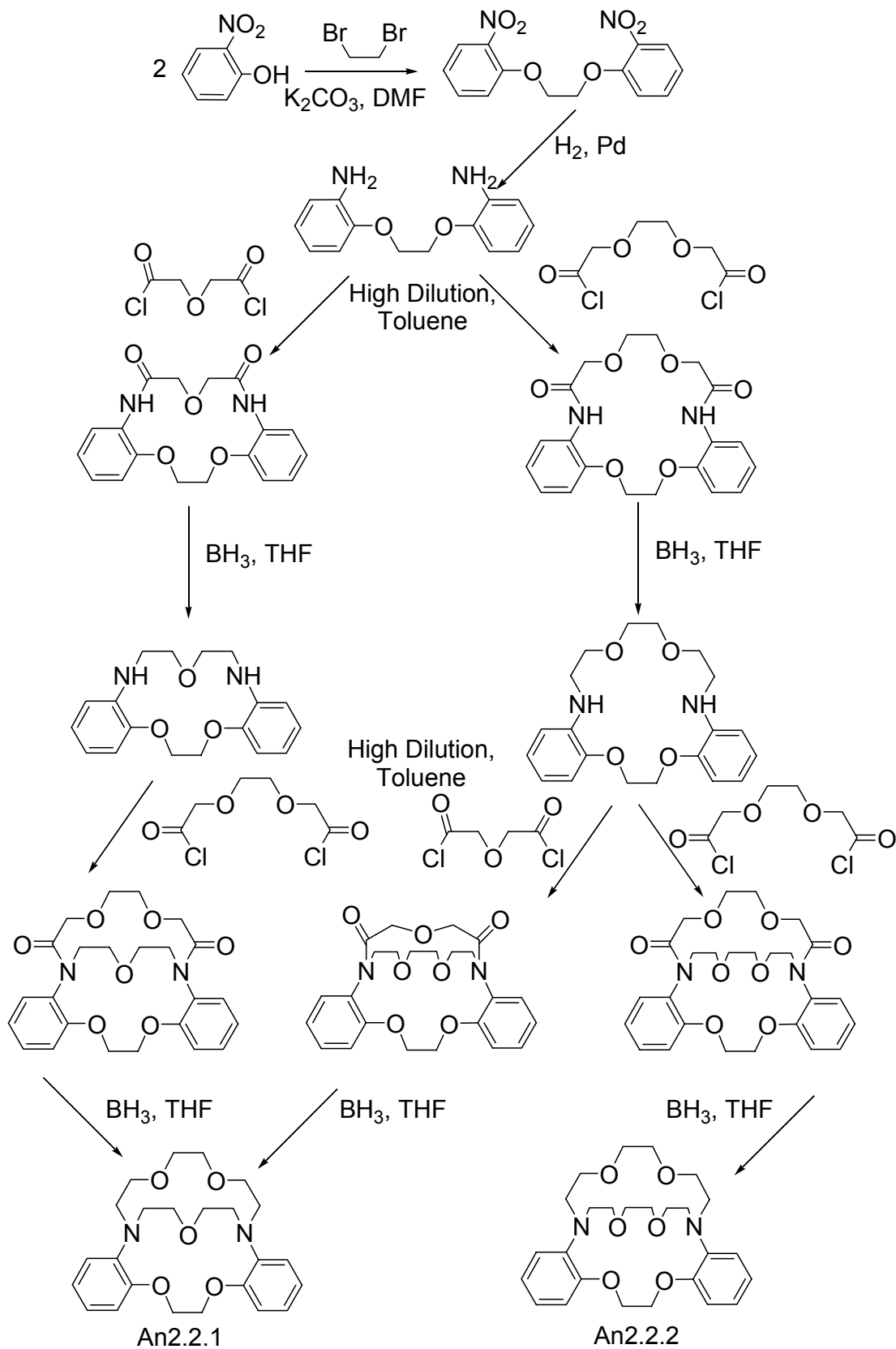
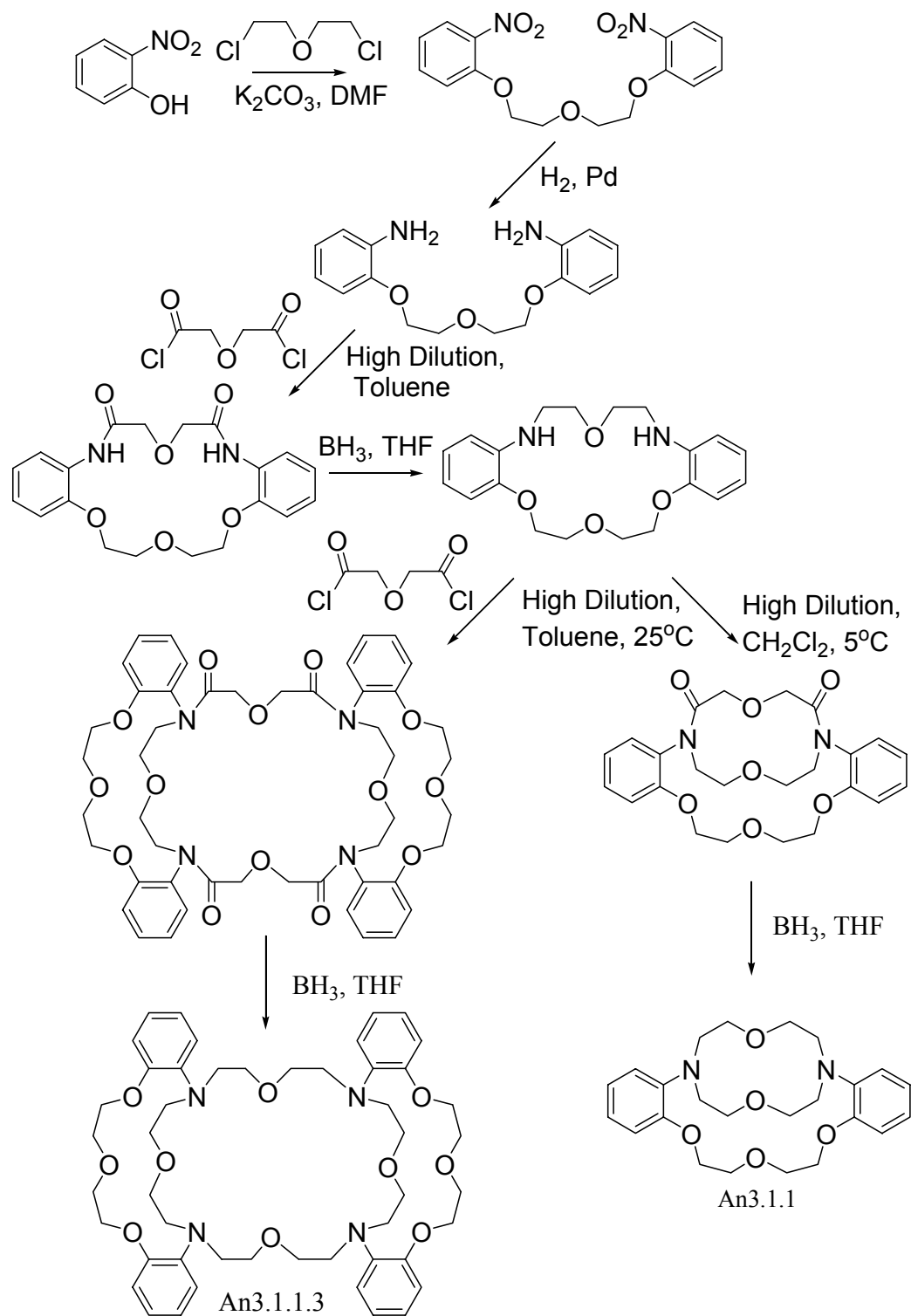


Figure 2-2. Balanced reaction between a diamine and diacid chloride with a scavenger base present.

Reduction of the monocyclic diamide product utilizing diborane is performed in the following step (2). A second high-dilution reaction of the monocyclic diamine with another diacyl chloride generates the bi- or tricyclic diamide (3). Subsequent reduction reaction of the bi- or tricyclic diamide with diborane yields the cryptand (4). The complete synthetic routes for cryptands An2.2.1 and An2.2.2, along with those for cryptands An3.1.1 and An3.1.1.3 are shown in Schemes 2-1 and 2-2, respectively. The general descriptions and specific details of the reactions involved in these synthetic schemes are presented in the following sections.



Scheme 2-1. Synthesis of An2.2.1 and An2.2.2.



Scheme 2-2. Synthesis of An3.1.1.3 and An3.1.1.

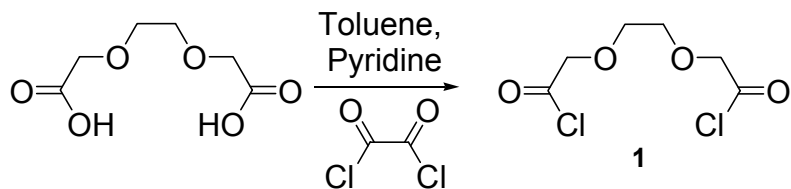
II. Summaries of Synthetic Methods

This section provides a general description for the synthetic steps to obtain the final cryptands An2.2.1, An2.2.2, An3.1.1, and An3.1.1.3. The specific details of each reaction, ^1H and ^{13}C NMR spectra, electrospray ionization mass spectrometry (ESI-MS) spectra, and X-ray crystal structures are located in the subsequent Experimental section.

A. Synthesis of acyclic diamines and starting materials

1. 2,2'-[ethane-1,2-diylbis(oxy)]diacetyl chloride, (**1**)

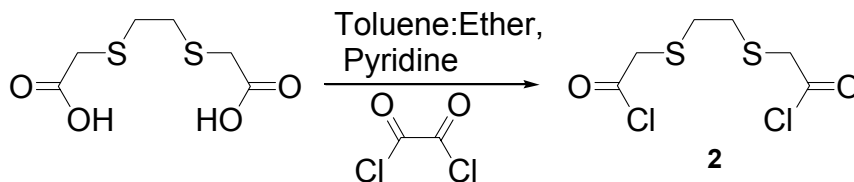
2,2'-[ethane-1,2-diylbis(oxy)]diacetic acid is chlorinated with ethanedioyl dichloride in toluene with a trace amount of pyridine present as shown in Scheme 2-3. Ethanedioyl dichloride is used in this exchange reaction because the by product oxalic acid decomposes to CO and CO₂. The removal of oxalic acid drives the equilibrium of the reaction to produce the acyl chloride in high yield.¹ Acid chlorides are the least stable carboxylic acid derivatives;² therefore, purification of the product is performed as quickly as possible with minimum exposure to water. Recrystallization is accomplished by dissolving the product in a mixture of ether and petroleum ether. The diacid chloride is frozen by submerging the flask in a mixture of dry ice and acetone with a temperature of -70 °C. The product is brought back to room temperature and the solvent, containing starting material and, impurities, is removed using a pipet.



Scheme 2-3. Synthesis of 2,2'-[ethane-1,2-diylbis(oxy)]diacetyl chloride, (**1**).

2. 2,2'-[ethane-1,2-diylbis(thio)]diacetyl chloride, (**2**)

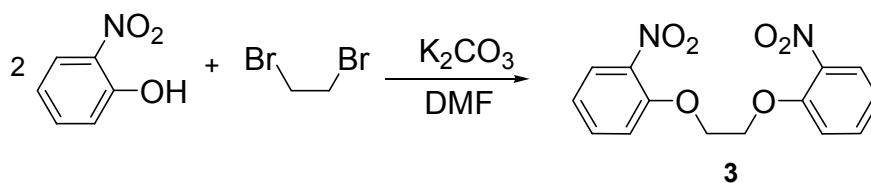
2,2'-[ethane-1,2-diylbis(thio)]diacetic diacid is a sulfur substituted dicarboxylic acid that can also be chlorinated with ethanedioyl dichloride as shown in Scheme 2-4. The reaction is performed in a mixture of toluene and dry ether. The product was recrystallized according to the methods used for **1** to give light yellow crystals.



Scheme 2-4. Synthesis of 2,2'-[ethane-1,2-diylbis(thio)]diacetyl chloride, (**2**).

3. 1,1'-[ethane-1,2-diylbis(oxy)]bis(2-nitrobenzene), (**3**)

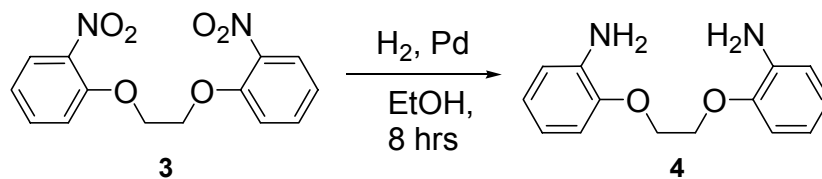
2-nitrophenol was alkylated with 1,2-dibromoethane in DMF with K_2CO_3 present as a base, to give the nitrobenzene bis-ether as shown in Scheme 2-5. This procedure was similar to the methods used by Sammes et al.³ The product was purified by recrystallization from glacial acetic acid.



Scheme 2-5. Synthesis of 1,1'-[ethane-1,2-diylbis(oxy)]bis(2-nitrobenzene), (**3**).

4. 2,2'-[ethane-1,2-diylbis(oxy)]dianiline, (**4**)

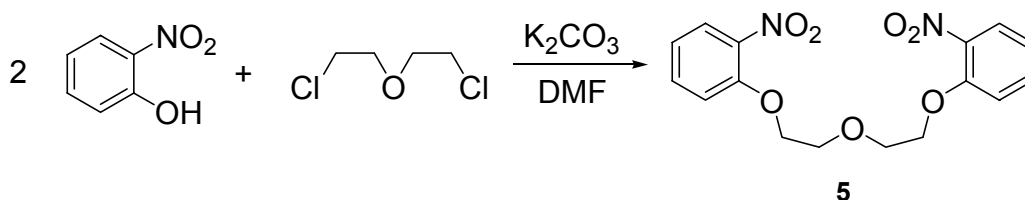
Catalytic reduction of the nitro groups on **3**, as shown in Scheme 2-6, was accomplished by the process employed by Sammes et al.³ The diamine product was separated from the catalyst by filtration after hydrogen uptake had ceased.



Scheme 2-6. Synthesis of 2,2'-[ethane-1,2-diylbis(oxy)]dianiline, (**4**).

5. 1,1'-[oxybis(2,1-ethanedioxy)]bis[2-nitro-benzene], (**5**)

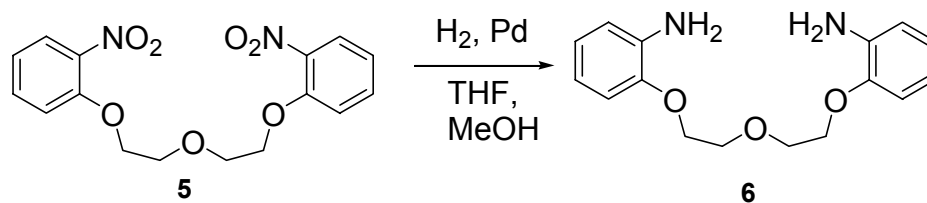
Alkylation of 2-nitrophenol with bis(2-chloroethyl) ether in DMF with K_2CO_3 present as a base, gave the dinitro-compound, **5** as shown in Scheme 2-7. The pure product was obtained by recrystallization from methanol. This procedure was similar to the methods described by Lockhart et al.⁴



Scheme 2-7. Synthesis of 1,1'-[oxybis(2,1-ethanedioxy)]bis[2-nitro-benzene], (**5**).

6. 2,2'-[oxybis(ethane-2,1-dioxy)]dianiline, (**6**)

The nitro groups on **5** were reduced by catalytic reduction as shown in Scheme 2-8. The diamine product, **6**, was separated from the catalyst by filtration after hydrogen uptake had finished.

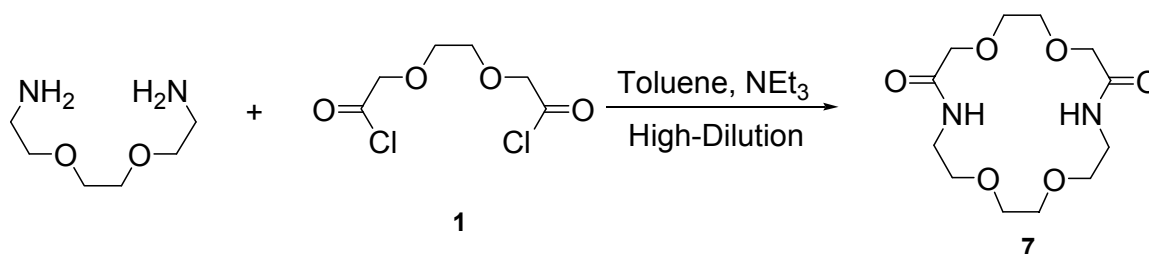


Scheme 2-8. Synthesis of 2,2'-[oxybis(ethane-2,1-dioxy)]dianiline, (**6**).

B. Synthesis of monocyclic diamides and diamines

7. 1,4,10,13-tetraoxa-7,16,diazacyclooctadecane-6,17-dione, 2.2*, (7)

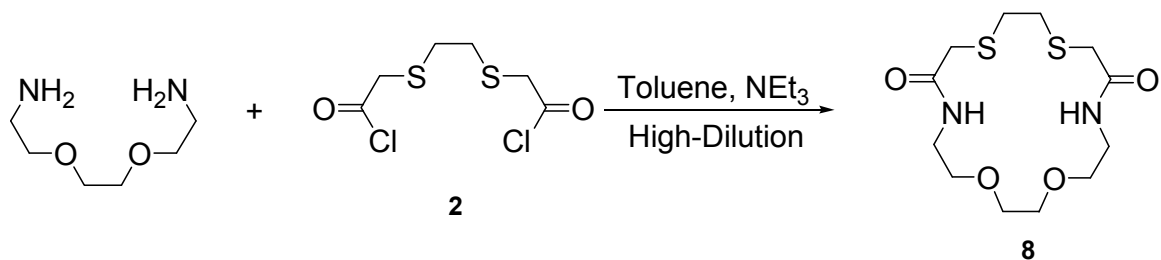
Acylation of the diamine, 2,2'-[ethane-1,2-diylbis(oxy)]diethanamine with **1** was accomplished under high-dilution conditions in toluene as shown in Scheme 2-9. The precipitation of triethylammonium chloride during the reaction was evident on the sides of the flask. This salt was separated by filtration and the pure diamide, **7**, was recrystallized from a benzene-heptane mixture.



Scheme 2-9. Synthesis of 2.2*, (7).

8. 1,4-Dioxa-10,13-dithia-7,16-diazacyclooctadecane-8,15-dione, 2.2_S*, (8)

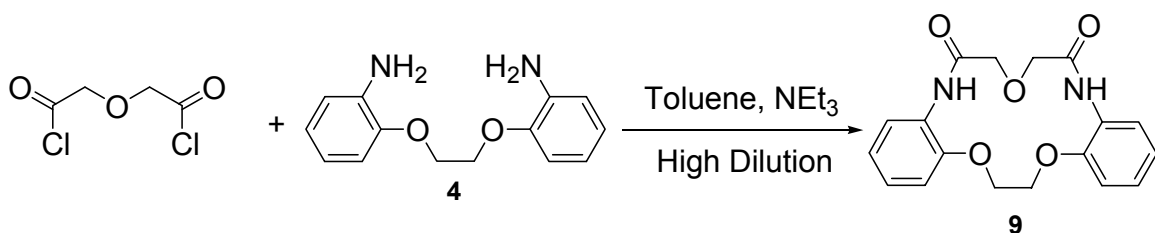
The acylation of the diamine, 2,2'-[ethane-1,2-diylbis(oxy)]diethanamine with **2** was performed under high-dilution conditions in toluene to give the dithiadiamide as shown in Scheme 2-10. Triethylammonium chloride precipitated during the reaction and was separated by filtration. The pure diamide, **8**, was recrystallized from a mixture of dichloromethane-hexane.



Scheme 2-10. Synthesis of 2.2_s*, (8).

9. 17,18-dihydro-5*H*,9*H*-dibenzo[*e,n*][1,4,10,7,13]trioxadiazacyclopentadecine-6,10(7*H*,11*H*)-dione, An2.1*, (9)

The acylation of **4** with 2,2'-oxydiacetyl chloride was carried out under high-dilution conditions in toluene by methods similar to those described by Formanovskii et al⁵ as shown in Scheme 2-11. Triethylamine was used as an acceptor for hydrogen chloride, which was produced during the reaction. The product was purified by recrystallization from ethanol.

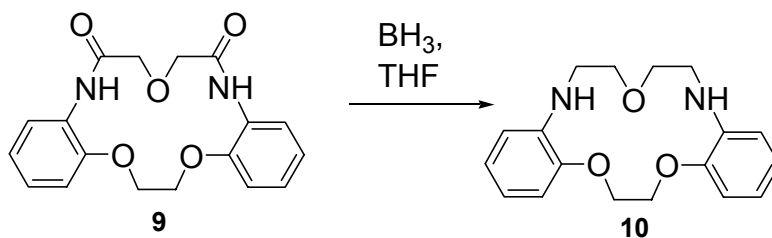


Scheme 2-11. Synthesis of An2.1*, (9).

10. 6,7,10,11,17,18-hexahydro-5*H*,9*H*-dibenzo[*e,n*][1,4,10,7,13]-trioxadiazacyclopentadecine, An2.1, (10)

The monocyclic diamine was prepared by the reduction of **9** in refluxing tetrahydrofuran containing ~ 1 M borane as shown in Scheme 2-12. A solution of 1:10

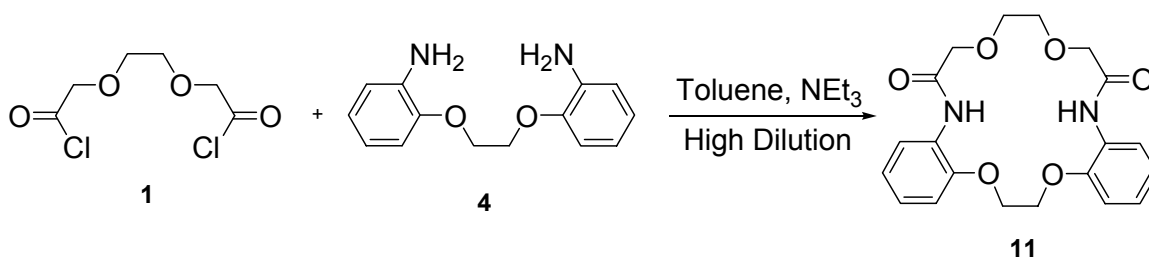
H₂O-THF was added during reflux to aid the reaction in going to completion.^{6,7} Partial evaporation of the organic solvent resulted in the precipitation of the pure product.



Scheme 2-12. Synthesis of An2.1, (**10**).

11. 9,10,20,21-tetrahydro-5*H*,12*H*-dibenzo[*e,q*][1,4,10,13,7,16]tetraoxadiazacyclooctadecine-6,13(7*H*,14*H*)-dione, An2.2*, (**11**)

The acyclic diamine, **4**, is acylated with 2,2'-[ethane-1,2-diylbis(oxy)]diacetyl chloride, **1**, under high-dilution conditions in toluene as shown in Scheme 2-13. Triethylammonium chloride precipitated out during the reaction and was separated by filtration. The pure diamide is recovered by recrystallization from ethanol.

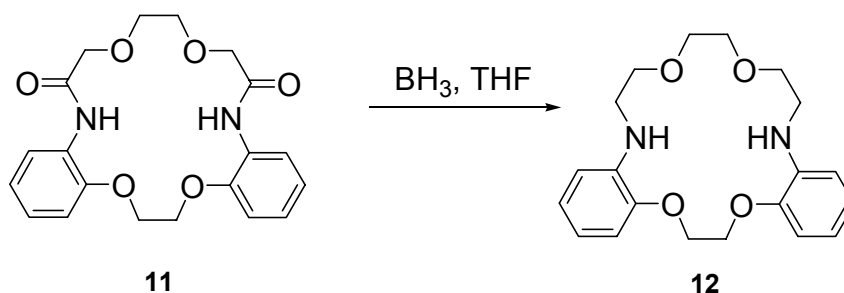


Scheme 2-13. Synthesis of An2.2*, (**11**).

12. 6,7,9,10,13,14,20,21-octahydro-5*H*,12*H*-dibenzo[*e,q*][1,4,10,13,7,16]tetraoxadiazacyclooctadecine, An2.2, (**12**)

Reduction of **11** using 1 M borane in refluxing tetrahydrofuran afforded the monocyclic diamine, **12** as shown in Scheme 2-14. A solution of 1:10 H₂O-THF was

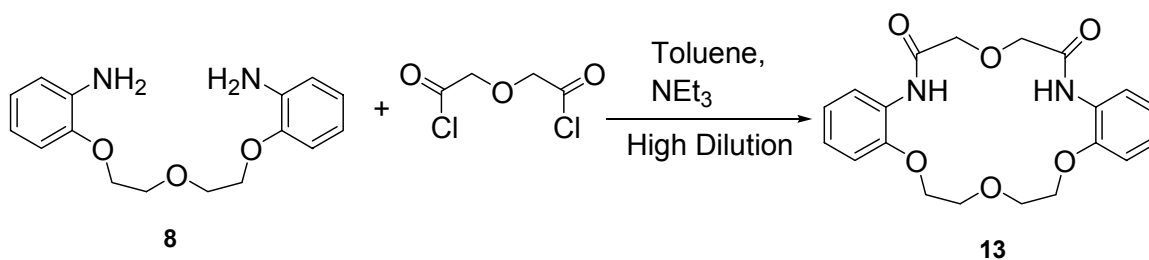
added during reflux to aid the reaction in going to completion.^{6,7} Partial evaporation of the organic solvent resulted in the precipitation of the pure product.



Scheme 2-14. Synthesis of An2.2, (**12**).

13. 6,7,9,10-tetrahydro-16*H*,20*H*-dibenzo[*h,q*][1,4,7,13,10,16]tetraoxadiazacyclooctadecine-17,21(18*H*,22*H*)-dione, An3.1*, (**13**)

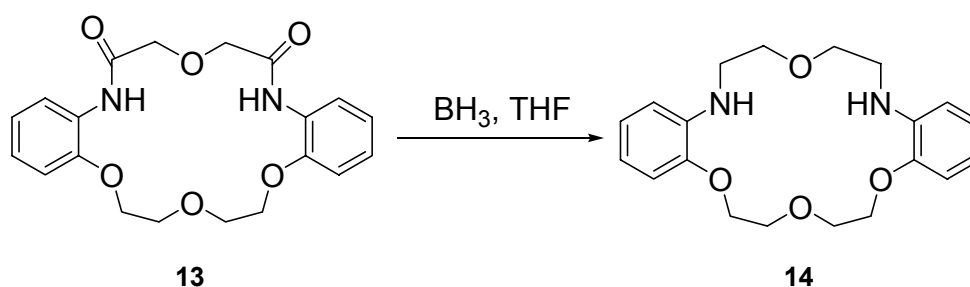
Condensation of **8** with the commercially available 2,2'-oxydiacetyl chloride under high-dilution conditions in toluene yielded the monocyclic diamide, **13**, as shown in Scheme 2-15. Triethylammonium chloride precipitated during the reaction and was separated by filtration. The pure product was recovered by recrystallization from a benzene-heptane mixture.



Scheme 2-15. Synthesis of An3.1*, (**13**).

14. 6,7,9,10,17,18,21,22-octahydro-16*H*,20*H*-dibenzo[*h,q*][1,4,7,13,10,16]tetraoxa-diazacyclooctadecine, An3.1, (**14**)

The monocyclic diamine, **14**, was prepared by the reduction of **13** using 1 M borane in refluxing tetrahydrofuran as shown in Scheme 2-16. A solution of 1:10 H₂O-THF was added during reflux to aid the reaction in going to completion.^{6,7} The organic solvent was removed by rotary evaporation and the pure product was obtained by filtration of the aqueous solution that remained.

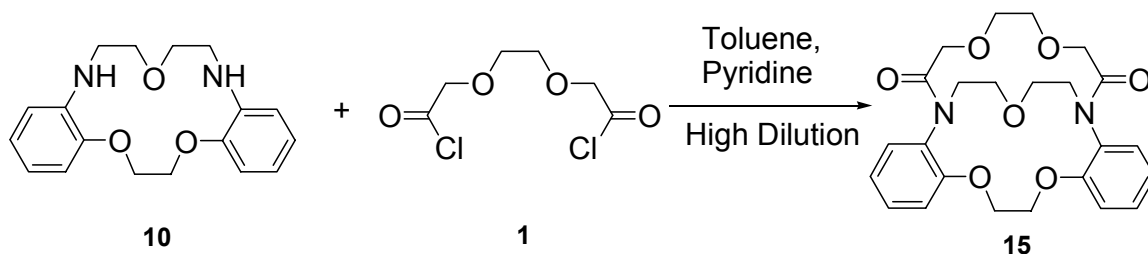


Scheme 2-16. Synthesis of An3.1, (**14**).

C. Synthesis of bicyclic diamines (cryptands)

15. 9,10,20,21-tetrahydro-5,14-(ethanoxyethano)dibenzo[*e,q*][1,4,10,13,7,16]tetraoxa-diazacyclooctadecine-6,13-dione, An2.1.2*, (**15**)

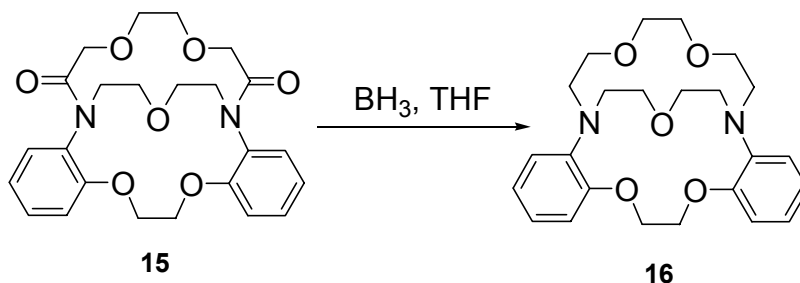
The condensation of **10** with **1** under high-dilution conditions in toluene yielded the bicyclic diamide, **15**, as shown in Scheme 2-17. Pyridine was added as a scavenger base but salt formation was not visible during the reaction. Pyridine was present in the mass spectrum at 80 m/z. Rotary evaporation of the organic solvent left a yellow oil. The polymer products and salts were removed by flash chromatography on silica gel to give the pure product.



Scheme 2-17. Synthesis of An2.1.2*, (**15**).

16. 6,7,9,10,12,13,20,21-octahydro-5,14-(ethanoxyethano)dibenzo[*e,q*]-
[1,4,10,13,7,16]tetraoxadiazacyclooctadecine, An2.2.1, (**16**)

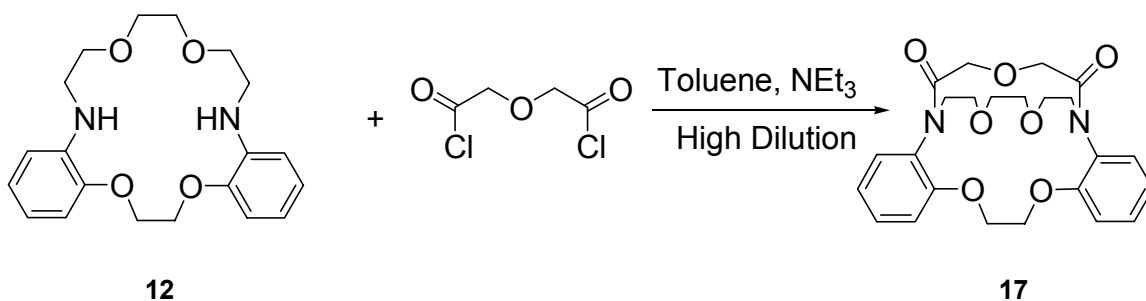
Cryptand An2.2.1, **16**, was prepared by the reduction of **15** using 1 M borane in refluxing tetrahydrofuran as shown in Scheme 2-18. A solution of 1:10 H₂O-THF was added during reflux to aid the reaction in going to completion.^{6,7} Rotary evaporation was used to remove the organic solvent. The aqueous solution was treated with 6 M HCl to hydrolyze any remaining nitrogen to borane bonds.⁸ The solution was made basic with NH₃ and the fully deprotonated ligand was extracted with chloroform. The pure product was obtained by recrystallization from a mixture of benzene and heptane.



Scheme 2-18. Synthesis of An2.2.1, (**16**).

17. 6,7,9,10,12,13,20,21-octahydro-5,14-(ethanooxyethano)dibenzo-[*e,q*]-
[1,4,10,13,7,16]tetraoxadiazacyclooctadecine-23,27-dione, An2.2.1*, (**17**)

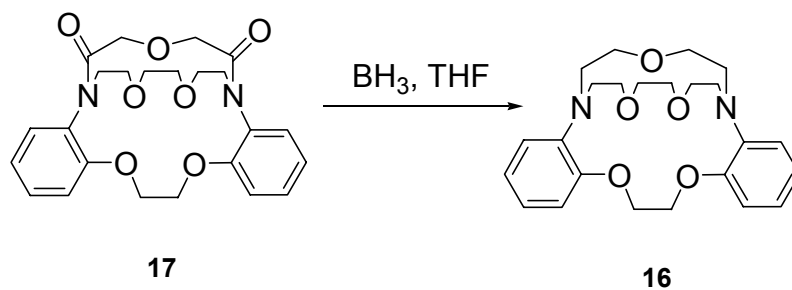
Condensation of **12** with the commercially available diacid chloride, 2,2'-oxydiacetyl chloride, under high-dilution conditions in toluene yielded the bicyclic diamide, **17**, as shown in Scheme 2-19. Triethylammonium salt formation was not visible during the reaction but was present in the mass spectrum. Rotary evaporation of the organic solvent left a mixture of a yellow oil and a white solid. The product was recovered by extraction with dichloromethane.



Scheme 2-19. Synthesis of An2.2.1*, (**17**).

18. 6,7,9,10,12,13,20,21-octahydro-5,14-(ethanooxyethano)dibenzo[*e,q*]-
[1,4,10,13,7,16]tetraoxadiazacyclooctadecine, An2.2.1, (**16**)

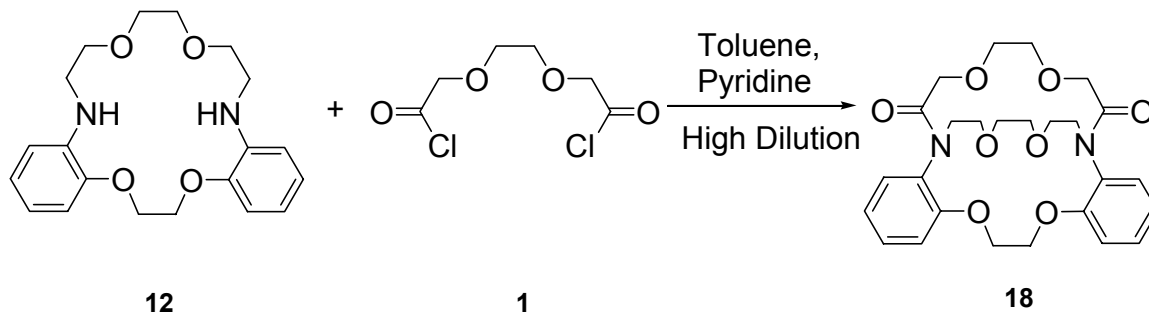
Cryptand An2.2.1, **16**, was also prepared by the reduction of **17** using 1 M borane in refluxing tetrahydrofuran as shown in Scheme 2-20. Water was added in a solution of 1:10 H₂O-THF during reflux to assist the reaction in going to completion.^{6,7} Rotary evaporation was used to remove the organic solvent. The aqueous solution was treated with 6 M HCl to hydrolyze any remaining nitrogen to borane bonds.⁸ The solution was made basic with NH₃ and the fully deprotonated ligand was extracted with chloroform. The product was recovered by recrystallization from a mixture of benzene and heptane.



Scheme 2-20. Synthesis of An2.2.1, (**16**).

19. 9,10,20,21-tetrahydro-5,14-(ethanoxyethanoxyethano)dibenzo[*e,g*]-
[1,4,10,13,7,16]tetraoxadiazacyclooctadecine-6,13-dione, An2.2.2*, (**18**)

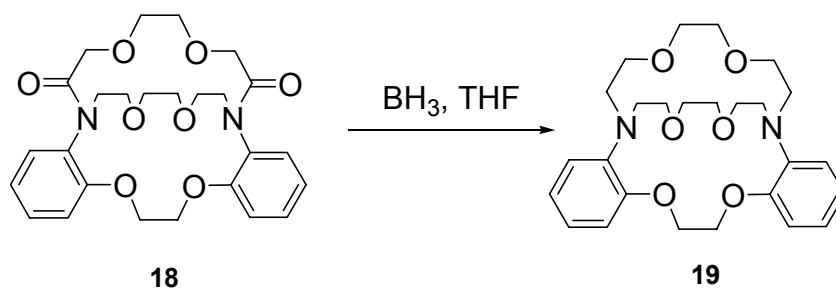
The 1 + 1 cycloaddition product of **12** with **1** under high-dilution conditions in toluene yielded the bicyclic diamide, **18**, as shown in Scheme 2-21. Pyridinium salt formation was not observed during the reaction. Rotary evaporation of the organic solvent left a yellow oil. The pure product was recovered by flash chromatography on silica gel and recrystallized from a mixture of benzene and heptane.



Scheme 2-21. Synthesis of An2.2.2*, (**18**).

20. 6,7,9,10,12,13,20,21-octahydro-5,14-(ethanooxyethano)dibenzo[*e,q*]-[1,4,10,13,7,16]tetraoxadiazacyclooctadecine, An2.2.2, (**19**)

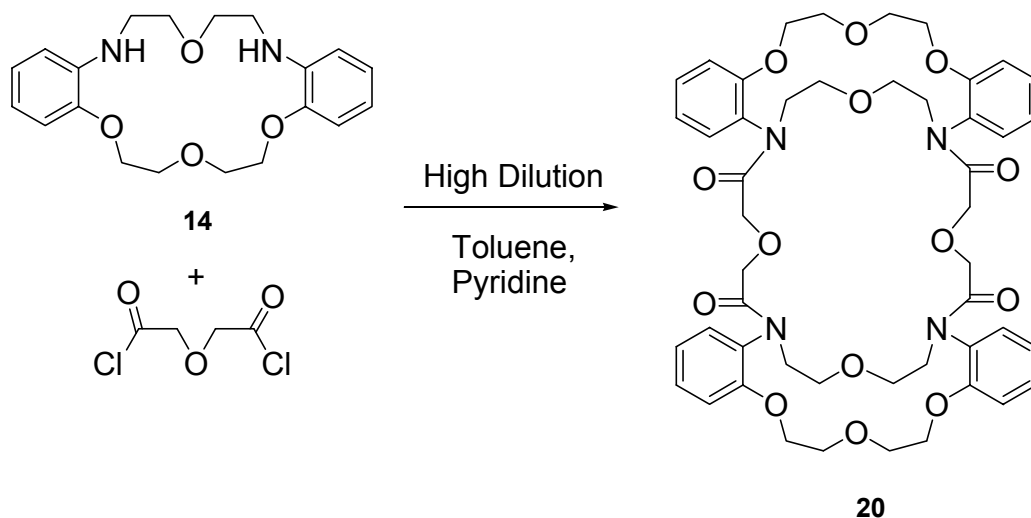
Cryptand An2.2.2, **19**, was made by the reduction of **18** using 1 M borane in refluxing tetrahydrofuran as shown in Scheme 2-22. The addition of water in a solution of 1:10 H₂O-THF during reflux was essential for the reaction to go to completion.^{6,7} The organic solvent was removed by rotary evaporation and the remaining solution was treated with 6 M HCl and made basic with LiOH. The product was extracted with chloroform and then recrystallized from a mixture of benzene and heptane.



Scheme 2-22. Synthesis of An2.2.2, (**19**).

21. 6,7,9,10,28,29,31,32-octahydro-16,44:22,38-di(ethanooxyethano)tetrabenzo[*h,q,z,i*]₁-[1,4,7,13,19,22,25,31,10,16,28,34]octaoxatetraazacyclohexatriacontine-17,21,39,43-tetrone, An3.1.1.3*, (**20**)

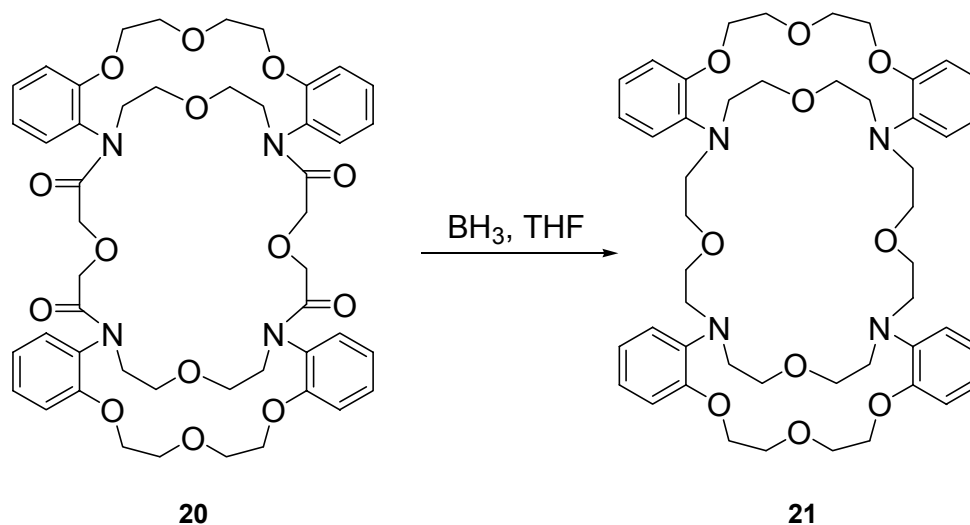
The 2 + 2 cycloaddition product of **14** with 2,2'-oxydiacetyl chloride under high-dilution conditions at room temperature in toluene yielded the tricyclic tetraamide, **20**, as shown in Scheme 2-23. Pyridinium salt formation was not observed during the reaction. A white solid precipitated out while the organic solvent was being removed by rotary evaporation. This solid was recovered and recrystallized from toluene as the pure tetraamide, **20**.



Scheme 2-23. Synthesis of An3.1.1.3*, (**20**).

22. 6,7,9,10,17,18,20,21,28,29,31,32,39,40,42,43-hexadeca-hydro-16,44:22,38-di(ethano-oxyethano)tetrabenzo[*h,q,z,i*][1,4,7,13,19,22,25,31,10,16,28,34]octaoxatetraazacyclohexatriacontine, An3.1.1.3, (**21**)

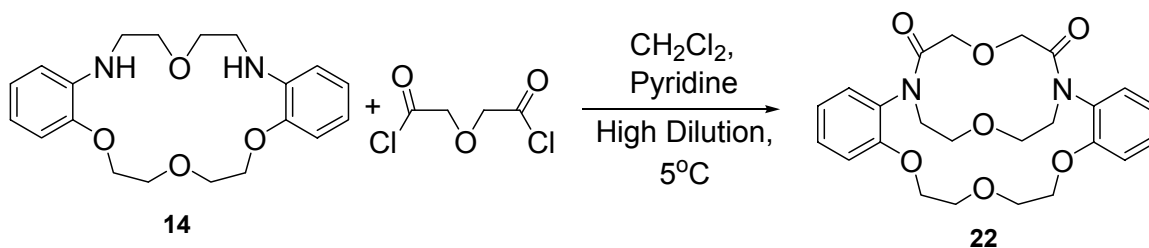
The tricyclic tetraamine, cryptand An3.1.1.3, **21**, was prepared by the reduction of **20** using 1 M borane in refluxing tetrahydrofuran as shown in Scheme 2-24. Water was added in a solution of 1:10 H₂O-THF during reflux to assist the reaction in going to completion.^{6,7} The organic solvent was removed by rotary evaporation and the remaining solution was treated with 6 M HCl and 6 M NH₃. The product was recovered by extraction with chloroform and recrystallization from a mixture of dichloromethane and methanol.



Scheme 2-24. Synthesis of An3.1.1.3, (**21**).

23. 6,7,9,10,-tetrahydro-16,22-(ethanoxyethano)dibenzo[*h,q*][1,4,7,13,10,16]tetra-oxadiazacyclooctadecine-17,21-dione, An3.1.1*, (**22**)

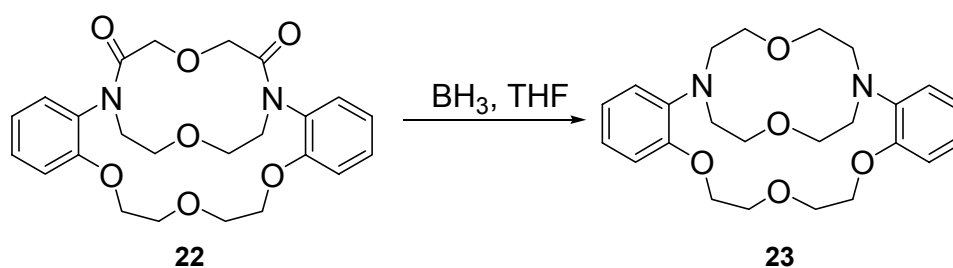
The reaction of **14** with 2,2'-oxydiacetyl chloride under high-dilution conditions at 5 °C in dichloromethane yielded a mixture of the bicyclic diamide, **22**, as shown in Scheme 2-25, and the tricyclic tetraamide, **20**. Pyridinium salt formation was observed during the reaction. Rotary evaporation was used to remove the organic solvent. The pure 1 + 1 cycloaddition product, **22**, was recovered by flash chromatography on silica gel and recrystallized from a mixture of dichloromethane and methanol.



Scheme 2-25. Synthesis of An3.1.1*, (**22**).

24. 6,7,9,10,17,18,20,21-octahydro-16,22-(ethanoxyethano)dibenzo[*h,q*]-
[1,4,7,13,10,16]tetraoxadiazacyclooctadecine, An3.1.1, (**23**)

Cryptand An3.1.1, **23**, was made by the reduction of **22** using 1 M borane in refluxing tetrahydrofuran as shown in Scheme 2-26. A solution of water was added as 1:10 H₂O-THF during reflux to assist the reaction in going to completion.^{6,7} The organic solvent was removed by rotary evaporation and the remaining solution was treated with 6 M HCl and 6 M NH₃. The product was extracted with chloroform.



Scheme 2-26. Synthesis of An3.1.1, (**23**).

III. Experimental

A. General Methods

NMR experiments were obtained on a Varian Mercury VX-300 MHz with Varian 4-nuclei autoswitchable PFG probe, Varian Inova 400 MHz with a Nalorac indirect detection gradient probe, and a Varian 600 MHz with Nalorac triple resonance indirect detection gradient probe. All pulse sequences were used as provided by Varian and all processing was done using standard Varian methods. The signals are referenced to the residual signal of the solvent (CHCl_3 at 7.24 ppm for ^1H and 77.23 ppm for ^{13}C , HDO at 4.80 ppm for ^1H , and DMSO at 2.50 ppm for ^1H). All coupling constants are given in Hz. Signals from ^1H NMR spectra are described as a singlet (s), broad singlet (bs), doublet (d), triplet (t), multiplet (m), doublet of doublets (dd), or triplet of doublets (td). The concentrations for all samples were in a range of 15-50 mg mL⁻¹.

Electrospray ionization mass spectrometry (ESI-MS) experiments were carried out on a Micromass Q-ToF instrument. This technique generally gives the mass to charge ratio (m/z) of the product without fragmentation. The mass spectra for all products obtained include proton peaks ($M + \text{H}^+$), sodium adduct peaks ($M + \text{Na}^+$), dimer ($M_2 + \text{Na}^+$) or trimer ($M_3 + \text{Na}^+$) sodium peaks, and doubly charged species ($M + 2\text{H}^+$). The spectra allow the investigator to determine if side products, unused reactants, or contaminants are present. Positive ion ESI-MS is used predominantly to investigate diamine, diamide, or cryptand products, while negative ion ESI-MS is used for carboxylic diacids.

X-ray crystallographic data were collected using a diffractometer with a Bruker APEX ccd area detector and graphite-monochromated MoK α ($\lambda = 0.71073 \text{ \AA}$) radiation.^{9,10} Samples were cooled to 100-120 K.¹¹ Cell parameters were determined from a nonlinear least-squares fit. Structures were solved by the direct method using the SHELXTL system.¹¹ Crystals suitable for X-ray crystallography were grown by evaporation or vapor diffusion method. Evaporation from solvent or a mixture of solvents at different rates and temperatures yielded suitable crystals for analysis. Vapor diffusion was accomplished by dissolving the analyte in a test tube with solvent 1. The test tube was placed in a sealed jar surrounded by solvent 2. The vapors from solvents 1 and 2 diffuse out and into the test tube, respectively. The analyte is less soluble in solvent 2 and crystallization occurs.

Synthesis of monocyclic intermediates and cryptands was done exclusively by slow addition of equimolar solutions of reagents utilizing high-dilution conditions. High-dilution synthesis is used in order to minimize the production of polymers and promote the formation of the monomeric macrocycle or cryptand. The high-dilution method favors the latter because the rate of intermolecular interaction (polymer production) has a second order concentration dependence, while the intramolecular ring closure reaction is a first order process.

B. Reagents

Distilled Deionized Water - D.D. H₂O. Distilled deionized water was used for all aqueous solutions and was prepared by distillation of deionized water by using a Corning Megapure System distillation apparatus, model MP-3A.

Toluene - C₇H₈. Reagent grade (Fisher Scientific) toluene was refluxed over sodium metal and stored over sodium chips prior to use.

Benzene - C₆H₆. Reagent grade (EMD) benzene was refluxed over sodium metal prior to use.

Chloroform - CHCl₃. Reagent grade (Fisher Scientific) CHCl₃ was distilled from CaCl₂ prior to use.

Dichloromethane - CH₂Cl₂. Reagent grade (Fisher Scientific) CH₂Cl₂ was distilled from CaH₂ prior to use.

Tetrahydrofuran - THF. Reagent grade (Fisher Scientific) THF was freshly distilled from CaH₂ prior to use.

Methanol - CH₃OH, MeOH. Reagent grade (Fisher Scientific) MeOH was refluxed over CaSO₄.

n-Heptane - HPLC grade (Fisher Scientific) *n*-heptane was used without further purification.

Borane - BH₃. Borane-tetrahydrofuran complex, 1 M in THF (Aldrich) was stored at 0 °C and used without further purification.

Diglycolyl chloride - C₄H₄Cl₂O₃. The purity of diglycolyl chloride (Aldrich, 95%) was verified by ¹H NMR and used without further purification.

3,6-Dioxaoctanedioic diacid - C₆H₁₀O₆. 3,6-dioxaoctanedioic diacid (Aldrich) is contaminated with H₂O. Removal of the water was done by azeotropic distillation with toluene using a Dean-Stark trap.^{12,13} Purification was also accomplished by recrystallization from ethyl acetate. In both cases, the product was dried under vacuum.

1,2-Dibromoethane - $C_2H_4Br_2$. The purity of 1,2-dibromoethane (Aldrich, 99+%) was verified by 1H NMR and used without further purification.

Ethanedioyl dichloride - $C_2O_2Cl_2$. Ethanedioyl dichloride or oxalyl chloride (Acros, 98%) was stored at 5 °C and used without further purification.

2,2'-[ethane-1,2-diylbis(oxy)]diethanamine - $C_6H_{16}N_2O_2$. The purity of 2,2'-[ethane-1,2-diylbis(oxy)]diethanamine (Texaco Chemical Company) was verified by 1H NMR and used without further purification.

2-Nitrophenol - $C_6H_5NO_3$. The purity of 2-nitrophenol (Aldrich, 98%) was verified by 1H NMR and used without further purification.

Bis(2-chloroethyl)ether - $C_4H_8OCl_2$. The purity of bis(2-chloroethyl)ether (Aldrich, 97%) was verified by 1H NMR and used without further purification.

Diethylene Glycol Bis(p-toluenesulfonate) - $C_{18}H_{22}O_7S_2$. The purity of diethylene glycol bis(p-toluenesulfonate) (Aldrich, 98%) was verified by 1H NMR and used without further purification.

1,2-Ethylenebis(thioglycolic diacid) - $C_6H_{10}O_4S_2$. 1,2-Ethylenebis(thioglycolic diacid) (TCI America) was used without further purification.

Pyridine - C_5H_5N . Reagent grade pyridine (Fisher) was used without further purification.

Triethylamine - $C_6H_{15}N$. Triethylamine (Aldrich) was freshly distilled prior to use.

Diatomaceous earth - Diatomaceous earth (Celite 521, Aldrich) was used as a filtering agent.

Ascarite beads - Ascarite II (Thomas Scientific) is NaOH on non-fibrous silicate carrier that is used to absorb CO₂.

Anhydrous Calcium Sulfate - CaSO₄. Anhydrous calcium sulfate (Drierite, Hammond) is used to absorb H₂O.

Hydrochloric Acid - HCl. Concentrated hydrochloric acid (EM Science) was used without further purification.

Acetic Acid, Glacial - CH₃CH₂COOH. Concentrated acetic acid, glacial, (Fisher) was used without further purification.

Ammonium Hydroxide - NH₄OH. Concentrated ammonium hydroxide (EM Science) was used without further purification.

Dimethyl-d₆-sulfoxide - C₂D₆OS, DMSO. DMSO (Cambridge Isotope Laboratories, 99.9%) was used without further purification.

Deuterium Oxide - D₂O. D₂O (Cambridge Isotope Laboratories, 99.9%) was used without further purification.

Chloroform D - CDCl₃. CDCl₃ (Cambridge Isotope Laboratories, 99.8%) was used without further purification.

C. Synthesis of acyclic diamines and starting materials

1. 2,2'-[ethane-1,2-diylbis(oxy)]diacetyl chloride (1)

The previously recrystallized and dried triglycolic diacid (16.2 g, 91.0 mmol) was placed in a 500 mL round bottom flask with toluene (100 mL). Ethanedioyl dichloride (20 mL, 230 mmol) was carefully added along with pyridine (5 drops). The

flask was sealed with a drying tube equipped with CaSO_4 and Ascarite beads. The solution was stirred for 48 h at room temperature and the color turned from a milky white to clear yellow. The reaction mixture was filtered through sand and the solvent was removed by rotary evaporation. Recrystallization was performed using a mixture of ethyl ether (12 mL) and petroleum ether (15 mL). The diacid chloride is frozen by submerging the flask in a mixture of dry ice and acetone with a temperature of $-70\text{ }^\circ\text{C}$. The product is brought back to room temperature and the solvent, containing starting material and, impurities, is removed using a pipet. This process is repeated three times. The remaining product is transferred to a tared flask, dried under vacuum, and stored at $0\text{ }^\circ\text{C}$. The amount recovered was 18.7 g (87.0 mmol) for a yield of 96%. The ^1H and ^{13}C NMR data is listed below and the spectra are found in Figures 2-3 and 2-4, respectively. The chemical shift values in the ^1H NMR spectra were in agreement with a previous literature report.¹²

^1H NMR (CDCl_3): $\delta = 4.46$ (s), 3.78 (s) ppm.

^{13}C NMR (CDCl_3): $\delta = 171.81, 76.40, 71.23$ ppm.

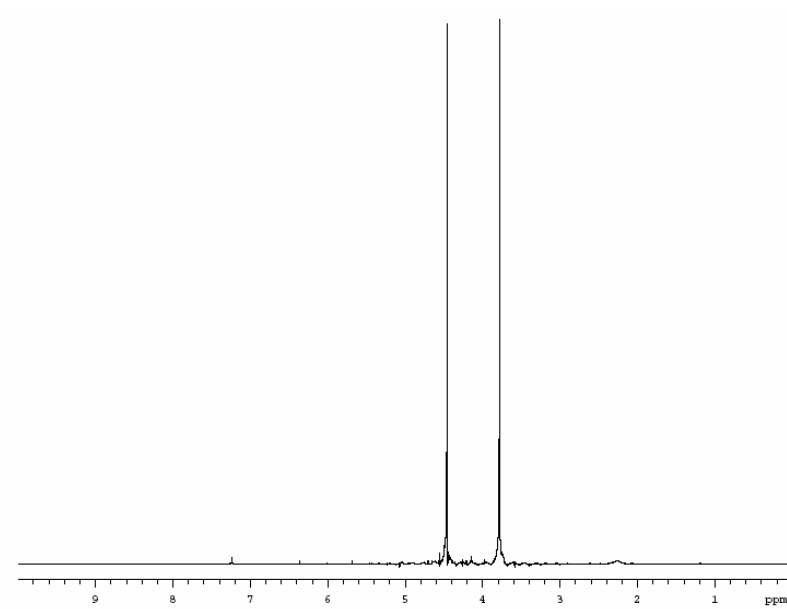


Figure 2-3. ^1H NMR of 2,2'-[ethane-1,2-diylbis(oxy)]diacetyl chloride, (**1**) in CDCl_3 .

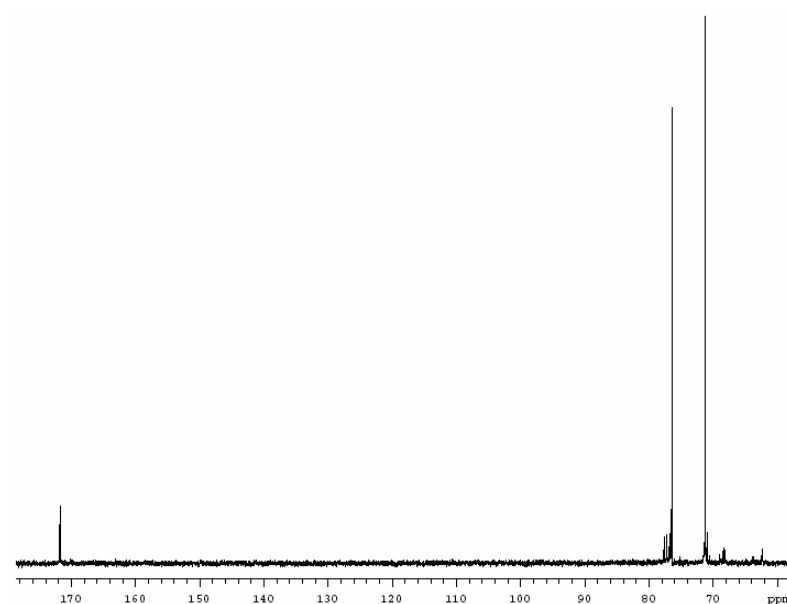


Figure 2-4. ^{13}C NMR of 2,2'-[ethane-1,2-diylbis(oxy)]diacetyl chloride, (**1**) in CDCl_3 .

2. 2,2'-[ethane-1,2-diylbis(thio)]diacetyl chloride (2)

4.19 g (19.9 mmol) of the commercially available 2,2'-[ethane-1,2-diylbis(thio)]diacetic diacid was placed in a 500 mL round-bottom flask outfitted with a drying tube containing CaSO₄ and Ascarite beads. Toluene (100 mL) and dry ether (100 mL) were added and the suspension containing undissolved diacid was stirred at room temperature. After 15 min, 8 mL (92.0 mmol) of ethanedioyl dichloride was added. The solid was fully dissolved after 5 h and then the solvent was removed by rotary evaporation. Recrystallization was accomplished by the same method as **1** using a mixture of ethyl ether (3 mL) and petroleum ether (12 mL). The product was transferred to a tared flask and the amount produced was 3.66 g (14.8 mmol) for a yield of 74%. This reaction was carried out by Michelle Mosher.

3. 1,1'-[ethane-1,2-diylbis(oxy)]bis(2-nitrobenzene) (3)

A 250 mL three-neck round bottom flask was equipped with a condenser, an inlet and an outlet for nitrogen gas, thermometer, heating mantle, magnetic stirring bar, and addition funnel. DMF (50 mL) was added to the flask followed by slow addition of 2-nitrophenol (32.8 g, 236 mmol) while stirring. The color of the solution changed from green to red. K₂CO₃ (35 g, 253 mmol) was added to deprotonate the 2-nitrophenol and the solution became more orange. Dibromoethane (10 mL, 115 mmol) was slowly added from the addition funnel which was then rinsed with DMF. The flask was heated until the temperature reached 120 °C, and the reaction was maintained at this temperature for 24 h. At this time the solution was allowed to cool, and then 90 mL of H₂O was added. The product precipitated out. The yellow solid was filtered, washed with H₂O, and dried

under vacuum. Recrystallization was accomplished with ethanol or acetic acid. Acetic acid was used more often because a smaller volume was required. The yield was 57%. The ^1H NMR data is listed below and the spectrum is shown in Figure 2-5. The mass spectrum is shown in Figure 2-6 with peaks at m/z of 245.2 ($\text{M} + \text{H}^+$) and 267.1 ($\text{M} + \text{Na}^+$).

^1H NMR (DMSO): $\delta = 7.85$ (d), 7.66 (t), 7.43 (d), 7.14 (t), 4.53 (s), 3.35 (s) ppm.

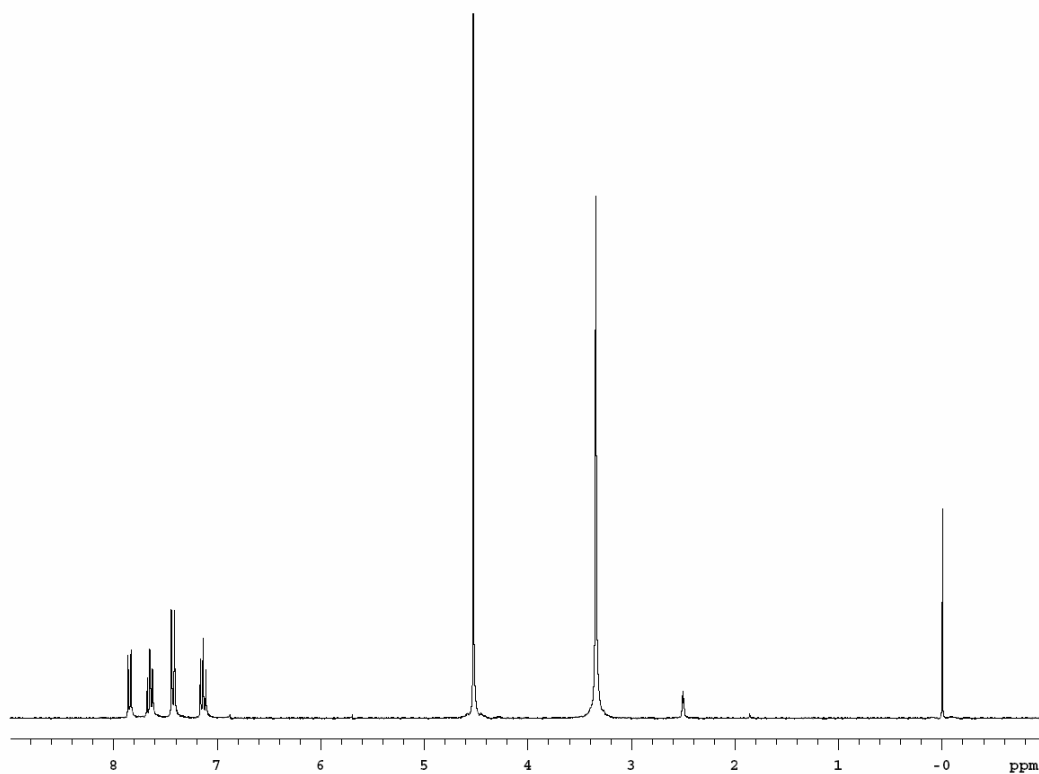


Figure 2-5. ^1H NMR of 1,1'-[ethane-1,2-diylbis(oxy)]bis(2-nitrobenzene), (**3**) in DMSO.

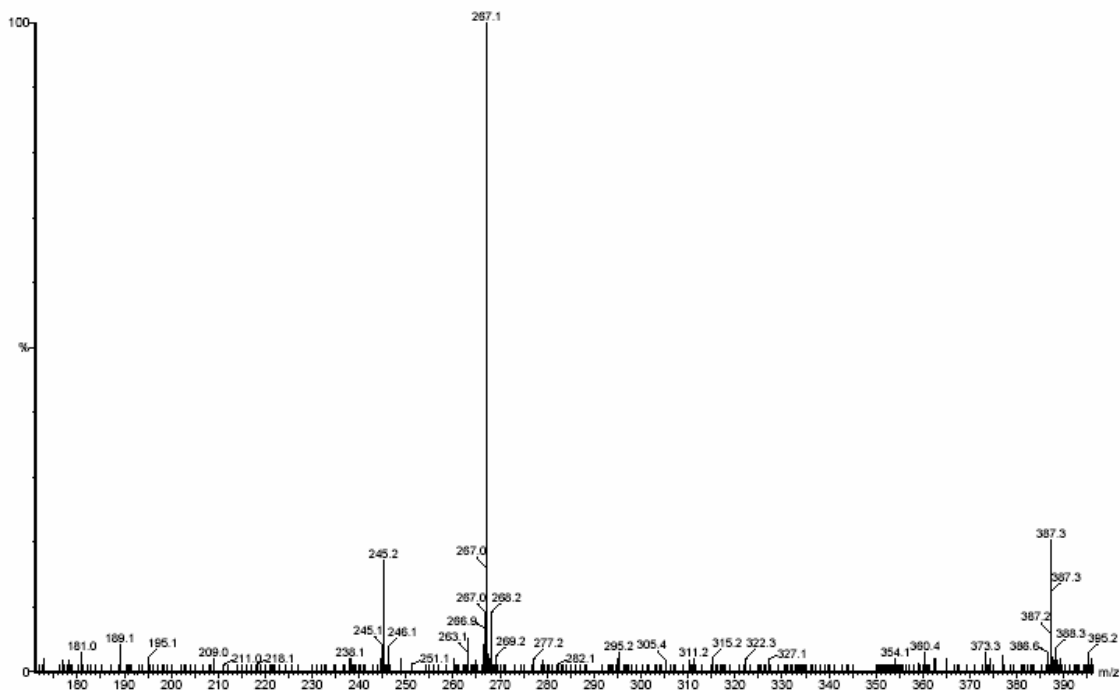


Figure 2-6. ESI-MS⁺ of 1,1'-[ethane-1,2-diylbis(oxy)]bis(2-nitrobenzene), (**3**) in MeOH.

4. 2,2'-[ethane-1,2-diylbis(oxy)]dianiline (**4**)

A hydrogenation apparatus outfitted with an automatic shaker, hydrogen gas reservoir, and vacuum line was used for the reduction of **3**. A 250 mL reaction vessel was filled with **3** (19.5 g, 0.0641 moles), 175 mL of ethanol, and 0.92 g of Pd on activated carbon (5%). The pressure was initially set to 18 psi and was repeatedly raised to that pressure for the next 3 h until the pressure no longer dropped. The hydrogenated product was filtered through diatomaceous earth with ethanol. The solvent was removed by rotary evaporation to give 14.3 g (0.0586 moles) of the product. The yield was 92%. The ¹H NMR data is listed below and the spectrum is shown in Figure 2-7. The mass spectrum is shown in Figure 2-8 with peaks at m/z of 245.1 (M + H⁺), 267.1 (M + Na⁺),

and 489.2 ($M_2 + H^+$). The chemical shift values in the 1H NMR spectra were in agreement with a previous literature report.¹⁴

1H NMR (DMSO): $\delta = 6.86$ (m), 6.68 (m), 6.52 (m), 4.66 (bs), 4.27 (s), 3.41 (bs) ppm.

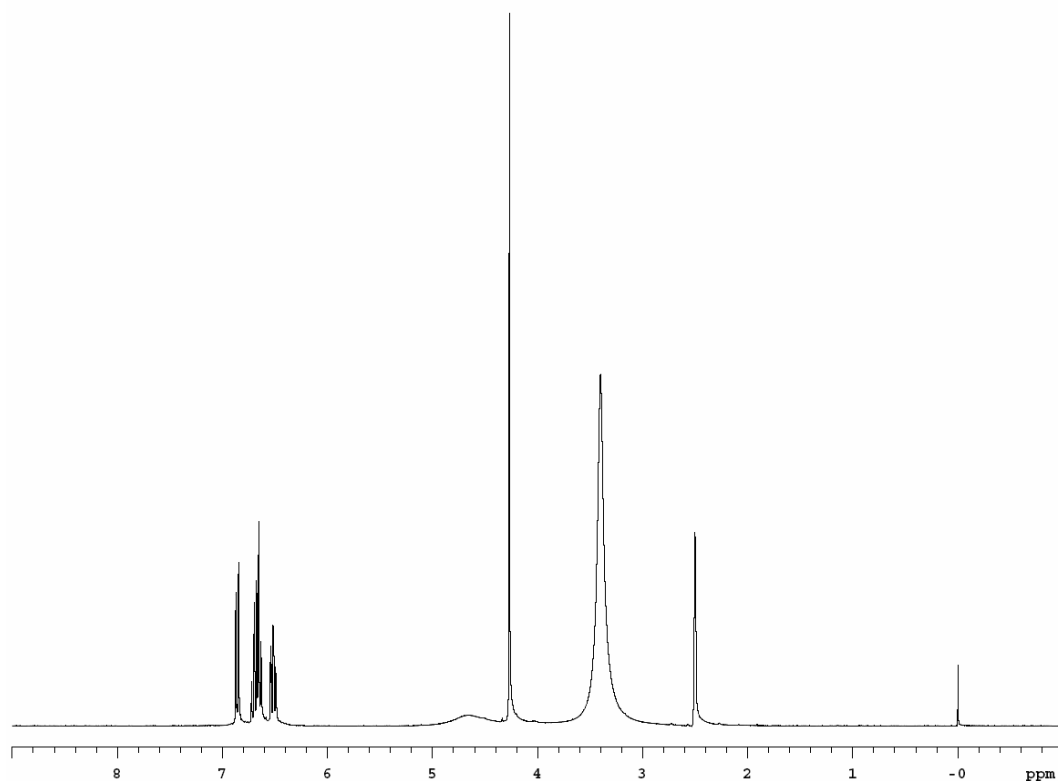


Figure 2-7. 1H NMR of 2,2'-[ethane-1,2-diylbis(oxy)]dianiline, (**4**) in DMSO.

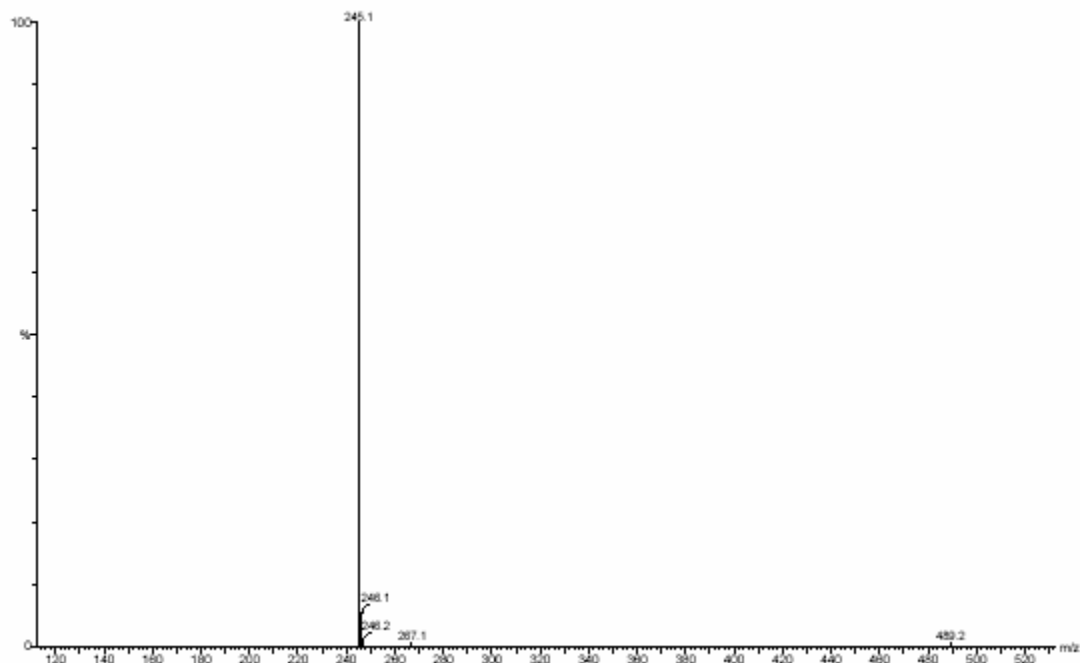


Figure 2-8. ESI-MS⁺ of 2,2'-[ethane-1,2-diylbis(oxy)]dianiline, (**4**) in MeOH.

5. 1,1'-[oxybis(2,1-ethanedioxy)]bis[2-nitrobenzene] (**5**)

A 250 mL three-neck round bottom flask was outfitted with a condenser, an inlet and an outlet for nitrogen gas, heating mantle, magnetic stirring motor, and addition funnel. DMF (120 mL) was added to the flask followed by the addition of 2-nitrophenol (5.12 g, 36.8 mmol) while stirring. The color of the solution was bright yellow. Then, K₂CO₃ (35 g, 253 mmol) was slowly added to deprotonate the 2-nitrophenol, and then the color of the solution became dark red. Bis(2-chloroethyl)ether (2.1 mL, 18 mmol) was added via the addition funnel which was then rinsed with DMF. The reaction was refluxed overnight. After the reaction had cooled, 60 mL of H₂O were added and everything dissolved. Solvent was removed from the reaction mixture by rotary evaporation until a yellow precipitate fell out of solution. The yellow solid was filtered,

washed with H₂O, and dried under vacuum. Additional product was recovered by adding more water to the red solution. The solid product was recrystallized from methanol to produce yellow crystals with a yield of 67%. The ¹H NMR data is listed below and the spectrum is shown in Figure 2-9. The mass spectrum is shown in Figure 2-10 with a peak at m/z of 371.1 (M + H⁺).

¹H NMR (CDCl₃): δ = 7.81 (dd), 7.50 (td), 7.09 (dd), 7.01 (td), 4.26 (t), 3.99 (t) ppm.

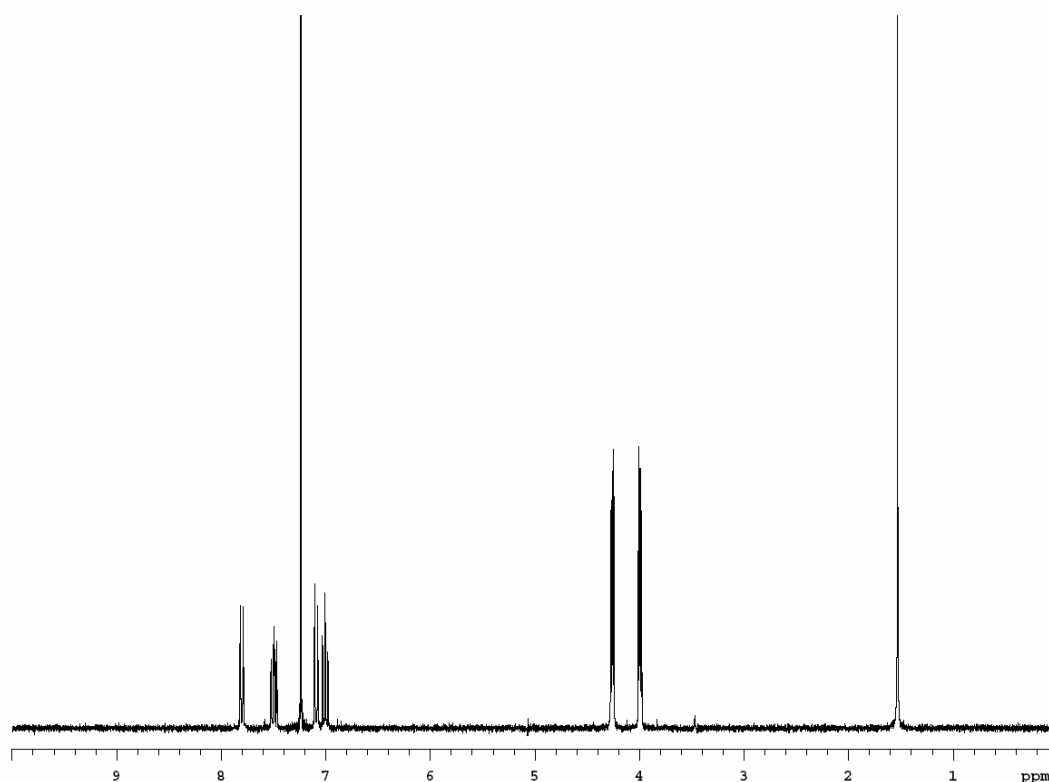


Figure 2-9. ¹H NMR of 1,1'-[oxybis(2,1-ethanediyoxy)]bis[2-nitro-benzene], (**5**) in CDCl₃.

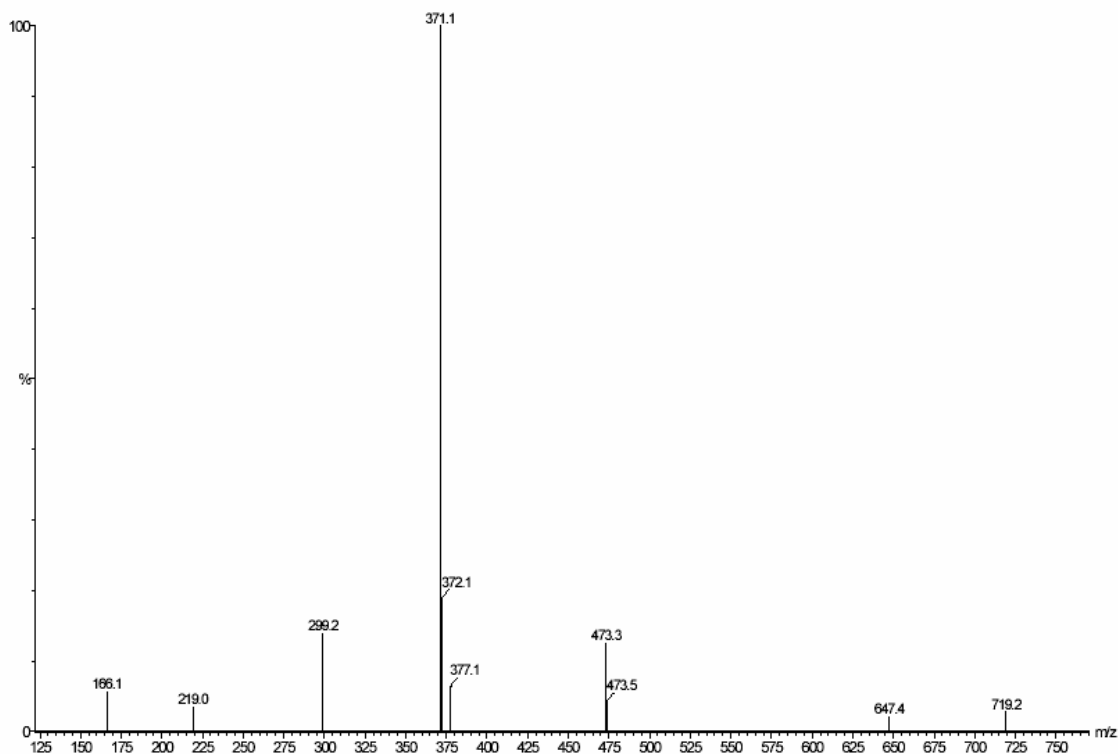


Figure 2-10. ESI-MS⁺ of 1,1'-[oxybis(2,1-ethanedioxy)]bis[2-nitro-benzene], (**5**) in MeOH.

6. 2,2'-[oxybis(ethane-2,1-dioxy)]dianiline (**6**)

The previously described hydrogenation apparatus was used for this reaction. A mixture of 75 mL ethanol and 50 mL THF was added to the 250 mL reaction vessel along with **5** (5.12 g, 0.0147 moles) and 1.14 g of Pd on activated carbon (5%). The hydrogen pressure was initially set to 14 psi. Gas consumption ceased after 3 h. The hydrogenation product was filtered through diatomaceous earth to remove the catalyst. The solvent was removed by rotary evaporation to give 4.21 g (0.0146 moles) of the product. The reaction was nearly quantitative with a yield of 99%. The ¹H NMR data is listed below and the spectrum is shown in Figure 2-11. The mass spectrum is shown in

Figure 2-12 with peaks at m/z of 289.2 ($M + H^+$) and 311.2 ($M + Na^+$). The chemical shift values in the 1H NMR spectra were in agreement with a previous literature report.¹⁴

1H NMR ($CDCl_3$): $\delta = 6.77-6.82$ (m), $6.64-6.71$ (m), 4.16 (t), 3.89 (t) ppm.

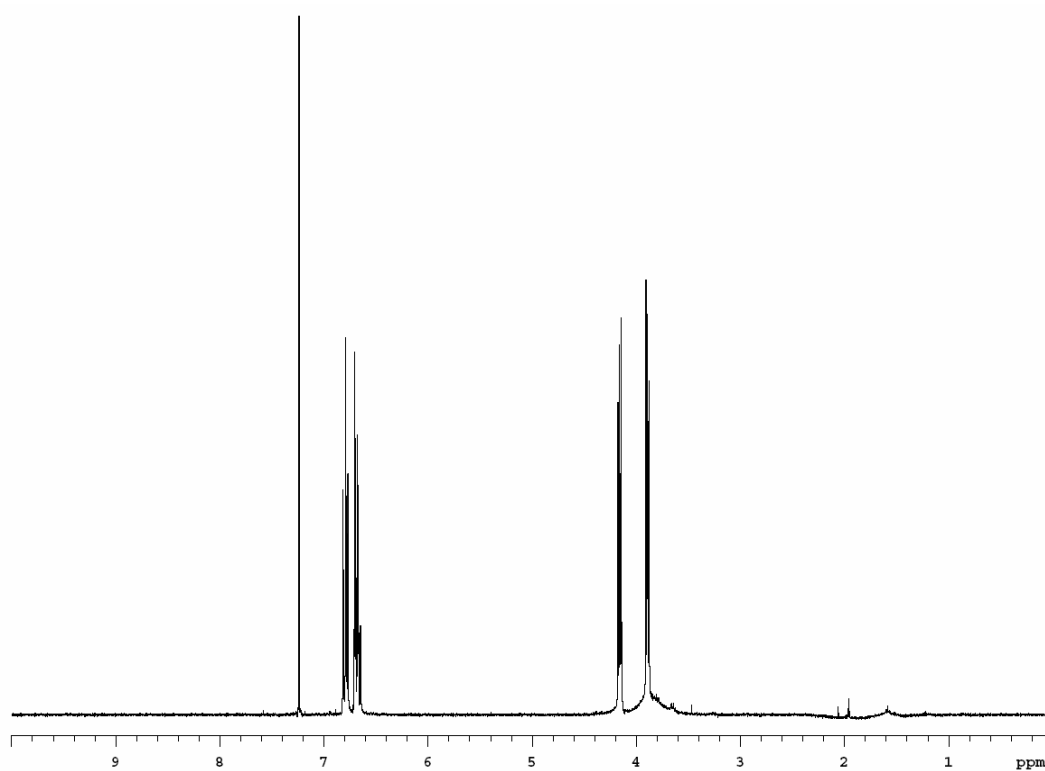


Figure 2-11. 1H NMR of 2,2'-[oxybis(ethane-2,1-diyloxy)]dianiline, (**6**) in $CDCl_3$.

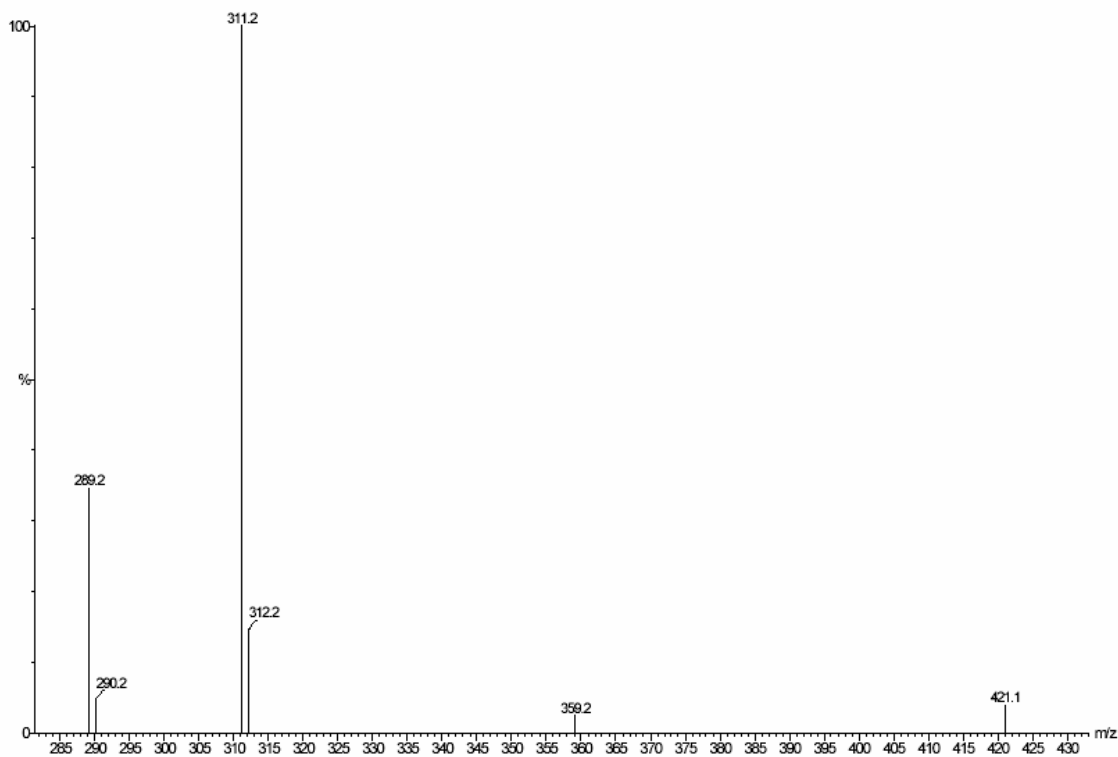


Figure 2-12. ESI-MS⁺ of 2,2'-[oxybis(ethane-2,1-diyloxy)]dianiline, (**6**) in MeOH.

D. Synthesis of monocyclic diamides and diamines

7. 1,4,10,13-tetraoxa-7,16-diazacyclooctadecane-6,17-dione, **2.2***, (**7**)

A 550 mL solution of the diamine 2,2'-[ethane-1,2-diylbis(oxy)]diethanamine (61.4 mmol, 0.1116 M) and a 500 mL solution of **1** (27.9 mmol, 0.0558 M) were prepared. The diamine solution was made using a two-fold molar excess to provide a scavenger base to consume the HCl produced. Equipment for the reaction included a 5 L Morton flask equipped with two 500 mL constant rate addition funnels, an inlet and an outlet for nitrogen gas, and a mechanical stirrer. An initial volume of 750 mL of toluene was placed in the flask and stirred at 1000 rpm under a nitrogen atmosphere. The two

solutions were placed in separate constant rate addition funnels and added at a rate of 1 mL/min. The drop rate was monitored to ensure equal rates of addition. The addition was complete after 8 h, and the reaction mixture was allowed to stir for an additional 15 h. Gelatinous salts formed on the sides of the flask and were filtered off before the solvent was removed by rotary evaporation. The white product precipitated out during evaporation and was then recrystallized from a benzene-heptane mixture. The yield was 54%. The ^1H NMR data is listed below and the spectrum is shown in Figure 2-13. The mass spectrum is shown in Figure 2-14 with peaks at m/z of 291.2 ($\text{M} + \text{H}^+$) and 313.2 ($\text{M} + \text{Na}^+$). Crystals suitable for X-ray crystallography were grown by vapor diffusion with heptane diffusing into a solution of **7** dissolved in benzene. The X-ray crystal structure unit cell for **7** contains two crystallographically independent molecules. Molecules A and B are shown in Figures 2-15 and 2-16, respectively.

^1H NMR (CDCl_3): $\delta = 7.06$ (bs), 4.02 (s), 3.62 (s), 3.57 (t), 3.50 (m) ppm.

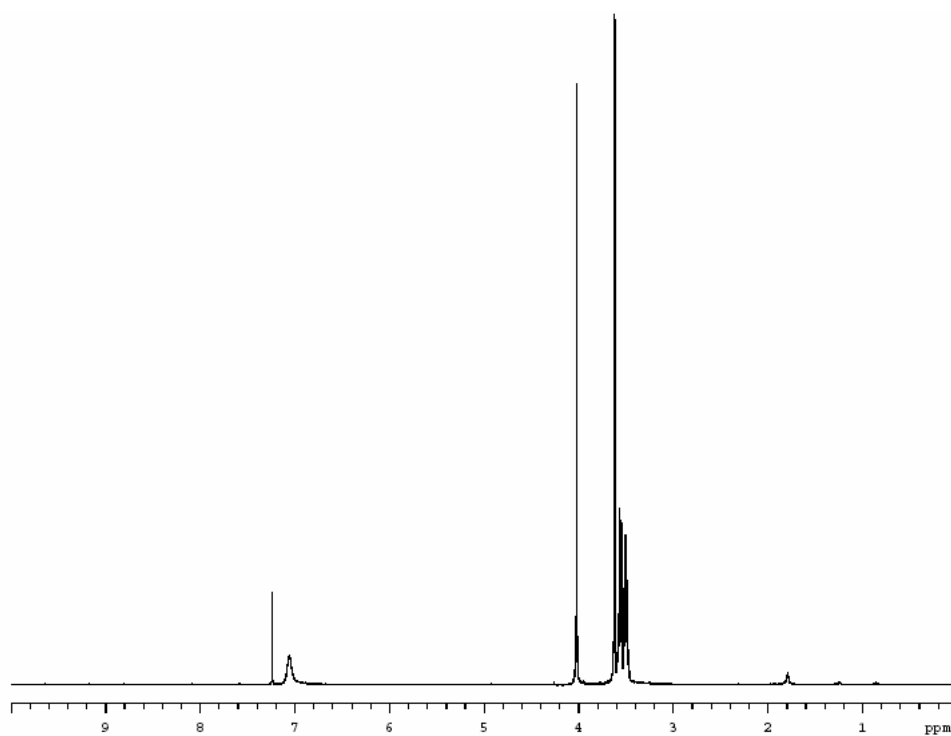


Figure 2-13. ^1H NMR of 2.2*, (7) in CDCl_3 .

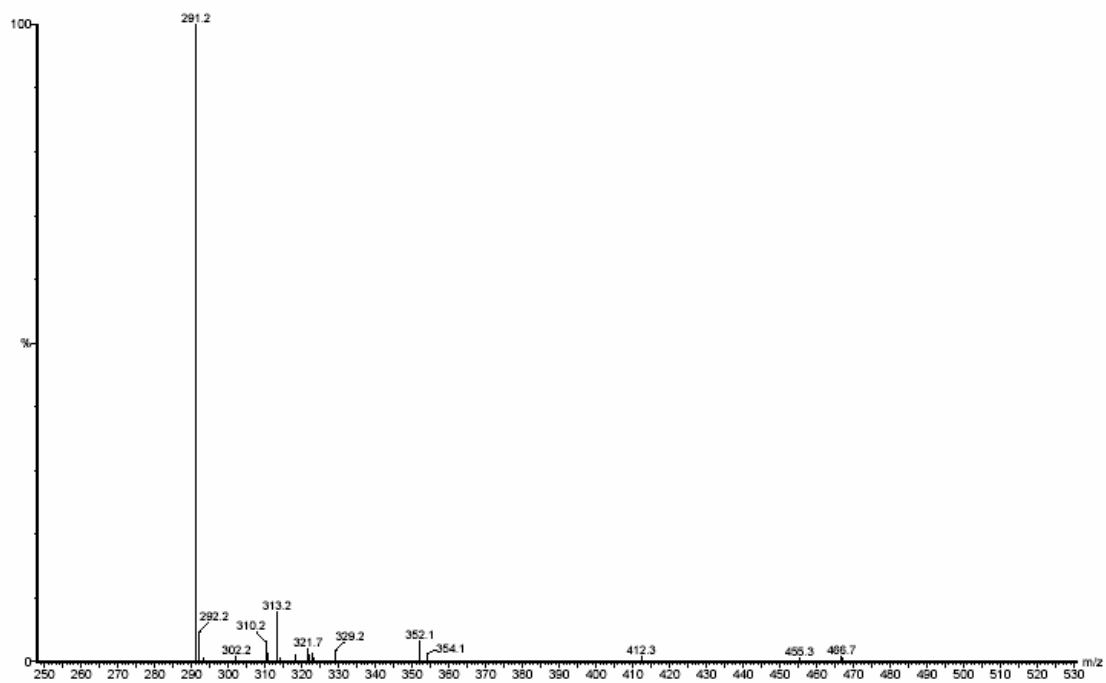


Figure 2-14. ESI-MS^+ of 2.2*, (7) in MeOH.

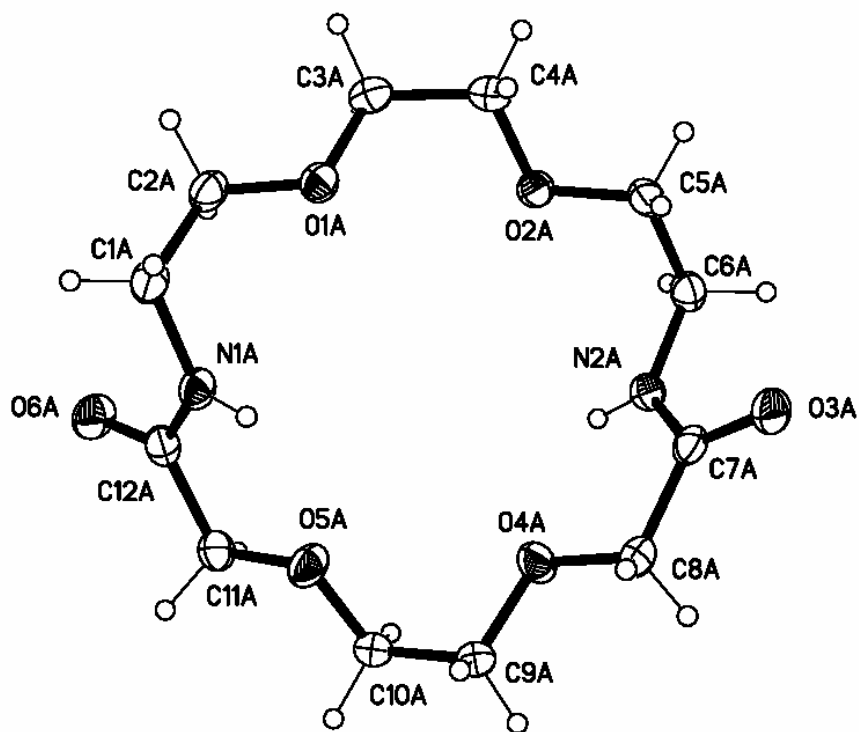


Figure 2-15. X-ray crystal structure of 2.2*, (7), Molecule A.

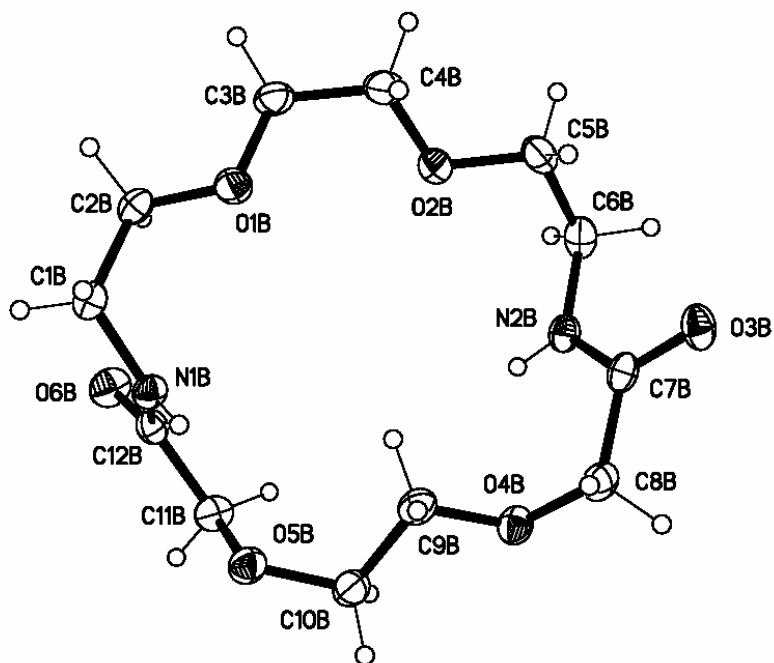


Figure 2-16. X-ray crystal structure of 2.2*, (7), Molecule B.

8. 1,4-dioxa-10,13-dithia-7,16-diazacyclooctadecane-8,15-dione, 2.2_S*, (8)

A 500 mL solution of the diamine 2,2'-[ethane-1,2-diylbis(oxy)]diethanamine (40.5 mmol, 0.08100 M) and a 500 mL solution of **2** (20.3 mmol, 0.04057 M) were prepared in toluene. The reaction methods were the same as those previously described for **7**. The addition was complete in 6.5 h. Reaction salts were filtered before the solvent was evaporated under vacuum. Flash chromatography on silica gel using CHCl₃ and MeOH (up to 5%) as the eluent gave the pure diamide. The product was obtained in a 37% yield. The ¹H NMR data is listed below and the spectrum is shown in Figure 2-17. The mass spectrum is shown in Figure 2-18 with peaks at m/z of 323.1 (M + H⁺) and 345.1 (M + Na⁺). Crystals suitable for X-ray crystallography were grown by vapor diffusion with hexane diffusing into a solution of **8** dissolved in dichloromethane. The X-ray crystal structure for **8** is shown in Figure 2-19.

¹H NMR (CDCl₃): δ = 7.45 (bs), 3.61 (s), 3.58 (t), 3.48 (m), 3.24 (s), 2.73 (s) ppm.

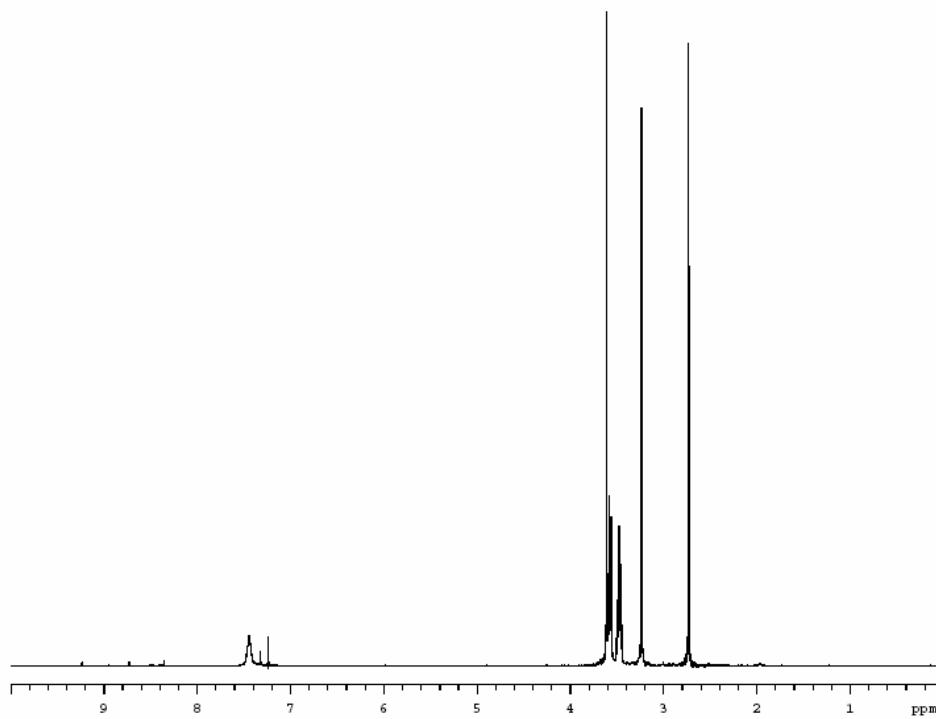


Figure 2-17. ¹H NMR of 2.2_S^{*}, (**8**) in CDCl₃.

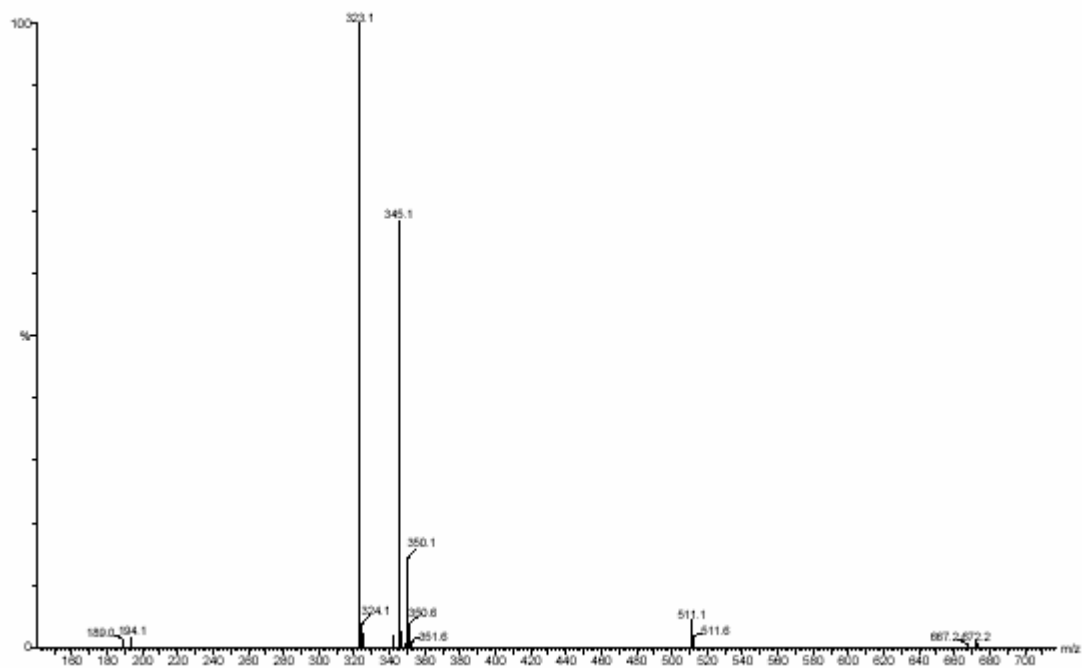


Figure 2-18. ESI-MS⁺ of 2.2_S^{*}, (**8**) in MeOH.

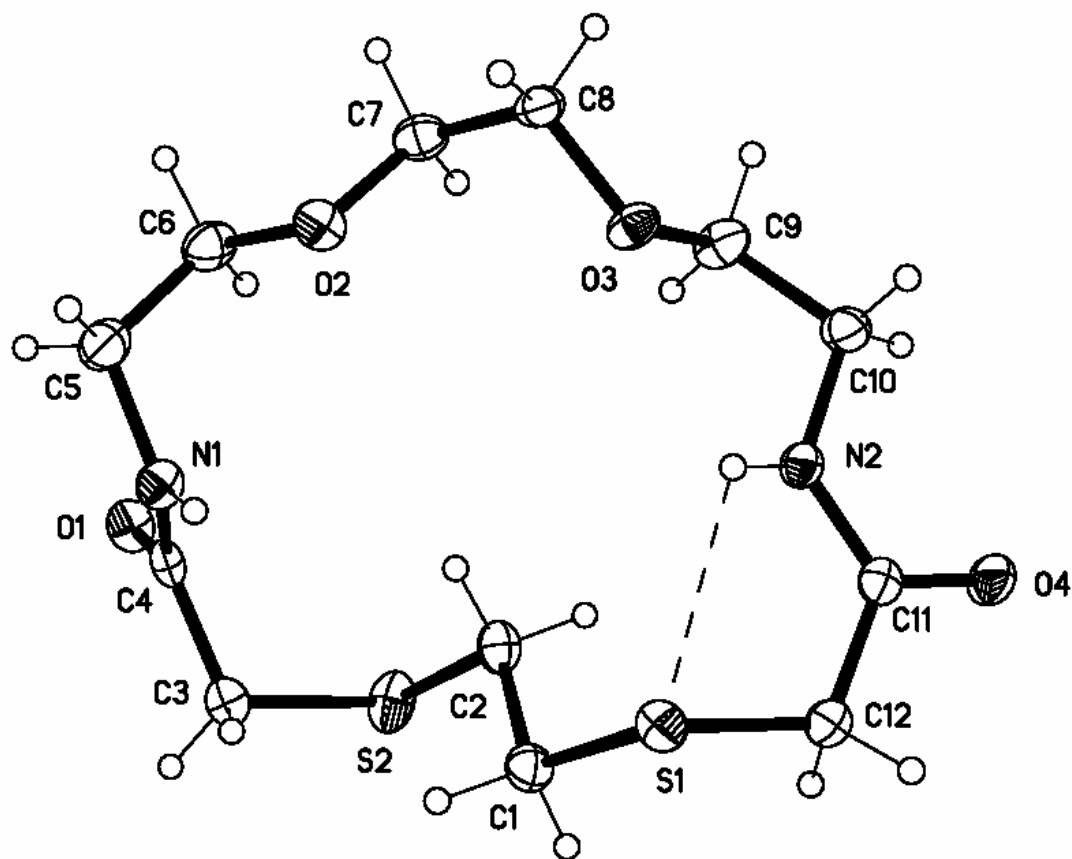


Figure 2-19. X-ray crystal structure of 2.2_s^{*}, (8).

9. 17,18-dihydro-5*H*,9*H*-dibenzo[*e,n*][1,4,10,7,13]trioxadiazacyclopentadecine-6,10(7*H*,11*H*)-dione, An2.1^{*}, (9)

A 350 mL solution (0.035 M) of **4** was prepared by dissolving 3.01 g (12.3 mmol) in 142 mL of DMF and 208 mL of toluene. An equimolar solution of the diacid chloride 2,2'-oxydiacetyl chloride was made by diluting 1.46 mL (12.3 mmol, $d = 1.44$ g/mL) to 350 mL with toluene. A 5 L Morton flask was prepared with a magnetic stirring bar, an inlet and an outlet for nitrogen gas, 400 mL of toluene, and 9.9 mL (123 mmol) of pyridine. Addition of the equimolar solutions of diamine and diacid chloride was carried out using 50 mL syringes and a syringe pump over a period of 6.5 h. Reaction salts were

filtered and the solvent was removed by rotary evaporation. The yellow paste that remained was recrystallized from ethanol to give a white crystalline product with a 60% yield. The ^1H and ^{13}C NMR data is listed below and the spectra are shown in Figures 2-20 and 2-21, respectively. The mass spectrum is shown in Figure 2-22 with peaks at m/z of 343.1 ($\text{M} + \text{H}^+$), 365.1 ($\text{M} + \text{Na}^+$), and 707.2 ($\text{M}_2 + \text{Na}^+$). Crystals suitable for X-ray crystallography were grown by slow evaporation of an ethanol solution. The X-ray crystal structure for **9** is shown in Figure 2-23.

^1H NMR (CDCl_3): $\delta = 9.03$ (s, 2H), 8.50 (dd, $J = 7.8, 1.7$ Hz, 2H), 7.09 (td, $J = 7.8, 1.7$ Hz, 2H), 7.05 (td, $J = 7.8, 1.6$ Hz, 2H), 7.02 (dd, $J = 7.8, 1.6$ Hz, 2H), 4.38 (s, 4H), 4.21 (s, 4H) ppm.

^{13}C NMR (CDCl_3): $\delta = 165.6, 146.8, 128.3, 124.5, 123.0, 120.1, 113.7, 70.6, 68.4$ ppm.

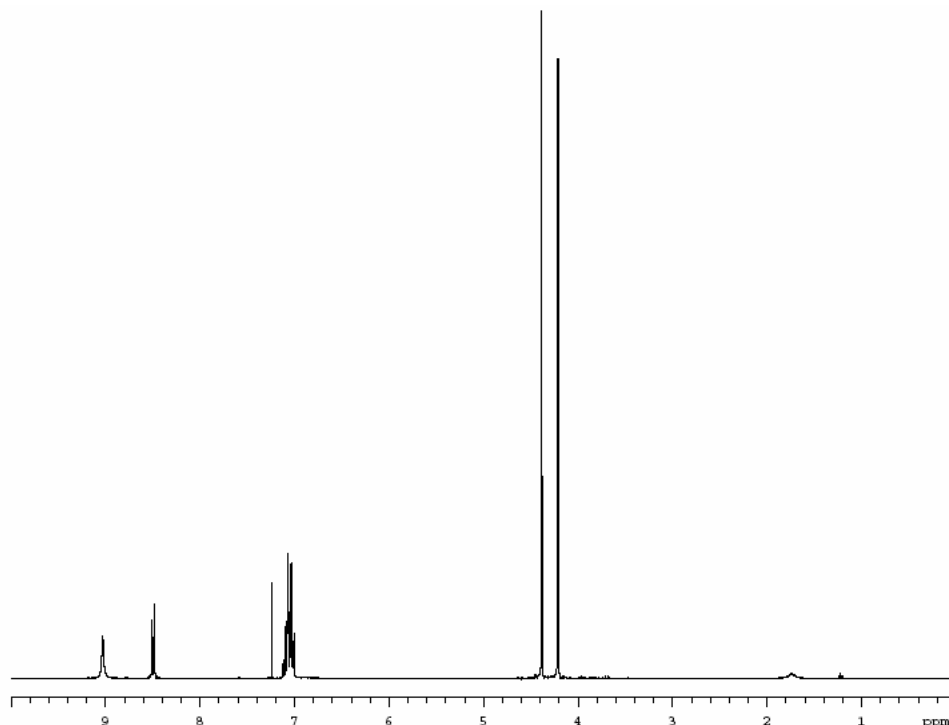


Figure 2-20. ^1H NMR of An2.1*, (**9**) in CDCl_3 .

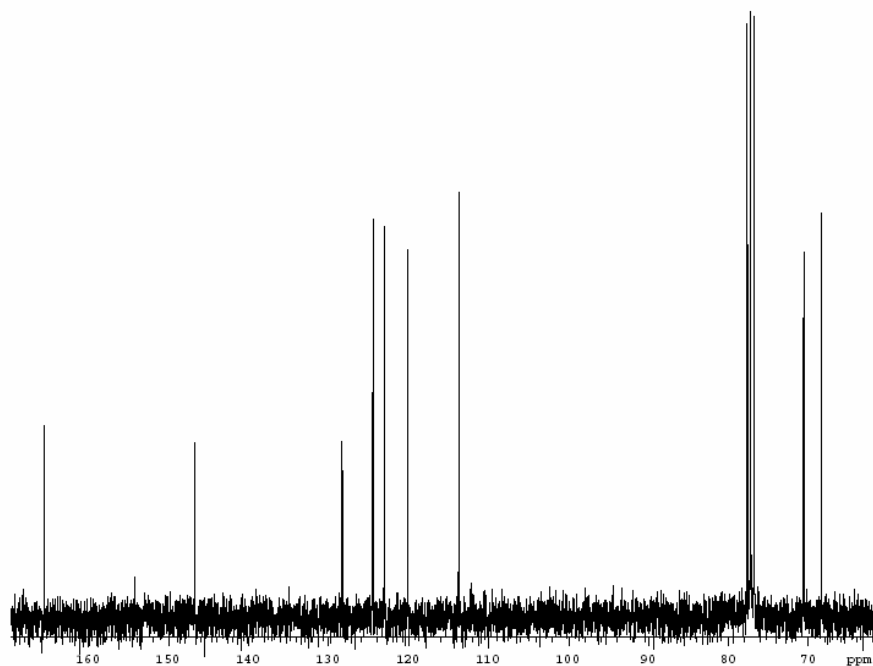


Figure 2-21. ^{13}C NMR of An2.1*, (**9**) in CDCl_3 .

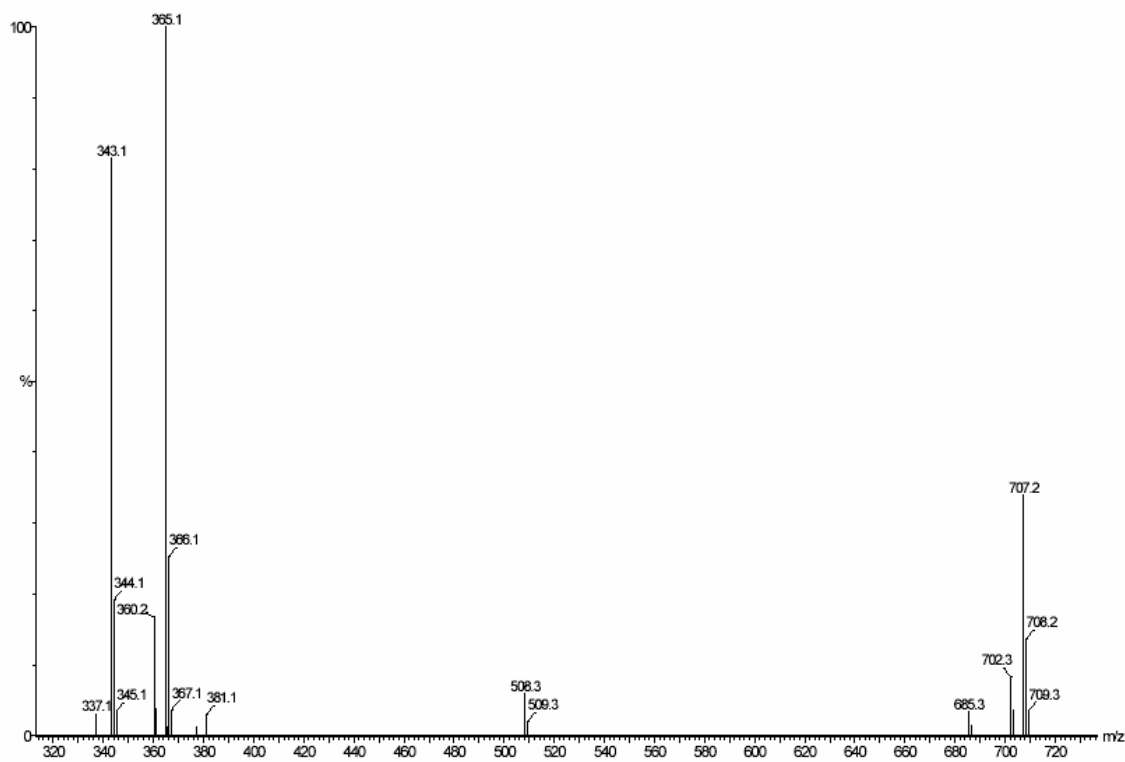


Figure 2-22. ESI- MS^+ of **9**, An2.1* in MeOH.

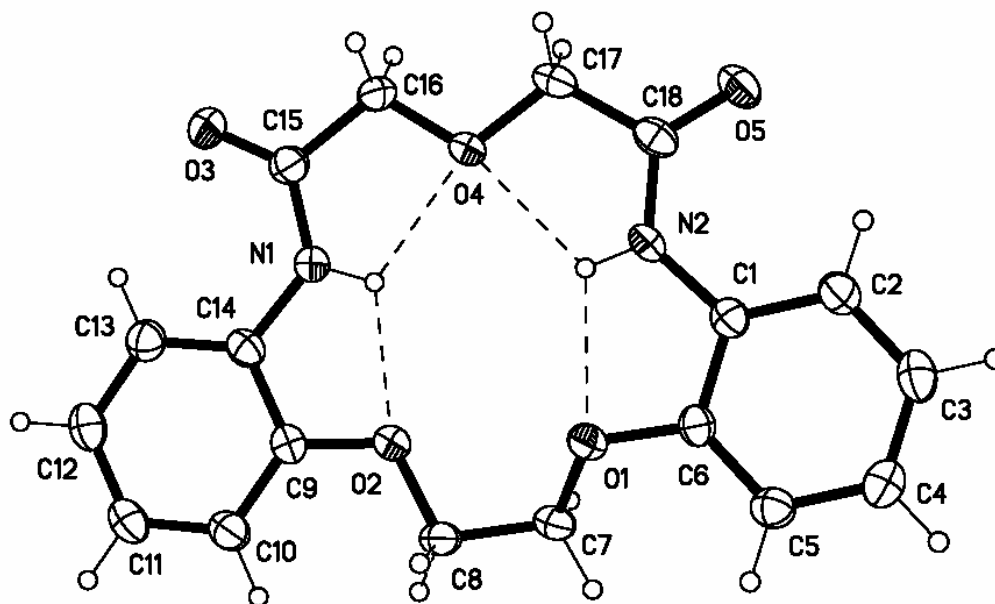


Figure 2-23. X-ray crystal structure of An2.1*, (9).

10. 6,7,10,11,17,18-hexahydro-5*H*,9*H*-dibenzo[*e,n*][1,4,10,7,13]trioxadiazacyclopentadecine, An2.1, (10)

To a 250 mL three-neck round bottom flask fitted with a condenser and an inlet and an outlet for nitrogen gas, was added 1.32 g (3.84 mmol) of **9** and 40 mL (40 mmol) of 1M borane-THF complex. The diamide dissolved upon addition of the reducing agent. The reaction was refluxed for 2 h, then 10 mL of a solution of 1:10 H₂O-THF was added dropwise over 1 h with a syringe pump. After 3 h, the solution was cooled and 30 mL of H₂O were added to destroy the excess reducing agent. The solvent was removed by evaporation under vacuum and a white residue remained. The product was washed with water and dried under vacuum. This reaction afforded a 97.7% yield. The ¹H NMR data is listed below and the spectrum is shown in Figure 2-24. The mass spectrum is shown in Figure 2-25 with peaks at *m/z* of 315.2 (M + H⁺), 337.2 (M + Na⁺), and 651.4 (M₂ +

Na⁺). Crystals suitable for X-ray crystallography were grown by vapor diffusion with heptane diffusing into a solution of **9** dissolved in benzene. The X-ray crystal structure for **9** is shown in Figure 2-26. The chemical shift values in the ¹H NMR spectra were in agreement with a previous literature report.⁵

¹H NMR (CDCl₃): δ = 6.80-6.91 (m), 6.61-6.68 (m), 4.93 (bs), 4.34 (s), 3.68 (t), 3.33 (m) ppm.

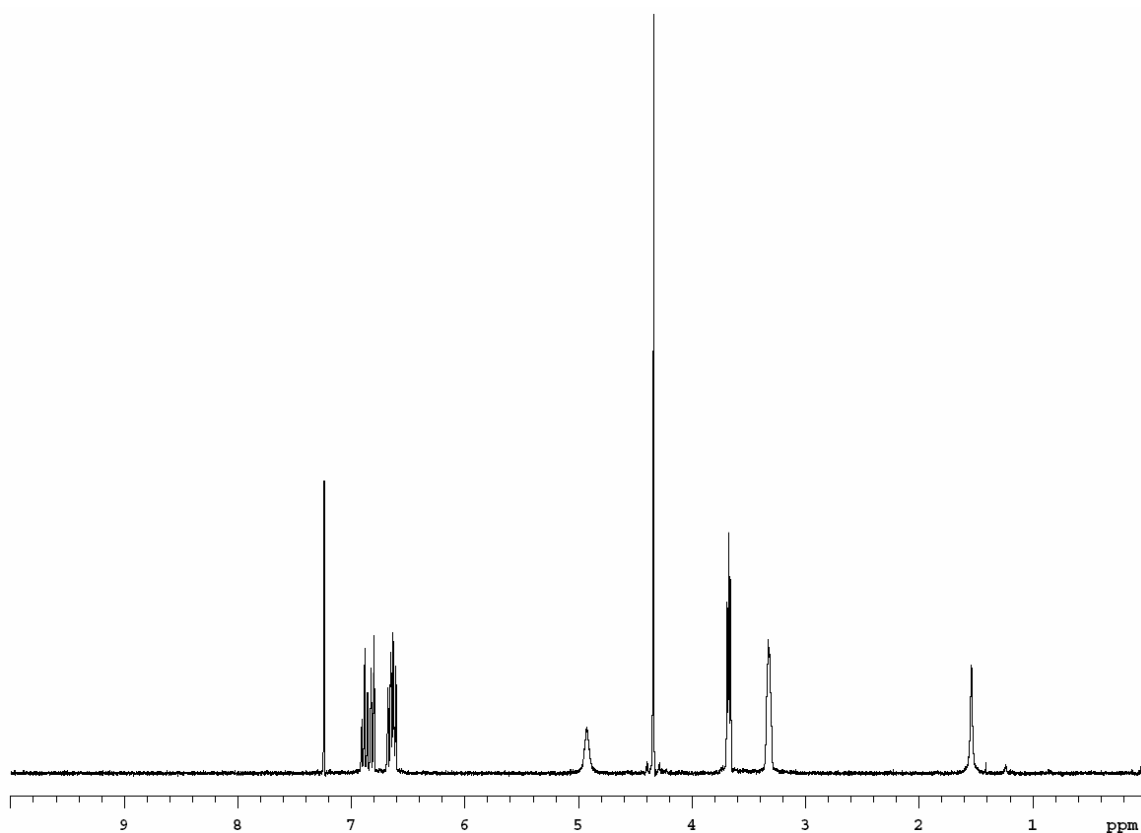


Figure 2-24. ¹H NMR of An2.1, (**10**) in CDCl₃.

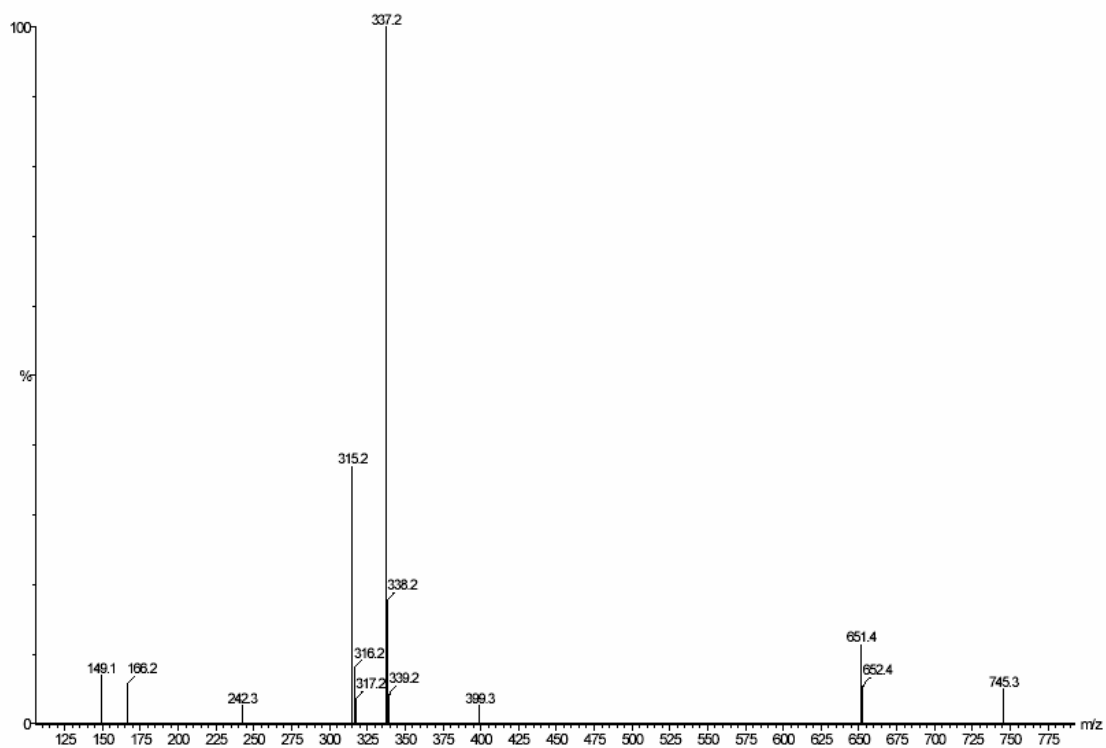


Figure 2-25. ESI-MS⁺ of An2.1, (10) in MeOH.

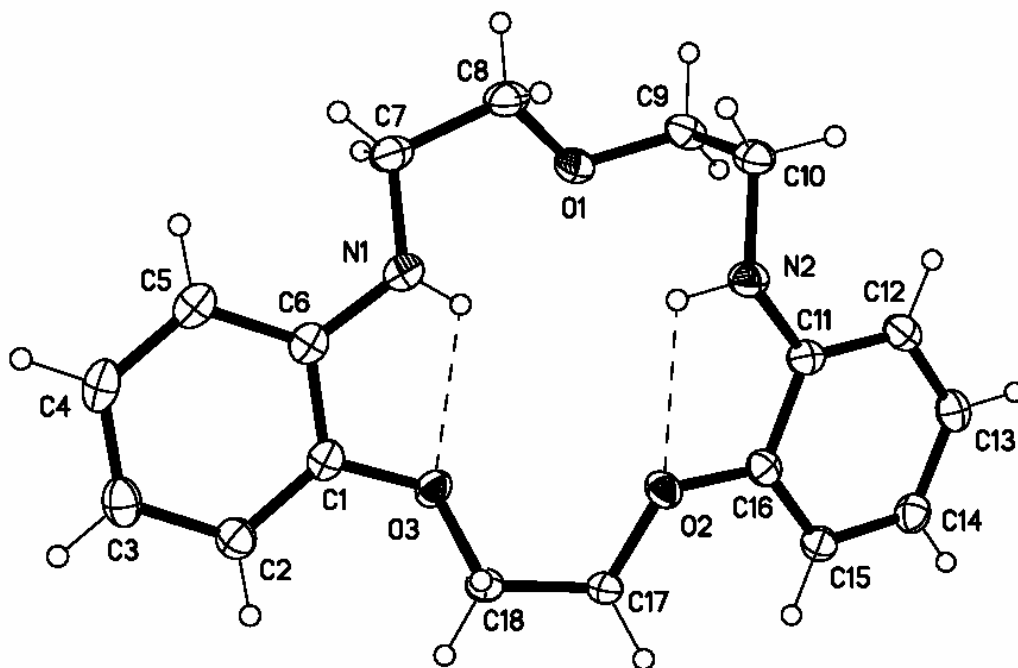


Figure 2-26. X-ray crystal structure of An2.1, (10).

11. 9,10,20,21-tetrahydro-5*H*,12*H*-dibenzo[*e,q*][1,4,10,13,7,16]tetraoxadiazacyclooctadecine-6,13(7*H*,14*H*)-dione, An2.2*, (11)

A 0.050 M solution of the diamine was prepared by dissolving 5.50 g (0.0225 mol) of **4** in 200 mL of DMF and 250 mL of toluene. A 0.05 M solution of 2,2'-[ethane-1,2-diylbis(oxy)]diacetyl chloride was prepared by dissolving 4.84 g (0.0225 mol) of **1** in 450 mL of toluene. A 5 L Morton flask was equipped with a mechanical stirrer, an inlet and an outlet for nitrogen gas, and two 500 mL constant rate addition funnels. Initially, 500 mL of toluene containing 32 mL (0.23 mol) of N(Et)₃ was added to the Morton flask. The solutions of diamine and diacid chloride were placed in separate addition funnels. The solutions were added at an equal, constant rate to the 5 L flask over a period of 7 h. During addition the contents of the 5 L flask were stirred at 1000 rpm. The reaction salts were filtered and the solvent was removed by rotary evaporation. The white paste was recrystallized from EtOH. The product was recovered as a white spongy material with a 53% yield. The ¹H and ¹³C NMR data is listed on the following page and the spectra are shown in Figures 2-27 and 2-28, respectively. The mass spectrum is shown in Figure 2-29 with peaks at m/z of 409.2 (M + Na⁺) and 795.3 (M₂ + Na⁺). Crystals suitable for X-ray crystallography were grown by vapor diffusion with heptane diffusing into a solution of **11** dissolved in benzene.

The X-ray crystal structure for **11** is shown in Figure 2-30. The chemical shift values in the ^1H NMR spectra were in agreement with a previous literature report.¹⁴

^1H NMR (CDCl_3): $\delta = 9.04$ (s, 2H), 8.34 (d, $J = 7.7$ Hz, 2H), 7.02 (t, $J = 7.7$ Hz, 2H), 6.96 (t, $J = 7.7$ Hz, 2H), 6.82 (d, $J = 7.7$ Hz, 2H), 4.42 (s, 4H), 4.10 (s, 4H), 3.81 (s, 4H) ppm.

^{13}C NMR (CDCl_3): $\delta = 167.1, 146.6, 127.3, 124.2, 121.6, 120.6, 110.8, 70.8, 70.0, 66.4$ ppm.

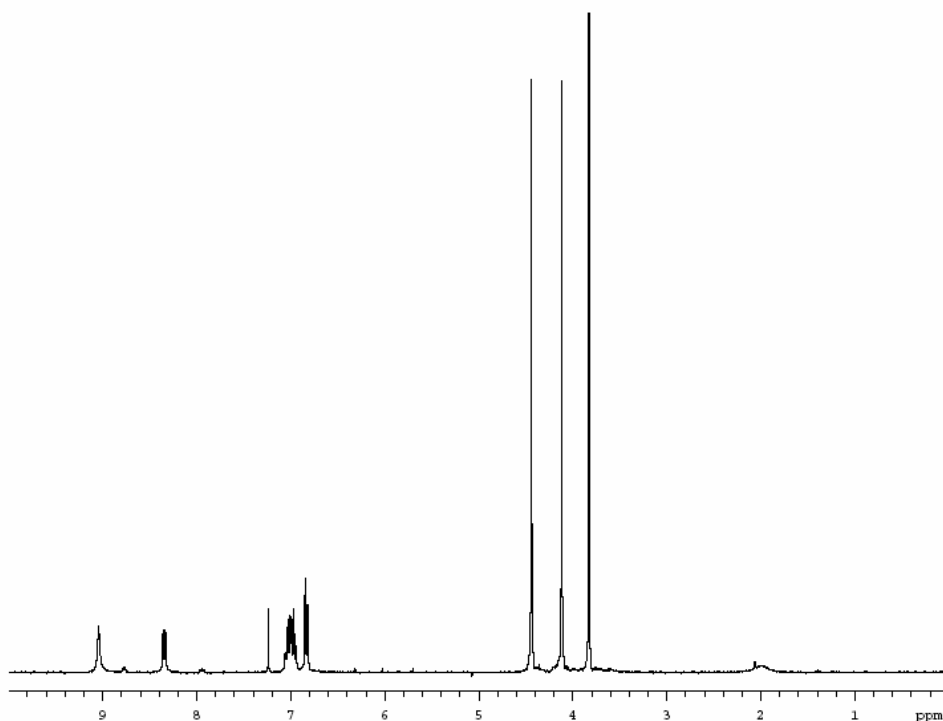


Figure 2-27. ^1H NMR of An2.2*, (**11**) in CDCl_3 .

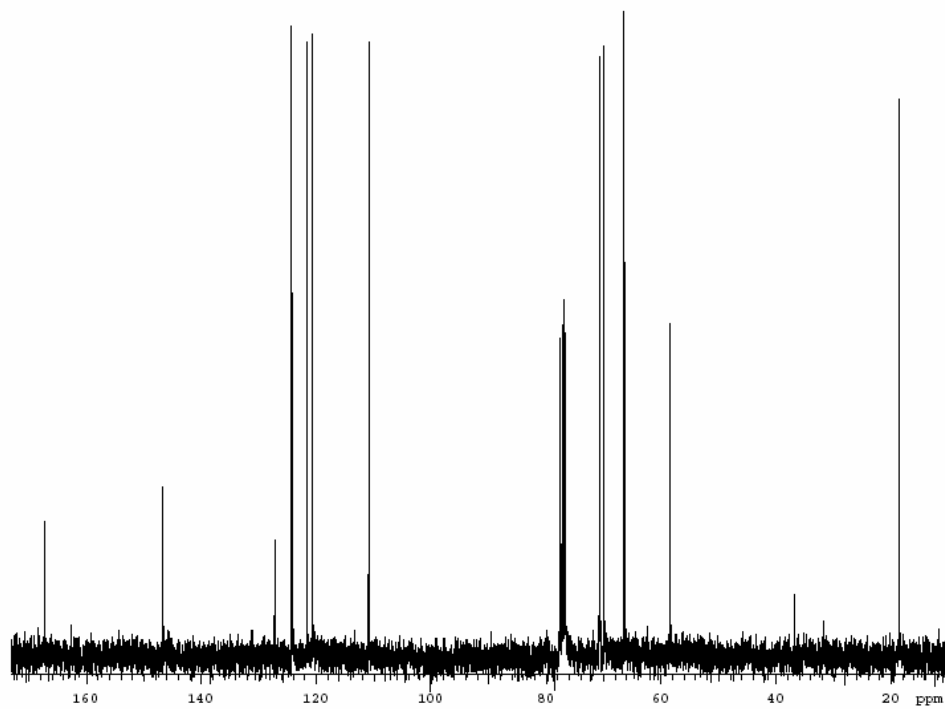


Figure 2-28. ^{13}C NMR of An2.2*, (11) in CDCl_3 .

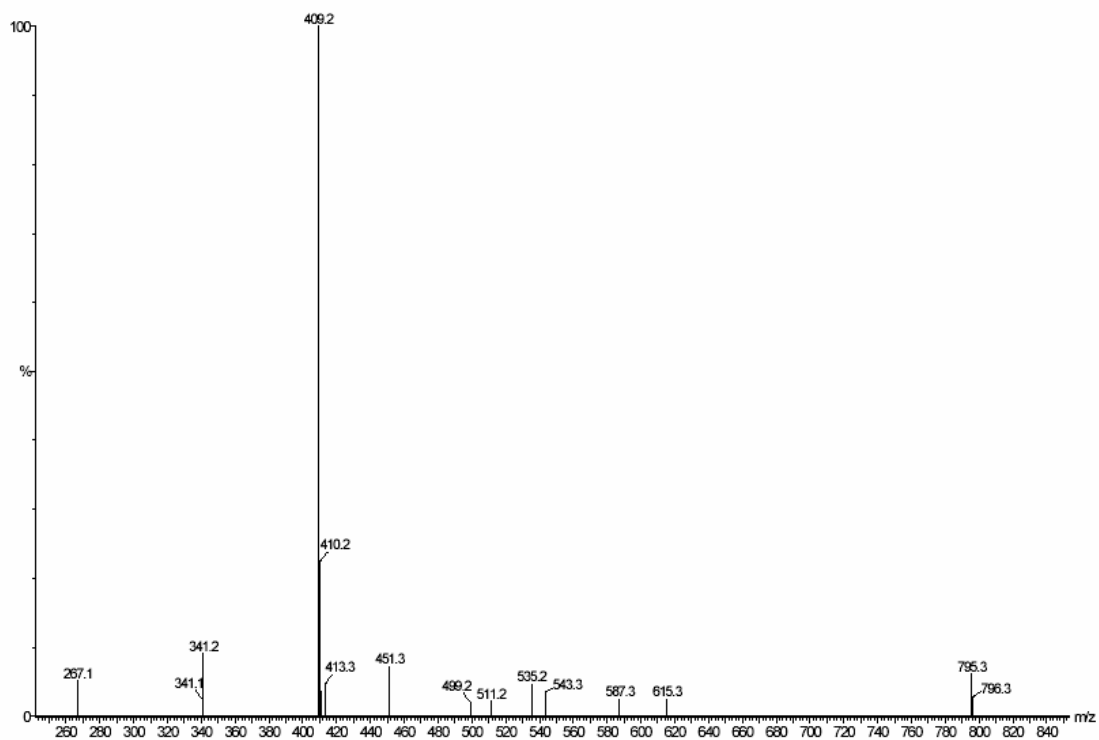


Figure 2-29. ESI-MS⁺ of An2.2*, (11) in MeOH.

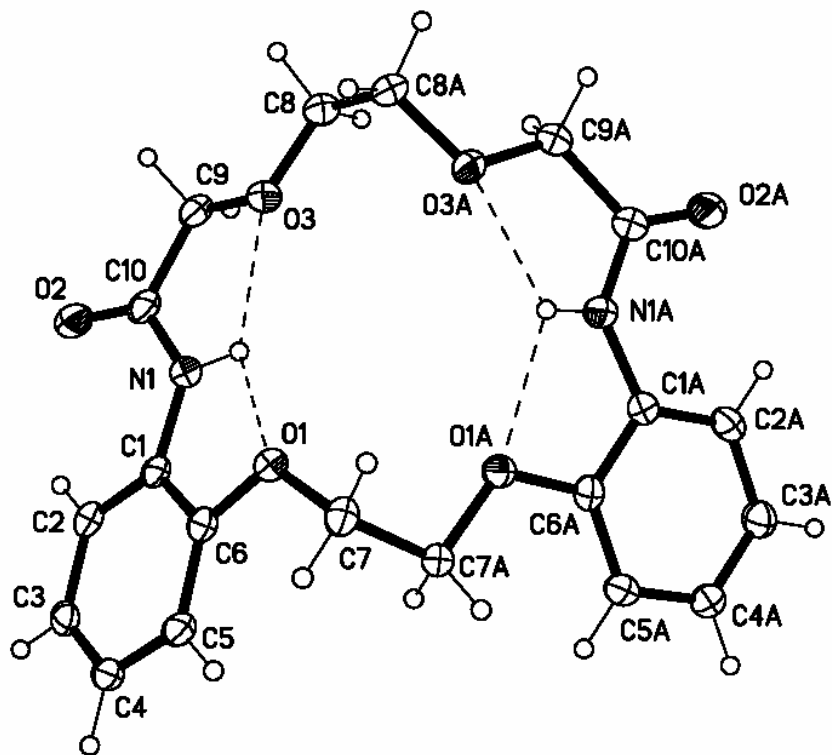


Figure 2-30. X-ray crystal structure of An2.2*, (11).

12. **6,7,9,10,13,14,20,21-octahydro-5*H*,12*H*-dibenzo[*e,q*][1,4,10,13,7,16]tetraoxa-diazacyclooctadecine, An2.2, (12)**

The monocyclic diamide **11** (4.19 g, 10.8 mmol) and 1M borane-THF complex (110 mL, 110 mmol) were added to a 200 mL three-neck round bottom flask fitted with a condenser and an inlet and an outlet for nitrogen gas. The diamide did not completely dissolve upon addition of the reducing agent. The reaction was refluxed for 45 min and then a 40 mL solution of 1:10 H₂O-THF was added dropwise over 1 h with a syringe pump. Gas evolution ceased after 20 mL, but the entire amount was added. The solution was cooled and 40 mL of H₂O were added and all of the white sludge went into solution. The organic solvent was removed by rotary evaporation leaving a white precipitate that

was filtered and washed with water. The product was dried under vacuum for 6 h and isolated in a 95.6% yield. The ^1H and ^{13}C NMR data is listed below and the spectra are shown in Figures 2-31 and 2-32, respectively. The mass spectrum is shown in Figure 2-33 with peaks at m/z of 359.2 ($\text{M} + \text{H}^+$) and 381.1 ($\text{M} + \text{Na}^+$). Crystals suitable for X-ray crystallography were grown by vapor diffusion with water diffusing into a solution of **12** dissolved in benzene. The X-ray crystal structure for **12** is shown in Figure 2-34.

^1H NMR (CDCl_3): $\delta = 6.84\text{-}6.90$ (m), $6.76\text{-}6.79$ (dd), $6.60\text{-}6.69$ (m), 4.37 (s), 3.70 (t), 3.59 (s), 3.32 (t) ppm.

^{13}C NMR (CDCl_3): $\delta = 146.08, 138.04, 121.84, 116.80, 110.42, 110.20, 70.59, 69.01, 66.48, 43.39$ ppm.

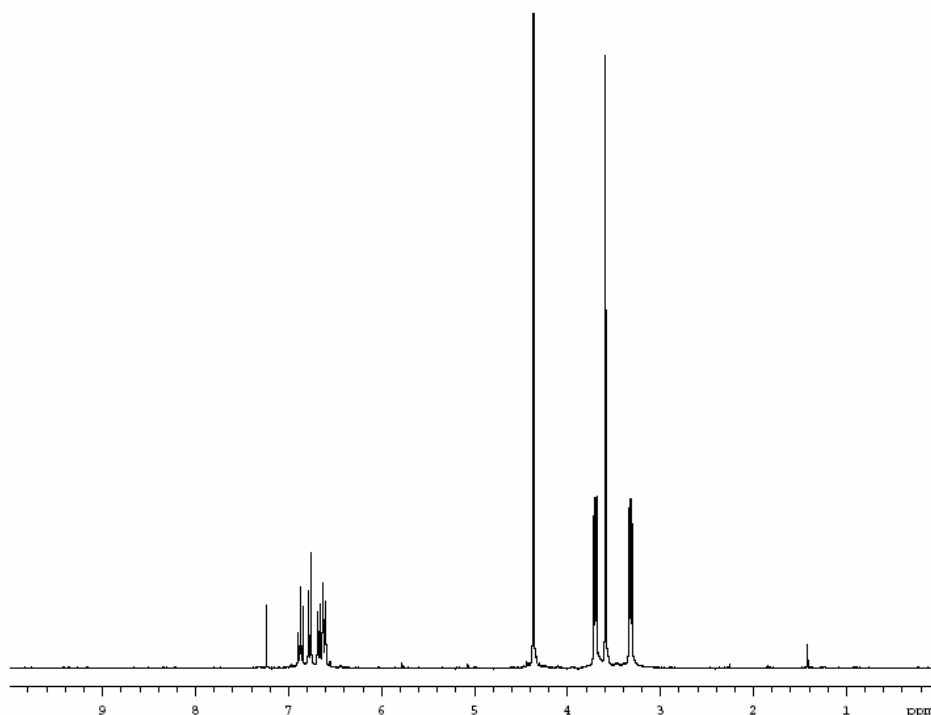


Figure 2-31. ^1H NMR of An2.2, (**12**) in CDCl_3 .

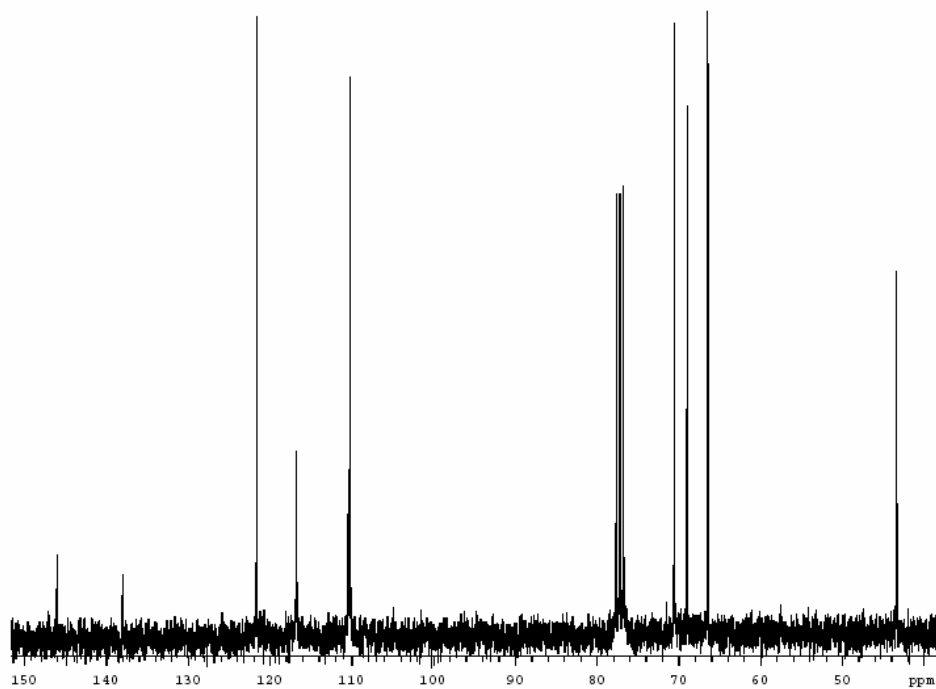


Figure 2-32. ^{13}C NMR of An2.2, (12) in CDCl_3 .

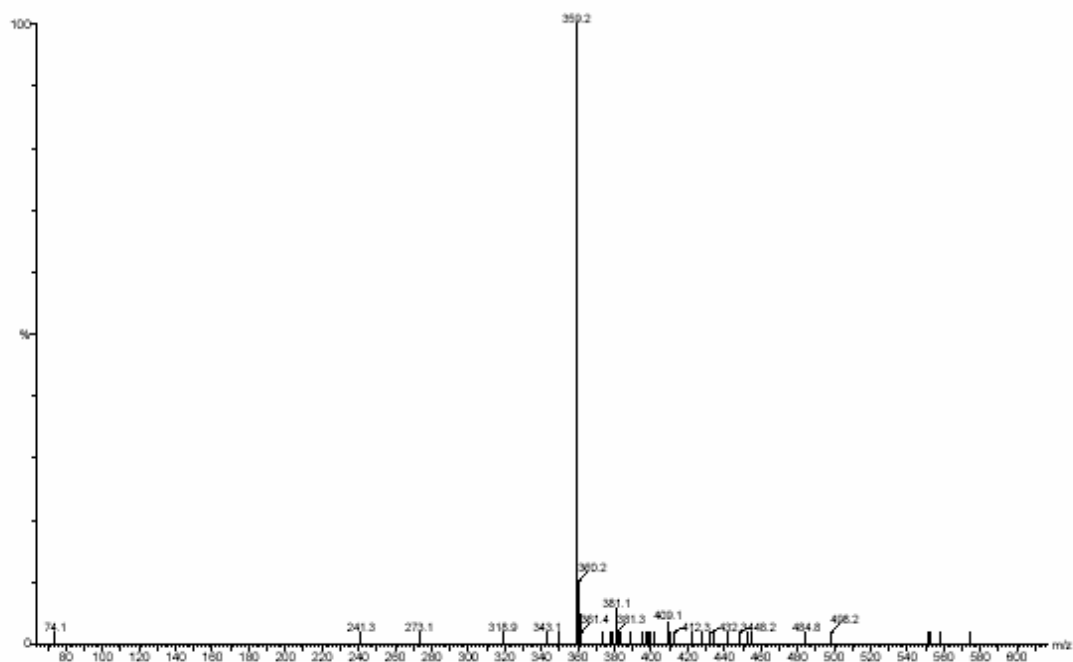


Figure 2-33. ESI- MS^+ of An2.2, (12) in MeOH.

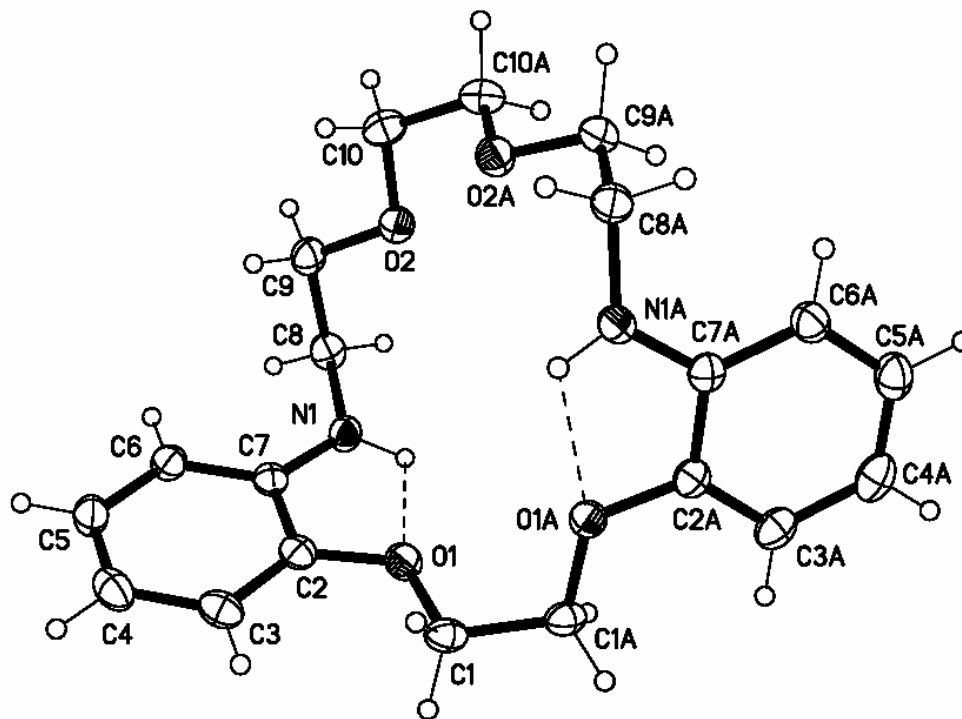


Figure 2-34. X-ray crystal structure of An2.2, (12).

13. 6,7,9,10-tetrahydro-16*H*,20*H*-dibenzo[*h,q*][1,4,7,13,10,16]tetraoxadiazacyclooctadecine-17,21(18*H*,22*H*)-dione, An3.1*, (13)

A 0.043 M solution of the diamine was prepared by dissolving 4.4 g (0.015 mol) of **6** in 350 mL of toluene and triethylamine (4.9 mL, 0.035 mol) was added as the scavenger base. A 0.049 M solution of 2,2'-oxydiacetyl chloride was prepared by dissolving 2.0 mL (0.017 mol) in 350 mL of toluene. A 5 L Morton flask was equipped with a mechanical stirrer, an inlet and an outlet for nitrogen gas, and two 500 mL constant rate addition funnels. Initially, 750 mL of toluene was added to the Morton flask. The solutions of diamine and diacid chloride were placed in separate addition funnels. The solutions were added at an equal, constant rate to the 5 L flask over a period

of 6 h. During addition the contents of the 5 L flask were stirred at 1000 rpm. The reaction salts were filtered and the solvent was removed by rotary evaporation. A light brown solid was recrystallized from a solvent mixture of benzene and heptane in 80% yield. The ^1H and ^{13}C NMR data is listed below and the spectra are shown in Figures 2-35 and 2-36, respectively. The mass spectrum is shown in Figure 2-37 with peaks at m/z of 387.2 ($\text{M} + \text{H}^+$) and 409.2 ($\text{M} + \text{Na}^+$). Crystals suitable for X-ray crystallography were grown by vapor diffusion with heptane diffusing into a solution of **13** dissolved in benzene. In the X-ray crystal structure of **13** the unit cell contains a water molecule (fractional occupancy = 0.50) and two crystallographically independent molecules. Molecules A (with H_2O) and B are shown in Figures 2-38 and 2-39, respectively. The chemical shift values in the ^1H NMR spectra were in agreement with a previous literature report.¹⁵

^1H NMR (CDCl_3): $\delta = 8.73$ (s, 2H), 8.22 (dd, $J = 7.9, 1.8$ Hz, 2H), 7.06 (td, $J = 7.9, 1.8$ Hz, 2H), 6.97 (td, $J = 7.9, 1.5$ Hz, 2H), 6.85 (dd, $J = 7.9, 1.5$ Hz, 2H), 4.25 (s, 4H), 4.21 (m, 4H), 3.84 (m, 4H) ppm.

^{13}C NMR (CDCl_3): $\delta = 166.4, 147.8, 126.7, 125.0, 121.5, 111.4, 71.8, 69.4, 67.9$ ppm.

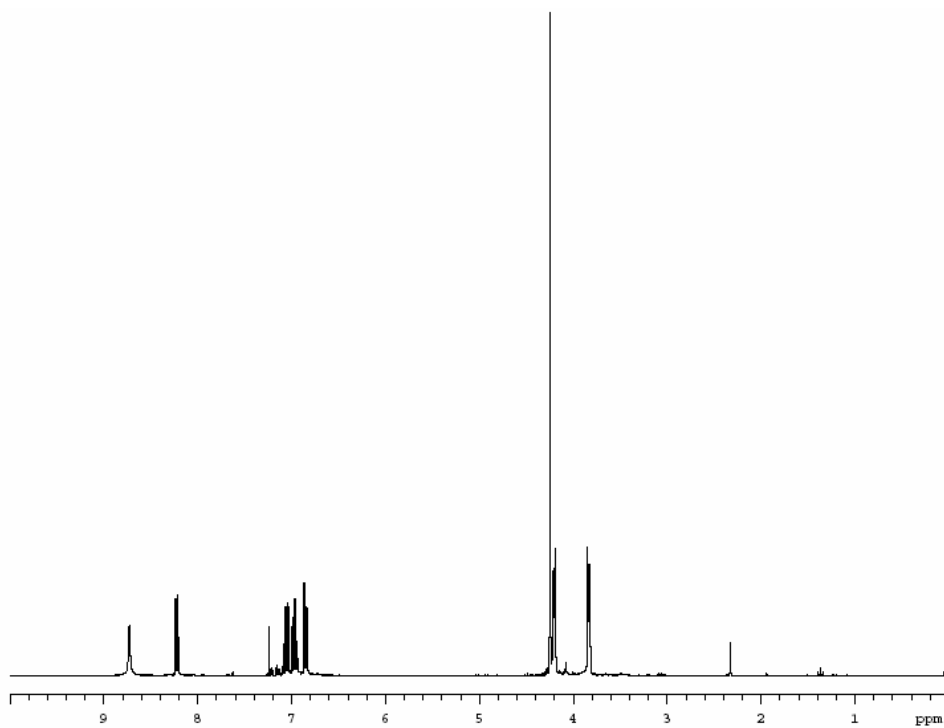


Figure 2-35. ^1H NMR of An3.1*, (**13**) in CDCl_3 .

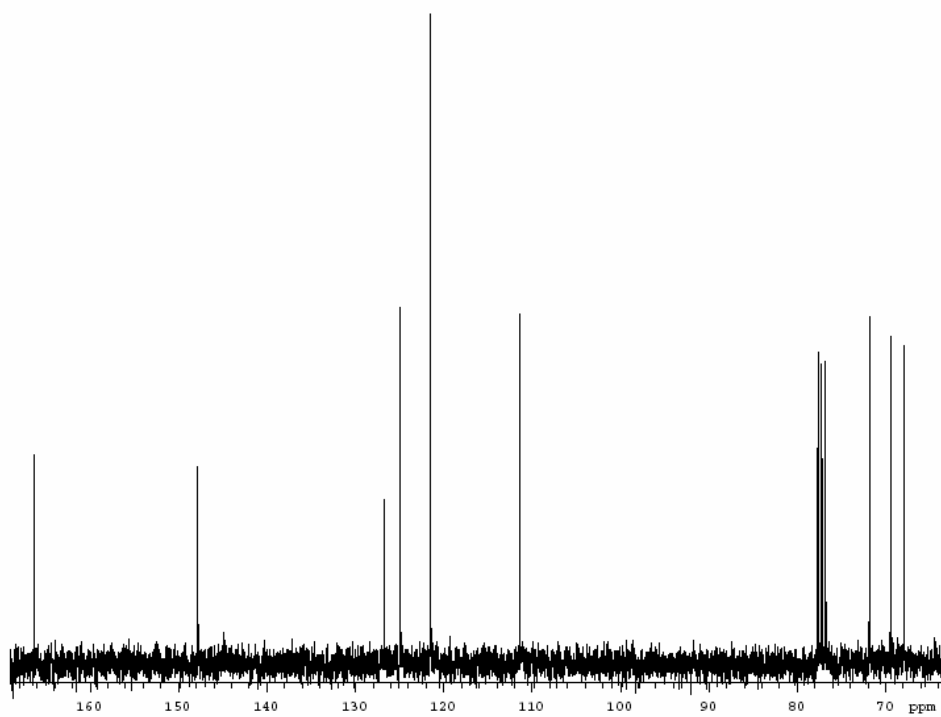


Figure 2-36. ^{13}C NMR of An3.1*, (**13**) in CDCl_3 .

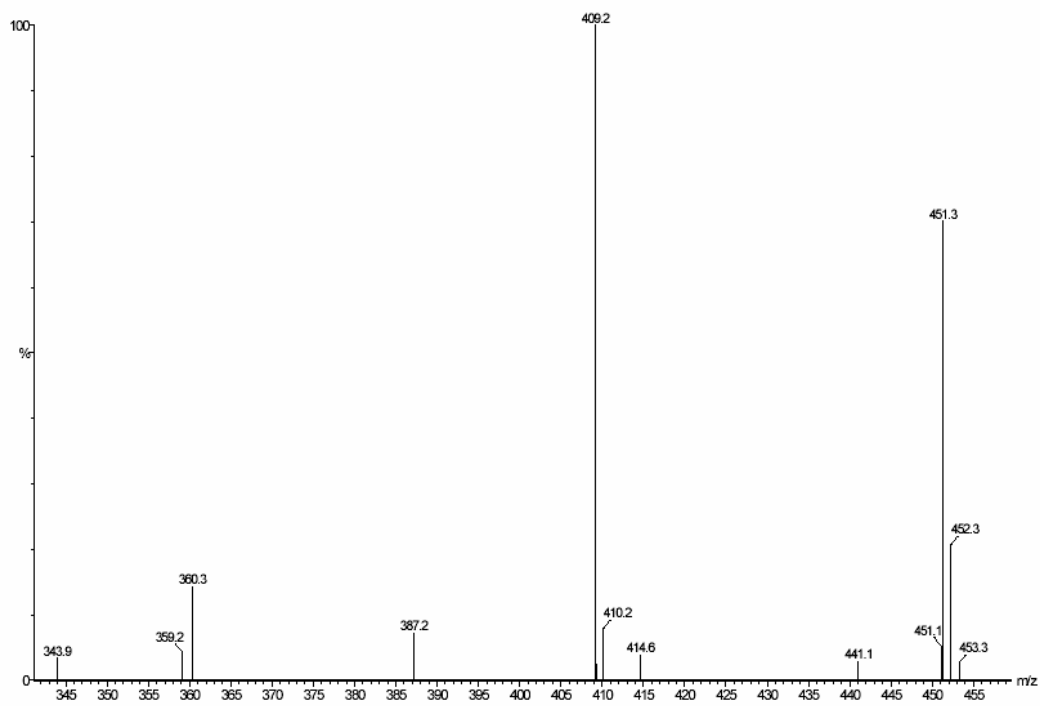


Figure 2-37. ESI-MS⁺ of An3.1*, (13) in MeOH.

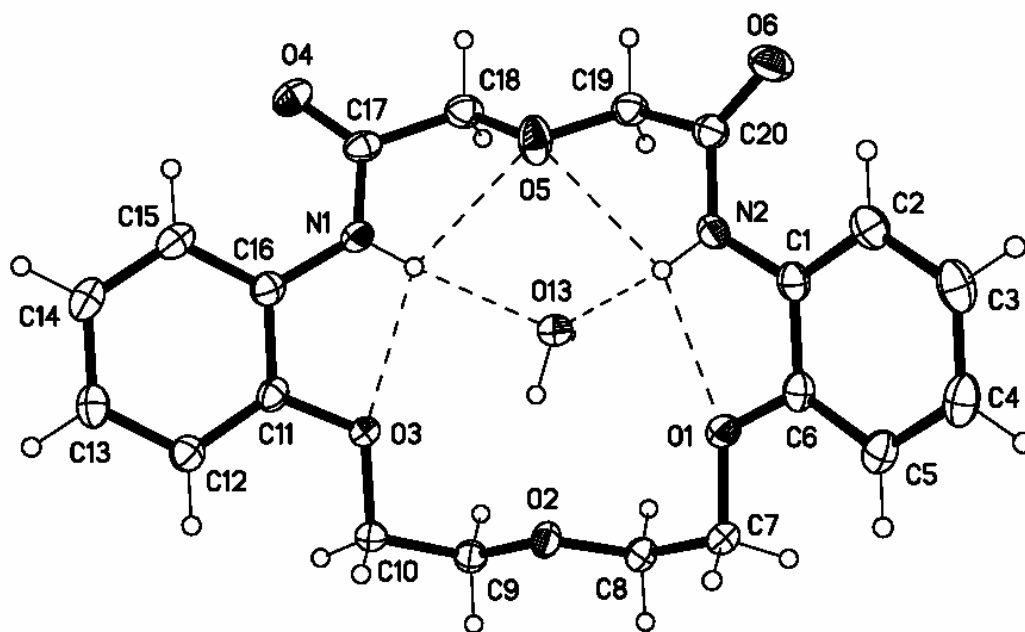


Figure 2-38. X-ray crystal structure of An3.1*, (13), Molecule A.

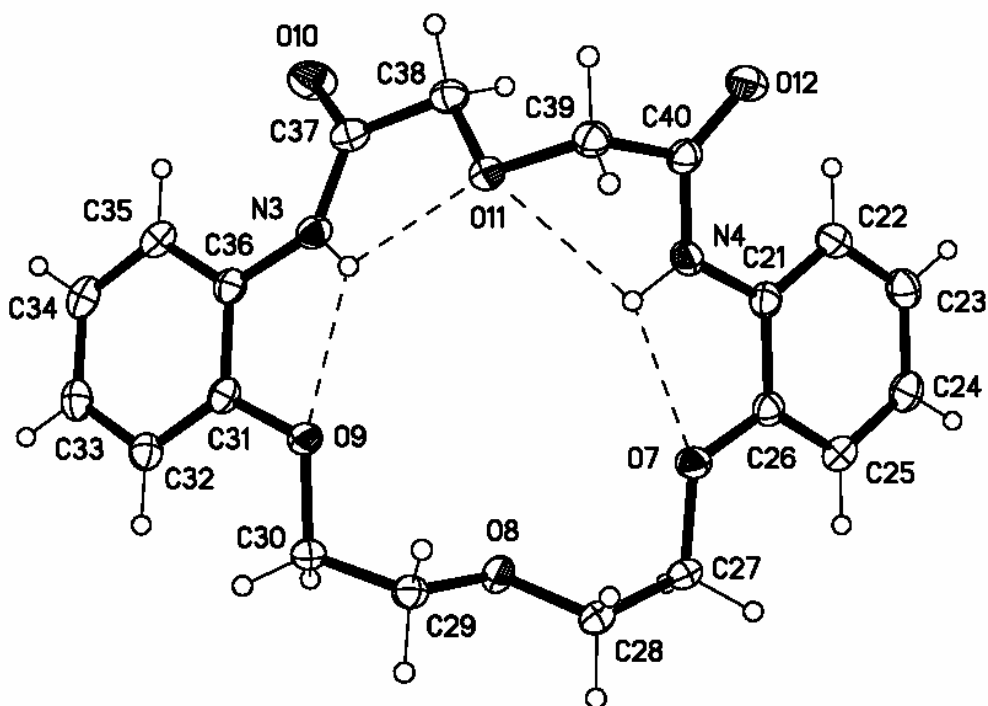


Figure 2-39. X-ray crystal structure of An3.1*, (13), Molecule B.

14. 6,7,9,10,17,18,21,22-octahydro-16*H*,20*H*,dibenzo[*h,q*][1,4,7,13,10,16]tetraoxa-diazacyclooctadecine, An3.1, (14)

To a 200 mL 3-neck round bottom flask surrounded by an ice bath was added 50 mL (50 mmol) of 1M borane-THF complex. The monocyclic diamide, **13**, (2.0 g, 5.2 mmol) was partially dissolved in THF and added slowly to the reaction mixture with a pipet. The pipet and beaker were thoroughly rinsed with THF. The solution was refluxed under a nitrogen atmosphere for 1 h. 20 mL of a solution of 1:10 H₂O-THF was added dropwise over 1 h with a syringe pump. Bubbling ceased before the addition was complete. The solution was allowed to cool to room temperature and 30 mL of H₂O were added to destroy the excess reducing agent. During removal of the organic solvent by

rotary evaporation a white solid precipitated from the solution. The white solid was filtered and washed with water. The product was dried under vacuum for 8 h. A yield of 95% was obtained. The ^1H and ^{13}C NMR data is listed below and the spectra are shown in Figures 2-40 and 2-41, respectively. The mass spectrum is shown in Figure 2-42 with peaks at m/z of 359.2 ($\text{M} + \text{H}^+$) and 381.2 ($\text{M} + \text{Na}^+$). Crystals suitable for X-ray crystallography were grown by slow evaporation of a methanol solution. The X-ray crystal structure for **14** is shown in Figure 2-43. The chemical shift values in the ^1H NMR spectra were in agreement with a previous literature report and are listed below.¹⁵

^1H NMR (CDCl_3): $\delta = 6.82\text{-}6.87$ (m), $6.57\text{-}6.73$ (m), 4.71 (bs), 4.16 (t), 3.93 (t), 3.78 (t), 3.28 (t) ppm.

^{13}C NMR (CDCl_3): $\delta = 146.53, 138.25, 121.42, 116.94, 110.18, 109.80, 69.91, 67.06, 43.80, 35.96$ ppm.

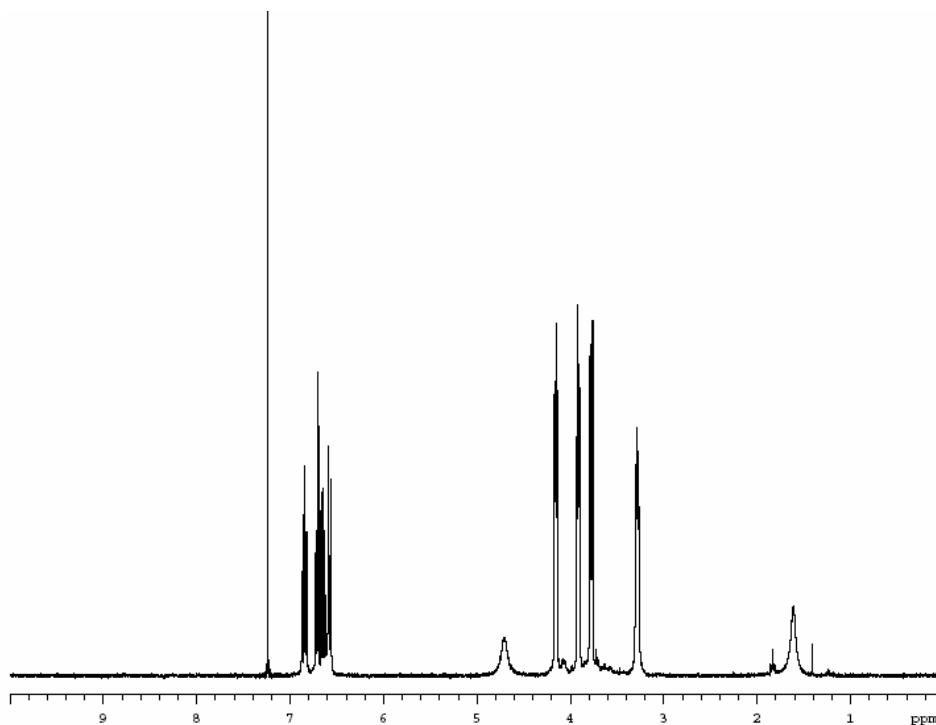


Figure 2-40. ^1H NMR of An3.1, (**14**) in CDCl_3 .

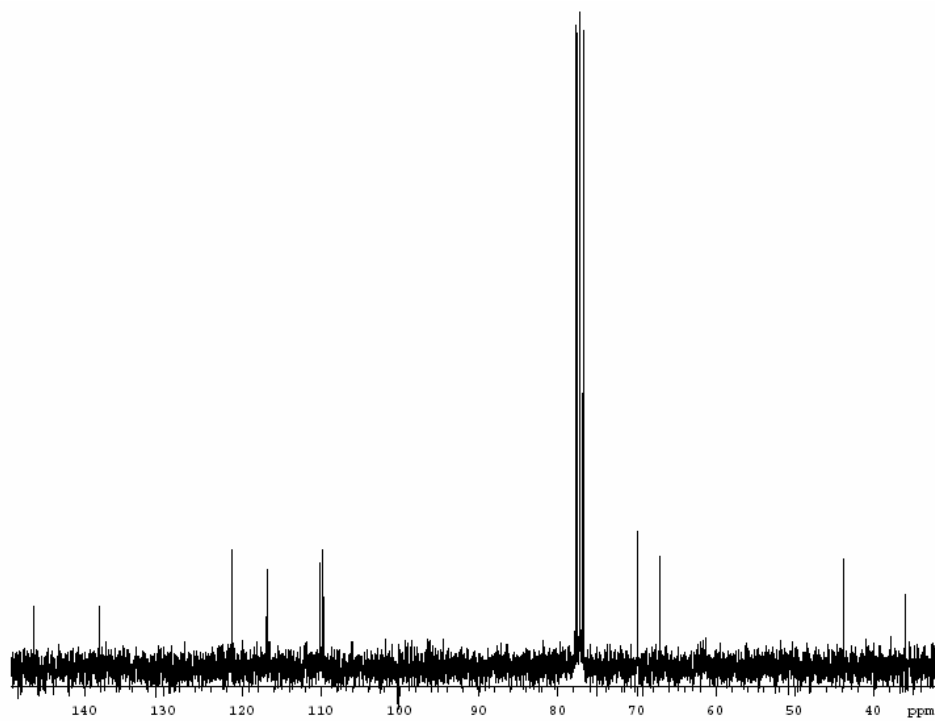


Figure 2-41. ^{13}C NMR of An3.1, (14) in CDCl_3 .

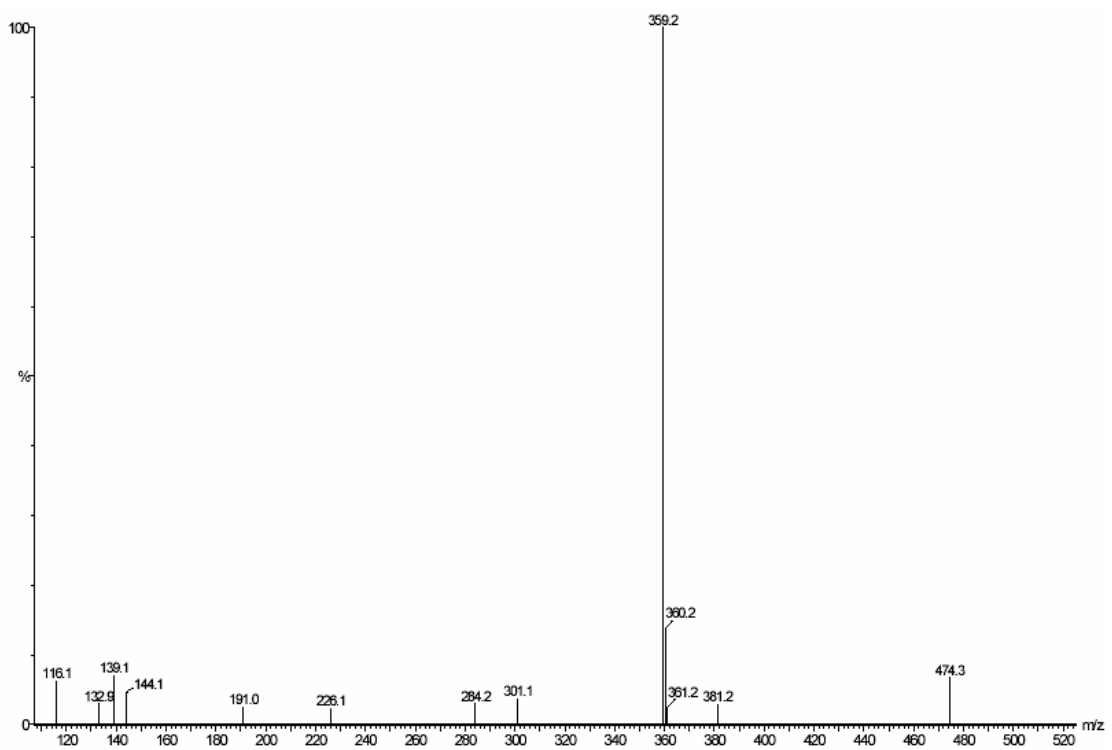


Figure 2-42. ESI-MS $^+$ of An3.1, (14) in MeOH.

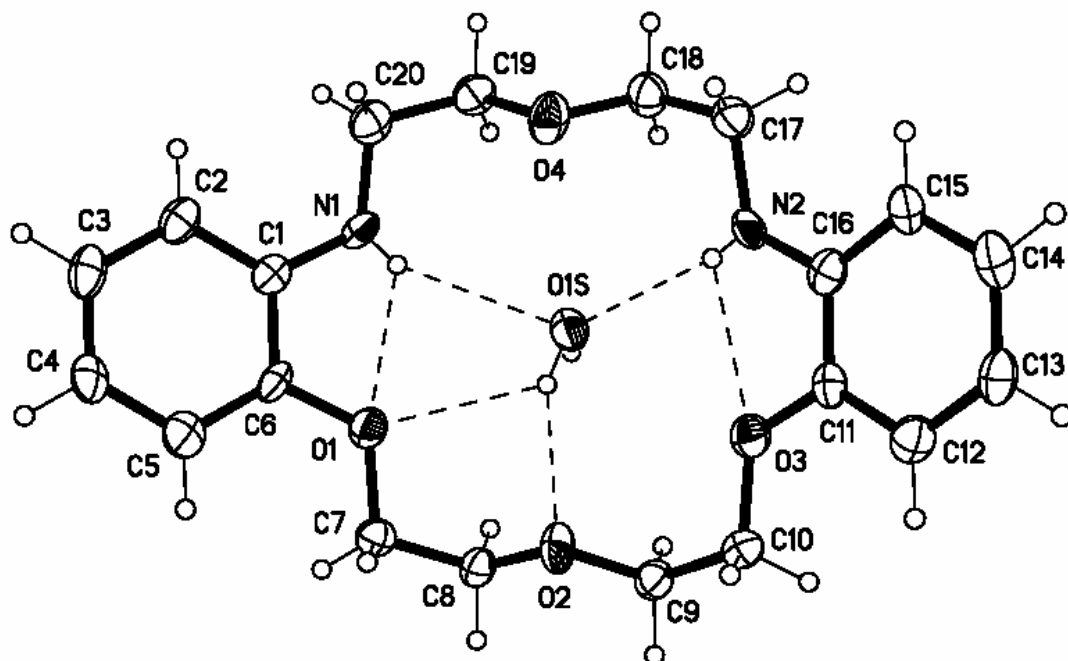


Figure 2-43. X-ray crystal structure of An3.1, (14).

E. Synthesis of bicyclic diamines (cryptands)

15. 9,10,20,21-tetrahydro-5,14-(ethanoxyethano)dibenzo[*e,q*][1,4,10,13,7,16]-tetraoxadiazacyclooctadecine-6,13-dione, An2.1.2*, (15)

A solution (0.0160 M) of the monocyclic diamine, **10**, was prepared by adding 1.51 g (0.00479 mol) to 300 mL of toluene. Pyridine (1.0 mL, 0.012 mol) was added to this solution as a scavenger base. A 0.0164 M solution of **1** was prepared by adding 1.06 g (0.00493 mol) of the diacid chloride to 300 mL of toluene. A 5 L Morton flask was equipped with a mechanical stirrer, an inlet and an outlet for nitrogen gas, and two 500 mL constant rate addition funnels. Initially, 750 mL of toluene was added to the Morton flask. The solutions of diamine and diacid chloride were placed in separate addition

funnels. During addition the contents of the 5 L flask were stirred at 1000 rpm. The equimolar solutions of **10** and **1** were added at the same rate for the first 180 mL of each solution. After this point, the solution of **1** was unintentionally added at a rate twice as fast as **10**. The pyridinium salts were filtered and the reaction solvent was removed by rotary evaporation. The pure bicyclic diamide **15** was recovered by flash chromatography on silica gel using CH₂Cl₂ and MeOH (up to 5%) as the eluent. Yellow crystals were collected in 11% yield. The mass spectrum is shown in Figure 2-44 with peaks at m/z of 457.2 (M + H⁺), 479.2 (M + Na⁺), and 935.4 (M₂ + Na⁺). Crystals suitable for X-ray crystallography were grown by vapor diffusion with heptane diffusing into a solution of **15** dissolved in dichloromethane. The X-ray crystal structure for **15** is shown in Figure 2-45.

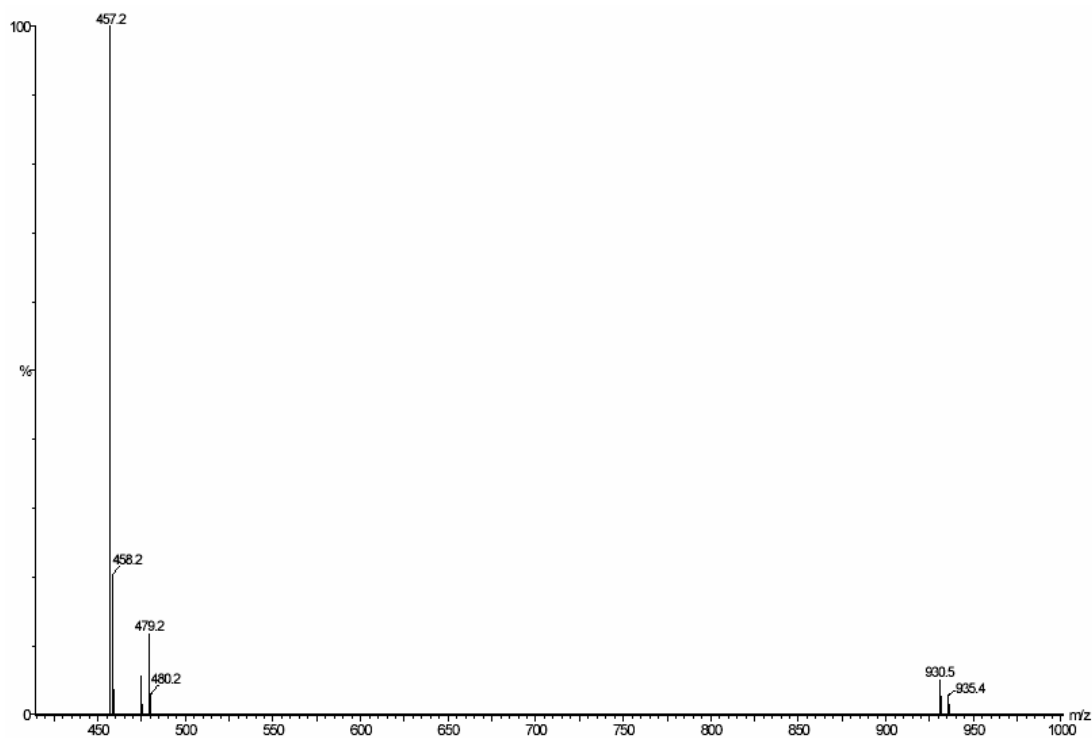


Figure 2-44. ESI-MS⁺ of An2.1.2*, (**15**) in MeOH.

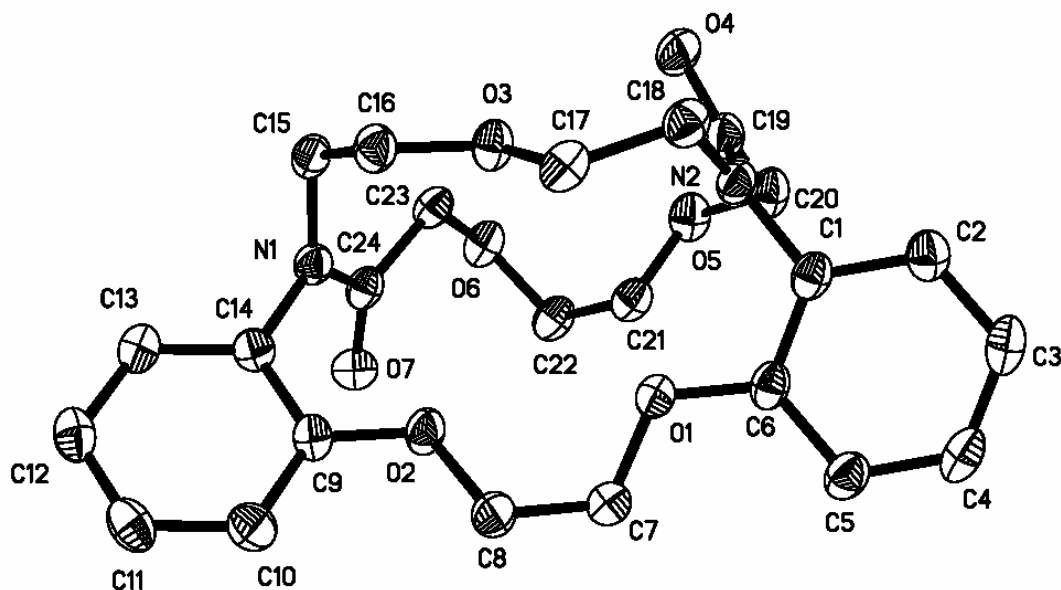


Figure 2-45. X-ray crystal structure of An2.1.2*, (**15**).

16. 6,7,9,10,12,13,20,21-octahydro-5,14-(ethanoxyethano)dibenzo[*e,q*]-[1,4,10,13,7,16]tetraoxadiazacyclooctadecine, An2.2.1, (16**)**

a) A 100 mL 3-neck round bottom flask was surrounded by an ice bath and was prepared with a condenser and an inlet and an outlet for nitrogen gas. A solution of the 1M borane-THF complex (8 mL, 8 mmol) was added to the flask, followed by the slow addition of 0.10 g (0.22 mmol) of **15** partially dissolved in THF. The reaction mixture was refluxed for 2 hr prior to the addition of 5 mL of a solution of 1:10 H₂O-THF with a syringe pump. The addition was complete after 30 min and the solution was allowed to cool to room temperature. The excess reducing agent was destroyed by the addition of 10 mL of H₂O. The organic solvent was removed by rotary evaporation. The remaining solution was treated with 10 mL of 6 M HCl, made basic with NH₃, and then extracted with CHCl₃ (3 x 50 mL). The CHCl₃ layer was dried with MgSO₄, filtered, and rotary

evaporated. During removal of the organic solvent a white solid precipitated from the solution. The solid was recovered from the CHCl_3 in a 60% yield.

b) To a 100 mL 3-neck round bottom flask equipped with a condenser and an inlet and an outlet for nitrogen gas, was added 0.508 g (1.11mmol) of **17** and 15 mL (15 mmol) of 1M borane-THF complex. The solution was refluxed for 1 hr and then a 15 mL solution of 10% $\text{H}_2\text{O}:\text{THF}$ was added with a syringe pump. The addition was complete after 1 h and the flask was allowed to cool to room temperature. Water (10mL) was added to destroy the excess reducing agent. The organic solvent was removed by rotary evaporation and the remaining aqueous solution was treated with concentrated 6 M HCl, 6 M NH_3 , and then extracted with CHCl_3 (3 x 40 mL). The product was recovered from the CHCl_3 layer in a 50% yield. The ^1H and ^{13}C NMR data is listed below and the spectra are shown in Figures 2-46 and 2-47, respectively. The mass spectrum is shown in Figure 2-48 with peaks at m/z of 451.2 ($\text{M} + \text{Na}^+$) and 879.5 ($\text{M}_2 + \text{Na}^+$). Crystals suitable for X-ray crystallography were grown by vapor diffusion with heptane diffusing into a solution of **16** dissolved in benzene. The X-ray crystal structure for **16** is shown in Figure 2-49.

^1H NMR (CDCl_3): $\delta = 6.86\text{-}6.97$ (m), $4.22\text{-}4.42$ (m), $3.97\text{-}4.06$ (m), $3.11\text{-}3.89$ (m) ppm.

^{13}C NMR (CDCl_3): $\delta = 153.19, 141.64, 122.02, 121.47, 119.95, 114.53, 70.88, 70.37, 69.71, 68.17, 56.22, 54.06$ ppm.

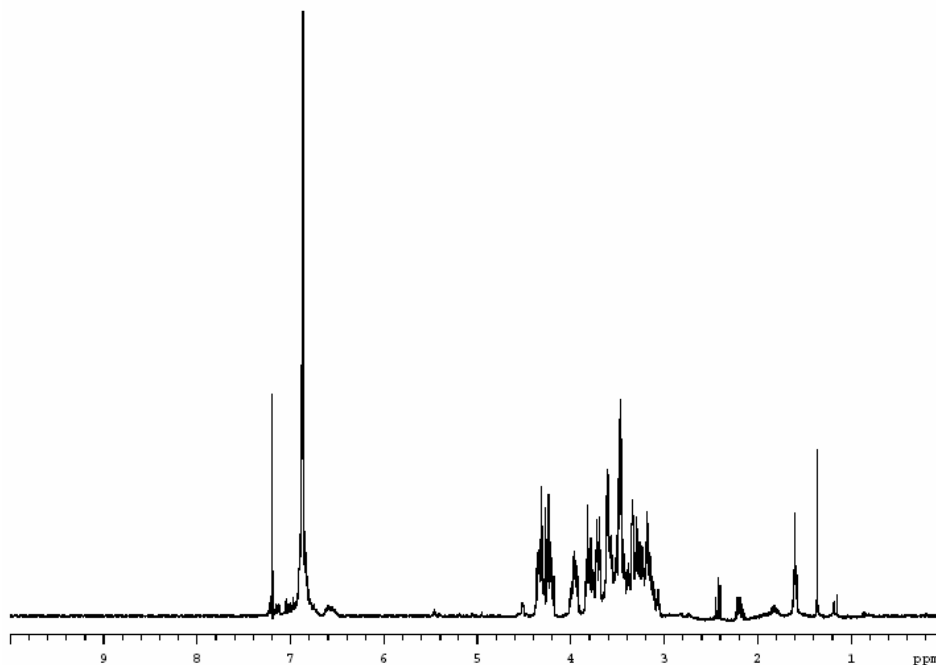


Figure 2-46. ^1H NMR of An2.2.1, (**16**) in CDCl_3 .

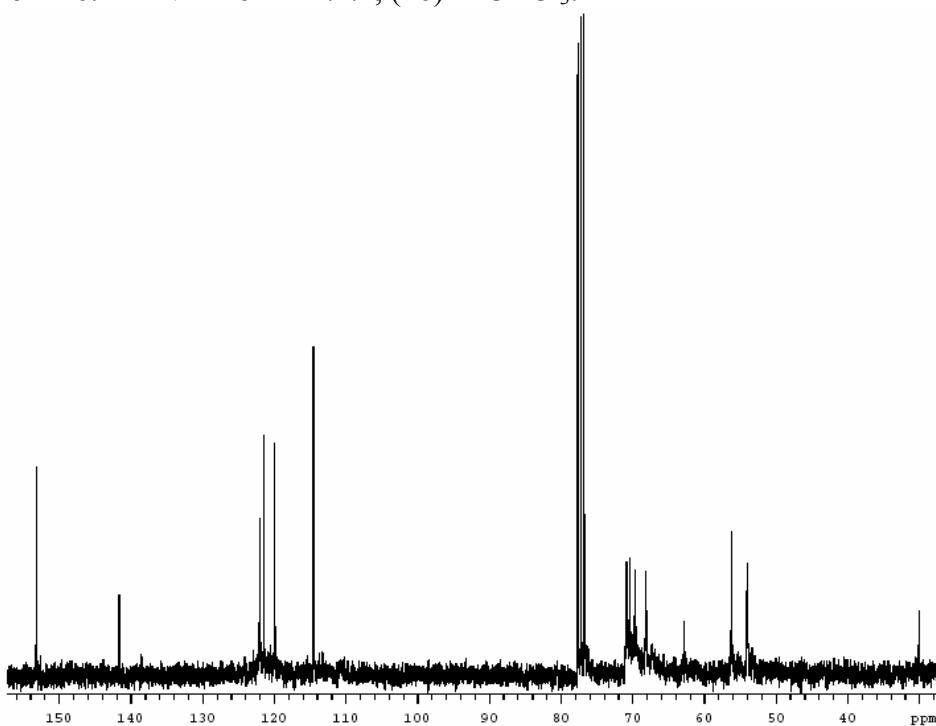


Figure 2-47. ^{13}C NMR of An2.2.1, (**16**) in CDCl_3 .

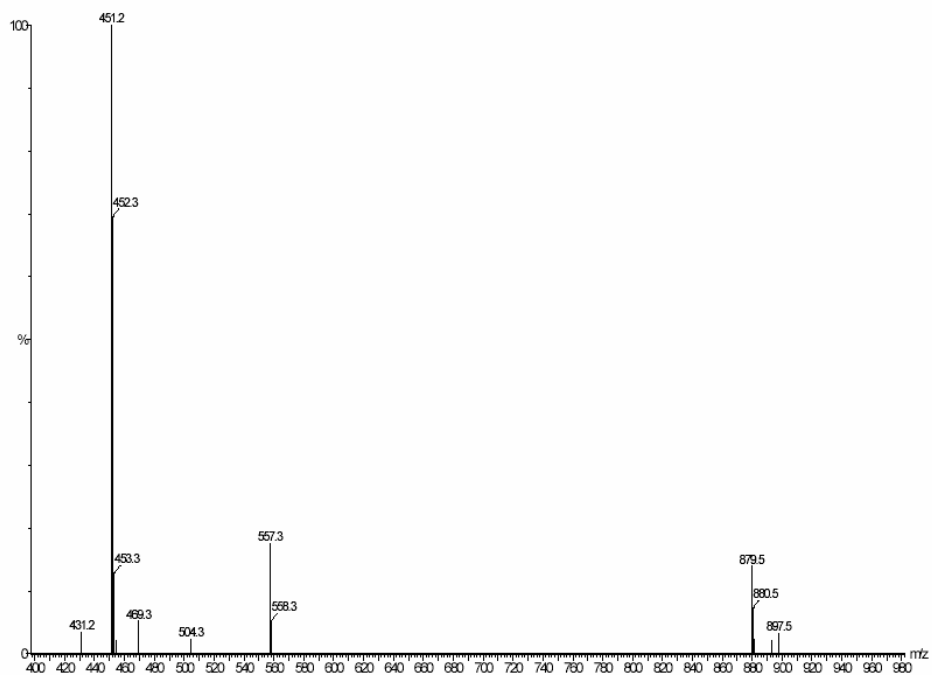


Figure 2-48. ESI-MS⁺ of An2.2.1, (16) in MeOH.

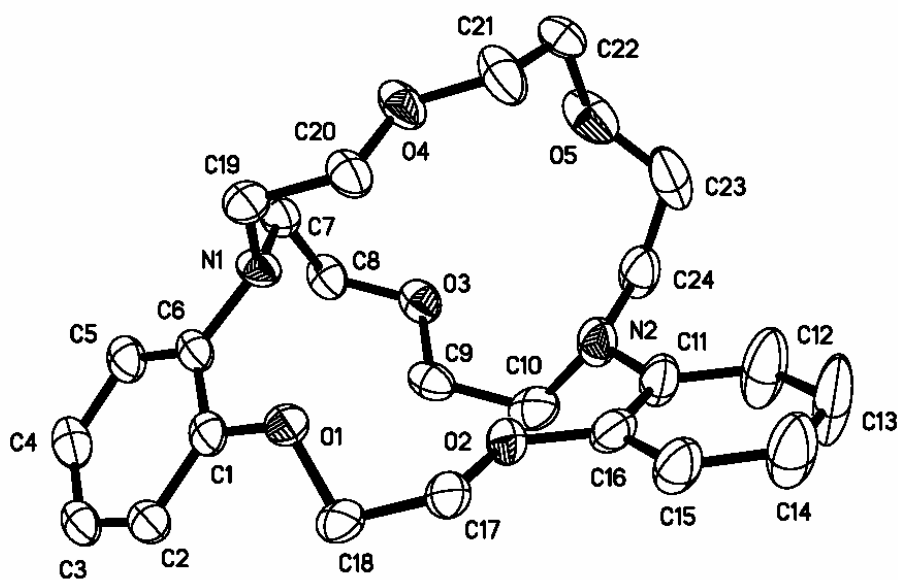


Figure 2-49. X-ray crystal structure of An2.2.1, (16).

**17. 6,7,9,10,12,13,20,21-octahydro-5,14-(ethanoxyethano)dibenzo[*e,q*]-
[1,4,10,13,7,16]tetraoxadiazacyclooctadecine-23,27-dione, An2.2.1*, (17)**

A 0.01096 M solution of **12** was prepared by adding 2.003 g (5.587 mmol) of the monocyclic diamine to a mixture of 290 mL of toluene and 220 mL of DMF. A 0.011 M solution of the diacid chloride was made by adding 0.67 mL (5.6 mmol) of 2,2'-oxydiacetyl chloride to 510 mL of toluene. A 5 L Morton flask was prepared with a mechanical stirrer, an inlet and an outlet for nitrogen gas, and an initial volume of 800 mL of toluene. Pyridine (4.5 mL, 0.056 mol) was added as a scavenger base. The equimolar solutions were added at the same rate with two 50 mL syringes powered by a syringe pump. The reaction solvent was removed by rotary evaporation. A yellow oil and white precipitate remained. The crude mixture was dissolved in water and the product was extracted with CH₂Cl₂. The bicyclic diamide **17** was obtained in a 65% yield. The mass spectrum is shown in Figure 2-50 with peaks at *m/z* of 457.3 (M + H⁺) and 479.2 (M + Na⁺). Crystals suitable for X-ray crystallography were grown by vapor diffusion with methanol diffusing into a solution of **17** dissolved in dichloromethane. The X-ray crystal structure unit cell for **17** contains two crystallographically independent molecules. Molecules A and B are shown in Figures 2-51 and 2-52, respectively.

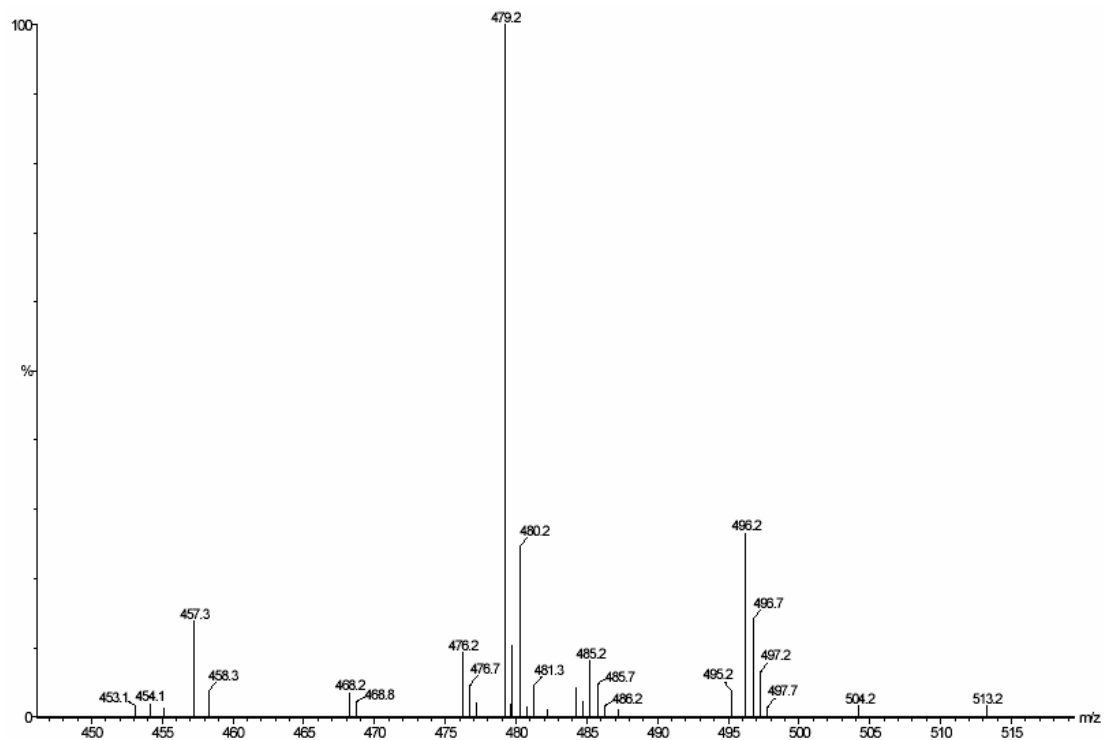


Figure 2-50. ESI-MS⁺ of An2.2.1* (17) in MeOH.

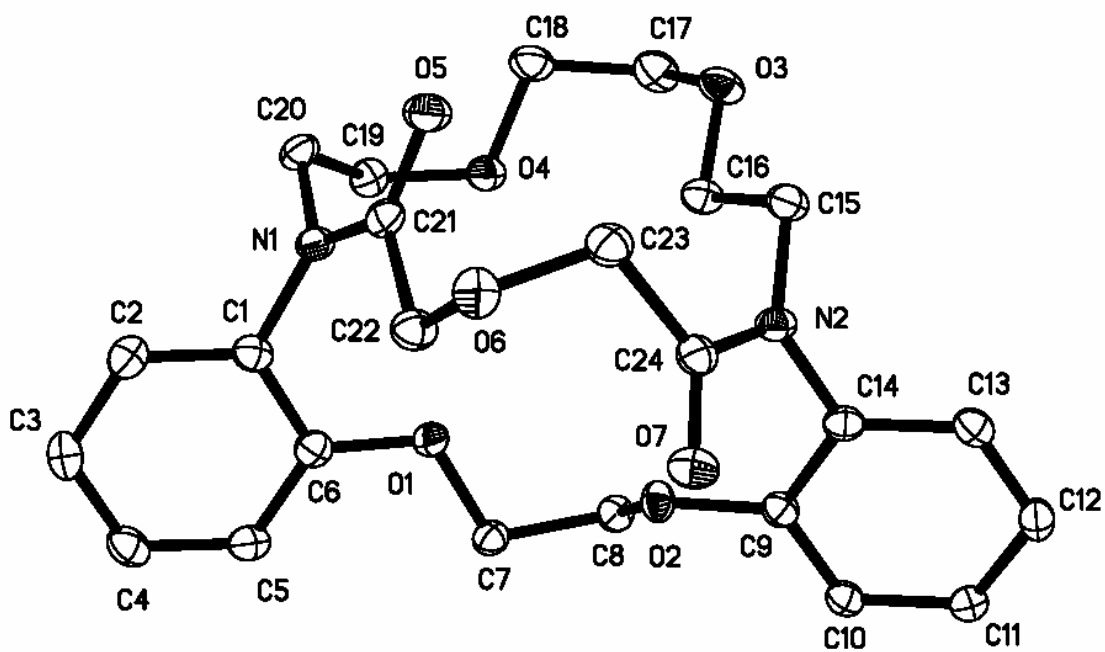


Figure 2-51. X-ray crystal structure of An2.2.1*, (17), Molecule A.

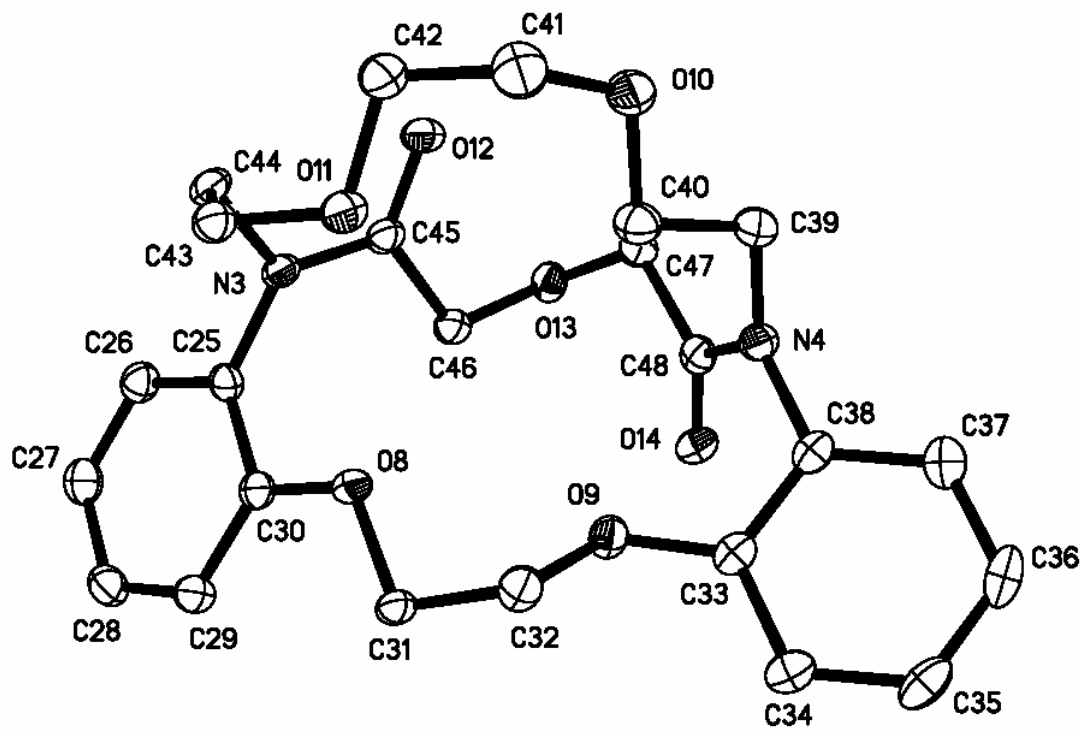


Figure 2-52. X-ray crystal structure of An2.2.1*, (17), Molecule B.

**18. 9,10,20,21-tetrahydro-5,14-(ethanooxyethanoxyethano)dibenzo[*e,q*]-
[1,4,10,13,7,16]tetraoxadiazacyclooctadecine-6,13-dione, An2.2.2*, (18)**

A 0.0164 M of **12** was prepared by adding 2.65 g (7.39 mmol) of the monocyclic diamine to a mixture of 250 mL of toluene and 200 mL of DMF. Pyridine (6.2 mL, 0.077 mol) was added to the diamine solution as a scavenger base. A 0.0172 M solution of the diacid chloride was made by adding 1.66 g (7.72 mmol) of **1** to 450 mL of toluene. A 5 L Morton flask was outfitted with a mechanical stirrer, an inlet and an outlet for nitrogen gas. An initial volume of 600 mL of toluene was added to the flask. Constant rate addition funnels were used to add the equimolar solutions at a similar rate to the reaction flask. The reaction solvent was removed by rotary evaporation and a yellow oil remained. The bicyclic diamide **18** was purified by flash column chromatography on silica gel using CH₂Cl₂ and MeOH (up to 10%) as the eluent. Recrystallization was accomplished from a solvent mixture of benzene and heptane. The yield was 32%. The mass spectrum is shown in Figure 2-53 with peaks at *m/z* of 501.3 (M + H⁺), 523.3 (M + Na⁺), and 1023.5 (M₂ + Na⁺). Crystals suitable for X-ray crystallography were grown by vapor diffusion with heptane diffusing into a solution of **18** dissolved in dichloromethane. The X-ray crystal structure for **18** is shown in Figure 2-54.

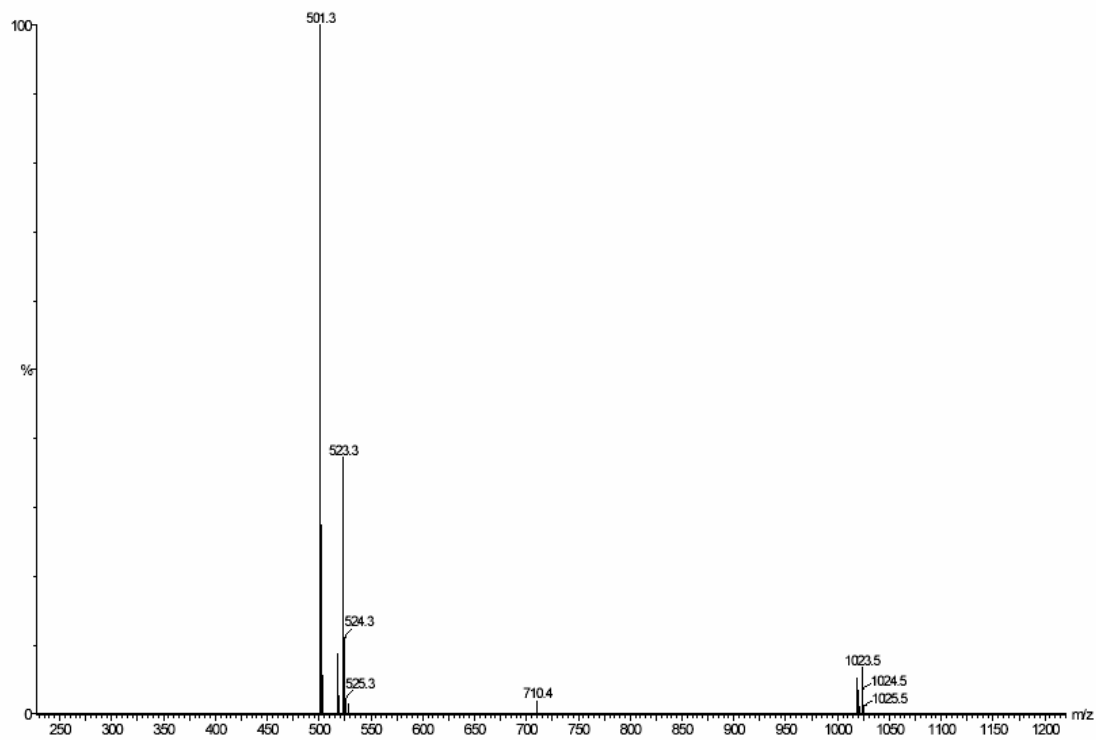


Figure 2-53. ESI-MS⁺ of An2.2.2*, (18) in MeOH.

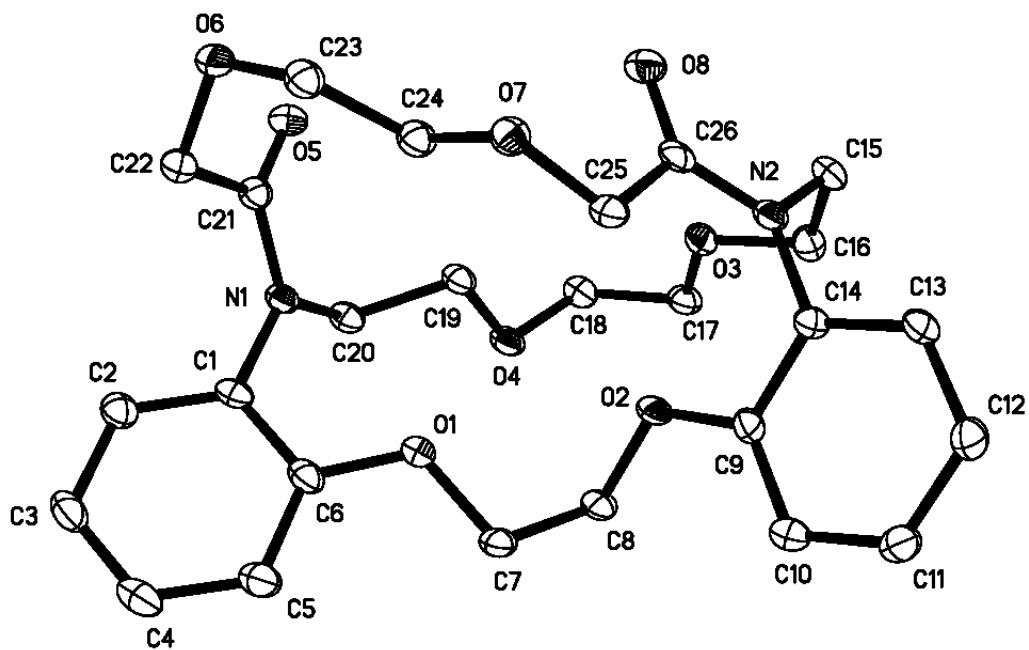


Figure 2-54. X-ray crystal structure of An2.2.2*, (18).

19. 6,7,9,10,12,13,20,21-octahydro-5,14-(ethanooxyethanoxyethano)dibenzo[e,g]-[1,4,10,13,7,16]tetraoxadiazacyclooctadecine, An2.2.2, (19)

A 200 mL 3-neck round bottom flask was surrounded by an ice bath and equipped with a condenser and an inlet and an outlet for nitrogen gas. The 1M Borane-THF complex (8 mL, 8 mmol) was added to the flask, followed by the slow addition of 0.505 g (1.01 mmol) of **18** dissolved in THF. The solution was refluxed for 1.5 h, then 18 mL of a solution of 1:10 H₂O-THF was added using a syringe pump. The addition was complete after 20 min and the solution was allowed to cool to room temperature. Addition of 20 mL of H₂O was added to destroy the excess reducing agent. The organic solvent was removed by rotary evaporation and the remaining aqueous solution was treated with 15 mL of 6 M HCl. The remaining solution was made basic with LiOH and then extracted with CHCl₃ (3 x 75 mL). The CHCl₃ layer was dried with Na₂SO₄, filtered, and the solvent removed by rotary evaporation. Recrystallization was accomplished from a solvent mixture of benzene and heptane. The product was obtained in quantitative yield (100%). The ¹H and ¹³C NMR data is listed below and the spectra are shown in Figures 2-55 and 2-56, respectively. The mass spectrum is shown in Figure 2-57 with a peak at m/z of 495.4 (M + Na⁺). Crystals suitable for X-ray crystallography were grown by vapor diffusion with heptane diffusing into a solution of **19** dissolved in dichloromethane. The X-ray crystal structure for **19** is shown in Figure 2-58. The chemical shift values in the ¹H NMR spectra were in agreement with a previous literature report.¹⁶

¹H NMR (CDCl₃): δ = 6.90-6.94 (m), 4.39 (s), 3.79-3.85 (m), 3.38-3.68 (m), 3.08-3.17 (m) ppm.

^{13}C NMR (CDCl_3): $\delta = 152.99, 141.58, 122.30, 121.84, 120.01, 115.79, 71.66, 69.59, 68.44, 54.10$ ppm.

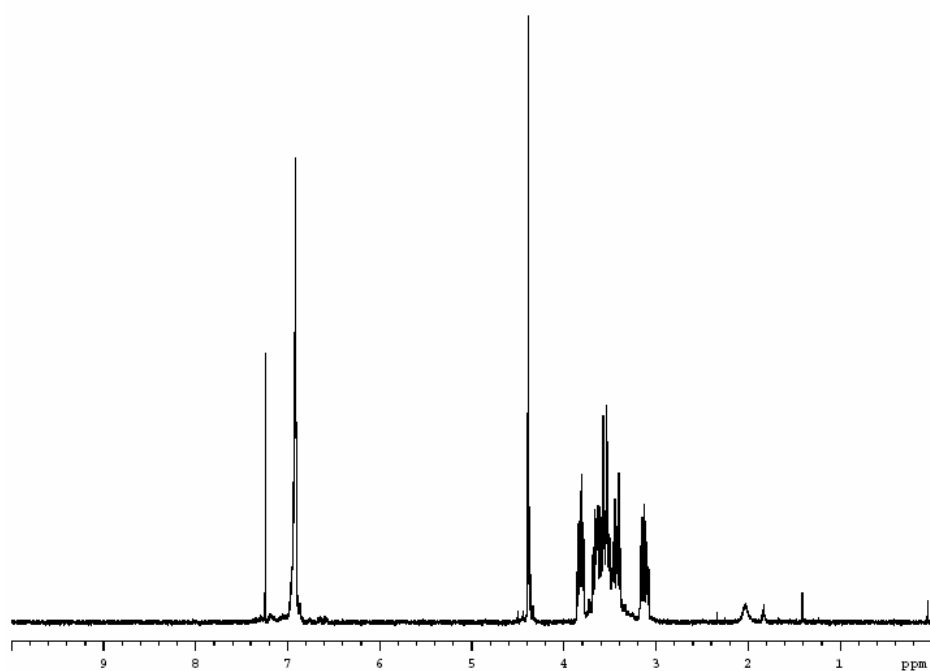


Figure 2-55. ^1H NMR of An2.2.2, (**19**) in CDCl_3 .

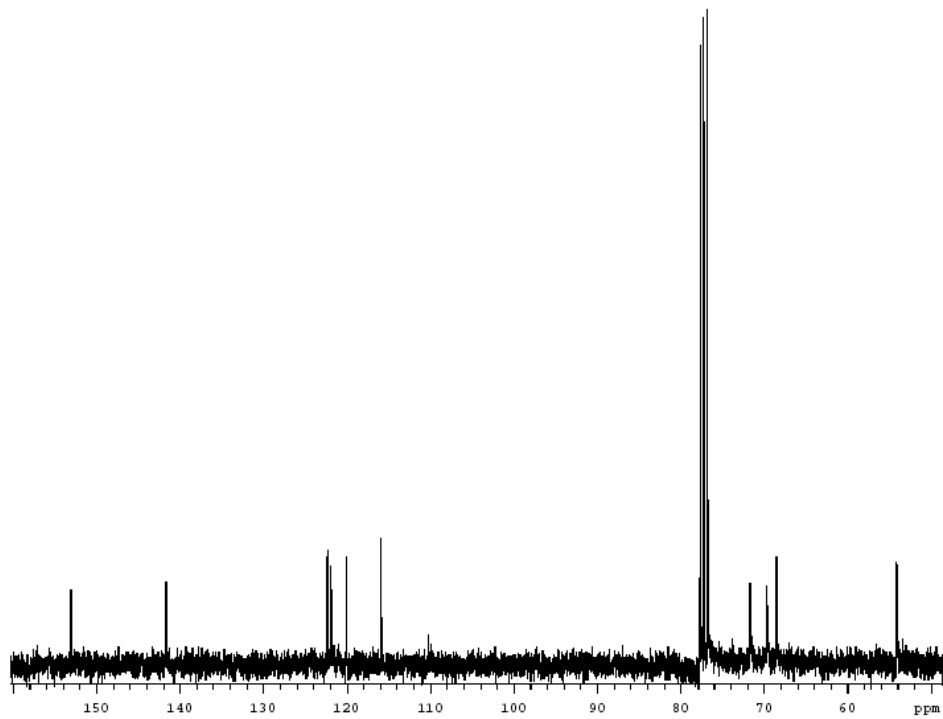


Figure 2-56. ^{13}C NMR of An2.2.2, (19) in CDCl_3 .

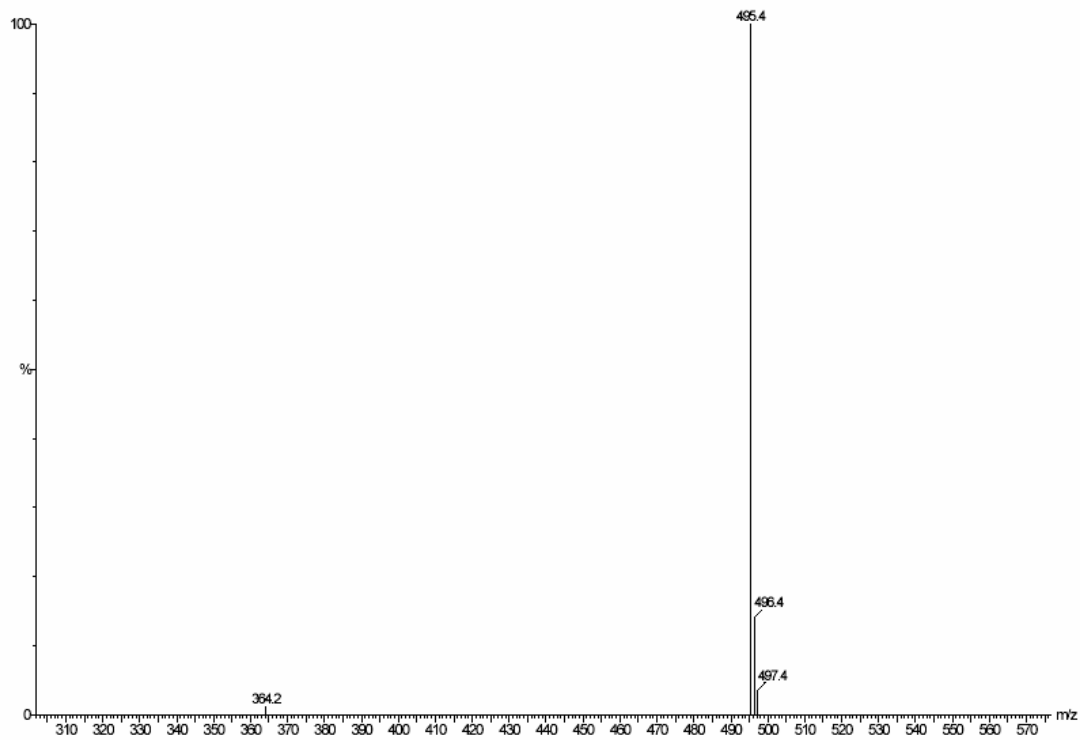


Figure 2-57. ESI-MS^+ of An2.2.2, (19) in MeOH.

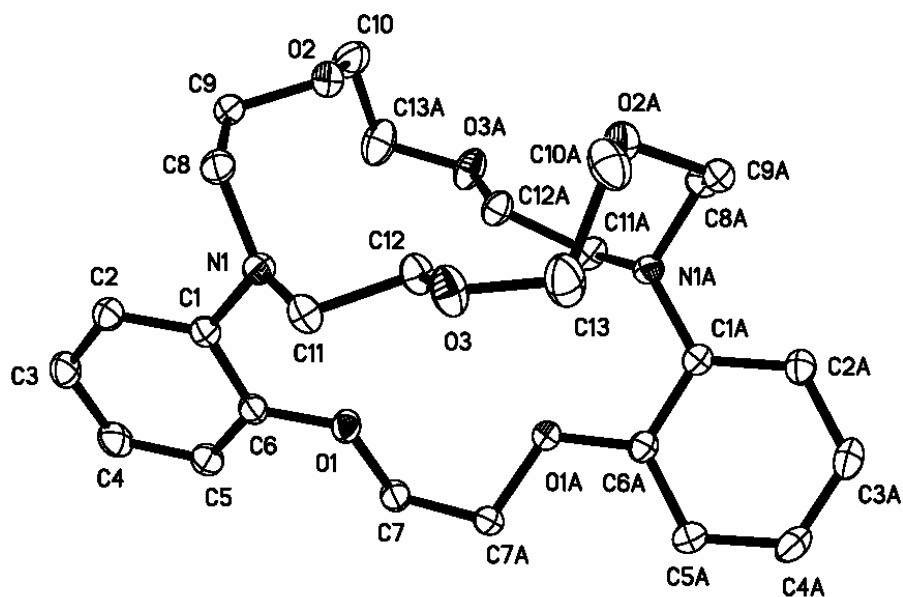


Figure 2-58. X-ray crystal structure of An2.2.2, (19).

**20. 6,7,9,10,28,29,31,32-octahydro-16,44:22,38-di(ethanooxyethano)tetrabenzo-
[*h,q,z,i*][1,4,7,13,19,22,25,31,10,16,28,34]octaoxatetraazacyclohexatriacontine-
17,21,39,43-tetrone, An3.1.1.3*, (20)**

A 0.0105 M solution of the monocyclic diamine was prepared by adding 1.511 g (4.216 mmol) of **14** to a mixture of 250 mL of toluene, 150 mL of DMF, and 0.9 mL (0.01 mol) of pyridine. A 0.0172 M solution of the diacid chloride was made by adding 0.52 mL (4.4 mmol) of 2,2'-oxydiacetyl chloride to 400 mL of toluene. A 5 L Morton flask was prepared with a mechanical stirrer, an inlet and an outlet for nitrogen gas, and an initial volume of 500 mL of toluene. The equimolar solutions were added with constant rate addition funnels at a similar rate. The reaction was stirred at 1000 rpm. Rotary evaporation was used to reduce the organic solvent to a volume of 150 mL. The product precipitated out as a white solid. The tricyclic tetraamide was recrystallized from

toluene and recovered for a 12% yield. The mass spectrum is shown in Figure 2-59 with a peak at m/z of 479.3 ($M_2 + 2Na^+$).

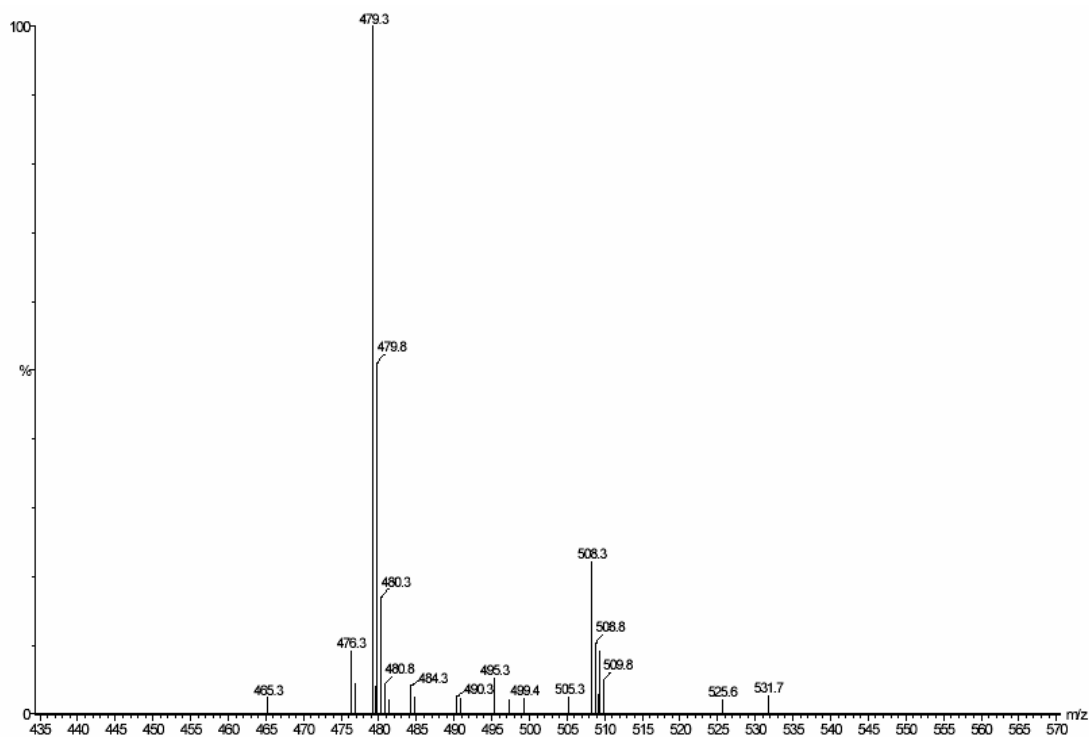


Figure 2-59. ESI-MS⁺ of An3.1.1.3*, (**20**) in MeOH.

21. 6,7,9,10,17,18,20,21,28,29,31,32,39,40,42,43-hexadecahydro-16,44:22,38-di(ethanoxyethano)tetrabenzo[*h,q,z,i*]₁[1,4,7,13,19,22,25,31,10,16,28,34]octaoxa-tetraazacyclohexatriacontine, An3.1.1.3, (21**)**

The tricyclic diamide **20** (0.163 g, 0.178 mmol) was added to a 200 mL 3-neck round bottom flask surrounded by an ice bath and equipped with a condenser and an inlet and an outlet for nitrogen gas. The 1M Borane-THF complex (5 mL, 5 mmol) was added to the flask slowly. The solution was refluxed for 4 h followed by the addition of 30 mL of a solution of 1:10 H₂O-THF using a syringe pump. The solution was allowed to cool to room temperature and 20 mL of H₂O were added to destroy the excess reducing agent.

The organic solvent was removed by rotary evaporation and the remaining solution was acidified with 15 mL of 6 M HCl, made basic with NH₃, and then extracted with CHCl₃ (3 x 75 mL). The CHCl₃ layer was dried with MgSO₄, filtered, and the solvent removed by rotary evaporation. The product was obtained in quantitative yield (100%). The ¹H and ¹³C NMR data is listed below and the spectra are shown in Figures 2-60 and 2-61, respectively. The mass spectrum is shown in Figure 2-62 with a peak at m/z of 429.2 (M₂ + 2H⁺). Crystals suitable for X-ray crystallography were grown by vapor diffusion with heptane diffusing into a solution of **21** dissolved in benzene. The X-ray crystal structure for **21** is shown in Figure 2-63.

¹H NMR (CDCl₃): δ = 6.77-6.91 (m), 4.15 (t), 3.94 (t), 3.77 (t), 3.55 (t), 3.37-3.45 (m) ppm.

¹³C NMR (CDCl₃): δ = 152.10, 140.90, 121.81, 121.28, 119.99, 113.47, 70.40, 70.14, 69.66, 68.19, 54.03, 52.28 ppm.

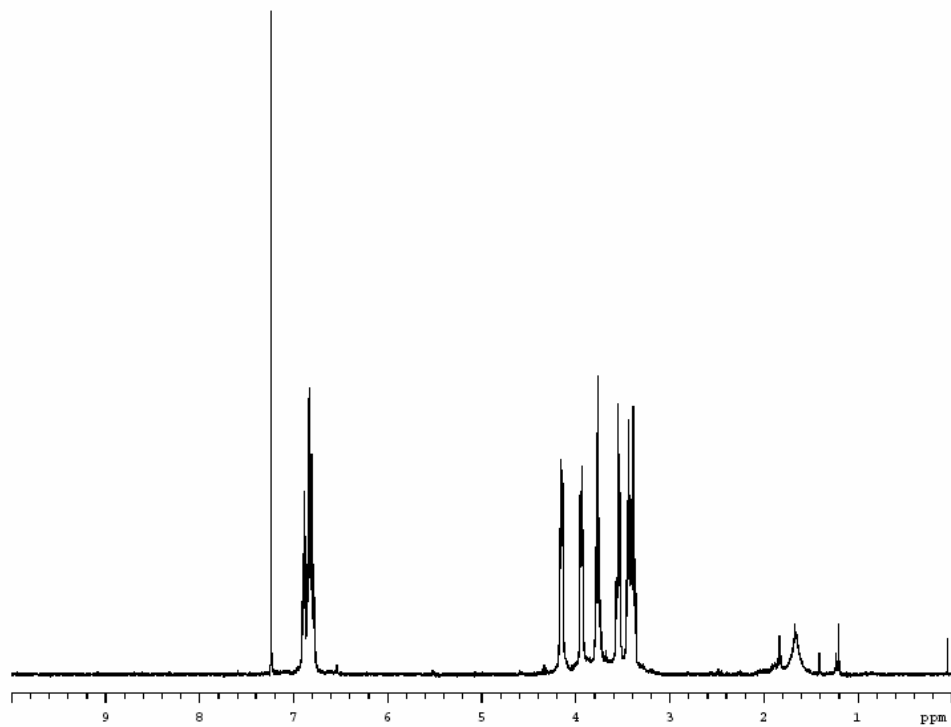


Figure 2-60. ^1H NMR of An3.1.1.3, (21) in CDCl_3 .

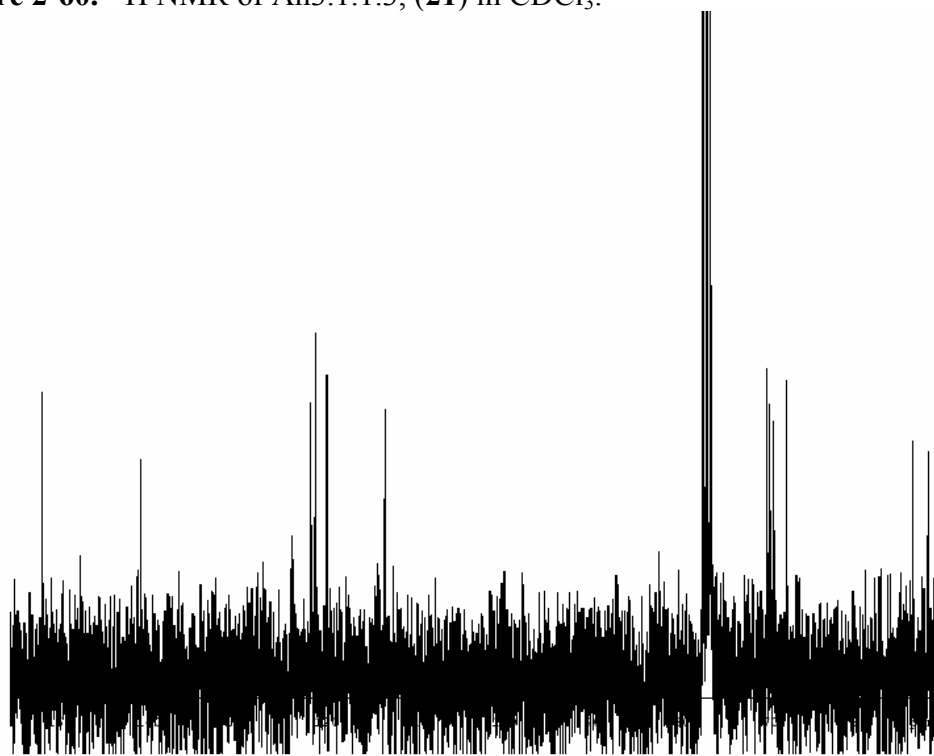


Figure 2-61. ^{13}C NMR of An3.1.1.3, (21) in CDCl_3 .

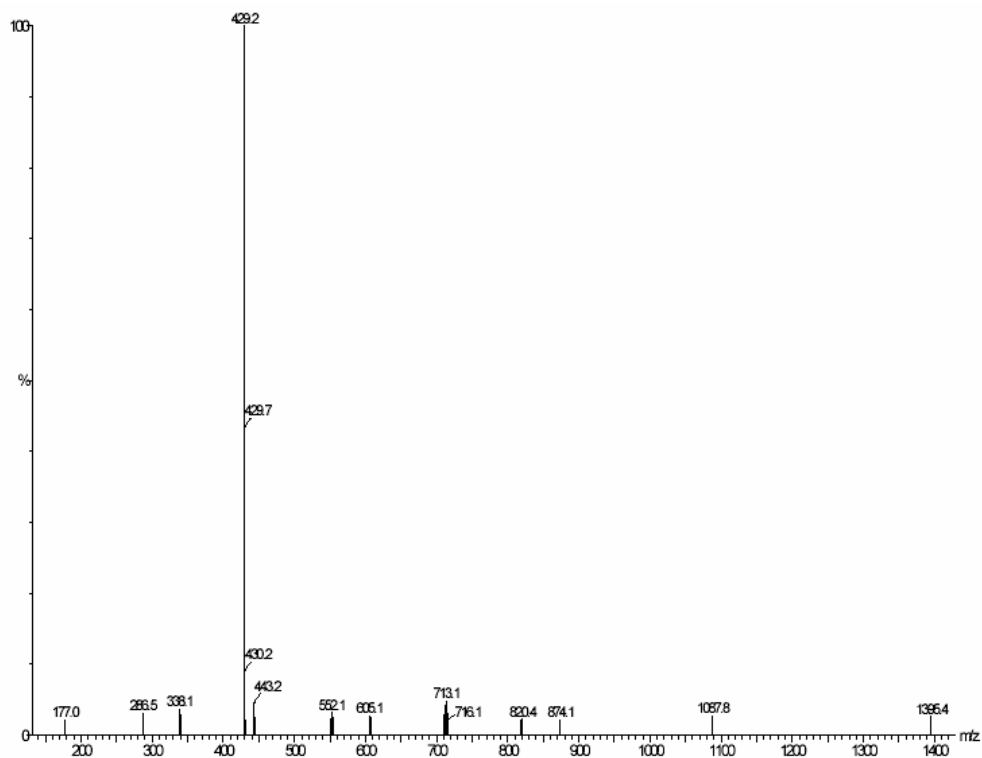


Figure 2-62. ESI-MS⁺ of An3.1.1.3, (21) in MeOH.

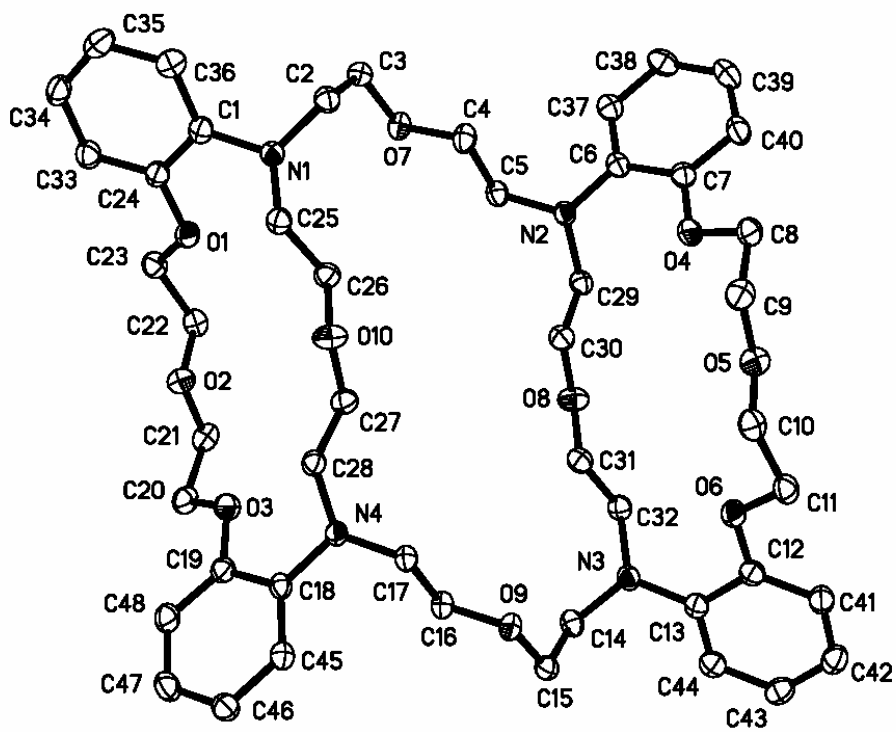


Figure 2-63. X-ray crystal structure of An3.1.1.3, (21).

**22. 6,7,9,10,-tetrahydro-16,22-(ethanooxyethano)dibenzo[*h,q*] [1,4,7,13,10,16]-
tetraoxadiazacyclooctadecine-17,21-dione, An3.1.1*, (22)**

A solution of the monocyclic diamine (0.0038 M) was prepared by adding 0.550 g (1.53 mmol) of **14** to 400 mL of CH₂Cl₂ containing 0.5 mL (0.006 mol) of pyridine. The diacid chloride solution (0.0043 M) was made by adding 0.20 mL (1.7 mmol) of 2,2'-oxydiacetyl chloride to 400 mL of CH₂Cl₂. A 5 L Morton flask was prepared with a mechanical stirrer, an inlet and an outlet for nitrogen gas, an initial volume of 500 mL of CH₂Cl₂. The flask was surrounded by an ice-bath and stirred at 1000 rpm. Constant rate addition funnels were used to add the equimolar solutions at a similar rate. Addition was complete after 7 h. Rotary evaporation was used to remove the solvent. The bicyclic diamide **22** was purified by flash column chromatography on silica gel using CH₂Cl₂ and MeOH (up to 10%) as the eluent. The ¹H and ¹³C NMR data is listed below and the spectra are shown in Figures 2-64 and 2-65, respectively. The mass spectrum is shown in Figure 2-66 with peaks at *m/z* of 457.3 (M + H⁺) and 479.3 (M + Na⁺). Crystals suitable for X-ray crystallography were grown by vapor diffusion with methanol diffusing into a solution of **22** dissolved in dichloromethane. The X-ray crystal structure for **22** is shown in Figure 2-67.

¹H NMR (CDCl₃): δ = 6.96-7.25 (m), 4.52 (m), 4.39-4.44 (m), 3.96 (m), 3.83-3.85 (m), 3.66-3.71 (m) ppm.

¹³C NMR (CDCl₃): δ = 168.78, 154.73, 131.34, 128.68, 128.04, 121.58, 114.12, 71.94, 70.12, 69.05, 68.49, 50.85 ppm.

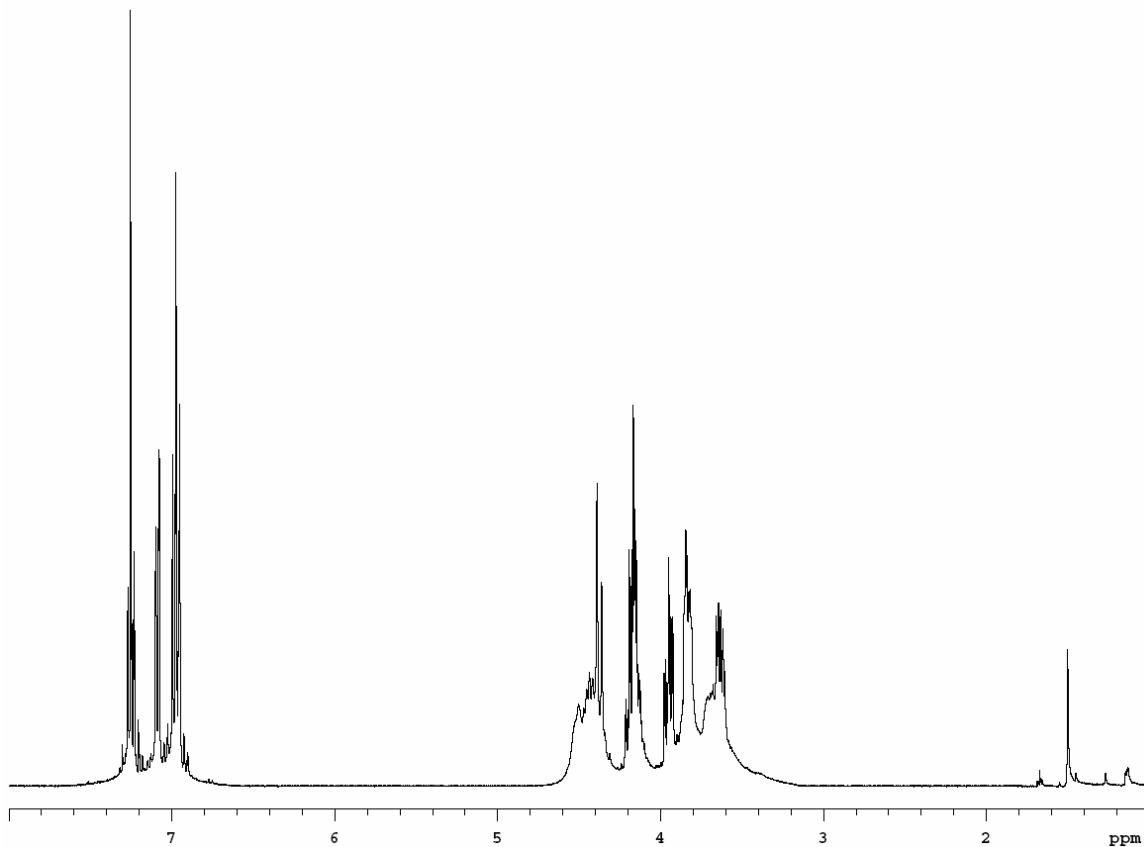


Figure 2-64. ^1H NMR of An3.1.1*, (**22**) at 58°C in CDCl_3 .

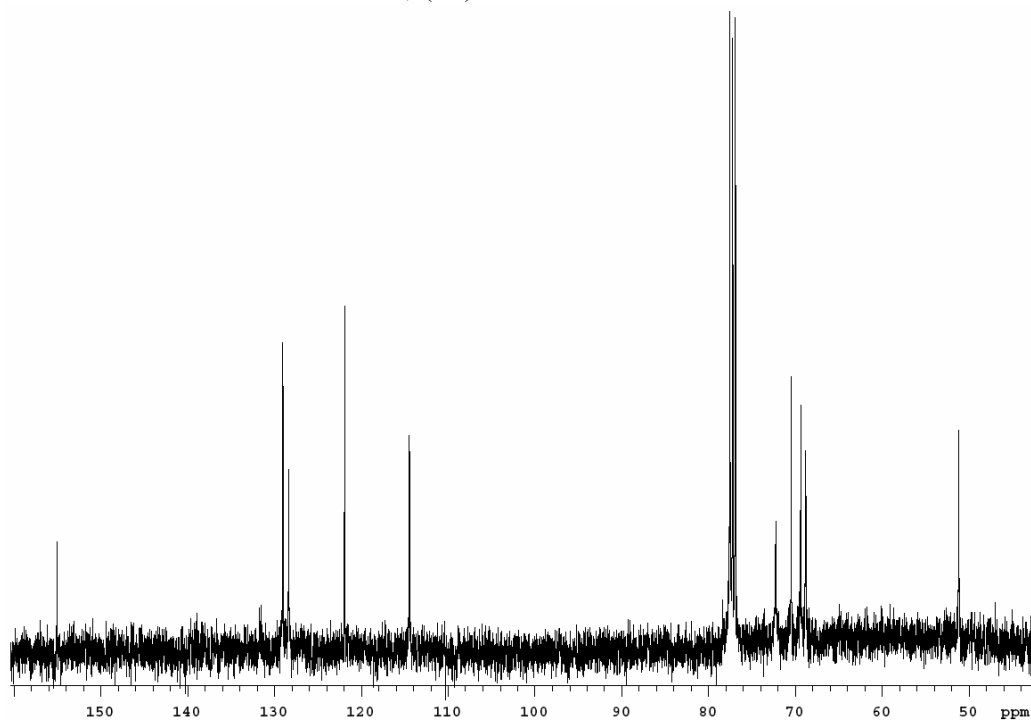


Figure 2-65. ^{13}C NMR of An3.1.1*, (**22**) at 58°C in CDCl_3 .

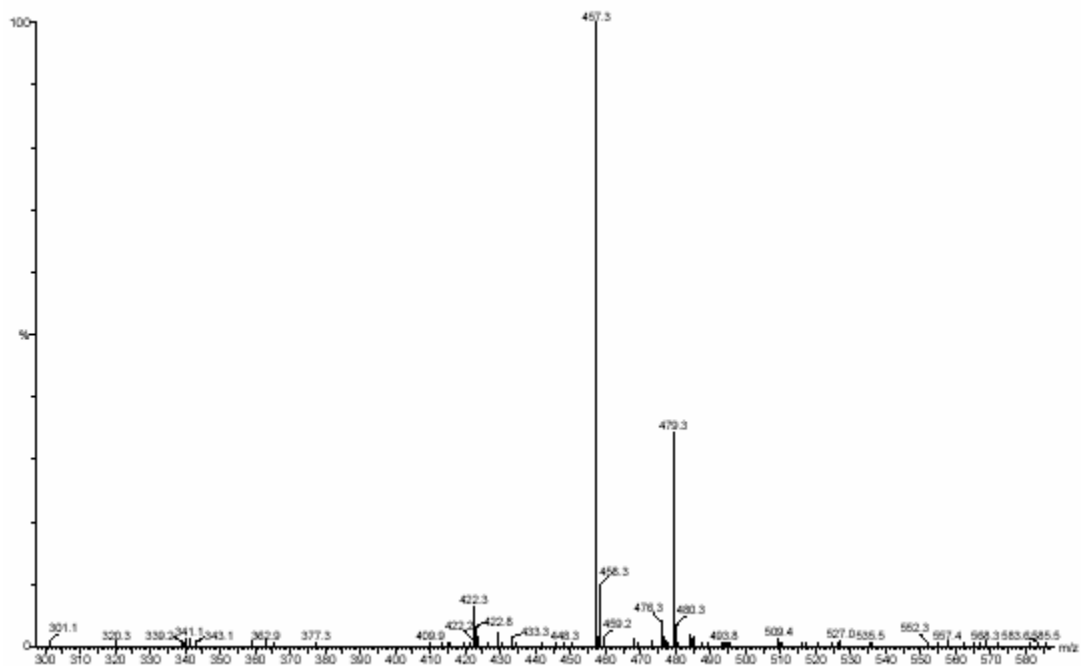


Figure 2-66. ESI-MS⁺ of An3.1.1*, (22) in MeOH.

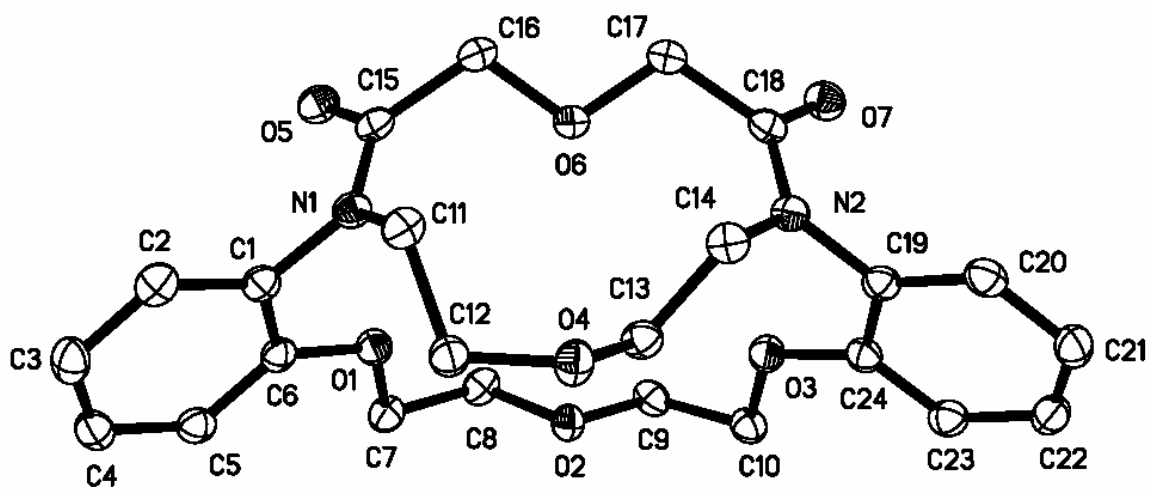


Figure 2-67. X-ray crystal structure of An3.1.1*, (22).

**23. 6,7,9,10,17,18,20,21-octahydro-16,22-(ethanoxyethano)dibenzo[*h,q*]-
[1,4,7,13,10,16]tetraoxadiazacyclooctadecine, An3.1.1, (23)**

A 50 mL 3-neck round bottom flask was surrounded by an ice bath and was prepared with a condenser and inlet and an outlet for nitrogen gas. 1M borane-THF complex (5 mL, 5 mmol) was added to the flask, followed by the slow addition of 0.16 g (0.35 mmol) of **22** dissolved in THF. The reaction mixture was refluxed for 1.5 hr prior to the addition of 6 mL of a 1:10 H₂O-THF solution using a syringe pump. The addition was complete after 45 min and the solution was allowed to cool to room temperature. The excess reducing agent was destroyed by the addition of 10 mL of H₂O. The organic solvent was removed by rotary evaporation. The remaining aqueous solution was treated with 5 mL of 6 M HCl, made basic with 6 M NH₃, and then extracted with CHCl₃ (3 x 50 mL). The CHCl₃ layer was dried with MgSO₄, filtered, and the solvent removed by rotary evaporation. A dark brown oil was recovered from the CHCl₃ layer and the mass spectrum shows a relatively pure product. However, thin-layer chromatography revealed multiple products and cryptand An3.1.1 could not be crystallized from this crude mixture. The mass spectrum is shown in Figure 2-68 with peaks at *m/z* of 429.2 (M + H⁺) and 451.2 (M + Na⁺).

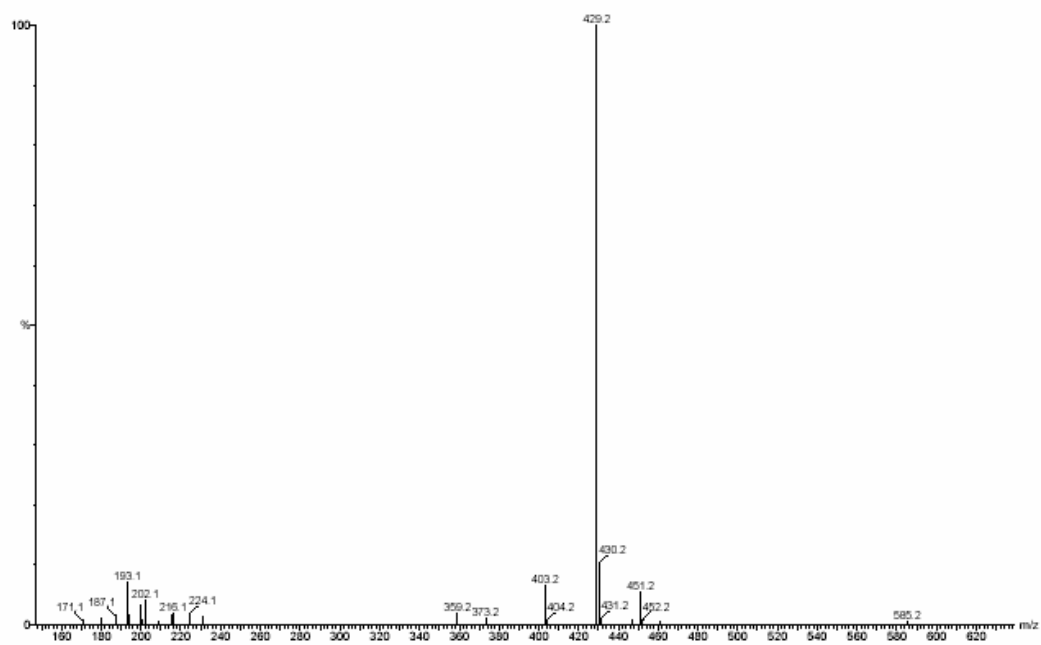


Figure 2-68. ESI-MS⁺ of An3.1.1, (23) in MeOH.

References

- (1) March, J.; Smith, M. B., *March's Advanced Organic Chemistry: Reactions, Mechanisms, and Structure*. 5th ed.; John Wiley & Sons, Inc.: New York, 2001, p 523-524.
- (2) Fox, M. A.; Whitesell, J. K., *Organic Chemistry*. 2nd ed.; Jones and Bartlett Publishers: Boston, 1997, p 626.
- (3) Sammes, P. G.; Goolamali, Z.; Crossley, R. *J. Chem. Soc. Perkin Trans. 2* **1994**, 1615-1623.
- (4) Lockhart, J. C.; Thompson, M. E. *J. Chem. Soc. Perkin Trans. 1* **1977**, 202-204.
- (5) Formanovskii, A. A.; Murakhovskaya, A. S. *Khim. Geterotsikl. Soedin.* **1985**, (2), 267-271.
- (6) Metcalfe, J. C.; Hesketh, T. R.; Morris, P. G.; Smith, G. A. *Biochim. Biophys. Acta* **1986**, 889, 72-83.
- (7) Metcalfe, J. C.; Hesketh, T. R.; Smith, G. A. *Biochem. J.* **1988**, 250, 227-232.
- (8) Gansow, O. A.; Kausar, A. R.; Triplett, K. B. *J. Heterocycl. Chem.* **1981**, 18, 297-302.
- (9) *SMART Software Reference Manual*, Bruker-AXS: Madison, WI, 1998.
- (10) *SAINTE Software Reference Manual*, Bruker-AXS: Madison, WI, 1998.
- (11) *SHELXTL*, Bruker-AXS: Madison, WI, 1997.
- (12) Sauvage, J. P. These de Doctorat d'Etat, Universite Louis Pasteur, Strasbourg, 1971.
- (13) Zubrick, J. W., *The Organic Chem Lab Survival Manual*. 4th ed.; John Wiley and Sons, Inc.: New York, 1997, p 369.
- (14) Kilic, Z.; Gunduz, N. *Synth. React. Inorg. Met.-Org. Chem.* **1986**, 16, (4), 457-474.
- (15) Aguilar, J. C.; Rodriguez de San Miguel, E.; de Gyves, J.; Bartsch, R. A.; Kim, M. *Talanta* **2001**, 54, 1195-1204.
- (16) Prasanna de Silva, A.; Nimal Gunaratne, H. Q.; Samankumara Sarchanayake, K. R. A. *Tetrahedron Lett.* **1990**, 31, (36), 5193-5196.

Chapter Three

Spectrophotometric studies of An2.2.1 and An2.2.2

I. Introduction

Methods used to determine metal ion complexation constants include potentiometric^{1,2}, calorimetric¹, NMR², and spectrophotometric³ titrations. The solubility of cryptands An2.2.1 and An2.2.2 ($\sim 10^{-4}$ M) in water is not sufficient for potentiometric titration methods ($\sim 10^{-3}$ M). BAPTA, as shown in Figure 3-1, is an acyclic benzoannulated tetraacetic acid compound that has similar chromophores as cryptands An2.2.1 and An2.2.2. Tsien³ showed that the peaks in the UV spectrum for BAPTA shift significantly to shorter wavelengths upon metal complexation. A similar change in the UV spectrum also occurs when the pH drops below 6.5. The chromophore conjugation of the nitrogens with the rings as seen in BAPTA is expected to change with degree of protonation (L , HL^+ , H_2L^{2+}) and when nitrogens are involved in metal ion complexation (ML) for cryptands An2.2.1 and An2.2.2.

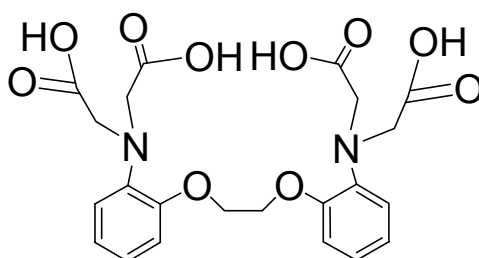
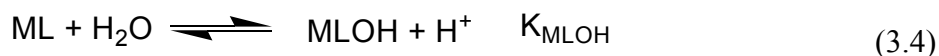


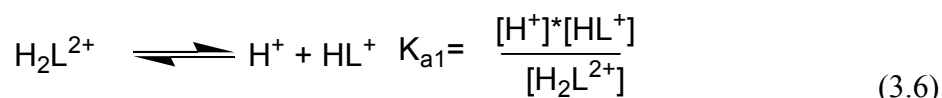
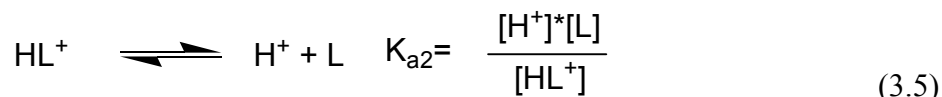
Figure 3-1. Structure of bis(*o*-aminophenoxy)ethane-*N,N,N',N'*-tetraacetic acid (BAPTA).

Spectrophotometric titrations were employed to investigate the areas of acid-base and metal ion complexation equilibria of An2.2.1 and An2.2.2. Cryptands An2.2.1 and An2.2.2 each have two nitrogen atoms that can undergo stepwise protonation (K_{H1} and

K_{H2}). Cryptands generally form one-to-one metal cryptate complexes (K_{ML}), and some cryptates can be involved in other side reactions (K_{MLOH}).⁴ These reactions and the associated equilibrium constants are defined by eqs 3.1-3.4.



Reactions with protons will be reported as protonation constants as opposed to acid dissociation constants. Protonation constants (K_{Hi}) are equal to the inverse of the appropriate dissociation constant (K_{ai}). The dissociation constants are described in eqs 3.5 and 3.6 and the difference in notation is shown in eqs 3.7 and 3.8.



$$K_{H2} = \frac{1}{K_{a1}}, \log K_{H2} = pK_{a1} \quad (3.7)$$

$$K_{H1} = \frac{1}{K_{a2}}, \log K_{H1} = pK_{a2} \quad (3.8)$$

Determination of the protonation constants is necessary prior to measurement of the metal ion complexation constants. Stability constants (K_{ML}) can be measured directly only where there is no interference from the protonation reaction. If this is not possible,

then conditional stability constants (K'_{ML}) are measured at a pH where there is competition from the protonation reactions. The intrinsic (or unconditional) stability constants can be determined for a given metal ion from the conditional stability constant data and the values of the ligand protonation constants.

II. Experimental

This section presents the chemicals and methodologies used for the spectroscopic determination of the protonation and complexation constants of An2.2.1 and An2.2.2.

A. Reagents

Distilled Deionized Water - D.D. H₂O. Distilled deionized water was used for all aqueous solutions and was prepared using a Corning Megapure System distillation apparatus, model MP-3A.

Perchloric Acid - HClO₄. Solutions containing HClO₄ at different concentrations were made from 70% redistilled acid, ~ 11.7 M (GFS Chemicals) and were used to adjust the pH of solutions.

Tetraethylammonium Hydroxide - (CH₃CH₂)₄NOH, Et₄NOH. Solutions containing Et₄NOH at different concentrations were made from 20% w/v concentrated base, ~ 1.5 M (Fluka chemical) by diluting with freshly boiled D.D. H₂O and storing under N₂. These solutions were used to adjust the pH of solutions.

Tetraethylammonium Perchlorate - (CH₃CH₂)₄NClO₄, TEAP. TEAP was made by titrating 20% tetraethylammonium hydroxide with 70% redistilled perchloric acid to one drop past the equivalence point. The equivalence point is distinct because of the large decrease in pH. The product was filtered and recrystallized five times from double distilled water to insure purity. The final product was vacuum dried for six hours.

Hexamethylenetetramine - Hexamine. Hexamine buffer (Aldrich, 99+%) was prepared by weight as a 20 % solution in water.

Potassium Chloride - KCl (Aldrich, 99.999%, puratronic) was dried in an oven at 110°C overnight. Solutions were prepared by weight.

Sodium Chloride - NaCl (Aldrich, 99.999%, puratronic) was dried in an oven at 110°C overnight. Solutions were prepared by weight.

Barium Chloride - BaCl₂ (Aldrich, 99.999%, metals basis) was used as obtained from Aldrich. Solutions were prepared by weight.

Strontium Chloride - SrCl₂·6H₂O (Alfa Aesar, 99.9965%, puratronic, metals basis) was used as obtained from Aldrich. Solutions were prepared by weight.

Calcium Chloride - CaCl₂·xH₂O (Aldrich, 99.999%, metals basis) was used to prepare solutions that were standardized by EDTA titration using EBT as an indicator and ammonia/ammonium chloride (pH 10) as a buffer.⁵

Cadmium Perchlorate - Cd(ClO₄)₂. Cd(ClO₄)₂ (Aldrich, 99.999%, metals basis) was used to prepare solutions that were standardized by EDTA titration using xylenol orange as an indicator and hexamine as a buffer.⁵

Lead Perchlorate - Pb(ClO₄)₂. Pb(ClO₄)₂ (Aldrich, 99.995+%, metals basis) was used to prepare solutions that were standardized by EDTA titration using xylenol orange as an indicator and hexamine as a buffer.⁵

Noncomplexing Tertiary Amines - Buffers used were described by Rorabacher and co-workers^{6,7} as noncomplexing tertiary amines that are incapable of forming complexes with metal ions. The buffers *N,N'*-diethylethylenediamine-*N,N'*-bis(3-propanesulfonic acid) (DESPEN, pK_{a1} = 5.62, pK_{a2} = 9.06), piperazine-*N,N'*-bis(2-ethanesulfonic acid) (PIPES, pK_{a1} = 2.67, pK_{a2} = 6.78), piperazine-*N,N'*-bis(3-propanesulfonic acid) (PIPPS, pK_{a1} = 3.79, pK_{a2} = 7.97), piperazine-*N,N'*-bis(4-

butanesulfonic acid) (PIPBS, $pK_{a1} = 4.29$, $pK_{a2} = 8.55$), 2-(*N*-morpholino)ethanesulfonic acid (MES, $pK_a = 6.06$), and 4-(*N*-morpholino)butanesulfonic acid (MOBS, $pK_a = 7.48$) were purchased from Sigma Chemical Company and GFS Chemicals.

Glassware - All glassware used for metal titrations was soaked overnight in an acid bath (3:1 v/v sulfuric acid:nitric acid) and rinsed thoroughly with distilled water before use.

B. pH Measurements

Measurements of pH were performed with a Fisher Scientific pH meter, model AR15 or 825MP, and an Orion Ross semi-micro combination pH electrode, model 8103 or an Orion Ross semi-micro combination pH electrode, model 8175BN. The pH meter was standardized each day before use with the commercially available (Fisher, Gram Pac) buffers potassium acid phthalate ($pH = 4.01$), potassium phosphate monobasic sodium phosphate dibasic ($pH = 6.86$), and borax ($pH = 9.18$). The internal filling solution for the electrode was dependent upon the ligand and metal used during analysis. For An2.2.2, a solution of $NaNO_3$ (10%) or TEAP (0.1 M) was used to minimize cation complexation for all pH measurements of solutions. An internal electrolyte solution of 0.1 M TEAP was used for all pH measurements of An2.2.1 solutions except for those containing K^+ because of the low solubility of $KClO_4$. A solution of KCl (3.5 M) was used as the internal solution for this case.

C. Standardization of Ligand Solutions

The concentrations of An2.2.1 and An2.2.2 in stock solutions were determined by spectrophotometric titrations because of the inaccuracy of weighing milligram samples and the possibility of samples being contaminated with an unknown amount of solvent. Samples of the stock solutions were diluted to $\sim 10^{-4}$ M and adjusted to pH 6.0-7.0. A 2.70 mL solution of the ligand and 5 mM PIPES buffer were titrated with 2-4 μ L aliquots of a standardized $\text{Pb}(\text{ClO}_4)_2$ solution until the spectra no longer changed with the addition of metal. Absorbance data for a selected wavelength was plotted versus metal concentration. Two different portions of the plot were used for analysis: the region where there is a linear increase in absorbance with the addition of metal and a region where there is no change upon the addition of metal. Data from each set was fit to a linear model using the least-squares method as shown in Figure 3-2.⁸ The linear equations ($\text{Abs}(\lambda) = m[\text{Pb}^{2+}] + b$) determined from the two sets of data were combined to find the concentration of $[\text{Pb}^{2+}]$ at the intersection of the two lines. The Kaleidagraph data results listed in the figures throughout this work are the output of the data fitting program and are not representative of the correct number of significant figures.

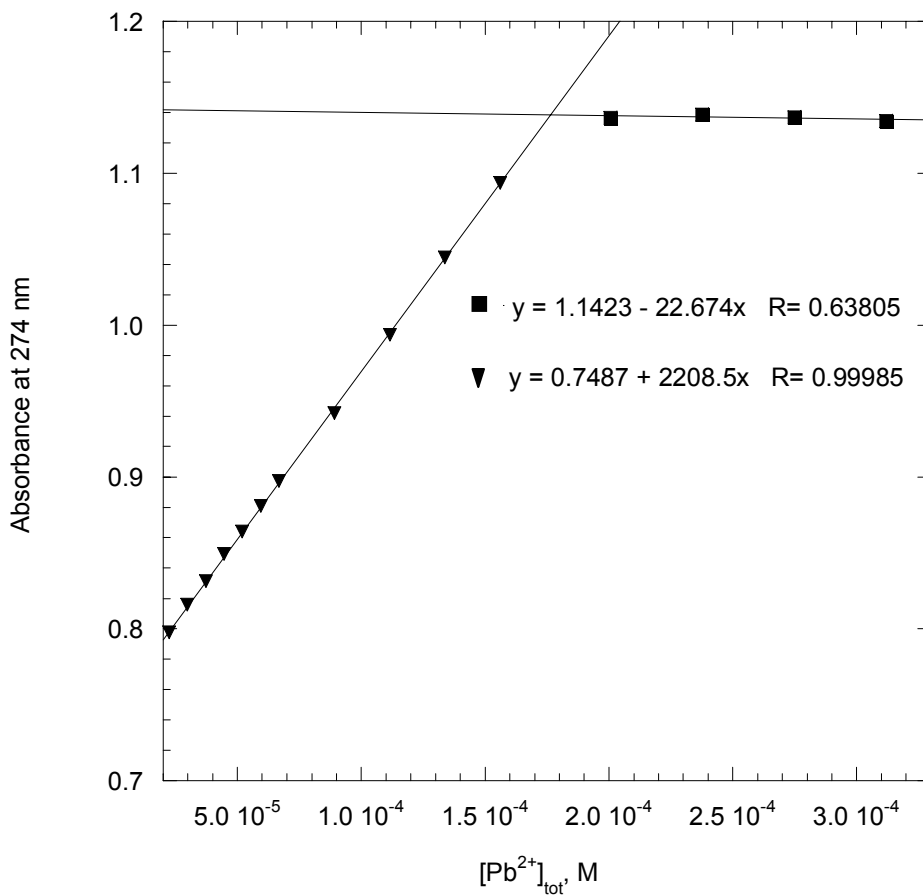


Figure 3-2. Plot of absorbance at 274 nm versus $[Pb^{2+}]$ for the standardization of An2.2.2, (19), at pH = 6.6.

Assuming 1:1 metal ion-ligand stoichiometry and that the metal ion reacts quantitatively i.e., $[ML] \geq 0.99 [M]$ added, the $[Pb^{2+}]$ value found corresponds to the equivalence point of the reaction, and is equal to the concentration of the dilute ligand solution. Subsequent correction for dilution gives the concentrations of the stock solution. Micropipets (Gilson) were used for solution preparation and the addition of stock metal solutions. Each addition was made using a new pipet tip (Rainin and Fisher). Calibration of the micropipets was done professionally (Calibration Services) by comparing the mass of double distilled water with the designated volume.

D. Spectrophotometric Analysis of An2.2.1 and An2.2.2

It was necessary to determine if cryptands obeyed the Beer-Lambert Law (eq. 3.9) in the concentration range 0.04 - 0.1 mM and pH ~ 2.7 to ~ 6.8. These concentration and pH ranges will be used in spectrophotometric titrations. In Equation 3.9, b refers to the pathlength of the cell, which is 1 cm in all cases, and c is the concentration of the ligand, M or mM.

$$A_{\lambda} = \epsilon_{\lambda}bc \quad (3.9)$$

The pH of a 0.1 mM solution of the cryptand and 5 mM PIPES was adjusted to either low (~ 2.7) or high (~ 6.8) pH using HClO₄ or Et₄NOH. The initial concentrations of An2.2.1 and An2.2.2 were 0.070 mM and 0.18 mM, respectively. The samples were maintained at 25 °C by an external temperature bath (Fisher) attached to the cuvette holder. The solution was allowed to equilibrate in the cell holder for 2 minutes, then the spectrum was scanned from 190 - 820 nm using the diode array spectrophotometer. The solution was then diluted by 0.5 mL using 5 mM buffer and inverted ten times to promote mixing and the spectrum recorded after a 2 min equilibration time. The process was repeated until the concentrations of the ligands were 0.025 mM and 0.068 mM for An2.2.1 and An2.2.2, respectively. Figures 3-3 and 3-5 show the absorbance versus wavelength spectra at low and high pH for An2.2.1, respectively and Figures 3-4 and 3-6 show the relationship of absorbance at a specific wavelength versus concentration for the respective spectra. The absorbance versus concentration data was fit using Kaleidagraph.⁸ Figures 3-7 and 3-9 show the absorbance versus wavelength spectra at low and high pH for An2.2.2, respectively and Figures 3-8 and 3-10 show the relationship of absorbance at a specific wavelength versus concentration for the

respective spectra. A linear concentration dependence was found at both low and high pH for An2.2.1 and An2.2.2. Molar absorptivity values for An2.2.1 at low and high pH were 4720(52) $M^{-1}cm^{-1}$ at 272 nm and 4900(66) $M^{-1}cm^{-1}$ at 278 nm, respectively. The molar absorptivity value for An2.2.2 at 272 nm (4160(38) $M^{-1}cm^{-1}$) was lower in comparison to An2.2.1 and the value for An2.2.2 at 276 nm was 4420(30) $M^{-1}cm^{-1}$. Cryptands An2.2.1 and An2.2.2 both have larger molar absorptivity values at the high pH range (278 nm and 276 nm, respectively) in comparison to the lower pH range (272 nm for both).

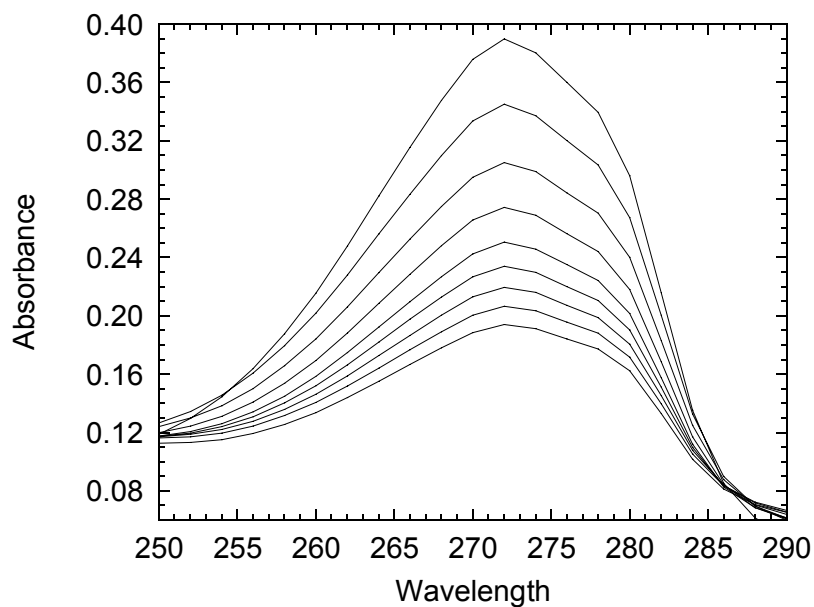


Figure 3-3. Absorbance versus wavelength for An2.2.1, (16), from 0.070 mM - 0.025 mM at pH = 2.5-3.1.

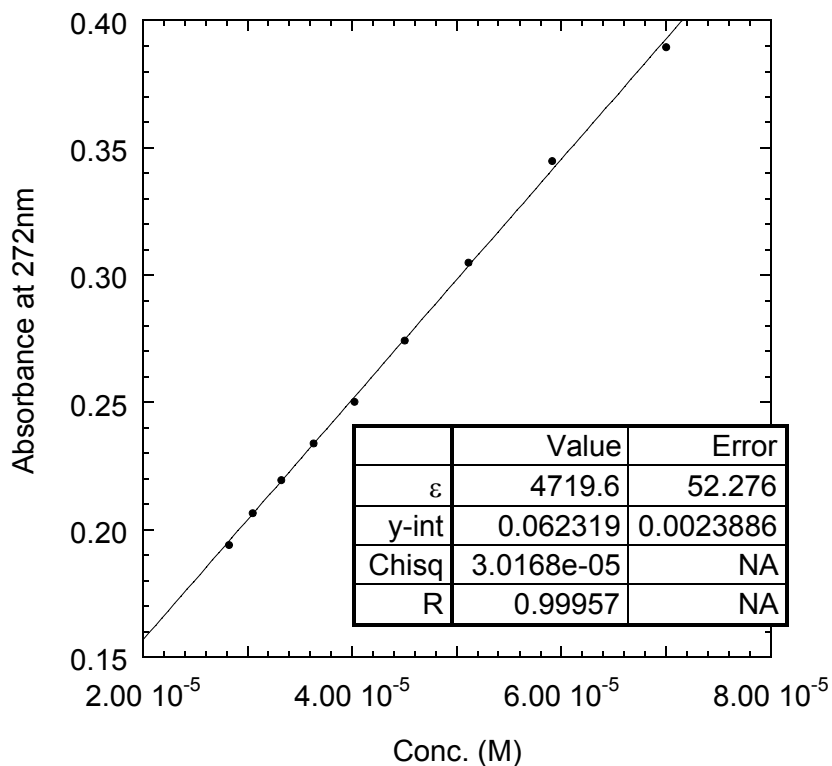


Figure 3-4. Absorbance at 272 nm versus concentration for An2.2.1, (16), at pH = 2.5-3.1. The solid line was calculated using eq 3.9 and the molar absorptivity, ϵ , is listed in the table.

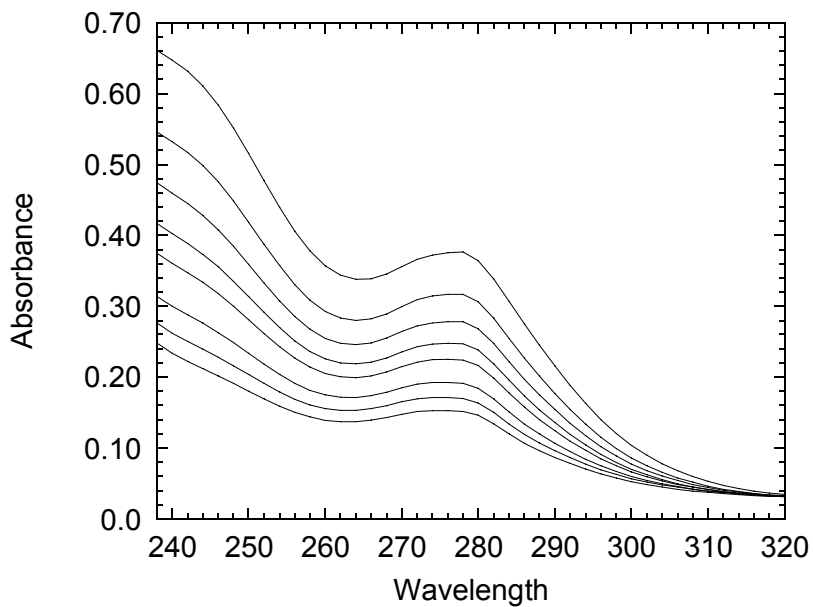


Figure 3-5. Absorbance versus wavelength for An2.2.1, (16), from 0.070 mM - 0.025 mM at pH = 6.0 - 6.6.

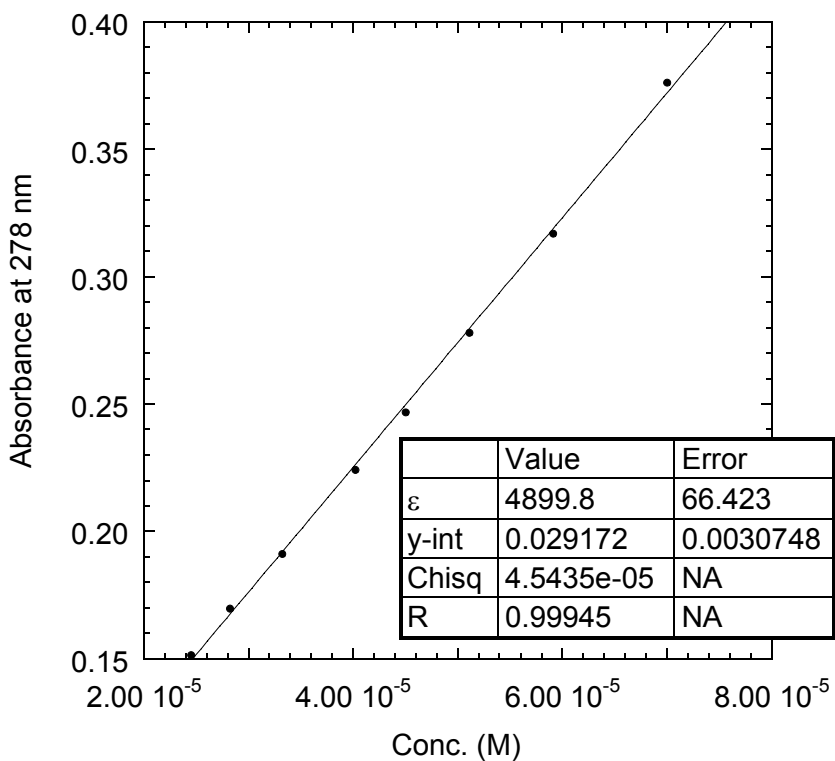


Figure 3-6. Absorbance at 278 nm versus concentration for An2.2.1, (16), at pH = 6.0 - 6.6. The solid line was calculated using eq 3.9 and the molar absorptivity, ϵ , is listed in the table.

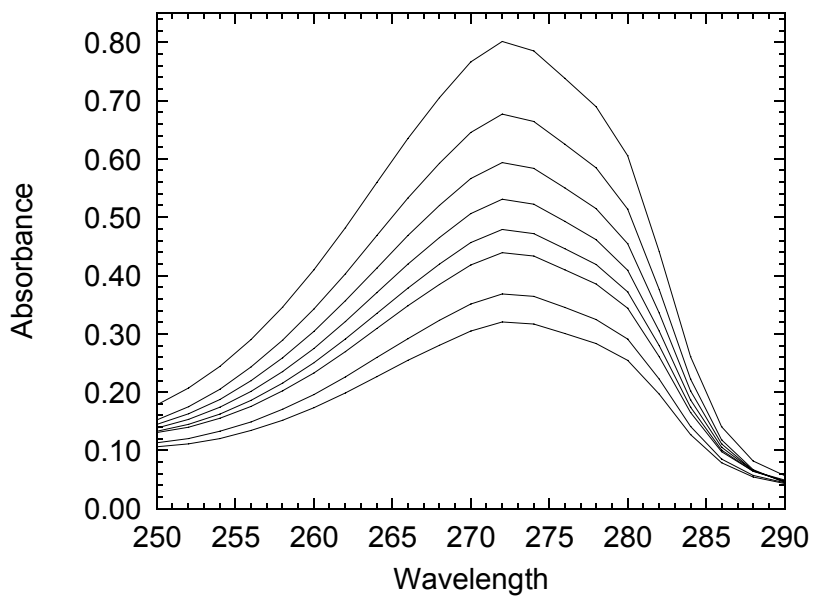


Figure 3-7. Absorbance versus wavelength for An2.2.2, (19), from 0.18 mM - 0.068 mM at pH = 2.4-3.0.

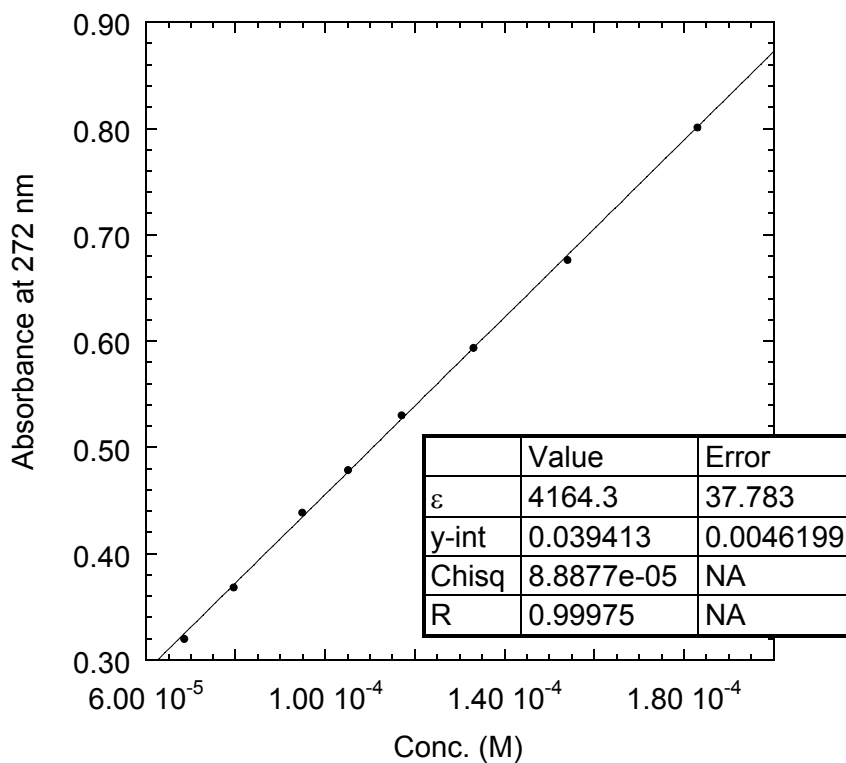


Figure 3-8. Absorbance at 272 nm versus concentration for An2.2.2, (19), at pH = 2.4-3.0. The solid line was calculated using eq 3.9 and the molar absorptivity, ϵ , is listed in the table.

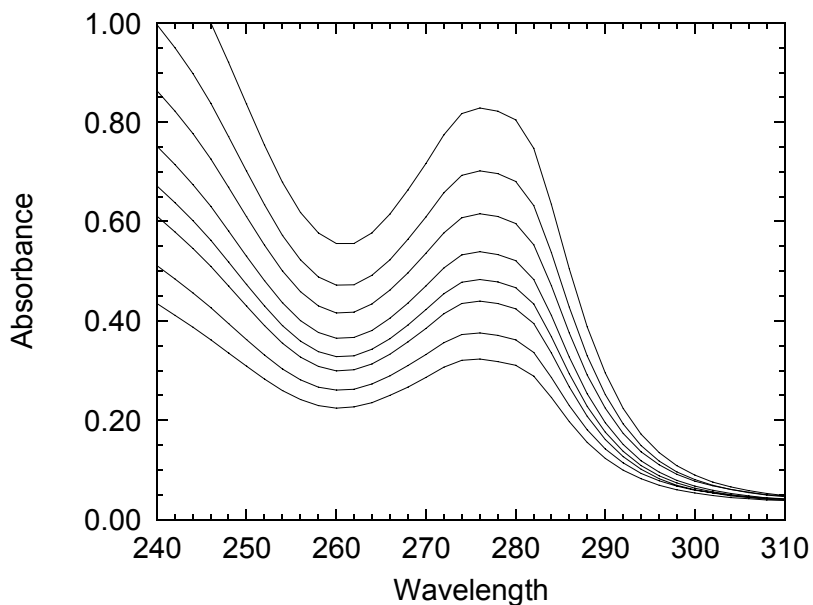


Figure 3-9. Absorbance versus wavelength for An2.2.2, (19), from 0.18 mM - 0.068 mM at pH = 6.2-6.6.

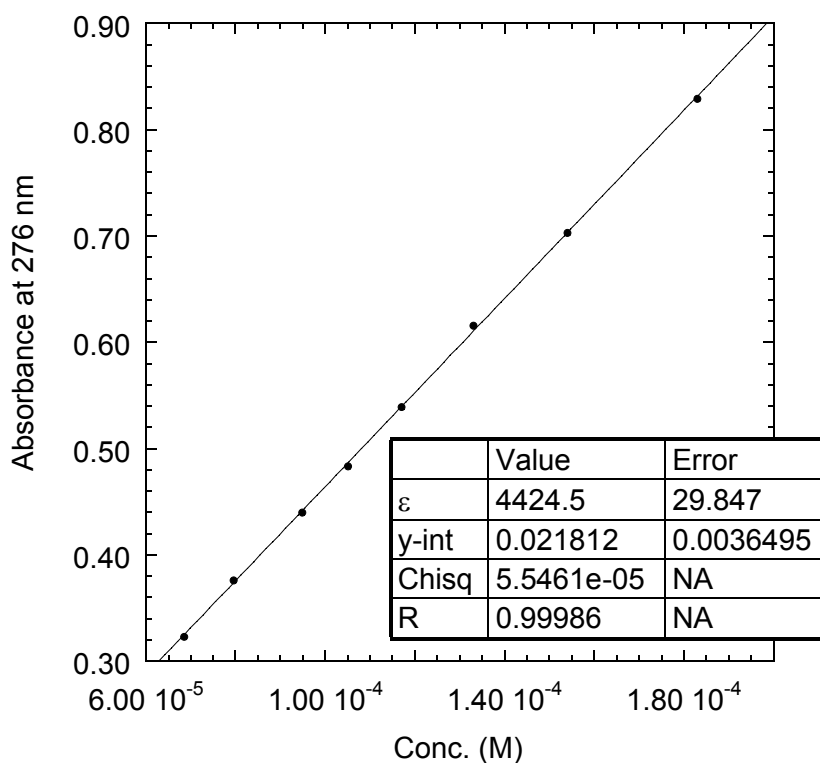


Figure 3-10. Absorbance at 276 nm versus concentration for An2.2.2, (19), at pH = 6.2-6.6. The solid line was calculated using eq 3.9 and the molar absorptivity, ϵ , is listed in the table.

E. Determination of Ligand Protonation Constants (K_H)

Ligand solutions for protonation constant measurements were prepared to have concentrations of 50-100 μM and were buffered from pH 2-10 with PIPES, PIPBS, DESPEN, and MOBS at 1 mM each. EDTA was added at a concentration of 0.1 mM to complex any metal contaminants. A blank solution of the buffers and EDTA did not have an absorbance signal ($\lambda > 250 \text{ nm}$) that would interfere with the ligands studied. Solution mixtures containing the ligand, buffers, and EDTA were initially treated with HClO_4 to lower the pH to 2. In addition to the standard buffers used to calibrate the pH meter, potassium chloride-hydrochloric acid buffer (pH = 2.00) and potassium biphthalate-hydrochloric acid buffer (pH = 3.00) were also used so the calibration would cover the entire pH range investigated. Titrations were carried out from the acidic to basic region or from the basic to acidic region by the addition of small aliquots of concentrated Et_4NOH or HClO_4 , respectively. Spectrophotometric data were obtained from 190 nm to 820 nm using a Hewlett Packard 8452A diode array spectrophotometer. The pH was first adjusted by the addition of HClO_4 or Et_4OH to the ligand solution and then the cuvette was inverted ten times to ensure adequate mixing. The cuvette was then inserted into the cell holder that which was equipped with an external temperature bath to maintain the solution at a constant temperature of 25°C . The cuvet was allowed to equilibrate for two minutes. Next, the spectrum was scanned with the spectrophotometer from 190 - 820 nm and then the pH was measured. This process was repeated until the absorbance did not change with pH. The total volume added in HClO_4 or Et_4OH was $\leq 5\%$ of the initial volume of ligand solution.

The protonation constants were obtained by fitting the absorbance versus pH data using a nonlinear least-squares program that is part of the Kaleidagraph graphics package. Because the cryptands have two protonation steps, the expression used to describe the observed absorbance, A_i , at any given wavelength is described by eq 3.10.

$$A_i = \frac{A_2 K_{H1} K_{H2} a_H^2 + A_1 K_{H1} a_H + A_0}{K_{H1} K_{H2} a_H^2 + K_{H1} a_H + 1} \quad (3.10)$$

The observed absorbance depends on the protonation constants K_{H1} and K_{H2} , defined in eqs 3-1 and 3-2, parameters A_0 , A_1 , and A_2 which are the limiting absorbance values for the unprotonated, monoprotated, and diprotated species of the ligand, respectively, and the hydrogen ion activity, a_H . The value a_H is calculated from the measured pH according to the equation:

$$a_H = 10^{-\text{pH}} \quad (3.11)$$

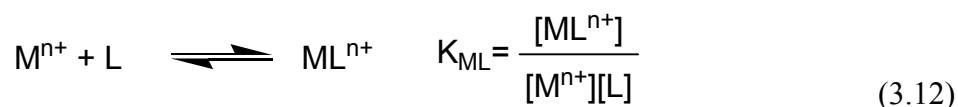
The nonlinear least-squares curve fitting program uses the Levenberg-Marquardt algorithm.⁸ Estimates for the values of K_{H1} , K_{H2} , A_0 , A_1 , and A_2 were made from plots of A_i vs pH and were refined by minimizing the $A_{\text{calc},i}$ vs A_i at each value of a_H .

SPECFIT/32 is another curve fitting program that uses a nonlinear least-squares method employing the Levenberg-Marquardt algorithm.⁹ The major difference between SPECFIT/32 and Kaleidagraph is that the former program utilizes multi-wavelength data sets. Therefore, K_{H1} and K_{H2} values are determined from the spectral range selected (200-400 nm), not a specific wavelength. For SPECFIT/32, the spectrophotometric data file (.wav format), abs. vs wavelength, is imported and the pH data and volume of titrant added is entered for each spectrum. The concentration of the analyte, number of protonation equilibria, and initial estimates of the protonation constants are also required

for the fitting process.¹⁰ A protonation equilibria model provides the predefined functions to fit the pH titration data sets. In this case, the chemical model is based on the equilibria defined by eqs 3.1 and 3.2.

F. Determination of Metal Binding Constants (K_{ML})

The metal ion complexation equilibrium for cryptands An2.2.1 and An2.2.2 is defined in eq 3.12 along with the corresponding equilibrium expression.



Based on the known values of the protonation constants, the metal ion titrations are first carried out at a pH greater than $\log K_{H1} + 2$ so that interference from protonation side reactions will be negligible. This simplifies the reaction in solution and establishes the metals that bind more strongly with the ligands. The test solutions typically contain 0.1 - 0.2 mM ligand and 5 mM DESPEN. The pH is raised to ~ 9 by the addition of Et_4NOH and the absorbance is recorded from 190 - 820 nm. Aliquots of metal ion solutions (10 mM - 2 M) are added and the absorbance is recorded. Some metals such as Pb^{2+} and Cd^{2+} will precipitate at this pH and therefore titrations were done at $\text{pH} \sim 7$. For each of these titrations, a plot is made of the fractional absorbance change versus the ratio total metal:total ligand concentration. The results of these plots will either show that the increase in fraction of absorbance change stops at 1:1 metal to ligand ratio or continues to increase. If there is no change, then the metal and ligand are fully or nearly fully complexed at 1:1 concentration. If the fraction of absorbance change continues to increase then the metal is bound more weakly and not fully complexed. Examples of

both scenarios for fractional absorbance change versus total metal divided by total ligand scenarios are shown in Figure 3-11.

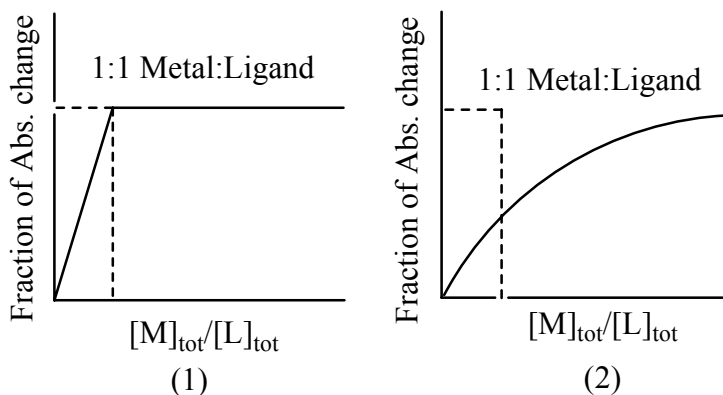


Figure 3-11. Metal ion titrations: (1) fully complexed at 1:1 stoichiometry (2) less than 50% complexed.

Stability constants can be directly determined from the titration data at pH \sim 9 for cases where only a fraction of the ligand is in the complexed form. The absorbance at any given wavelength, A_i , depends on the complex formation constant, K_{ML} , the concentration of uncomplexed metal ion, $[M]$, and the limiting absorbance values A_1 and A_0 for the metal-ligand complex and the uncomplexed ligand, respectively. This relationship is shown in the following equation:

$$A_i = \frac{A_1 K_{ML} [M] + A_0}{K_{ML} [M] + 1} \quad (3.13)$$

For a metal-ligand titration where complexation is quantitative at pH \sim 9, the formation constant cannot be directly determined because the error from data fitting would be very high. If the pH is decreased then the percentage of ligand in a protonated form increases and competition exists between the formation of the metal ion complex and protonation of the ligand. Therefore, the ligand is no longer present as just the free

ligand and the expression for the metal ion complexation equilibrium is written as a conditional (pH dependent) stability constant denoted as K'_{ML} as shown in eq 3.14.

$$K'_{ML} = \frac{[ML^{n+}]}{[M^{n+}][L']} \quad (3.14)$$

In this expression $[L']$ is the total concentration of all forms of the uncomplexed ligand as shown in eq 3.15.

$$[L'] = [L] + [HL]^+ + [H_2L]^{2+} \quad (3.15)$$

To obtain the intrinsic stability constant, K_{ML} , from the conditional stability constant value, K'_{ML} , the side reactions of the protonation reactions (eqs 3.1 and 3.2) must be accounted for. This is done using equations 3.16 and 3.17.

$$K'_{ML} = \frac{[ML]}{[M][L']} = \frac{[ML]\alpha_L}{[M][L]} = K_{ML}\alpha_L \quad (3.16)$$

$$\alpha_L = \frac{[L]}{[L']} = (1 + K_{H1}a_H + K_{H1}K_{H2}a_H^2)^{-1} \quad (3.17)$$

For a metal titration at a lower pH, the absorbance at any given wavelength, A_i , now depends on the conditional stability constant, K'_{ML} , concentration of the uncomplexed metal ion $[M]$, and the limiting absorbance values A_1 and A_0 for the metal ion-ligand complex and the uncomplexed ligand, respectively, as shown in the following equation:

$$A_i = \frac{A_1 K'_{ML} [M] + A_0}{K'_{ML} [M] + 1} \quad (3.18)$$

A nonlinear least-squares program (Kaleidagraph) was used to find K_{ML} or K'_{ML} , A_1 , and A_0 . Estimates of A_1 and A_0 are obtained from the metal ion titration spectra. Initial estimates for K_{ML} or K'_{ML} are obtained from fractional absorbance versus

metal:ligand ratio plots. The fraction of total absorbance change, f , is linearly related to the fraction of ligand complexed. Therefore, concentration of the metal-ligand complex is proportional to the initial concentration of ligand, C_L and f as shown in eq 3.19.

$$[\text{ML}] = f * C_L \quad (3.19)$$

Estimates of the ligand and metal ion concentrations ($[\text{L}]$, $[\text{M}]$) are determined by subtracting the concentration of metal ion-ligand complex, $[\text{ML}]$, from the initial concentration of ligand or metal ion, respectively. These concentrations are used to calculate an initial estimate K_{ML} or K'_{ML} for the data fitting process. The measured absorbance, A_i is plotted versus initial metal ion concentration, $[\text{M}]_i$, and the data is fit by using Equation 3-13 or Equation 3-17 and the initial guesses for K_{ML} or K'_{ML} , A_0 , and A_1 . The value of K_{ML} or K'_{ML} obtained from the data fitting program is then used to calculate new metal concentrations for each step of the titration. This is done by finding the concentration of the metal ion-ligand complex by using the value of K_{ML} (K'_{ML}), the total concentration of ligand, C_L , and the total concentration of metal, C_M , as shown in eq 3.20.

$$[\text{ML}] = \frac{K'_{\text{ML}}(C_L + C_M) + 1 - ((K'_{\text{ML}}(C_L + C_M) + 1)^2 - 4K'_{\text{ML}}{}^2 C_L C_M)^{1/2}}{2K'_{\text{ML}}} \quad (3.20)$$

The metal ion-ligand concentration is then subtracted from the total metal ion concentration to get a new set of free metal ion concentrations for the curve fitting program. The curve fitting process is repeated using the values for K_{ML} or K'_{ML} , A_0 , and A_1 from the previous data fitting cycle. This calculation process is repeated until the values of K_{ML} (K'_{ML}), A_0 , and A_1 change $\leq 2\%$ from the previous cycle.

The only exception to the previously described procedure and data analysis is the determination of the formation constant for cryptand An2.2.2 with lead. A very large (\geq

6) formation constant of cryptand An2.2.2 with $\text{Pb}(\text{ClO}_4)_2$ requires the formation constant to be measured at a very low pH (~ 2) where the ligand is predominantly ($\geq 95\%$) present as the diprotonated species. The kinetics of the ligand and metal interaction at this pH are slowed down considerably so the titrations are accomplished by batch analysis. Batch analysis is different from the previously described method of analysis because multiple solutions are prepared to contain various amounts of metal and a fixed concentration of ligand. The solutions are prepared separately and allowed sufficient time to reach equilibrium (~ 48 hrs). Plots of absorbance versus total metal and absorbance versus the product of total metal and alpha are both used to fit K'_{ML} . This is done to correct for the variance in pH between the solutions. The plot of absorbance versus total metal is fit using the previously described method and eq 3.18. The plot of absorbance versus the product of total metal and alpha is fit using the equation below. The value of K_{ML} obtained from the data fitting program is then used to calculate new metal concentrations for each step of the titration.

$$A_i = \frac{A_1 K_{\text{ML}} [\text{M}] \alpha_L + A_0}{K_{\text{ML}} [\text{M}] \alpha_L + 1} \quad (3.21)$$

In order to use SPECFIT/32 to determine the metal ion-complexation constants, a suitable model is selected from the program.⁹ The spectrophotometric data is imported as well as the volume of the aliquot of metal added and the concentration of the metal ion solution for each spectrum. A metal ion-complexation equilibria model (eqs. 3-1 - 3.3) is used to fit the metal ion titration sets. Initial guesses for the metal ion complexation constants must be provided by the operator and are determined from the fraction of absorbance versus metal to ligand ratio plots.¹⁰

References

- (1) Buschmann, H.-J. *Inorg. Chim. Acta* **1986**, *120*, 125-129.
- (2) Cox, B. G.; Firman, P.; Gudlin, D.; Schneider, H. *J. Phys. Chem.* **1982**, *86*, 4988-4992.
- (3) Tsien, R. Y. *Biochemistry* **1980**, *19*, 2396-2404.
- (4) Taylor, R. W.; Springer, M. E. *Inorg. Chem.* **1988**, *27*, 165-168.
- (5) Vogel, A. I. *Vogel's textbook of Quantitative Chemical Analysis*, 5th ed.; Longman Scientific & Technical: New York, 1989.
- (6) Rorabacher, D. B.; Kandegedara, A. *Anal. Chem.* **1999**, *71*, 3140-3144.
- (7) Rorabacher, D. B.; Kandegedara, A.; Yu, Q.; Xu, Y. *Anal. Biochem.* **1997**, *253*, 50-56.
- (8) *Kaleidagraph*; version 3.09; Synergy Software: Reading, PA, 1997.
- (9) *SPECFIT/32*, version 3.0; Spectrum Software Associates: Marlborough, MA, 2000.
- (10) Maeder, M.; Zuberbuhler, A. D. *Anal. Chem.* **1990**, *62*, 2220-2224.

Chapter Four

Results and Discussion

I. Structures and NMR Assignments of Monocyclic Ligands

Monocyclic diamides are intermediates in the synthesis of diaza-crown ethers and macrobicyclic cryptand ligands¹, and are also of interest for their potential use as molecular or anion receptors^{2,3}. An important aspect of receptors is the preferred position of the amide N-H moieties that serve as hydrogen bond donors. Each pair of amide N-H groups may adopt an endo-endo⁴, endo-exo⁵, or exo-exo orientation with respect to the macrocycle cavity. This orientation may be affected by structural factors such as ring size, type of donor atoms, and the incorporation of benzene rings into the backbone chain of the macrocycle. The first section will report the results of an investigation of the monocyclic diamides **7**, **8**, and **11** in the solid-state and the subsequent section will describe an investigation of monocyclic diamides **9**, **11**, and **13** in the solid-state and in solution.

The parent 18-membered macrocyclic diamide, **7**, the benzoannelated derivative, **11**, and the thioether derivative, **8**, were synthesized according to the methods described in Chapter 2 and are shown in Figure 4-1. Macrocyclic diamide **8a**, a thioether derivative with the amide groups on the dioxa chain, was previously studied by our group.⁵ These compounds allow investigation of the structural effects of changing the donor atoms (**7** vs. **8**), the addition of benzylic rings (**7** vs. **11**), and the position of the carbonyl groups (**8** vs. **8a**⁵) on the orientation of the amide groups. Each macrocyclic diamide will be described by the overall shape, donor atom orientation, cavity size, torsion angle sequences, arrangement of amide groups, and hydrogen-bonding arrangement. The

donor atoms will be described as endodentate or exodentate, which indicates whether they point towards or away from the cavity, respectively.⁶ A torsion angle for a chain A-B-C-D is the dihedral angle between the planes A-B-C and B-C-D and will be described as anti, *a* (90-180°) or gauche, *g* (30-90°).

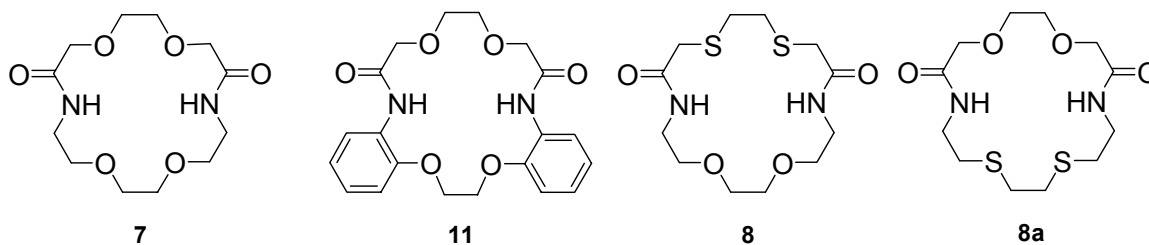


Figure 4-1. Monocyclic diamides 2.2*, (**7**), An2.2*, (**11**), 2.2_S*, (**8**), and **8a**.

Solid-state structures for compound **7** show two different forms of the molecule, A and B, as shown in Figures 4-2 and 4-3. The cavity of molecule A exists in a relatively flat arrangement with all six donor atoms N1A, N2A, O1A, O2A, O4A, and O5A adopting endodentate positions. Molecule A has a cavity size that can be characterized by distances between opposite donor atoms: N1A:N2A 5.68 Å; O1A:O4A 5.39 Å; O2A:O5A 5.52 Å. In contrast, the donor atoms N1B, O4B, and O5B in molecule B adopt an exodentate conformation. This results in a larger cavity size in comparison to molecule A based on the corresponding donor atom distances: N1B:N2B 5.73 Å; O1B:O4B 5.85 Å; O2B:O5B 5.96 Å. Molecules A and B have the same torsion angle sequence *gga, aga, agg* for the N—C—C—O—C—C—O—C—C—N chain that does not contain amide groups. For the chains with amide groups the C—O—C—C—O—C torsion angle sequences for molecules A and B are *a,aga,a* and *g,aag,a*, respectively.

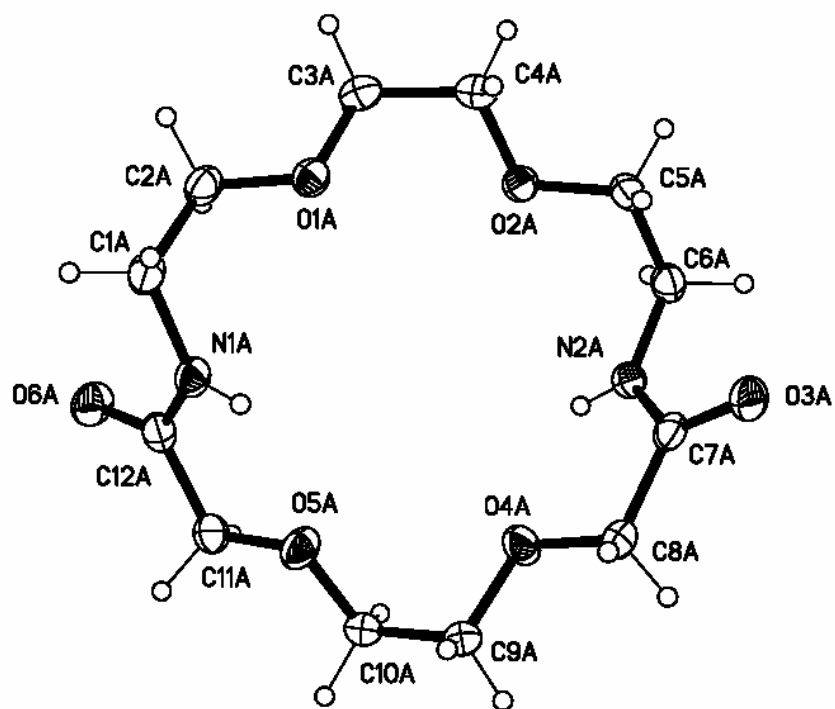


Figure 4-2. X-ray crystal structure of 2.2*, (7), Molecule A.

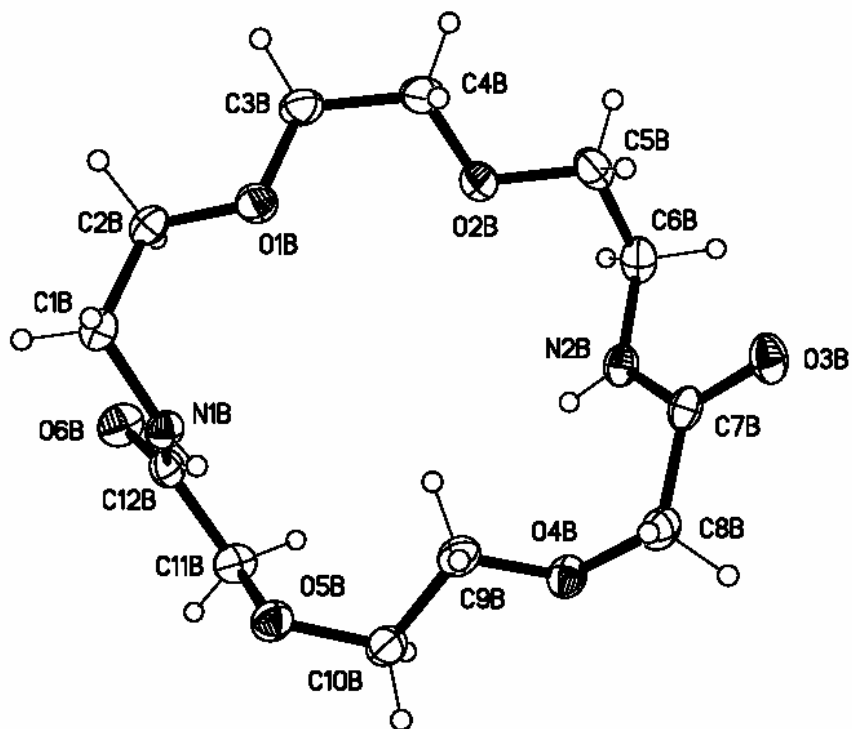


Figure 4-3. X-ray crystal structure of 2.2*, (7), Molecule B.

The amide groups in both molecules (H—N—C=O) exhibit *trans* orientation and are involved in hydrogen-bonding. Least-squares calculations for molecule A show that the amide groups N1A—C12A[O6A]—C11A and N2A—C7A[O3A]—C8A are planar with average deviations of $\leq 0.0005 \text{ \AA}$ and $\leq 0.0024 \text{ \AA}$, respectively. The dihedral angle between the least-squares planes of the amides is 54.2° .

Molecule B shows greater distortion in the planarity of the amide groups as evidenced by larger average deviations from the least-squares planes for N1B—C12B[O6B]—C11B, $\leq 0.008 \text{ \AA}$, and N2B—C7B[O3B]—C8B, $\leq 0.0026 \text{ \AA}$; furthermore, there is a larger dihedral angle of 119.4° between the least-squares planes. Both molecules of compound 7 have only intermolecular hydrogen bonds. Figure 4-4 shows the chain of hydrogen bonds present for molecule A. Each molecule A has four hydrogen bonds associated with it.

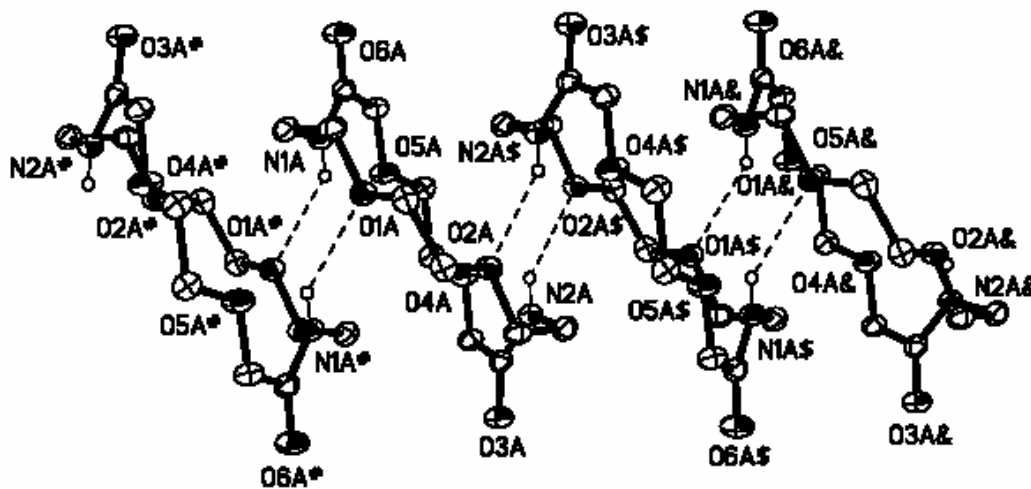


Figure 4-4. X-ray crystal structure of 2.2*, (7), showing the formation of hydrogen-bonded chains for molecule A. Displacement ellipsoids are drawn at 50% probability level. Hydrogen bonds are indicated by dashed lines. Symmetry transformations used to generate equivalent molecules: molecule # 1-x, 1-y, 1-z; molecules \$ and & -x, 1-y, 1-z.

Molecule A consists of polymeric chains that are linked by two distinct intermolecular hydrogen bonds (N-H...O; Table 4-1) involving the amide hydrogen atom and an ether oxygen in the adjacent molecule as shown in Figure 4-4. Amide atom N1A acts as a hydrogen bond donor, *via* atom H1A and atom N2A *via* H2A with ether atoms O1A# and O2A\$, respectively. The number sign (#) and dollar symbol (\$) are used to denote the equivalent atoms from neighboring molecules. Figure 4-5 shows the chain of hydrogen bonds that link individual forms of molecule B together. Each molecule B has four hydrogen bonds associated with it.

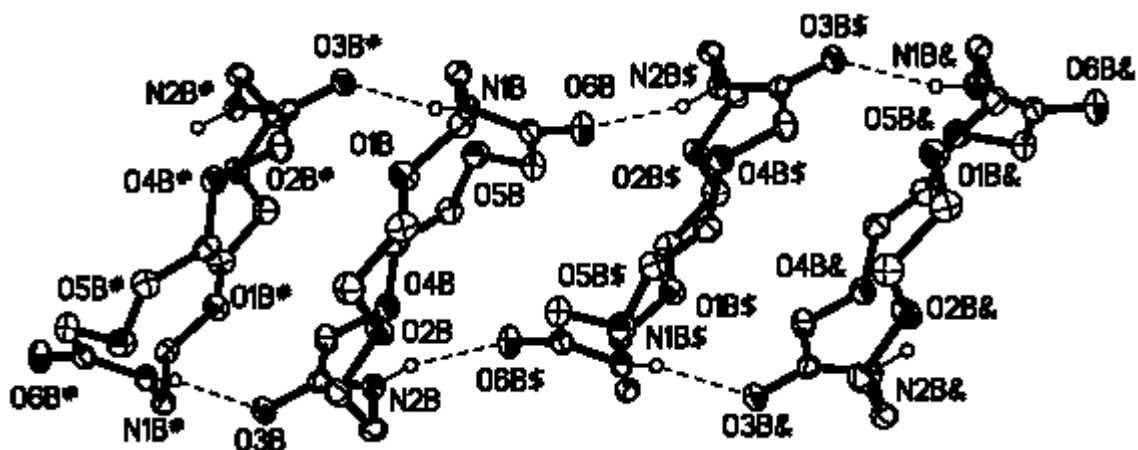


Figure 4-5. X-ray crystal structure of 2.2*, (7), showing the formation of hydrogen-bonded chains for molecule B. Displacement ellipsoids are drawn at 50% probability level. Hydrogen bonds are indicated by dashed lines. Symmetry transformations used to generate equivalent molecules: molecule # 1-x, 2-y, -z; molecules \$ and & 1-x, 1-y, -z.

In this case the intermolecular hydrogen bonds involve interactions between the amides N1B *via* H1B and N2B *via* H2B and carbonyl oxygens O3B# and O6B\$, respectively. The number sign (#) and dollar symbol (\$) are used to denote the equivalent atoms from different neighboring molecules. Table 4-1 shows the hydrogen bond distances (d) and angles (\angle) for the hydrogen bond donor (D), acceptor (A), and hydrogen (H) atoms in 7.

Table 4-1. Hydrogen bond parameters for 2.2*, (7).^a

D-H...A	d(D-H) ^b	d(H...A) ^b	d(D...A) ^b	∠(DHA) ^c
N1A-H1A...O1A#	0.832(15)	2.295(15)	3.0087(12)	144.0(13)
N2A-H2A...O2A\$	0.830(15)	2.205(15)	2.9581(12)	150.9(13)
N1B-H1B...O3B#	0.844(15)	2.068(15)	2.8667(12)	157.7(13)
N2B-H2B...O6B\$	0.865(15)	1.993(15)	2.8228(13)	160.3(13)

^aUncertainty in least significant digits in parentheses. ^bValues in units of Angstroms (Å). ^cValues in units of degrees (°).

Compound **11** differs from **7** by the incorporation of benzylic rings into the backbone of the macrocycle. The solid-state structure of **11** is shown in Figure 4-6. Compound **11** is similar to molecule A of **7** because all of the donor atoms N1, N1A, O1, O3, O1A, and O3A are endodentate. The cavity of compound **11** is smaller than the parent compound **7** with donor atom distances of N1:N1A 5.64 Å; O1:O3A 4.68 Å; O1A:O3 5.01 Å.

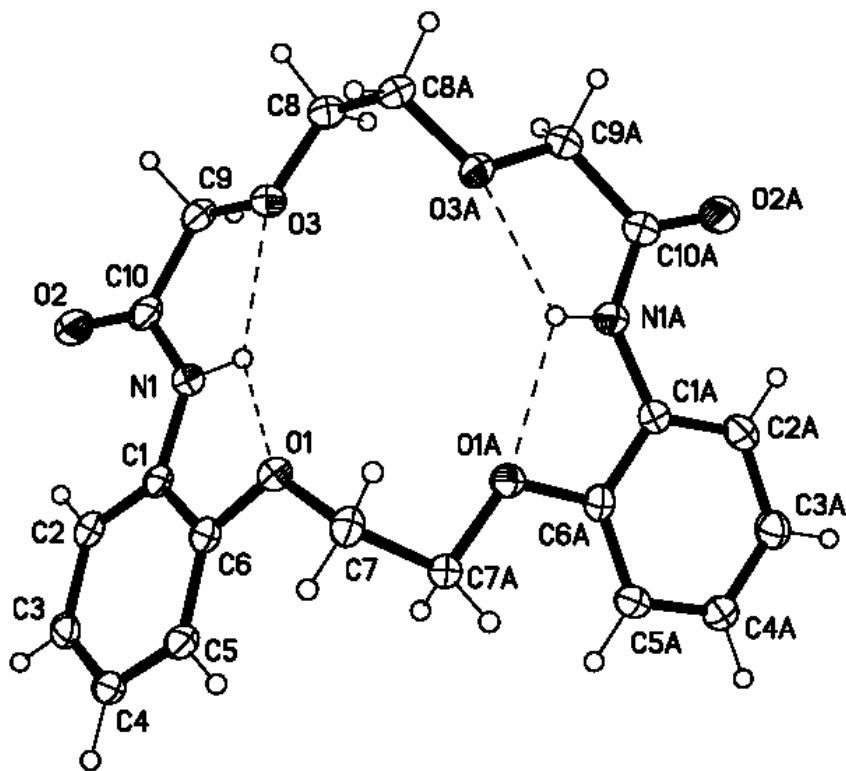


Figure 4-6. X-ray crystal structure of An2.2*, (**11**).

In comparison with **7** the structural change of **11** is evident in the significant difference in torsion angle sequences for both the non-amide side N—C—C—O—C—C—O—C—C—N (*aga, gga, aga*) and the amide side C—O—C—C—O—C (*a, gga, a*) of the molecule. Least-squares calculations for **11** show that the amide groups N1—C10[O2]—C9 and N1A—C10A[O2A]—C9 are planar but with significantly different average deviations of ≤ 0.0005 and ≤ 0.007 , respectively. The dihedral angle between the least-squares planes of the amides is 128.2° . Two other least-squares planes are present in the molecule, defined by the benzene rings, and the dihedral angle between these planes is 106.0° . Figure 4-7 shows compound **11** in a different view without hydrogens so the angle between the benzene rings is visible. Least-squares calculations for the benzene ring plane defined by C1, C2, C3, C4, C5, and C6 have average deviations of ≤ 0.005 Å and the three donor atoms O1, O3, and N1 have average deviations from that plane ≤ 0.05 Å. The planarity of the benzene ring made up of C1A, C2A, C3A, C4A, C5A, and C6A has a lower average deviation of ≤ 0.004 Å, but the donor atoms O1A, O3A, and N1A are further out of that plane with average deviations ≤ 0.3 Å.

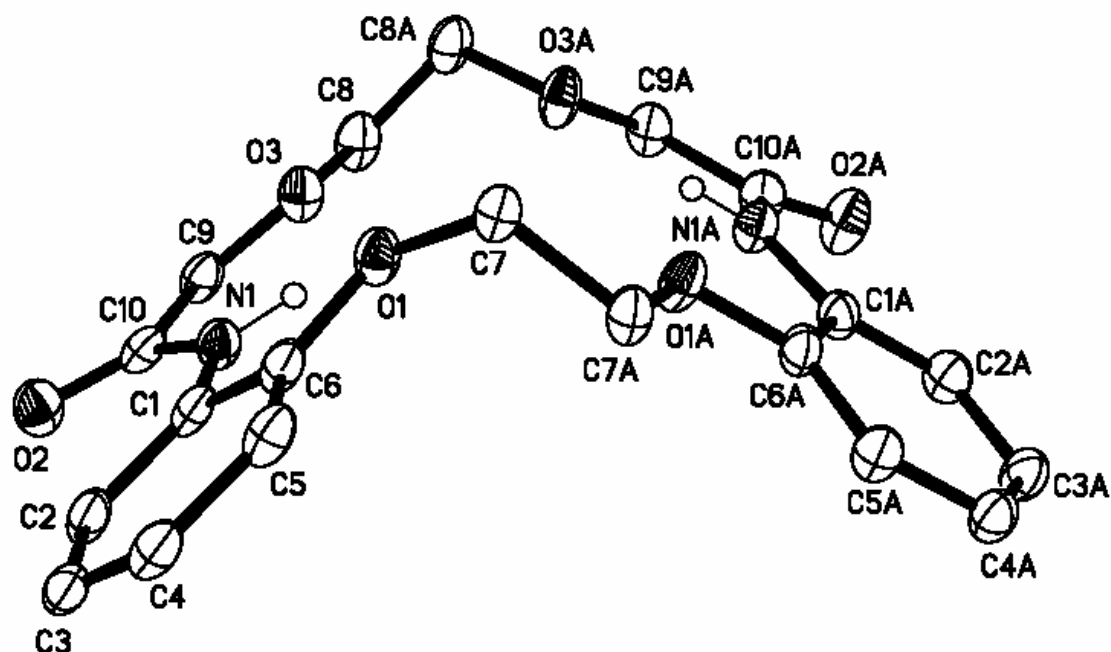


Figure 4-7. X-ray crystal structure of An2.2*, (**11**), showing the angle between the benzene rings.

Due to the rigidity of the benzene rings, compound **11** contains only four intramolecular hydrogen bonds (N-H \cdots O; Table 4-2) between the amides and adjacent ether oxygens.

Table 4-2. Hydrogen bond parameters for An2.2*, (**11**).^a

D-H \cdots A	d(D-H) ^b	d(H \cdots A) ^b	d(D \cdots A) ^b	\angle (DHA) ^c
N1-H1 \cdots O1	0.93(3)	2.16(3)	2.584(3)	106.3(19)
N1-H1 \cdots O3	0.93(3)	2.11(3)	2.589(3)	111(2)
N1A-H1A \cdots O1A	0.90(3)	2.13(2)	2.623(3)	113(2)
N1A-H1A \cdots O3A	0.90(3)	2.15(3)	2.588(3)	108.9(19)

^aUncertainty in least significant digits in parentheses. ^bValues in units of Angstroms (Å). ^cValues in units of degrees (°).

The 18-membered monobenzo diamide derivative shown in Figure 4-8 was prepared and also has different structural properties from compound **7**.⁷ This derivative had two intramolecular hydrogen bonds between amide nitrogens and ether oxygens proximal to the amides and one intermolecular hydrogen bond between the amide and a carbonyl oxygen in an adjacent molecule.

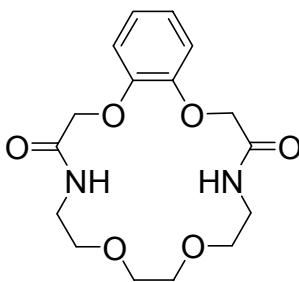


Figure 4-8. Monobenzo 18-membered diamide.⁷

In **8**, sulfur donor atoms are substituted for the oxygen atoms in one bridge of the parent compound **7**. The solid-state structure of **8** is shown in Figure 4-9. The donor atoms N1, N2, O2, and O3 have an endodentate orientation while donor atoms S1 and S2 are exodentate. Compound **8** has the largest cavity size of the macrobicyclic diamides based on the donor atom distances: N1:N2 6.13 Å; O2:S1 5.84 Å; O3:S2 5.77 Å. Although the chain that does not contain amide groups in **8** is the same as **7**, the torsion angle sequence for N—C—C—O—C—C—O—C—C—N is different with a sequence of *gga, agg, aga* in comparison to *gga, aga, agg*. The chain that does contain amide groups, C—S—C—C—S—C, has a torsion angle sequence of *g,gag,g* which is different from both **7** and **11**. Least-squares calculations of the amide groups N1—C4[O1]—C3 and N2—C11[O4]—C12 reveal that they have similar planarity with average deviations of ≤ 0.0002 Å and ≤ 0.0003 Å, respectively. The dihedral angle between these least-squares planes is 81.9°.

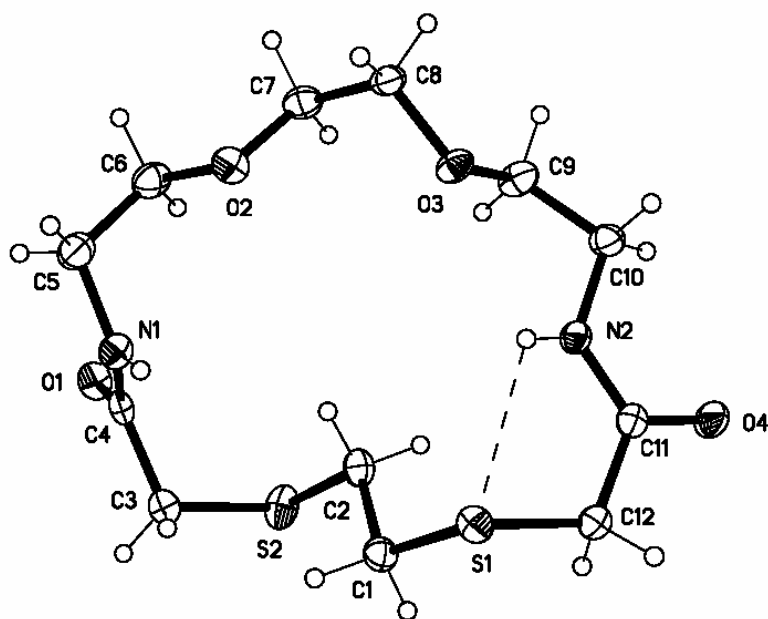


Figure 4-9. X-ray crystal structure of 2.2_s^* , (**8**).

In the solid-state, compound **8** is made up of polymeric chains formed by intermolecular hydrogen bonds (N-H \cdots O) between the amide (N1) and carbonyl oxygen (O4#) as shown in Table 4-3. The number sign (#) is used to denote an equivalent atom from a neighboring molecule.

Table 4-3. Hydrogen bond parameters for 2.2_s^* , (**8**).^a

D-H \cdots A	d(D-H) ^b	d(H \cdots A) ^b	d(D \cdots A) ^b	\angle (DHA) ^c
N1-H1 \cdots O4#	0.83(2)	2.01(2)	2.8353(18)	175.3(19)
N2-H2 \cdots S1	0.80(2)	2.603(19)	3.0503(15)	116.9(16)

^aUncertainty in least significant digits in parentheses. ^bValues in units of Angstroms (Å). ^cValues in units of degrees (°).

Amide atom N1 acts as a hydrogen bond donor, *via* atom H1 with O4#. An intramolecular hydrogen bond (N-H \cdots S) between the other amide and thioether occurs on the amide side between the atom N2 *via* atom H2 with S1. Figure 4-10 shows the polymeric chains of **8**.

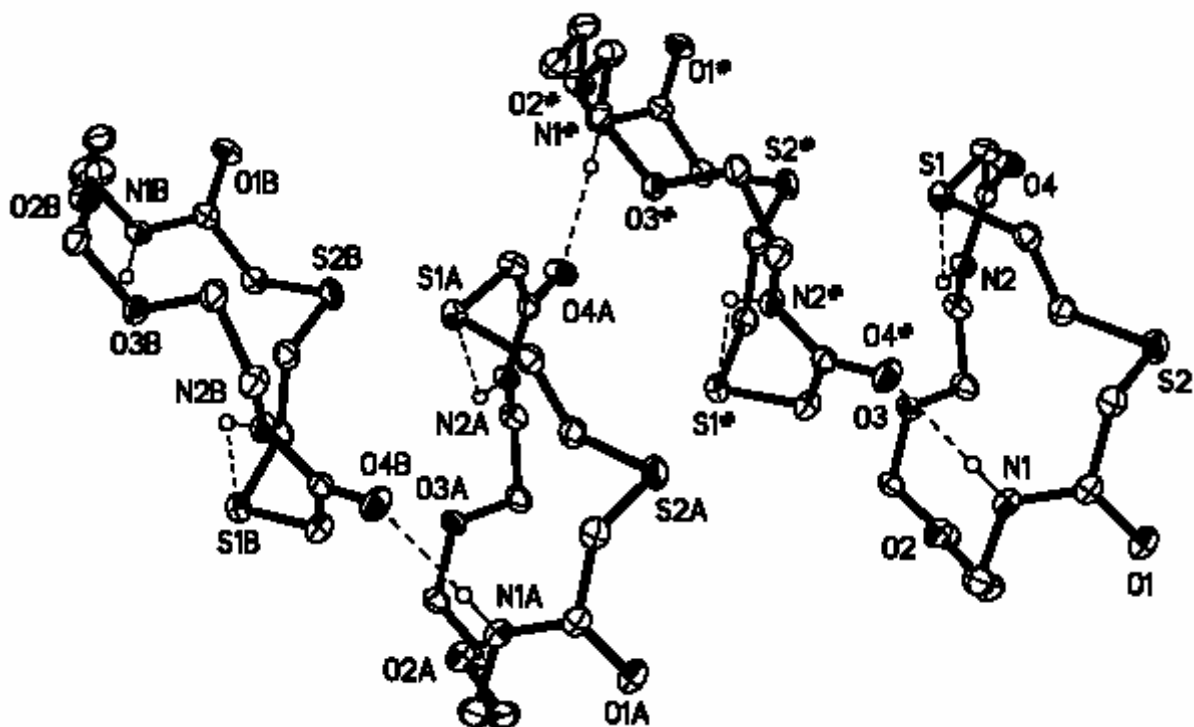


Figure 4-10. X-ray crystal structure of $2.2S^*$, (**8**), showing the formation of hydrogen-bonded chains. Displacement ellipsoids are drawn at 50% probability level. Hydrogen bonds are indicated by dashed lines. Symmetry transformations used to generate equivalent molecules: molecule # $-x, 1-y, 1-z$; molecules A and B $1-x, -y, -z$.

An X-ray structure of a related 18-membered macrocyclic diamide (**8a**) that had the amides on the ether side of the ring instead of the thioether side was previously reported by our group.⁵ Derivative **8a** had an intermolecular hydrogen bond between the amide hydrogen and carbonyl oxygen of a neighboring molecule and an intramolecular hydrogen bond between the other amide nitrogen and other carbonyl oxygen. The structure of **8a** was different from **8** in that the hydrogen bonds only involved amide hydrogens and carbonyl oxygens and that one carbonyl oxygen points into the center of the cavity. The similarities between the molecules in the solid-state were that both derivatives had one intermolecular and one intramolecular hydrogen bond and both derivatives were made up of molecular chains.

All 18-membered macrocyclic amides mentioned have intermolecular H-bonds except compound **11**. In this case, planarity of anilino and adjacent amide groups result in the amide hydrogen adopting an endo orientation. The most flexible diamide (**7**) has only intermolecular H-bonds. The conformational constraints imposed by the -SCCS-subunit (**8**, **8a**⁵) and benzo groups (**11** and the monobenzo compound shown in Figure 4-8⁷) result in a mixture of intra- and intermolecular H-bonds. Where intramolecular H-bonds are found to involve ether or thioether atoms, the H-bonds always involve the acceptor atom on the carbonyl moiety side. In the case of **11**, intramolecular hydrogen bonds involve ether oxygens in both bridges.

The monocyclic amides **9**, **11**, and **13** were isolated during the synthesis of several benzoannelated cryptands according to the methods described in Chapter 2 and were selected to study the effects of ring size (**9** vs. **11**) and location of the amide moieties within the macrocyclic ring (**11** vs. **13**) on the orientation of the amide groups. The presence of a benzene subunit adjacent to the amide provides a means to assess the relative position of the amide group with respect to the aromatic ring in the solution state. Previous NMR studies have shown that the *ortho* hydrogens in *N*-acylanilines can be shifted downfield significantly with respect to the other aromatic protons⁸⁻¹⁰. The magnitude of the shift depends on degree of co-planarity of the amide carbonyl group with the aromatic ring and the presence of H-bond acceptors for the amide proton⁸⁻¹⁰. Although proton NMR spectra have been reported for **11**¹¹ and **13**¹²⁻¹⁶, the assignments are incomplete or differ from each other. This section will report the complete assignment of the ¹H and ¹³C NMR spectra of **9**, **11**, and **13** in CDCl₃, the solid-state

structures of **9** and **13**, and the correlation found in all three diamides between the structures in solution and in the solid-state.

1-D ^1H and ^{13}C NMR spectra along with gCOSY, gHMBC, gHMQC, HMQC, and HSQC were used to assign the proton and carbon chemical shifts. The splitting patterns for the aromatic protons of **9** were obtained from spectra acquired using 600 MHz ^1H NMR. The ^1H and ^{13}C chemical shift and coupling constant data for **9**, **11**, and **13** are listed in Tables 4-4, 4-6, and 4-8, respectively while Tables 4-5, 4-7, and 4-9 show the gCOSY, gHMBC, gHMQC, HMQC, and HSQC signals for each compound. The numbering schemes shown in Figure 4-11 are used to define the NMR assignments given in Tables 4-4 - 4-9.

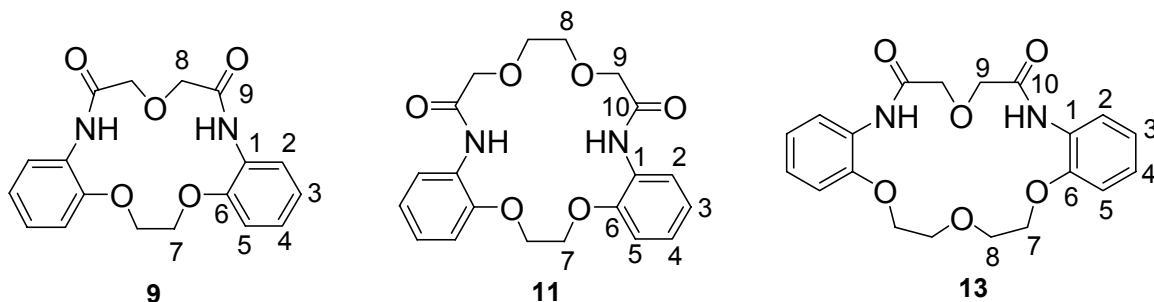


Figure 4-11. NMR numbering scheme for macrocyclic amides An2.1*, (**9**), An2.2*, (**11**), and An3.1*, (**13**).

A COSY (CORrelation SpectroscopY) experiment will provide cross peaks for protons coupled to other protons.¹⁷ HMQC (Heteronuclear Multiple Quantum Correlation) and HSQC (Heteronuclear Single Quantum Correlation) experiments both provide information regarding the one-bond connection of carbons to hydrogens. HMBC (Heteronuclear Multiple Bond Correlation) experiments suppress one bond carbon to hydrogen signals and show 2-3 bond signals. NOESY (Nuclear Overhauser Effect SpectroscopY) irradiates one proton nucleus and the resultant signals reveal the identity

of protons that are close in space ($\sim 4 \text{ \AA}$) to the irradiated proton regardless if geminal or vicinal coupling occurs.¹⁷

The synthesis of compound **9** has been reported by Formanovskii and Murakhovskaya¹⁸ and their characterization included the melting point, elemental analysis, and IR spectra. ¹H and ¹³C NMR data was not reported.

Table 4-4. ¹H and ¹³C NMR data for An2.1*, (**9**).

	δC C (ppm)	H	δH (ppm)	Coupling constants (Hz)	Multiplicity
1	128.3				
2	120.1	2	8.50 (2H)	$J(2, 3) = 7.8; J(2, 4) = 1.7$	dd
3	123.0	3	7.05 (2H)	$J(3, 2) = 7.8; J(3, 4) = 7.8; J(3, 5) = 1.6$	td
4	124.5	4	7.09 (2H)	$J(4, 3) = 7.8; J(4, 5) = 7.8; J(4, 2) = 1.7$	td
5	113.7	5	7.02 (2H)	$J(5, 4) = 7.8; J(5, 3) = 1.6$	dd
6	146.8				
7	68.4	7	4.38 (4H)		s
8	70.6	8	4.21 (4H)		s
9	165.6				
		NH	9.03 (2H)		s

The HSQC of **9** made known the direct linkage of protons (H2-H5, H7 and H8) to carbons (C2-C5, C7 and C8), quarternary carbons that were not connected to any hydrogens (C1, C6, C9), and the hydrogen signal that was not connected to any carbon (NH). 1D NOESY experiments of **9** included irradiation of H2 which gave peaks at 9.03 ppm (NH) and 7.02-7.09 ppm (H3-H5) and irradiation of H7, resulting in peaks at 7.02-7.09 ppm (H3-H5). These results elucidated the location of the aromatic protons H2 and H5, as well as the singlet protons H8 and H7 adjacent to the carbonyl and ether, respectively. The *ortho* proton (H2) on the benzene ring is shifted downfield significantly compared to the other aromatic protons.

Table 4-5. H-H and C-H correlation NMR data for An2.1*, (**9**).

C	H	gHMBC	gCOSY	HSQC
1				
2	2	NH	H5	H2
3	3			H3
4	4	C2		H4
5	5		H2	H5
6		C7, C2		
7	7			H7
8	8			H8
9		C8		
	HN			

The solid-state structure of **9** in Figure 4-12 shows the amide moiety in the *trans* arrangement with intramolecular hydrogen bonds between the amides and adjacent ether oxygens. The donor-acceptor distances and angles for the two hydrogen bonds between N1...O2 and N2...O1 are 2.586(2) Å, 112.6(16)° and 2.617(2) Å, 110.6(16)°, respectively. There are two other hydrogen bonds present from the amides to the ether oxygens on the other bridge. The donor-acceptor distances and angles for the hydrogen bonds between N1...O4 and N2...O4 are 2.619(2) Å, 111.3(16)° and 2.640(2) Å, 112.8(16)°, respectively. The solid-state structure of the parent amide (2.1*) without the benzene rings also has bifurcated hydrogen bonds between the amide nitrogens and both adjacent ether oxygens.¹⁹

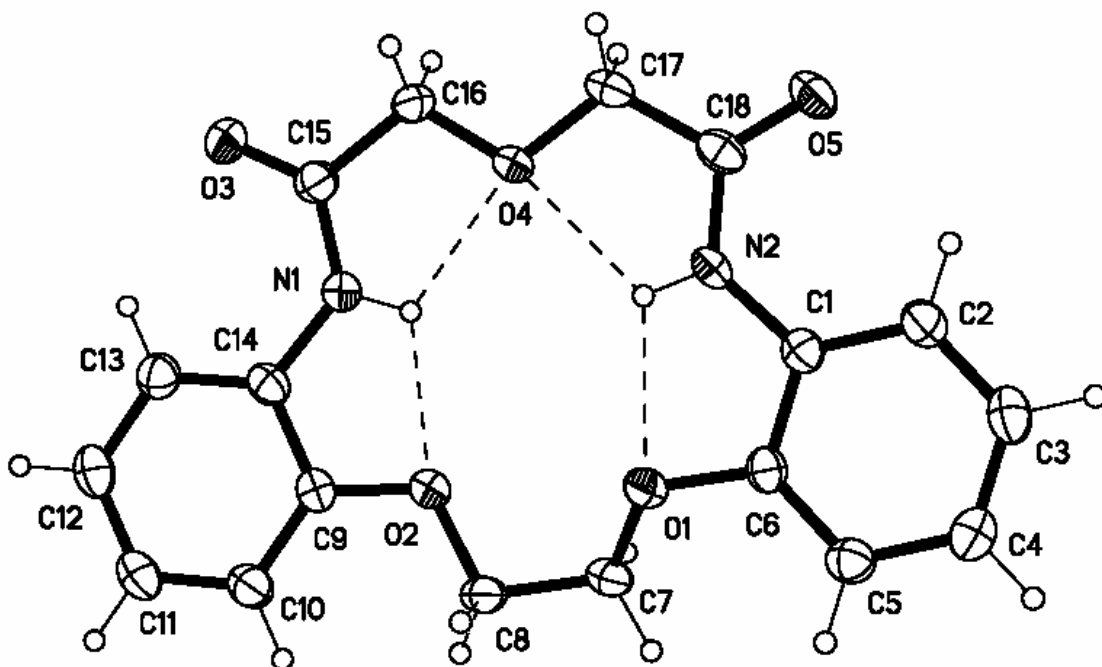


Figure 4-12. X-ray crystal structure of An2.1*, (9).

The synthesis and characterization of the monocyclic amide **11** has been reported by Kilic and Gunduz.¹¹ Only the chemical shift values for H7 and some of the aromatic protons agree with the previously reported values.¹¹

Table 4-6. ¹H and ¹³C NMR data for An2.2*, (11).

C	δ C (ppm)	H	δ H (ppm)	Coupling constants (Hz)	Multiplicity
1	127.3				
2	120.6	2	8.34 (2H)	$J(2, 3) = 7.7$	d
3	121.6	3	6.96 (2H)	$J(3, 2) = 7.7; J(3, 4) = 7.7$	t
4	124.2	4	7.02 (2H)	$J(4, 3) = 7.7; J(4, 5) = 7.7$	t
5	110.8	5	6.82 (2H)	$J(5, 4) = 7.7$	d
6	146.6				
7	66.4	7	4.42 (4H)		s
8	70.0	8	3.81 (4H)		s
9	70.8	9	4.10 (4H)		s
10	167.1	NH	9.04 (2H)		s

The earlier report proposed that downfield signals observed at 8.5 ppm (O-H) and 9.2 ppm (N-H) could be attributed to contributions from lactim and lactam tautomers, respectively. This conclusion was based on characteristic IR bands for the existence of O-H groups and C=N stretching found. Figure 4-13 shows the resonance structures possible for this type of interaction.¹¹



Figure 4-13. Lactam (a) and lactim (b) forms of amides.

However, the HMQC of **11** shows a direct bond from C2 to the proton with a signal at 8.3 ppm. Therefore, the signals at 8.34 ppm and 9.03 ppm can be assigned to the *ortho* aromatic proton (H2) and the amide proton. The large downfield shift of the *ortho* proton (H2) in comparison to the other aromatic protons is consistent with the pattern in compound **9**.

Table 4-7. H-H and C-H correlation NMR data for An2.2*, (**11**).

C	H	gHMBC	gCOSY	gHMQC
1				
2	2	C4, C6	H3	H2
3	3	C1, C5	H2, H4	H3
4	4	C2, C6	H3, H5	H4
5	5	C1, C3, C4	H4	H5
6				
7	7	C6		H7
8	8	C9		H8
9	9	C8, C10		H9
10				
	NH			

1D NOESY irradiation of H2 gave signals at 9.04 ppm (N-H) and 6.82-7.02 ppm (H3-H5), and irradiation of H5 gave a signal at 4.42 ppm (H7). These experiments made clear the assignments of H2 and H5 proton positions around the benzene ring. The

NOESY correlation of H7 and H5 also helped with the distinction between the location of the three singlets H7, H8, and H9.

The intramolecular hydrogen-bonding in the solid-state of **11** was presented earlier in Table 4-2 and is similar to **9** in that both amides have bifurcated hydrogen bonds to the ether oxygens. The solid-state structure shown earlier in Figure 4-6 also shows the amide moieties of **11** in the *trans* orientation.

The ^1H chemical shift values have been reported for **13**, although the peak assignments were not made^{12,15} or were not given for all protons^{13,14,16}. In general, the values of the individual chemical shifts and the peak assignments (when given) agree with those reported in Table 4-8. However, our assignments for H7 and H8 are opposite to those given in one report¹³, and in another case, the magnitude of all chemical shifts given differ from ours by ~ 0.3 ppm¹⁵. The chemical shifts and peak assignments given in Table 4-8 agree most closely with those in d_6 -DMSO reported by Markovich et al.¹⁶ and in CDCl_3 by Formanovskii et al.¹⁴. However, H3-H5 were not assigned by these authors, and the value for the amide proton reported by the latter (8.08 ppm)¹⁴ differs significantly from ours (8.73 ppm) and the others (8.75 - 9.00 ppm)^{12,15,16}. The value for H2 given in Table 4-8 (8.22 ppm) falls in the range (7.9 - 8.30 ppm) reported by other groups¹²⁻¹⁵.

Table 4-8. ^1H and ^{13}C NMR data for An3.1*, (**13**).

C	δC (ppm)	H	δH (ppm)	Coupling constants (Hz)	Multiplicity
1	126.7				
2	121.5	2	8.22 (2H)	$J(2, 3) = 7.9; J(2, 4) = 1.8$	dd
3	121.5	3	6.97 (2H)	$J(3, 2) = 7.9; J(3, 4) = 7.9; J(3, 5) = 1.5$	td
4	125.0	4	7.06 (2H)	$J(4, 3) = 7.9; J(4, 5) = 7.9; J(4, 2) = 1.8$	td
5	111.4	5	6.85 (2H)	$J(5, 4) = 7.9; J(5, 3) = 1.5$	dd
6	147.8				
7	67.9	7	4.21 (4H)		m (5 lines)
8	69.4	8	3.84 (4H)		m (5 lines)
9	71.8	9	4.25 (4H)		s
10	166.4	NH	8.73 (2H)		s

The assignments of H2 and H5 in the respective positions around the aromatic ring were made possible by the HMBC correlation of C2 with the amide hydrogen. Irradiation of H7 in **13** showed peaks at 3.84 (H8) and 6.85 (H5). The large downfield shift of H2 in **13** is consistent with the pattern found in compounds **9** and **11**.

Table 4-9. H-H and C-H correlation NMR data for An3.1*, (**13**).

C	H	gHMBC	gCOSY	HMQC
1				
2	2	C1, C4, C6	H3	H2
3	3	C1, C2, C4, C5	H2	H3
4	4	C1, C2, C3, C5, C6		H4
5	5	C1, C2, C3, C4, C6		H5
6				
7	7	C6, C8	H8	H7
8	8	C7, C8	H7	H8
9	9	C9, C10		H9
10	NH	C2		

In the solid-state structure of **13**, the unit cell contains a water molecule (fractional occupancy = 0.50) located near the center of the cavity of one macrocycle that forms hydrogen bonds with the amide protons and with the ether oxygen of an adjacent

molecule. Molecule A shown in Figure 4-14 has a water molecule encapsulated in the cavity and molecule B shown in Figure 4-15 has an empty cavity. The amides in both molecules have *trans* arrangement. The intramolecular hydrogen bond patterns of compounds **9** and **11** are consistent in **13** where the amide protons are hydrogen-bonded with the adjacent ether oxygens.

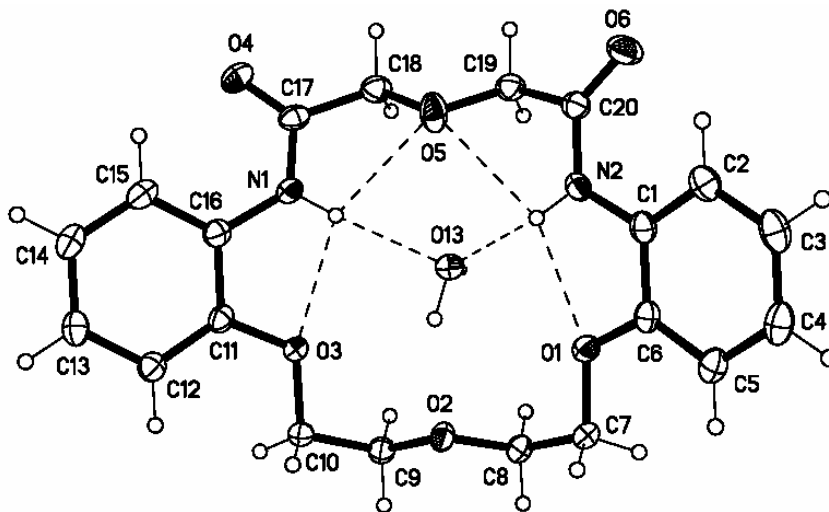


Figure 4-14. X-ray crystal structure of An3.1*, (**13**), Molecule A.

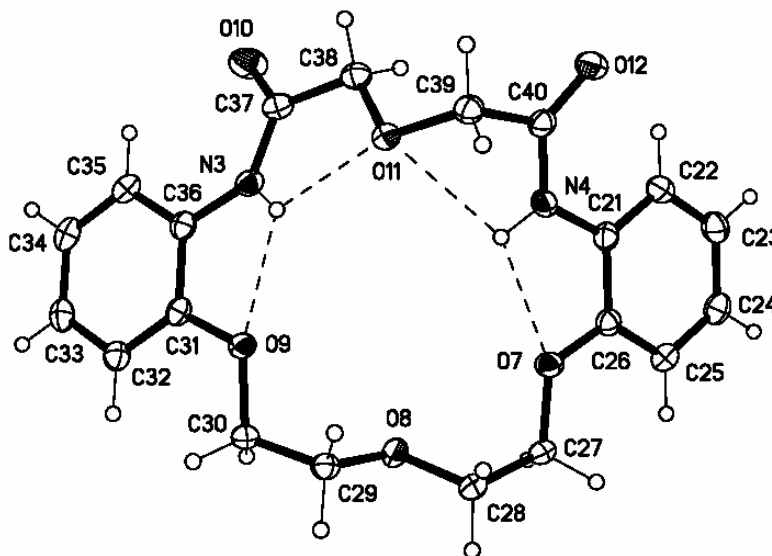


Figure 4-15. X-ray crystal structure of An3.1*, (**13**), Molecule B.

Molecule A has trifurcated hydrogen bonds between the amides with the ether oxygens and the water molecule. Molecule B has bifurcated hydrogen bonds between the ether oxygens. The donor-acceptor distances and angles for the hydrogen bonds are listed in Table 4-10.

Table 4-10. Hydrogen bond parameters for An3.1*, (**13**).^a

D-H...A	d(D-H) ^b	d(H...A) ^b	d(D...A) ^b	∠(DHA) ^c
N(1)-H(1)...O(3)	0.821(16)	2.337(15)	2.6313(14)	101.9(12)
N(1)-H(1)...O(5)	0.821(16)	2.360(15)	2.7213(15)	107.5(12)
N(1)-H(1)...O(13)	0.821(16)	2.259(16)	3.044(2)	160.1(15)
N(2)-H(2)...O(1)	0.873(15)	2.215(14)	2.6169(14)	107.8(11)
N(2)-H(2)...O(5)	0.873(15)	2.564(14)	2.8218(15)	98.0(10)
N(2)-H(2)...O(13)	0.873(15)	2.144(16)	2.993(2)	164.3(13)
N(3)-H(3)...O(9)	0.849(15)	2.218(14)	2.6104(14)	108.2(12)
N(3)-H(3)...O(11)	0.849(15)	2.158(14)	2.6149(14)	113.5(12)
N(4)-H(4)...O(7)	0.848(15)	2.153(15)	2.5824(14)	111.1(12)
N(4)-H(4)...O(11)	0.848(15)	2.595(14)	2.8568(14)	99.3(11)

^aUncertainty in least significant digits in parentheses. ^bValues in units of Angstroms (Å). ^cValues in units of degrees (°).

The amide moieties of the solid-state structures for **9**, **11**, and **13** are essentially planar (mean dev ≤ 0.0068 Å) with a *trans* arrangement of the carbonyl oxygen and amide hydrogen atoms, with the latter also close to the amide plane (dev ≤ 0.1592 Å). The amide hydrogen atoms are orientated toward the center of the macrocycle cavity, resulting in an *exo-exo* disposition of the carbonyl oxygen atoms. This conformation is stabilized by intramolecular hydrogen bonds between the amide protons and the proximal ether oxygen atoms. There are no intermolecular hydrogen bonds found in these structures except for those in **13** that involve a water molecule. The extent of the downfield shift of the aromatic proton in the *ortho* position is affected by the proximity and extent of co-planarity of the amide carbonyl group and the *ortho* aromatic hydrogen atom. These parameters can be defined by the O_{amide} - H_{o,arom} distance and the dihedral

angle between the planes defined by the benzene ring and the four-atom amide group. The respective parameters are 2.359 Å, 11.1°, 2.307 Å, 1.1°, for **9**; 2.311 Å, 13.8°, 2.317 Å, 12.7°, for **11**; and 2.347 Å, 17.1°, 2.323 Å, 14.3° for the anhydrous form of **13**. For the hydrated form of **13** the corresponding values are 2.288 Å, 16.2°, 2.402 Å, and 27.1°. The small dihedral angles (av ~14°) indicate that the carbonyl group is nearly coplanar with the benzene moiety, and if similar conformations are maintained in solution, the aromatic *ortho* hydrogen atom would be located in the deshielding region of the anisotropic field associated with the carbonyl group.

For compounds **9**, **11**, and **13** the number of ¹H and ¹³C peaks found indicates that the left and right halves of each molecule are equivalent. In compounds **9** and **11** there is rapid interconversion between conformers of the O-C-C-O, therefore, all sets of ethylene protons are singlets. However, the multiplets found for both sets of ethylene protons (H7, H8) in **13** suggest that rapid conformational change does not occur for this part of the macrocycle. If rapid conformational change did occur, these protons (H7,H8) would each be triplets. There is little variation of the ¹H and ¹³C chemical shifts for comparable nuclei among the three compounds, and the ¹³C chemical shifts for various nuclei occur in the expected regions.^{14,17} For compounds **9**, **11**, and **13** the *ortho* proton (H2) on the benzene ring is shifted downfield significantly compared to the other aromatic protons. A measure of this shift can be defined in terms of the difference $\delta_{\text{H2}} - \delta_{\text{H4}}$ ¹⁰, whose values were calculated and found to decrease in the following manner; 1.41 ppm (**9**), 1.32 ppm (**11**), 1.16 ppm (**13**). These values are close to that of the model compound *o*-methoxy-*N*-acetylaniline, where $\delta_{\text{H2}} - \delta_{\text{H4}} = 1.32 \text{ ppm}$ ¹⁰. The observed downfield shifts of H2 are consistent with a conformation for macrocycles **9**, **11**, and **13** wherein the carbonyl

groups adopt an exo-exo orientation and are relatively coplanar with the benzene rings. This conformation would maximize the effect of magnetic anisotropy, due to the carbonyl group, on H2.^{8-10,14,16} The trend in $\delta_{\text{H2}} - \delta_{\text{H4}}$ values also shows a qualitative inverse relationship with the average magnitude of the dihedral angles between benzene ring and amide group found in the solid-state. These angles increase as follows, (6.1°) **9**, (13.2°) **11**, (15.7°) **13**, suggesting that the solid-state structures are similar to those in a non-polar solvent like CHCl₃. Markovich et al.¹⁶ previously suggested similarities between the solid-state and solution structures of **13** based on the small changes observed in position of the IR bands for the N-H moiety in the solid-state (mineral oil suspension) and in solution (C₄Cl₆). Furthermore, Biernat et al.^{13a} interpreted results from studies of **13** with a shift reagent (Eu(dpm)₃)^{13b} to indicate that the carbonyl groups were exodentate and the amide protons were orientated into the macrocycle cavity forming hydrogen bonds with the ether oxygen atoms. The solid-state structures show that these conformations are stabilized by multiple intramolecular hydrogen bonds involving the amide protons and the ether oxygen atoms. The chemical shifts of the amide protons are 9.03, 9.04, and 8.73 for **9**, **11**, and **13**, respectively. Comparison with the value of 7.85 ppm for *o*-methoxy-*N*-acetylaniline¹⁰ suggests that the amide protons of **9**, **11**, and **13** are more extensively hydrogen-bonded compared to the model compound.¹⁰ Thus, the downfield shifts for N-H and the *ortho* proton (H2) are consistent with the proposed conformation of macrocycles **9**, **11**, and **13** in solution.

II. Structures and NMR Assignments of Bicyclic and Tricyclic Compounds

The solid-state structures of cryptands An2.2.1, An2.2.2, and An3.1.1.3 reveal the arrangement of the donor atoms, orientation of the donor atoms (endodentate vs. exodentate), the size of the cavity, and the orientation of the benzene rings. These characteristics can be compared with other cryptand and cryptate structures to determine the effects of the addition of the benzene rings. The solid-state structure of cryptand An2.2.1 is shown in Figure 4-16. The ligand has an unsymmetrical cavity with some donor atoms in an endodentate orientation (N1, N2, O1, and O2) and the others (O3, O4, and O5) in an exodentate orientation. This arrangement of atoms pointing in and out of the cavity resulted in a twisted structure as evident from the very different distances for comparable oxygen to oxygen arrangements (O1...O5: 6.14 Å, O2...O4: 4.58 Å). The shortest O...O nonbonding distance is 3.83 Å (O3...O5) and the largest is 6.14 Å (O1...O5). Least-squares calculations for benzene rings 1 (C1-C6) and 2 (C11-C16) show that the average deviations of the carbon atoms from the calculated planes are 0.0018 Å and 0.0055 Å, respectively. The dihedral angle between the least-squares planes of the benzene rings is 43.9° also shows the twisted nature of the cryptand structure.

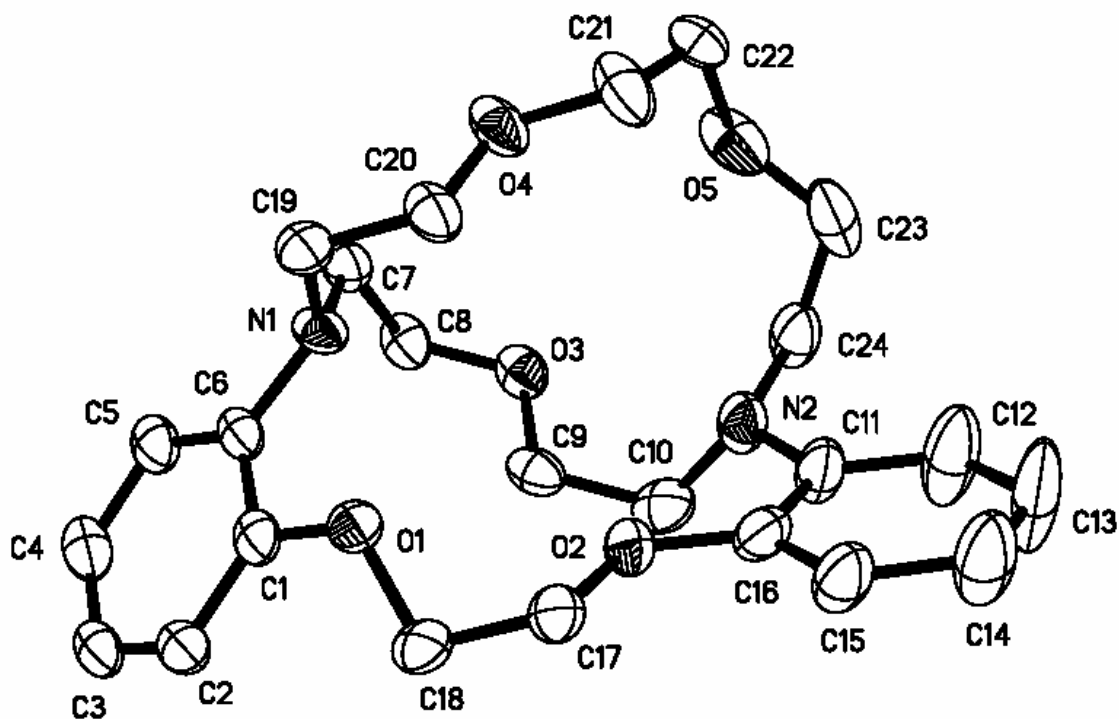


Figure 4-16. X-ray crystal structure of An2.2.1, (16).

The parent cryptand 2.2.1 has not been characterized by X-ray crystallography but some cryptate complexes have been.^{20,21} The N...N nonbonding distances of cobalt, sodium, and potassium 2.2.1 cryptates were 4.20 Å, 4.944 Å, and 5.143 Å, respectively.^{20,21} The considerable flexibility of the parent cryptand should be restricted by the presence of the benzene rings in cryptand An2.2.1. Although cryptand 2.2.1 complexed all three metals in the solid-state, the stability constants are higher for Na⁺ and Co²⁺ (5.4 for both) in comparison to K⁺ (<2.5).²² This suggests that cryptand 2.2.1 is more suited for the smaller cations Na⁺ (0.97 Å) and Co²⁺ (0.72 Å) in contrast to the larger K⁺ (1.33 Å).²³ The N...N nonbonding distance of 4.72 Å of An2.2.1 is close to the corresponding value for the Na-2.2.1 cryptate (4.944 Å). Because these distances are

similar, it would seem likely that cryptand An2.2.1 will be the right size to accommodate cations such as Na^+ (0.97 Å) and Cd^{2+} (0.97 Å).²³

The ^1H spectrum shown in Figure 4-17 has a large number of peaks due to the six inequivalent sets of alkyl protons.

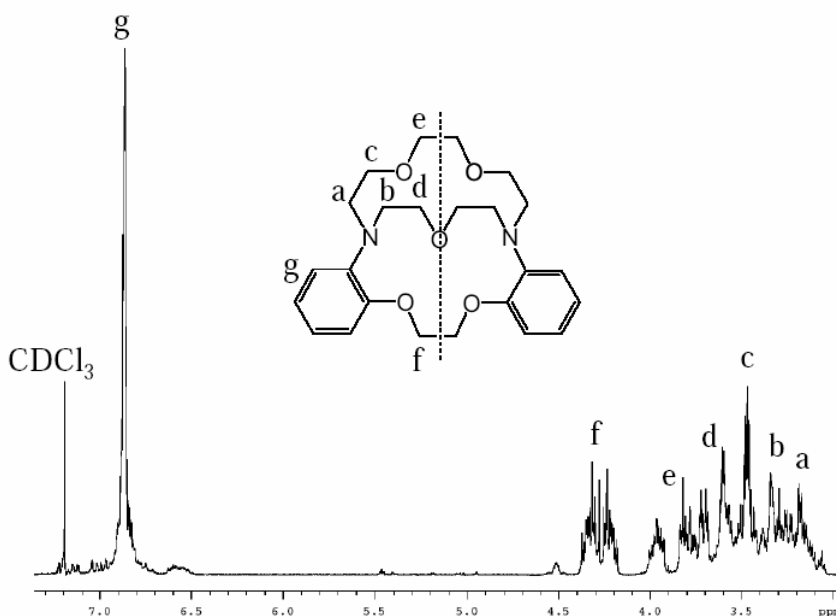


Figure 4-17. ^1H NMR peak assignment for An2.2.1, (**16**), in CDCl_3 .

The methylene protons in cryptands shown in Figure 4-18 consist of sets of alkyl protons coupled to each other located between either nitrogens or oxygens (X and Z).¹⁷ The identity of the donor atoms X and Z (nitrogen or oxygen) will determine if the chemical shifts of the sets of alkyl protons are similar ($X = Z$) or if they are different ($X \neq Z$).¹⁷ Because cryptands have restricted rotation around C-C bonds, the system is described as an AA'XX' system and a difference exists between the coupling constant of proton H_a to H_x and H_a to $\text{H}_{x'}$.¹⁷ Therefore, protons H_a and $\text{H}_{a'}$ are chemically equivalent but not magnetically equivalent.²⁴ This type of system has a very complex spectra but if the protons were equivalent and the bridge was more mobile the system would most likely

have a spectra with two triplets.¹⁷ Protons H_a and $H_{a'}$, located next to nitrogen atoms ($X = N$), are distinguishable from the other sets of alkyl protons because there are less sets than those that are next to oxygen atoms and because they are shifted further upfield.

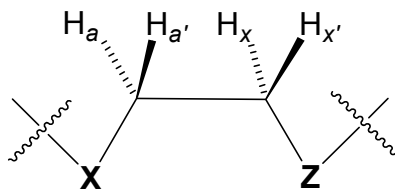


Figure 4-18. Methylene protons in cryptands.

In Cryptand An2.2.1 the right and left halves of the cryptand are equivalent because there are a total of six sets of alkyl protons ($AA'XX'$ system) and two of the sets are located upfield. The proton assignments shown in Figure 4-17 were made possible by the COSY correlation of proton b to d. Protons a and b are upfield because of their position next to the nitrogen while f is the farthest downfield of the methylene protons due to the ether environment next to the benzene rings. The aromatic protons (g) can not be resolved from this spectrum.

The carbon 13 spectrum is divided into four sections: quarternary carbons (1, 6), aromatic carbons (2-5), carbons next to ether groups (7, 9, 10, 12) and carbons next to the amines (8, 11) as seen in Figure 4-19. An impurity is located at ~ 63 ppm. An HMBC peak from carbon 1 to proton a provided the information to distinguish the quarternary carbons from each other. Carbons 2-5 have distinct signals but the chemical shifts for the attached protons could not be resolved (as shown in Figure 4-17). Therefore, these carbons (2-5) could not be assigned.

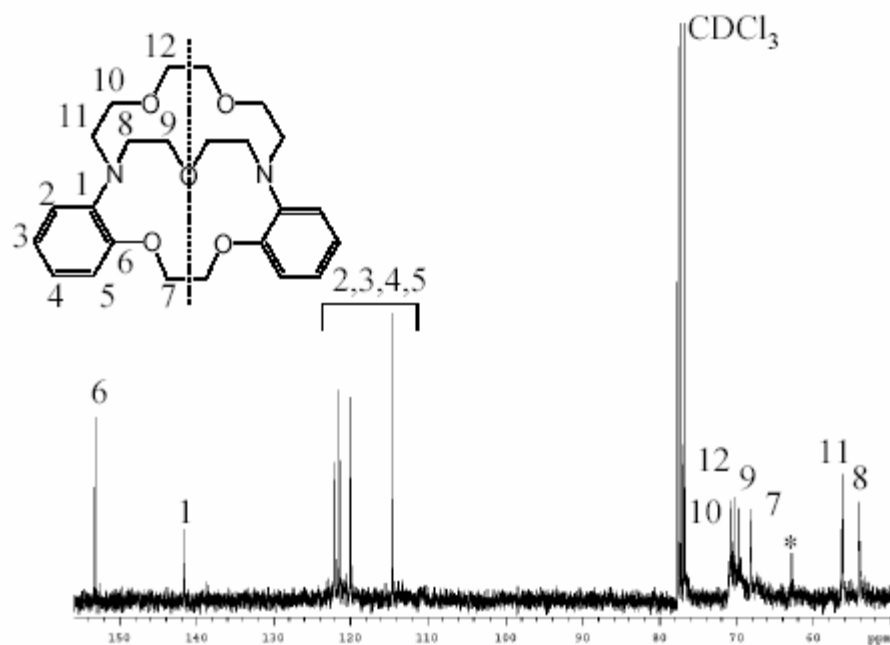


Figure 4-19. ^{13}C NMR peak assignment for An2.2.1, (**16**), in CDCl_3 .

The HSQC spectrum of An2.2.1 is shown in Figure 4-20. The HSQC identified the carbon to hydrogen one-bond connections. The inset in Figure 4-20 shows the aromatic portion of the spectra. The HSQC spectrum reveals that one of the six sets have coupling constants that overlap and therefore show up as one spot at ~ 3.5 ppm.

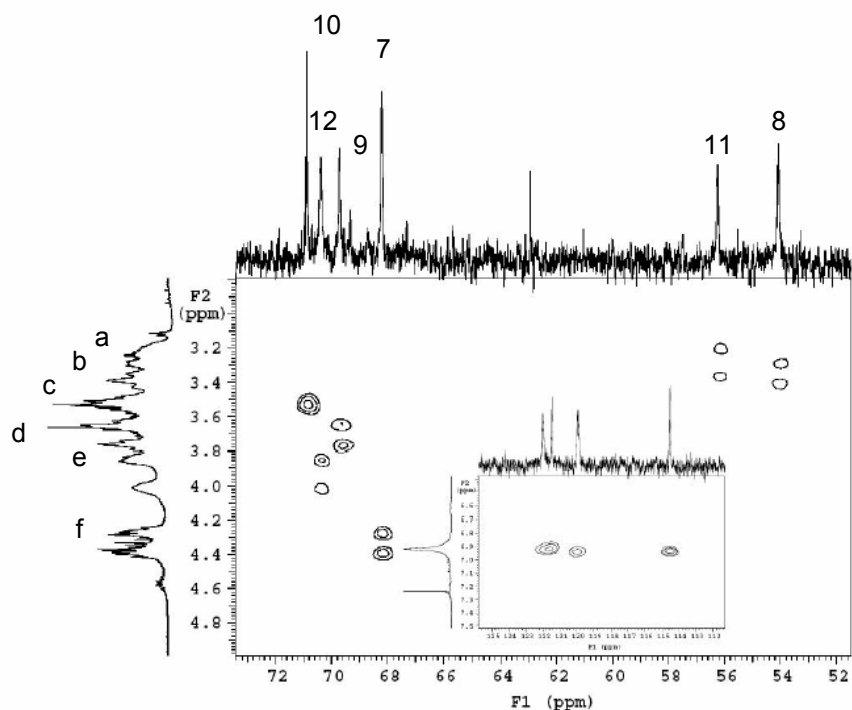


Figure 4-20. HSQC of An2.2.1, (16), in CDCl_3 .

The solid-state structure of An2.2.2 is shown in Figure 4-21 and has a more spherical cavity compared to An2.2.1. The cavity has an $\text{N}\cdots\text{N}$ nonbonding distance of 5.417 Å and the comparable oxygen to oxygen nonbonding distances for O1-O3A, O1-O2A, O2-O2A, and O3-O3A are 4.620 Å, 5.810 Å, 4.754 Å and 6.240 Å, respectively. The later distance is caused by the exodentate orientation of donor atoms O3 and O3A. The other six donor atoms (N1, N1A, O1, O1A, O2, and O2A) are pointing towards the cavity. In contrast, the parent cryptand 2.2.2 has a much longer $\text{N}\cdots\text{N}$ nonbonding distance of 6.871 Å and the oxygen to oxygen distances on the different chains range from 3.745 Å to 4.697 Å.²⁵ The torsion angle for the O-C-C-O group containing O1, O1A is -62.4° . The comparable angles in the alkyl bridges are -81.8° for O2A, O3 and O2, O3A.

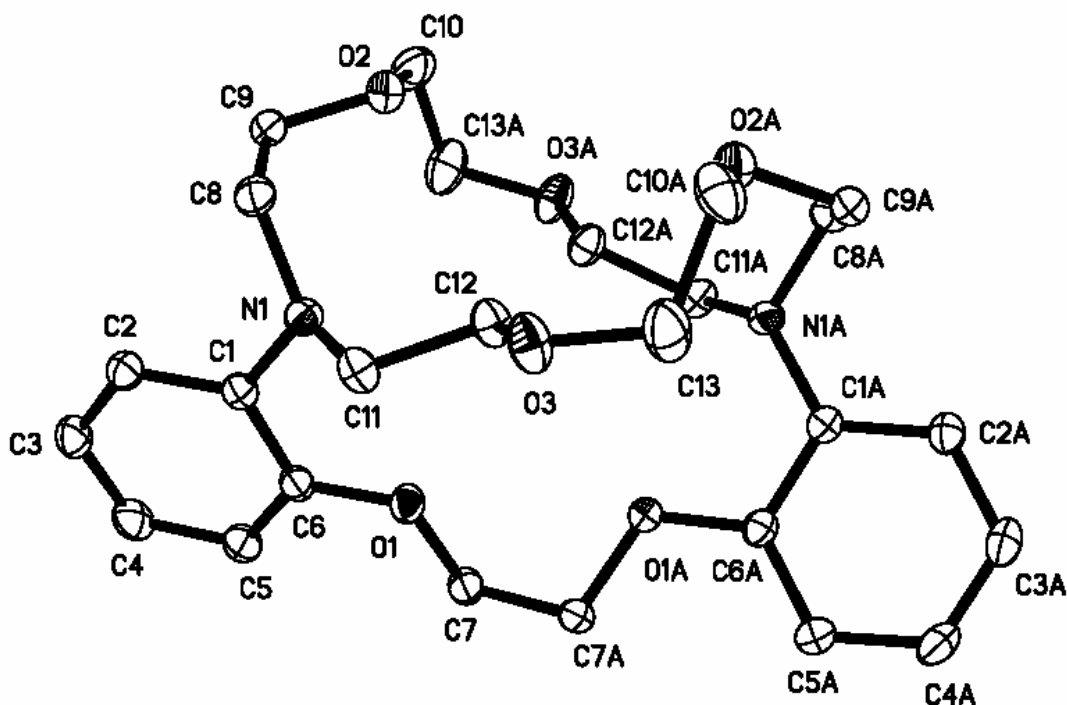


Figure 4-21. X-ray crystal structure of An2.2.2, (19).

Least-squares calculations for the benzene rings 1 (C1-C6) and 2 (C1-C6A) show the carbon atoms are planar with average deviations of 0.0071 for both. The dihedral angle between the least-squares planes of the benzene rings is 44.5°. This angle is similar to that of An2.2.1 (43.9°) and reveals a consistent orientation due to the presence of the benzene rings.

The ^1H NMR of An2.2.2 in Figure 4-22 shows the peak assignment for each proton group. The ^1H NMR has only four sets of alkyl protons (AA'XX' system) with one set located upfield. These assignments agree with those reported for a derivative of An2.2.2 with a methyl group *para* to the nitrogen on one of the benzene rings.²⁶

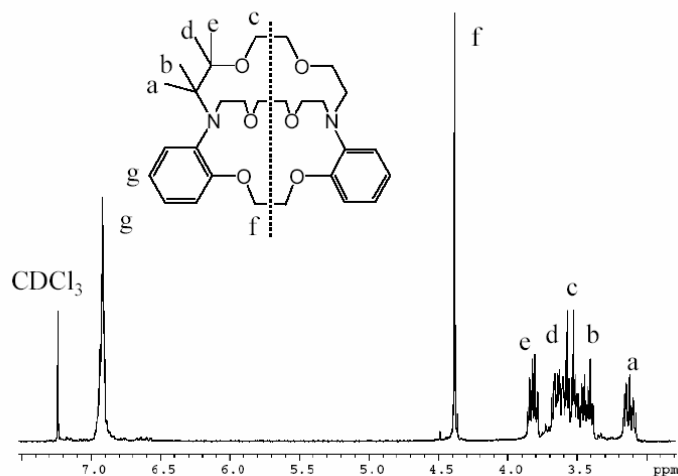


Figure 4-22. ^1H NMR peak assignment for An2.2.2, (**19**), in CDCl_3 .

The carbon 13 spectrum for An2.2.2 is divided into four sections: quarternary carbons (1, 6), aromatic carbons (2-5), carbons next to ether groups (7, 9, 10) and a carbon next to an amine (8) as seen in Figure 4-23. There are total of ten distinct carbon signals and only four are alkyl carbon signals. This indicates that the left and right halves of the molecule are equivalent as well as the alkyl bridges (Figs. 4-22, 4-23).

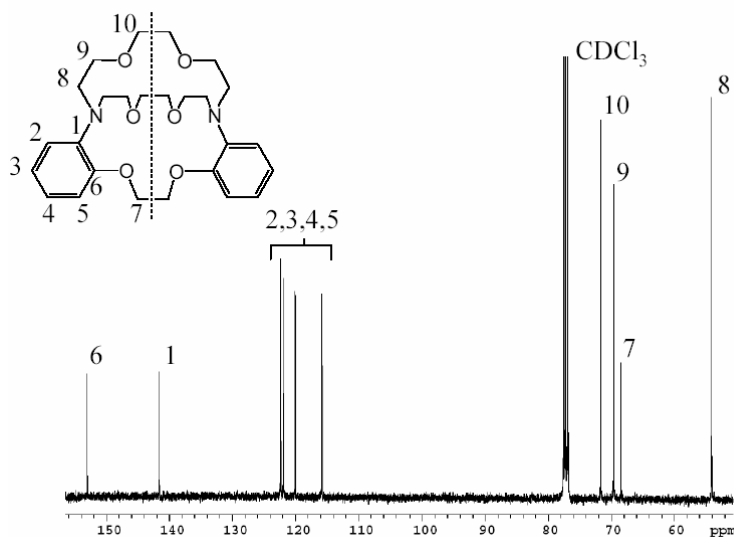


Figure 4-23. ^{13}C NMR peak assignment for An2.2.2, (**19**) in CDCl_3 .

The HSQC spectrum of An2.2.2 is shown in Figure 4-24. The inset in Figure 4-24 shows the aromatic portion of the spectra with the hydrogens (6.9-7.0 ppm) being unresolved similar to the case for An2.2.1. Due to the symmetry of An2.2.2, there is only one signal for a carbon next to a nitrogen donor atom (C8) and the HSQC shows a direct connection to the most upfield hydrogen sets H_a, H_b. The singlet methylene proton (4.4 ppm,) farthest downfield is connected to the most upfield carbon signal in the group of ether carbons.

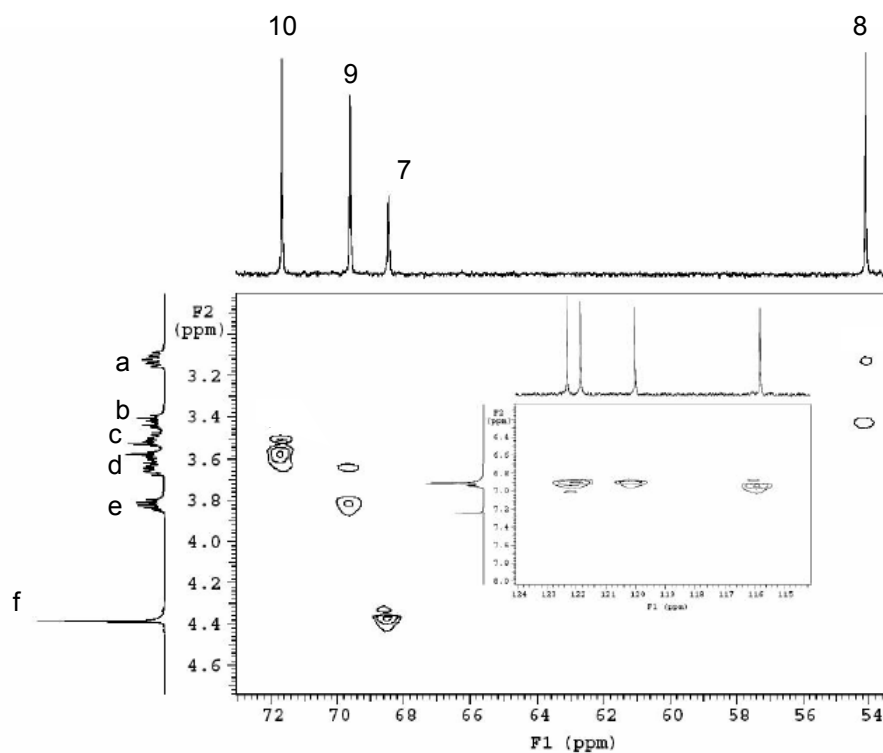


Figure 4-24. HSQC of An2.2.2, (**19**), in CDCl₃.

The HSQC also provides information showing which hydrogen atoms are connected to the same carbon. The HSQC showed that protons a and b as well as protons d and e are linked to the carbon atoms C8 and C9, respectively. Carbons 7 and 10 are only linked to one set of protons each. The HMBC peaks of carbon 6 to proton f and

carbon 1 to proton a allowed for the distinction between the quarternary carbons 1 and 6. The aromatic carbons (2-5) cannot be assigned because the protons on the aromatic ring cannot be resolved. Carbons 8 and 9 were assigned to the same bridge because of an HMBC correlation between carbon 9 and proton a. Carbon 10 had HMBC correlations to protons d and e, but not to protons a or b. An HMBC correlation between carbon 6 and proton f provided the information needed to assign the protons f and c to their respective positions.

Cryptand An3.1.1.3 is the 2 + 2 cycloaddition product obtained from the attempt to synthesize cryptand An3.1.1 by the high-dilution method. Although the product was not deliberately made, it has properties of interest that are significantly different from those of cryptands An2.2.1, An2.2.2, and An3.1.1. Several groups²⁷⁻²⁹ have prepared macrotricyclic compounds similar to An3.1.1.3 and they are shown in Figure 4-25.

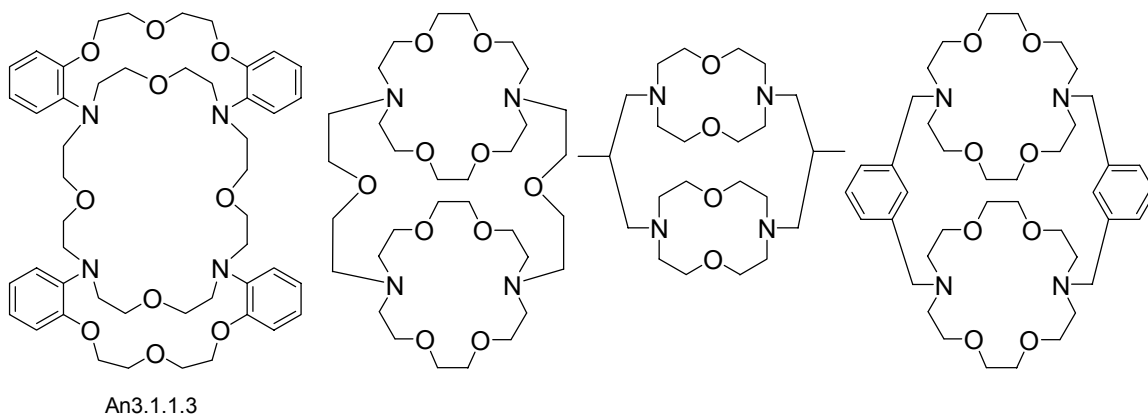


Figure 4-25. An3.1.1.3, (21), and other macrotricyclic cryptands.

Cylindrical macrotricyclic compounds are composed of two rings and two bridges.²⁷ The cryptands reported in the literature have symmetric bridges within the monocyclic rings, while the bridges linking the monocyclic rings differ from those in the monocycles. In cryptand An3.1.1.3, the bridges within the monocyclic rings are

asymmetric and the bridges linking the monocyclic rings are identical to the smaller bridge of each monocycle. Because An3.1.1.3 has two distinct receptor sites, it has the potential to accommodate multiple guests in comparison to a single guest as expected for cryptands An2.2.1, An2.2.2, and An3.1.1. Cylindrical cryptands have been reported to form inclusion complexes with $^+\text{H}_3\text{N}-(\text{CH}_2)_n-\text{NH}_3^+$ dications of various chain lengths ($n = 3-12$)³⁰, binuclear complexes that contain two metal cations³¹, and cascade complexes which are made up of an anion bridging two coordinated metals³². The solid-state structure of An3.1.1.3 is shown in Figure 4-26 and confirms that there are three different binding regions present for the cylindrical cryptand. These include the two 18-membered rings (cavity 1: N1, N4, O1, O2, O3, O10; cavity 3: N2, N3, O4, O5, O6, O8) and a 24-membered ring that forms a central cavity (cavity 2: N1, N2, N3, N4, O7, O8, O9, O10). The donor atoms O1, O2, and O3 are endodentate towards cavity 1, donor atoms O4, O5, and O6 are endodentate towards cavity 3, and donor atoms N1, N2, N3, and N4 are endodentate towards cavity 2. Donor atoms O7, O8, O9, and O10 are exodentate with respect to all three cavities. The monocycles that make up cavities 1 and 3 are virtually the same size with N \cdots N nonbonding distances for N1 \cdots N4 and N2 \cdots N3 of 7.203 Å and 7.232 Å, respectively. The O \cdots O nonbonding distances 4.402 Å for O2 \cdots O10 and 4.333 Å for O5 \cdots O8 also support this claim. The 24-membered central cavity has an oblong shape characterized by O \cdots O nonbonding distances of 10.022 Å for O7 \cdots O9 and 5.464 Å for O8 \cdots O10 and N \cdots N nonbonding distances for N1 \cdots N3 and N2 \cdots N4 of 10.667 Å and 7.781 Å, respectively.

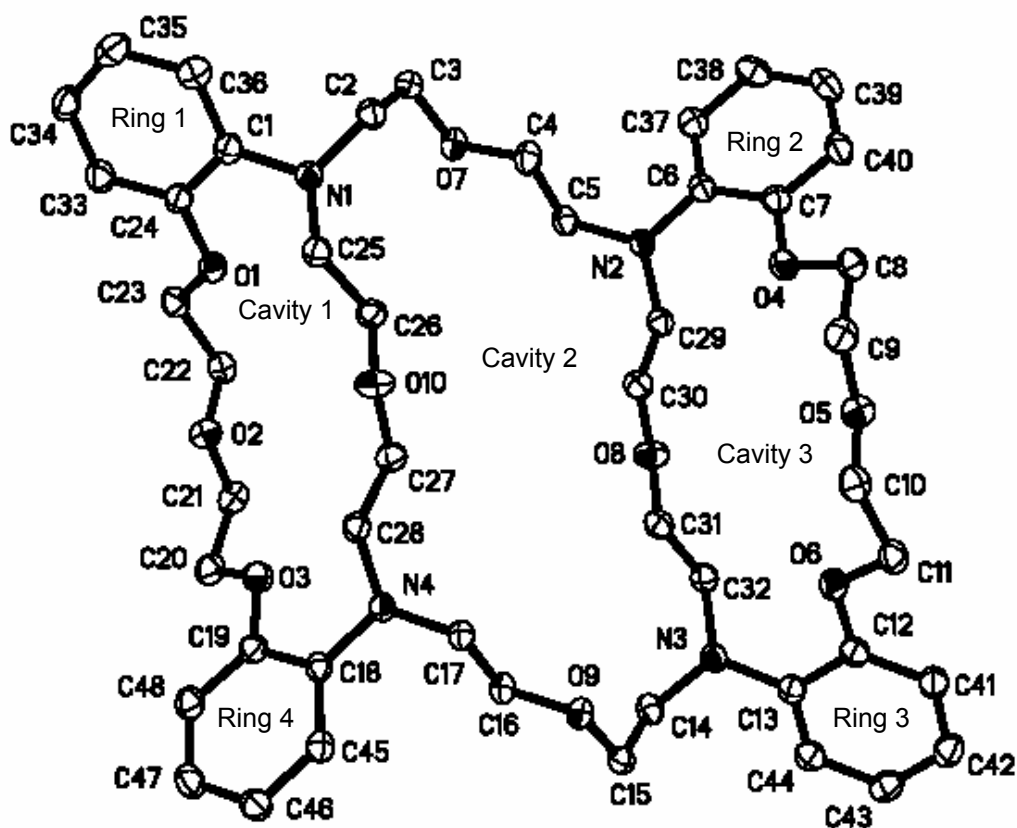


Figure 4-26. X-ray crystal structure of An3.1.1.3, (21).

Figure 4-27 shows cryptand An3.1.1.3 from a different view in order to see the arrangement of the benzene rings. The benzene rings are orientated in an x-shaped arrangement. Least-squares calculations for the benzene rings 1 (C1, C24, C33-C36), 2 (C6, C7, C37-C40), 3 (C12, C13, C41-C44), and 4 (C18, C19, C45-C48) show the carbon atoms are planar with average deviations of 0.0061 Å, 0.0179 Å, 0.0052 Å, and 0.0145 Å, respectively. The dihedral angles between the benzene rings for cavities 1 (ring 1 and 4) and 3 (ring 2 and 3) are 60.1° and 55.8°, respectively. The benzene rings of cavities 1 and 3 diagonal from each other (rings 1 and 3; rings 2 and 4) are virtually on the same plane evidenced by dihedral angles of 6.7° between benzene rings 1 and 3 and 4.7° between benzene rings 2 and 4.

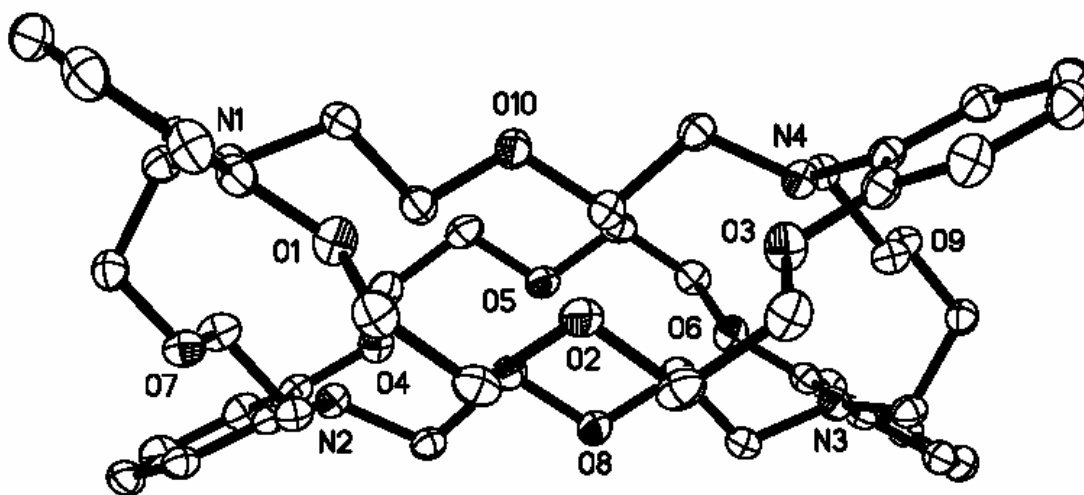


Figure 4-27. X-ray crystal structure of An3.1.1.3, (21), viewed along O2-O5 axis.

Figure 4-28 shows cryptand An3.1.1.3 from another view so the arrangement of the three cavities is visible. From this perspective, cavity 1 and cavity 3 are orientated below and above cavity 2, respectively. The overall shape of the molecule is comparable to a flight of steps.

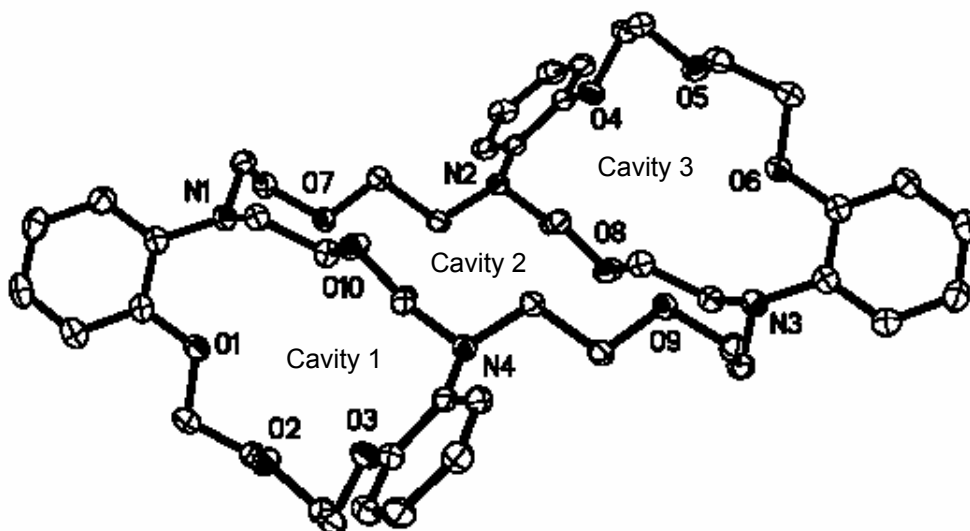


Figure 4-28. X-ray crystal structure of An3.1.1.3, (21), viewed along N2-N4 axis.

The ESI⁺-MS spectra of An3.1.1.3 is shown in Figure 4-29. The m/z ratios of 429.2 and 429.7 are indicative of the molecular ion peak (M) and the M + 1 isotope peak for An3.1.1.3 (integer mass = 856). The molecular weight is divided by two because the ligand is doubly protonated. This does not occur for the cryptands An2.2.1, An2.2.2, or An3.1.1 because the presence of two protons is not electrostatically favorable. The presence of two nitrogens separated by ~10 Å allows the cryptand to become doubly protonated.

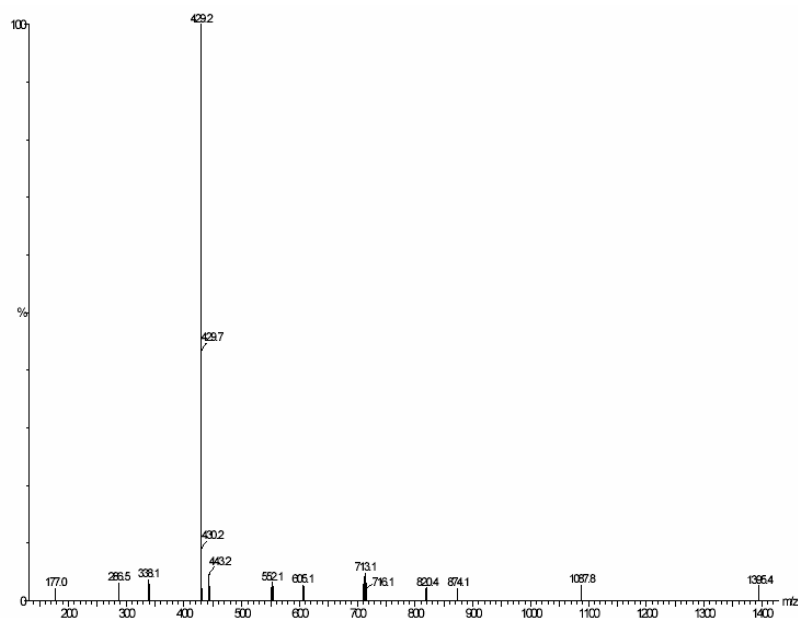


Figure 4-29. ESI⁺-MS of An3.1.1.3, (**21**).

The full characterization of **22** (An3.1.1*), the bicyclic diamide precursor of cryptand An3.1.1, was completed to validate the production of the desired 1 + 1 cycloaddition product in the high-dilution reaction. Conditions were changed from the previous high dilution reaction that yielded exclusively the 2 + 2 cycloaddition product in an attempt to shift the reaction to favor 1 + 1 cycloaddition. The modified procedure

gave the previous product, An3.1.1.3*, that was confirmed by X-ray crystallography unit cell measurements, and An3.1.1*. The X-ray structure in Figure 4-30 confirms the formula and structure of the bicyclic diamide An3.1.1*. A related diamide without the benzene rings has been made but the carbonyl groups are on the bridge containing three ether oxygens.³³ Least-squares calculations for the benzene rings 1 (C1-C6) and 2 (C19-C24) show the carbon atoms are planar with average deviations of 0.0025 Å and 0.0048 Å, respectively. The dihedral angle between the least-squares planes of the benzene rings is 48.0°. The dihedral angles between the least-squares planes of the benzene rings vary significantly among the other bicyclic diamides An2.2.1* (21.9° and 27.6°), An2.1.2* (34.3°), and An2.2.2* (137.9°).

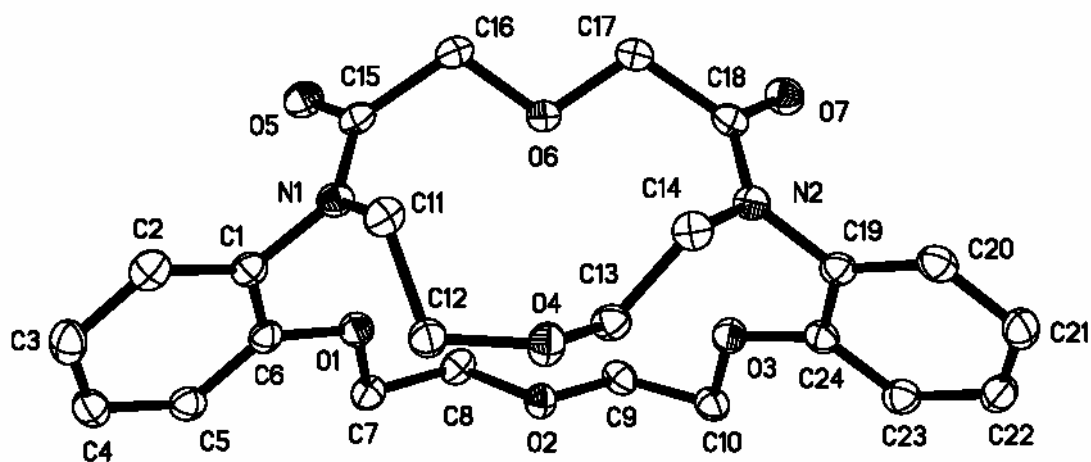


Figure 4-30. X-ray crystal structure of An3.1.1*, (22).

The numbering scheme for An3.1.1* used to describe the NMR results is shown in Figure 4-31. NMR experiments performed at room temperature gave complex spectra with a large number of peaks, many of them being very broad. The complexity of the spectra was a result of the inequivalent sets of alkyl protons (AA'XX' system) as previously described. This was due, in part, to additional conformational restrictions that

were imposed by the amide moieties.^{17,34} All NMR experiments were conducted at 58° C in an attempt to resolve the broad peaks. Even though the temperature was increased, the methylene protons were still inequivalent for four (H8, H9, H10, H12) out of the five sets (H7). NOESY experiments for H2, H4, and H5 show correlation peaks to H9, nothing, and H7, respectively. The distances between these protons found in the solid-state are in good agreement with the limit of detection (~ 4 Å) for NOESY experiments.¹⁷ In the solid-state, proton H2 has distances from H9 and H9' of 2.47 Å and 3.78 Å, respectively and H5 is 2.17 Å and 2.36 Å from protons H7 and H7', respectively.

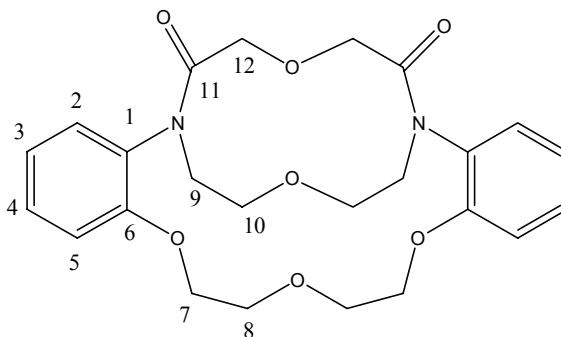


Figure 4-31. NMR numbering scheme for An3.1.1*, (**22**).

Table 4-11 shows the chemical shifts and peak assignments from the ¹H, ¹³C, and 2D NMR experiments. The aromatic protons have chemical shift values from 6.96 - 7.25 ppm. This is distinctly different from the monocycle, An3.1* where H2 is shifted significantly (~1.2 ppm) downfield because of deshielding from the carbonyl oxygens. In the solid-state structure of An3.1*, each amide moiety and adjacent benzene ring are nearly co-planar (14.3°, 17.1°) and the H2 distances from the adjacent carbonyl oxygens are between 2.29 Å and 2.40 Å. For An3.1.1*, the H2 protons are not deshielded by the carbonyl oxygens evidenced by the normal chemical shift. In the solid-state, the distances between the protons (H2 and H20) and the carbonyl oxygens (O5 and O7) have

distances of 3.70 Å and 3.80 Å, respectively, and the dihedral angles between the planes defined by the benzene ring and the adjacent four-atom amide group are 104.0° and 99.0°, respectively.

Table 4-11. NMR peak assignments for An3.1.1*, (**22**) at 58 °C in CDCl₃.

C	δ C (ppm)	H	δ H (ppm)	COSY	HSQC	HMBC
1	131.34					H2, H3, H5
2	128.04	2	7.09	H3, H5	H2	H4
3	121.58	3	6.96	H2, H4	H3	H5
4	128.68	4	7.25	H3, H5	H4	H2
5	114.12	5	6.96	H2, H4	H5	H3
6	154.73					H2, H4, H5
7	69.05	7	4.17	H8, H8'	H7	
8	70.12	8	3.85	H8', H7	H8, H8'	H8'
		8'	3.96	H8		
9	50.85	9	3.71	H9', H10	H9, H9'	
		9'	4.44	H10, H9		
10	68.49	10	3.66	H9, H9', H10	H10, H10'	H9', H10
		10'	3.83	H10		
11	168.78					H12
12	71.94	12	4.39	H12'	H12, H12'	H12
		12'	4.52	H12		

III. Structures of Cryptate Complexes

The determination of crystal structures for cryptate complexes will show if the metal is encapsulated in the ligand in the solid-state, identify the donor atoms that are coordinated to the metal ion, and reveal if the metal ion is coordinated to any anion donor atoms. Comparison between the solid-state structure of the free cryptand and metal ion cryptates for $\text{An}2.2.2 \cdot \text{K}^+ \cdot \text{ClO}_4^-$, $\text{An}2.2.2 \cdot \text{Pb}^{2+} \cdot (\text{NCS}^-)_2$, and $2.2_{\text{B}}.2_{\text{B}} \cdot \text{Pb}^{2+} \cdot \text{NCS}^-$ will show conformational changes that occur as a result of metal ion complexation. Structural changes upon complexation of the cryptand $\text{An}2.2.2$ to form the cryptate $\text{An}2.2.2 \cdot \text{K}^+ \cdot \text{ClO}_4^-$ will be compared with that of $2.2.2$ to form cryptate $2.2.2 \cdot \text{K}^+$.^{25,35} The cryptates $2.2_{\text{B}}.2_{\text{B}} \cdot \text{Pb}^{2+} \cdot \text{NCS}^-$, $2.2.2 \cdot \text{Pb}^{2+} \cdot \text{NCS}^- \cdot \text{SCN}^-$ and $2_{\text{N}}2_{\text{N}}2_{\text{N}} \cdot \text{Pb}^{2+}$ will be compared to establish trends associated with the ligands.³⁶ Cryptands $2.2.2$, $2.2_{\text{B}}.2_{\text{B}}$, and $2_{\text{N}}2_{\text{N}}2_{\text{N}}$ are shown in Figure 4-32.

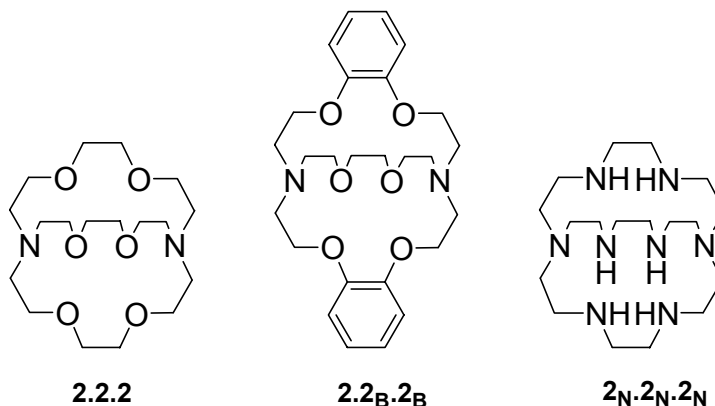


Figure 4-32. Cryptands $2.2.2$, $2.2_{\text{B}}.2_{\text{B}}$, and $2_{\text{N}}2_{\text{N}}2_{\text{N}}$.

The solid-state structure of $\text{An}2.2.2 \cdot \text{K}^+ \cdot \text{ClO}_4^-$ is shown in Figures 4-33 and 4-34. The potassium cation is located inside the cryptand cavity coordinated to all eight donor atoms (N1, N2, O1, O2, O3, O4, O5, and O6) of cryptand $\text{An}2.2.2$ and to two oxygen atoms from a perchlorate anion (O1A and O2A) for a total coordination number of 10.

The average metal ion donor atom distances for cryptand An2.2.2 are 2.80 Å for K-O, which is slightly shorter in comparison to the average distance of 2.96 Å for K-N. The K-O metal-donor atom distances range from 2.71-2.95 Å while the range for K-N is 2.94-2.98 Å. The distance between perchlorate anion oxygen atoms and potassium are longer than those from the ligand with distances of 3.08 Å and 3.10 Å for O1A and O2A, respectively.

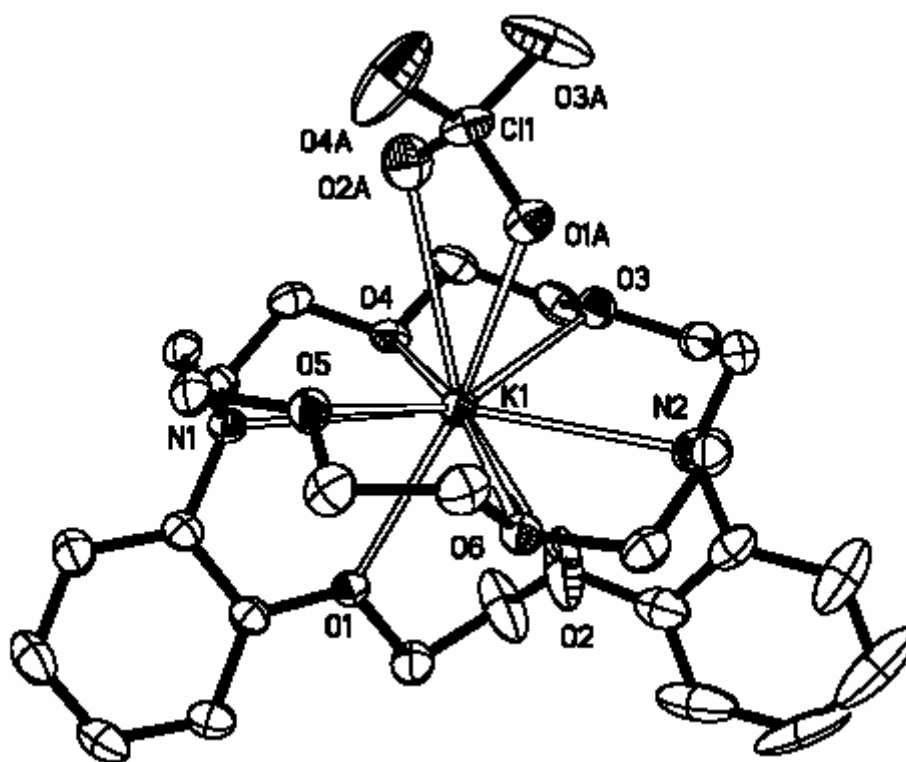


Figure 4-33. X-ray crystal structure of An2.2.2·K⁺·ClO₄⁻.

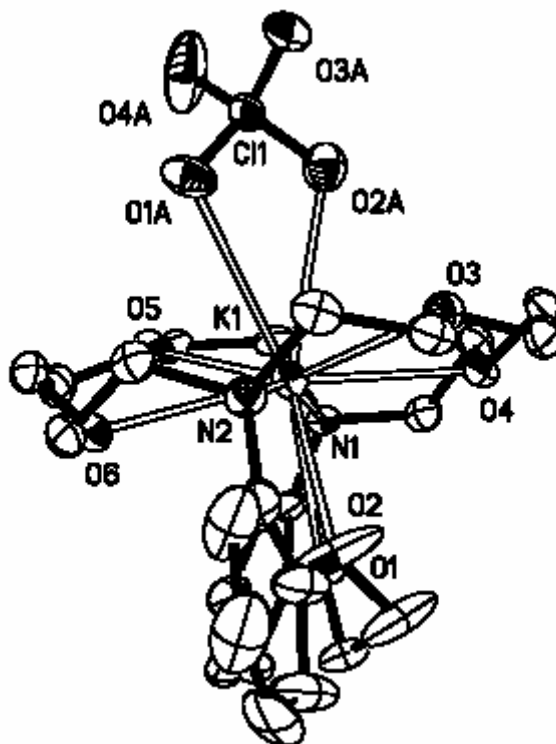


Figure 4-34. X-ray crystal structure of $\text{An}_{2.2.2} \cdot \text{K}^+ \cdot \text{ClO}_4^-$ viewed along N1-N2 axis.

Figure 4-35 shows the metal center and coordination geometry of $\text{An}_{2.2.2} \cdot \text{K}^+ \cdot \text{ClO}_4^-$. Least-squares calculations show that a plane is defined by N1, O3, O4, and K1 with an average deviation of 0.0581 Å. A second least-squares plane exists involving the metal (K1) and anion atoms (O1A, O2A, Cl1) with an average deviation of 0.0119 Å. The dihedral angle between these two planes is 80.8°. Least-squares calculations for benzene rings 1 (C1-C6) and 2 (C9-C14) in $\text{An}_{2.2.2} \cdot \text{K}^+ \cdot \text{ClO}_4^-$ show that the average deviations of the carbon atom from the calculated planes are 0.0083 Å and 0.0241 Å, respectively. The dihedral angle between the least-squares planes of the benzene rings undergoes very little change from 44.5° in $\text{An}_{2.2.2}$ to 42.1° in $\text{An}_{2.2.2} \cdot \text{K}^+ \cdot \text{ClO}_4^-$.

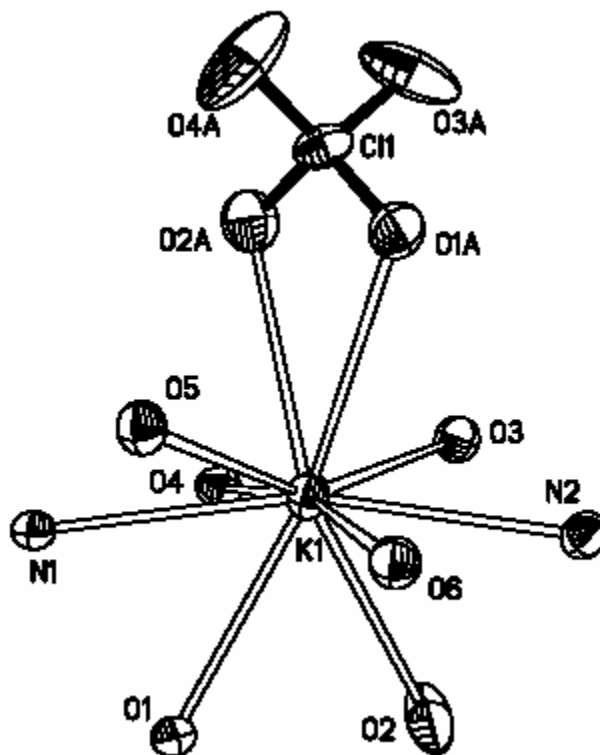


Figure 4-35. Metal center and coordination geometry of $\text{An2.2.2}\cdot\text{K}^+\cdot\text{ClO}_4^-$.

The O-C-C-O torsion angles for the potassium cryptate complex are very similar for the oxygen atom pairs O5-O6, O3-O4, and O1-O2 with angles of -66.0° (2), -67.8° (2), and 63.9° (3), respectively. Cryptand An2.2.2 has O-C-C-O torsion angles of -81.8° (O2A, O3; O2, O3A) and -62.4° (O1, O1A). The latter correspond to oxygen atoms O1 and O2 as shown in Figures 4-33 - 4-35. The three atom angle ($\angle\text{N-M-N}$) between the nitrogen bridgeheads and the metal ion is $164.79(5)^\circ$. The cryptand cavity of An2.2.2 expands in size to accommodate the metal ion (K^+) evident by the increase in $\text{N}\cdots\text{N}$ non-bonding distance from 5.417 \AA to 5.870 \AA . The exodentate donor atoms (O3 and O3A) from cryptand An2.2.2 have rotated to endodentate positions in $\text{An2.2.2}\cdot\text{K}^+\cdot\text{ClO}_4^-$. This oxygen atom pair is indistinguishable in $\text{An2.2.2}\cdot\text{K}^+\cdot\text{ClO}_4^-$ and therefore could be atoms O6 and O4 or O3 and O5. Figure 4-36 shows the packing diagram of $\text{An2.2.2}\cdot\text{K}^+\cdot\text{ClO}_4^-$.

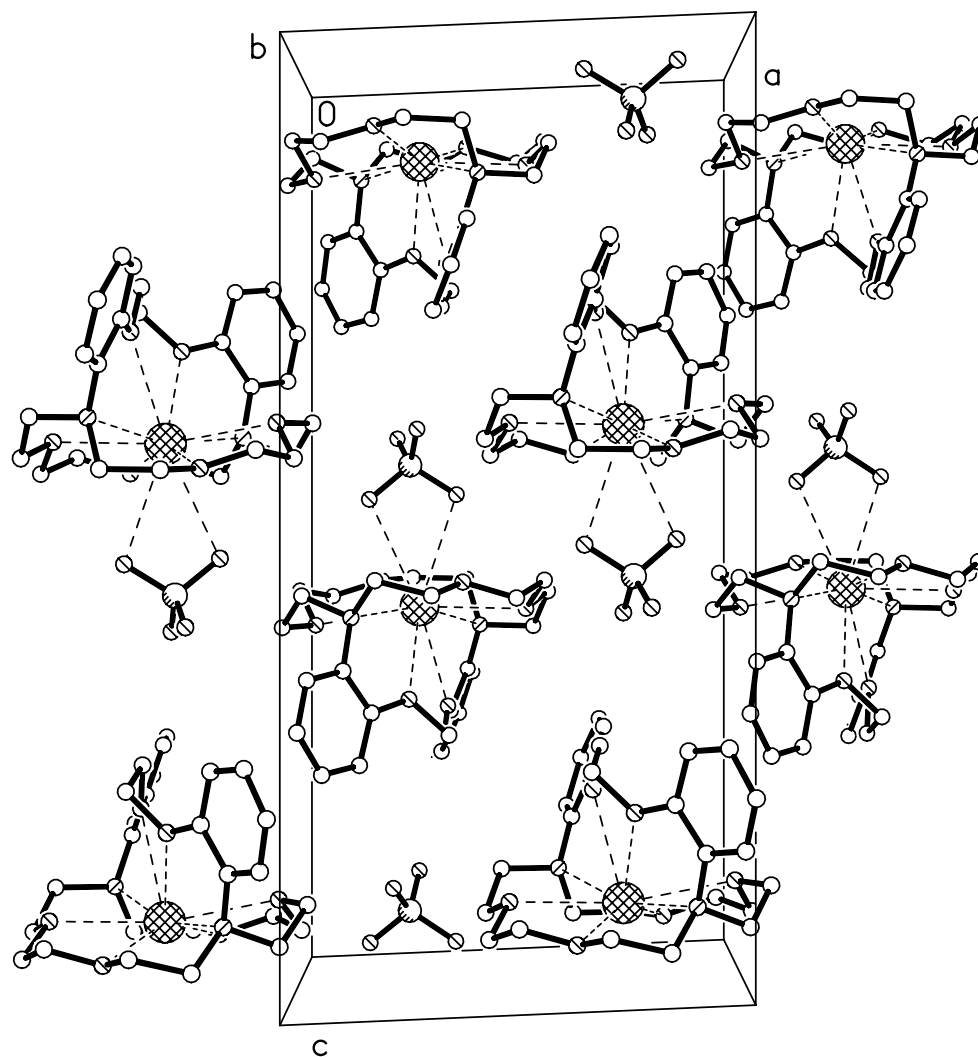


Figure 4-36. Packing diagram of $\text{An}2.2.2 \cdot \text{K}^+ \cdot \text{ClO}_4^-$.

In comparison to the parent cryptand 2.2.2 and the cryptate $2.2.2 \cdot \text{K}^+$, the conformational changes of cryptand An2.2.2 to accommodate the potassium ion seem relatively small. The $\text{N} \cdots \text{N}$ non-bonding distance for cryptand 2.2.2 changes from 6.87 Å to 5.75 Å for $2.2.2 \cdot \text{K}^+$ and the average values of the O-C-C-O torsion angles change from 177° to 51° .^{25,35} The three atom angle ($\angle \text{N-M-N}$) between the nitrogen bridgeheads and the metal ion is linear (180.0°) for $2.2.2 \cdot \text{K}^+$.³⁵

A mass spectrum of $\text{An2.2.2}\cdot\text{K}^+\cdot\text{ClO}_4^-$ cryptate was obtained by dissolving a crystal from the X-ray structure analysis batch in methanol. The ESI^+ -MS spectrum is shown in Figure 4-37. The molecular mass of free ligand An2.2.2 (472) is not seen, because the ligand is fully complexed by sodium ($m/z = 495$) and potassium ($m/z = 511$).

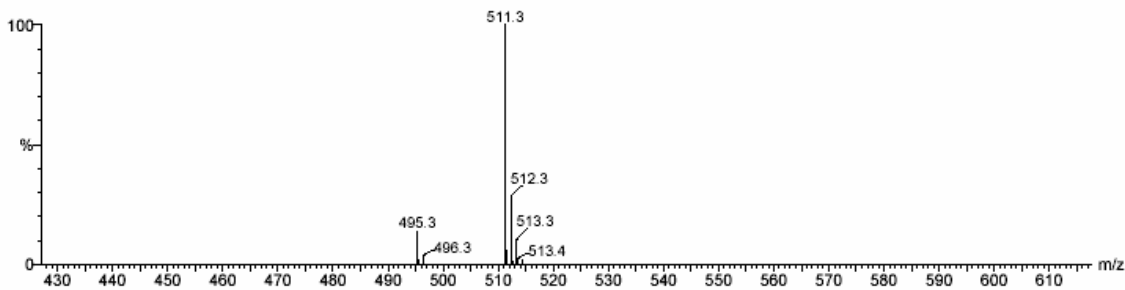


Figure 4-37. ESI^+ -MS of $\text{An2.2.2}\cdot\text{K}^+\cdot\text{ClO}_4^-$ in MeOH.

The identification of molecular ion peaks is also substantiated by comparing the relative intensities of the peaks in the mass spectrum with the relative abundance of the isotopes of potassium. The potassium isotopes are listed in Table 4-12.

Table 4-12. Relative abundance of the elemental isotopes of potassium.²³

Metal	Isotope	Relative Abundance
K	39	93.10
	40	0.02
	41	6.88

Figure 4-38 shows a portion of the ESI^+ -MS of a solution of the $\text{An2.2.2}\cdot\text{K}^+\cdot\text{ClO}_4^-$ crystal (bottom) along with a calculated isotopic distribution model for this complex (top). There is excellent agreement for the position (m/z) and relative intensities to confirm the sample as the $\text{An2.2.2}\cdot\text{K}^+$ complex.

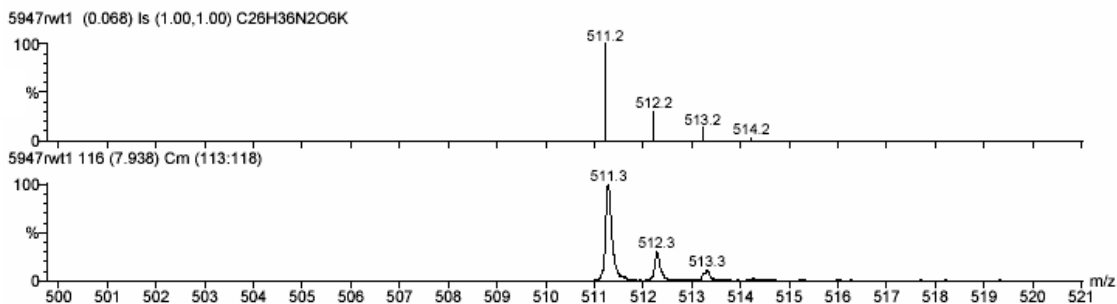


Figure 4-38. Calculated isotope distribution (top) and ESI⁺-MS of An2.2.2·K⁺ (bottom).

A crystal of An2.2.2·Pb²⁺·(NCS⁻)₂ was subjected to X-ray diffraction analysis. Unfortunately, the molecule was found to sit on a crystallographic mirror plane. Because the molecule does not possess a mirror plane, all atoms (except the metal) were disordered and refined with an occupancy factor of 0.5. Restraints on the positional and displacement parameters of all carbon, nitrogen, and oxygen atoms were required. Therefore, the atom positions, bond distances, and bond angles are not reliable. However, the general features of the compound could be discerned from a structure based on the average positions of the atoms. This solid-state structure of An2.2.2·Pb²⁺·(NCS⁻)₂ is shown in Figure 4-39 and the packing diagram is shown in Figure 4-40. The lead cation is centrally located inside the cryptand cavity with all eight donor atoms (N1, N10, O4, O7, O13, O16, O21, and O24) having an endodentate orientation suitable for coordination to the metal ion. In addition, the nitrogen atoms from two thiocyanate anions (N35 and N37) appear to be coordinated giving a total coordination number of 10.

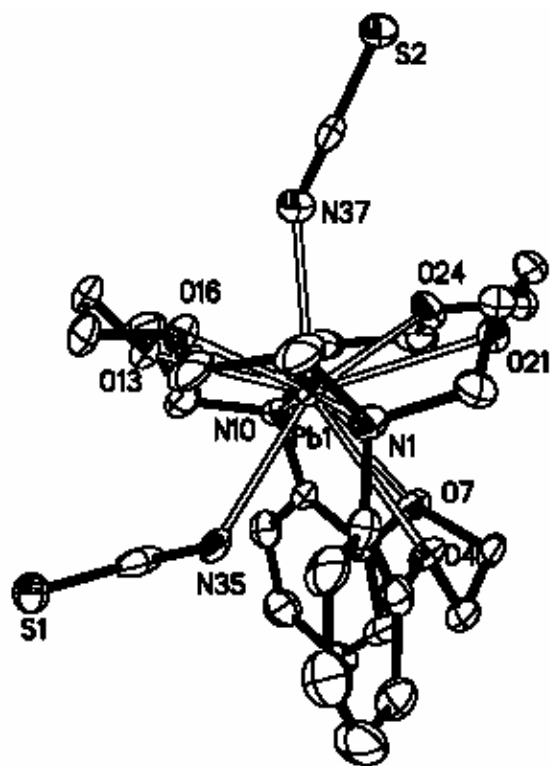


Figure 4-39. X-ray crystal structure of $\text{An}2.2.2 \cdot \text{Pb}^{2+} \cdot (\text{NCS}^-)_2$ viewed along N1-N10 axis.

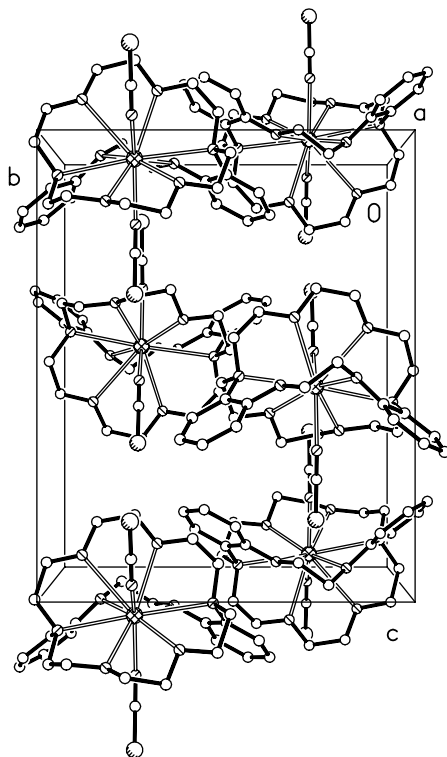


Figure 4-40. Packing diagram of $\text{An}2.2.2 \cdot \text{Pb}^{2+} \cdot (\text{NCS}^-)_2$.

The atom positions, distances, and angles in cryptate $\text{An2.2.2}\cdot\text{Pb}^{2+}\cdot(\text{NCS}^-)_2$ are not reliable and cannot be compared with the other cryptates or cryptand An2.2.2 because all atoms (except the metal) were disordered in the solid-state structure. The parent cryptand $2.2.2$ and cryptate $2.2.2\cdot\text{Pb}^{2+}\cdot\text{NCS}^-\cdot\text{SCN}^-$ show considerable differences in structure such as average torsion angles (177° vs. 59°) and the $\text{N}\cdots\text{N}$ non-bonding distance (6.87 \AA vs. 5.76 \AA).^{25,36}

The $\text{An2.2.2}\cdot\text{Pb}^{2+}\cdot(\text{NCS}^-)_2$ complex was characterized using ESI^+ -MS by dissolving a crystal from the sample used for the X-ray structure analysis in methanol. The spectrum is shown in Figure 4-41. The complex has two main peaks contributed by the masses of the singly charged $\text{An2.2.2}\cdot\text{Pb}^{2+}\cdot\text{NCS}^-$ complex ($m/z = 739$) and the doubly charged $\text{An2.2.2}\cdot\text{Pb}^{2+}$ complex ($m/z = 340$). The doubly charged complex is observed centered at $m/z = 340$ because the x-axis for mass spectra is mass/charge ratio ($680/2$).

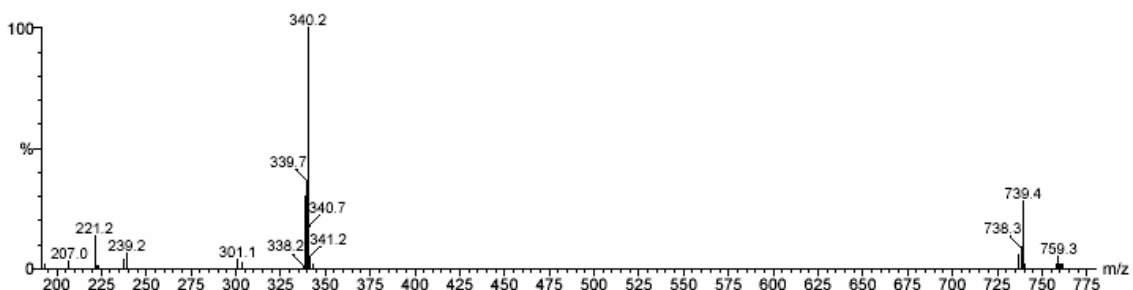


Figure 4-41. ESI^+ -MS of $\text{An2.2.2}\cdot\text{Pb}^{2+}\cdot(\text{NCS}^-)_2$.

Lead has four isotopes, listed in Table 4-13, that provide a distinct pattern for the molecular ion dominated by a $\sim 1:1:2$ signal ratio (^{204}Pb is negligible).

Table 4-13. Relative abundance of the elemental isotopes of lead.²³

Metal	Isotope	Relative Abundance
Pb	204	1.5
	206	23.6
	207	22.6
	208	52.3

The experimental (bottom) and calculated (top) mass spectra for the peaks associated with $\text{An2.2.2}\cdot\text{Pb}^{2+}$ and $\text{An2.2.2}\cdot\text{Pb}^{2+}\cdot\text{NCS}^-$ are shown in Figures 4-42 and 4-43, respectively. The calculated isotope distribution patterns were obtained from the Mass Lynx software package.³⁷ There is excellent agreement for the position (m/z) and relative intensities for $\text{An2.2.2}\cdot\text{Pb}^{2+}$ ($m/z = 340$) and the $\text{An2.2.2}\cdot\text{Pb}^{2+}\cdot\text{NCS}^-$ ($m/z = 739$) complex.

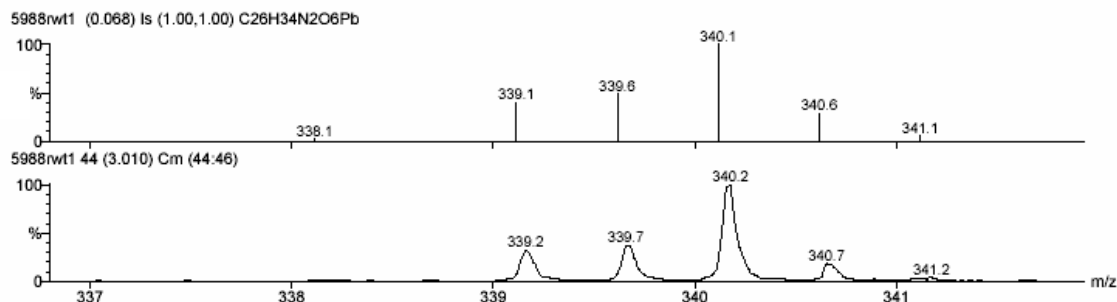


Figure 4-42. Calculated isotope distribution (top) and ESI^+ -MS of $\text{An2.2.2}\cdot\text{Pb}^{2+}$ (bottom).

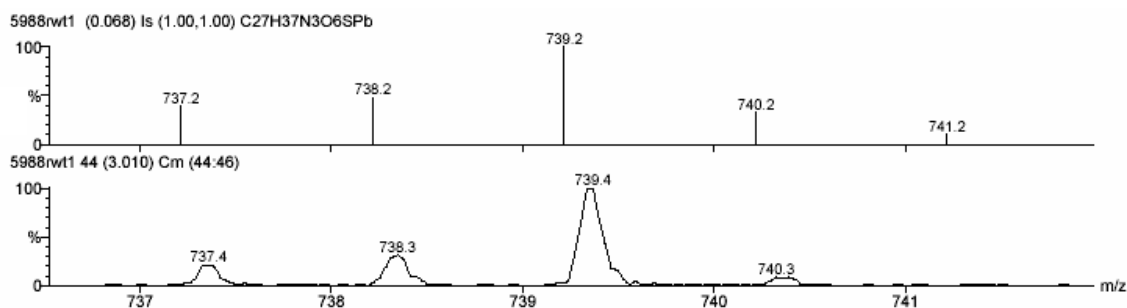


Figure 4-43. Calculated isotope distribution (top) and ESI^+ -MS of $[\text{An2.2.2}\cdot\text{Pb}^{2+}\cdot\text{NCS}]^+$ (bottom).

The X-ray crystal structure of the $2.2_{\text{B}}.2_{\text{B}}\cdot\text{Pb}^{2+}\cdot\text{NCS}^-$ complex was determined to allow comparison with the solid-state structures of the uncomplexed $2.2_{\text{B}}.2_{\text{B}}$ ligand³⁸ and with other lead cryptates $2.2.2\cdot\text{Pb}^{2+}\cdot\text{NCS}^- \cdot \text{SCN}^-$ and $2_{\text{N}}2_{\text{N}}2_{\text{N}}\cdot\text{Pb}^{2+}$.^{36,39} Figures 4-44 and 4-45 show the X-ray structure of $2.2_{\text{B}}.2_{\text{B}}\cdot\text{Pb}^{2+}\cdot\text{NCS}^-$ complex with lead located inside the cavity coordinated to all eight donor atoms of cryptand $2.2_{\text{B}}.2_{\text{B}}$ and to one nitrogen from a thiocyanate anion for a total coordination number of 9.

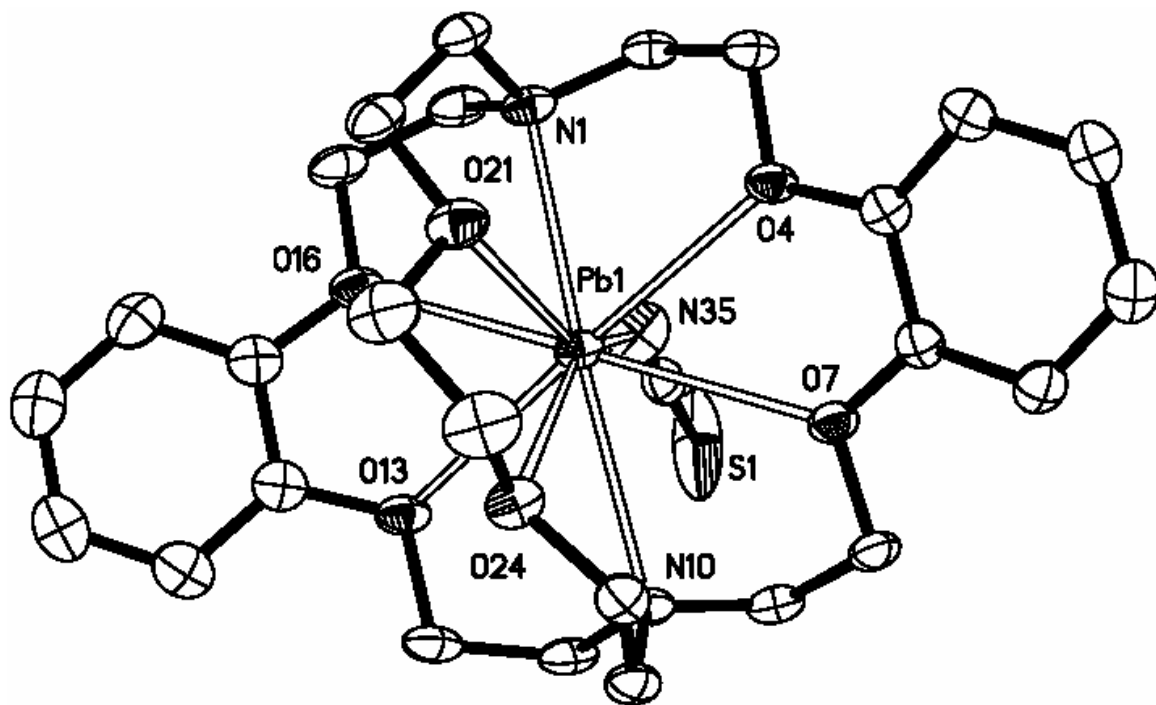


Figure 4-44. X-ray crystal structure of $2.2_{B.2B} \cdot \text{Pb}^{2+} \cdot \text{NCS}^-$.

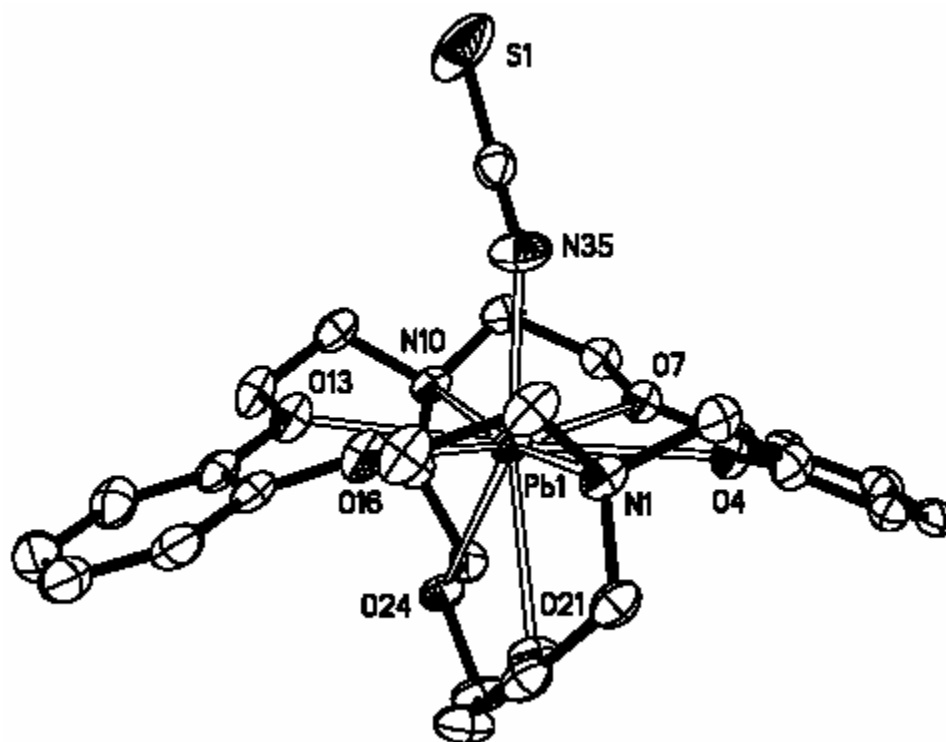


Figure 4-45. X-ray crystal structure of $2.2_{B.2B} \cdot \text{Pb}^{2+} \cdot \text{NCS}^-$ viewed along N1-N10 axis.

The average metal-donor atom distances from cryptand 2.2_B.2_B to the metal for Pb-O and Pb-N are 2.76 Å and 2.77 Å, respectively. The Pb-O and Pb-N metal-donor atom distances range from 2.69-2.83 Å and 2.71-2.83 Å, respectively. The thiocyanate ligand has a shorter bond length with Pb-N = 2.47 Å. Figure 4-46 shows the metal center and coordination geometry of 2.2_B.2_B·Pb²⁺·NCS⁻. Least-squares calculations show that a plane exists between Pb1, O4, O7, O13, O16, N1, and N10 with an average deviation from the plane of 0.0736 Å. The donor atoms from the non-benzo bridge (O21 and O24) are below the plane and the donor atom from the thiocyanate ligand (N35) is above the plane as shown in Figure 4-46. A least-squares calculation of the plane with only the ligand donor atoms of 18-membered dibenzo monocycle (N1, N10, O4, O7, O13, and O16) has an average deviation from the plane of 0.0526 Å, and Pb1 is just below that plane (0.175 Å). Therefore, the 18-membered monocycle of 2.2_B.2_B that includes the benzo bridges adopts an almost flat arrangement in the cryptate 2.2_B.2_B·Pb²⁺·NCS⁻.

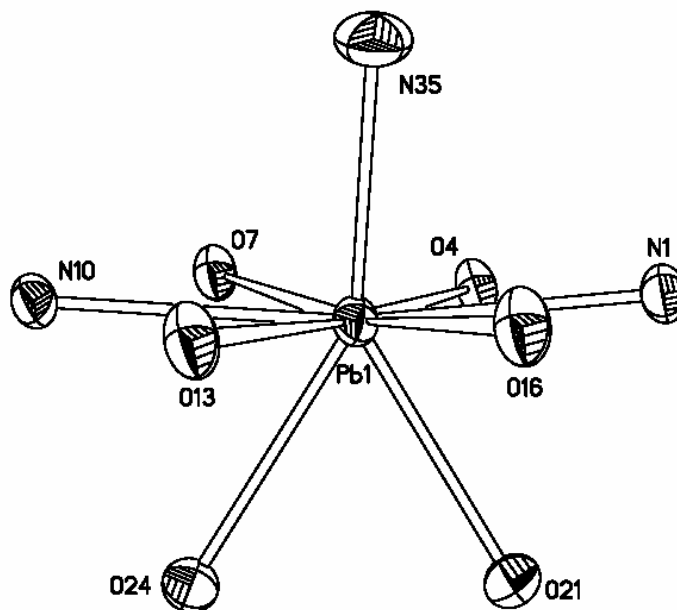


Figure 4-46. Metal center and coordination geometry of 2.2_B.2_B·Pb²⁺·NCS⁻.

Least-squares calculations for benzene rings 1 (C5, C6, C27-C30) and 2 (C14, C15, C31-C34) in $2.2_{\text{B}}.2_{\text{B}}\cdot\text{Pb}^{2+}\cdot\text{NCS}^-$ show that the average deviations of the carbon atom from the calculated planes are 0.0087 Å and 0.0043 Å, respectively. The dihedral angle between the least-squares planes of the benzene rings is 41.1°. The O-C-C-O torsion angle for the non-benzo bridge oxygen pair (O21, O24) is -66.9°, while those for the benzo bridge oxygen pairs (O4, O7) and (O13, O16) are -0.3° and -2.4°, respectively, distinctly different because of the constraint imposed by the benzene rings. The N...N non-bonding distance in $2.2_{\text{B}}.2_{\text{B}}\cdot\text{Pb}^{2+}\cdot\text{NCS}^-$ is 5.522 Å and the three atom angle ($\angle\text{N-M-N}$) between the nitrogen bridgeheads (N1, N10) and the metal ion is 171.26(8)°.

The torsion angles in the uncomplexed ligand $2.2_{\text{B}}.2_{\text{B}}$ do not undergo much alteration upon lead complexation from the comparison of torsion angles between the oxygen pairs of $2.2_{\text{B}}.2_{\text{B}}$ and $2.2_{\text{B}}.2_{\text{B}}\cdot\text{Pb}^{2+}\cdot\text{NCS}^-$ (-4.8°, -6.1°, and 71.4° vs. -0.3°, -2.4°, and -66.9°).³⁸ However, the lone exodentate atom (O24) does change to endodentate orientation. The dihedral angle between the benzene rings in the cryptand $2.2_{\text{B}}.2_{\text{B}}$ changes considerably from 127.9° to 41.1° in the cryptate $2.2_{\text{B}}.2_{\text{B}}\cdot\text{Pb}^{2+}\cdot\text{NCS}^-$ and the N...N non-bonding distance increases from 5.161 Å to 5.522 Å. Figure 4-47 shows the packing diagram for $2.2_{\text{B}}.2_{\text{B}}\cdot\text{Pb}^{2+}\cdot\text{NCS}^-$.

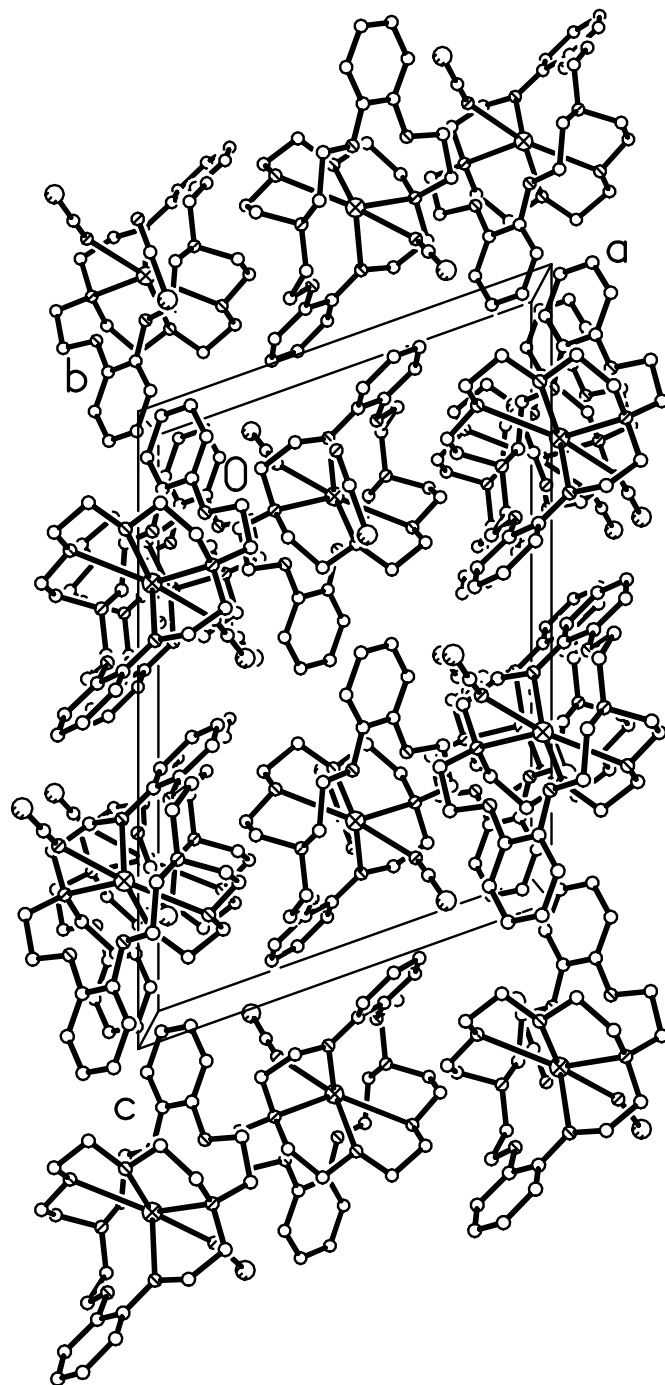


Figure 4-47. Packing diagram for $2.2_{\text{B}}.2_{\text{B}}\cdot\text{Pb}^{2+}\cdot\text{NCS}^{-}$.

The $2.2_{\text{B}}.2_{\text{B}}\cdot\text{Pb}^{2+}\cdot\text{NCS}^{-}$ complex was characterized using ESI⁺-MS by dissolving a crystal from the sample used for the X-ray structure analysis in methanol. The spectrum is shown in Figure 4-48. The mass spectrum is composed of the $2.2_{\text{B}}.2_{\text{B}}\cdot\text{Pb}^{2+}\cdot\text{I}^{-}$ complex

($m/z = 807$), the doubly charged $2.2_B.2_B \cdot Pb^{2+}$ complex ($m/z = 340$), and the $2.2_B.2_B \cdot Na^+$ complex ($m/z = 495$).

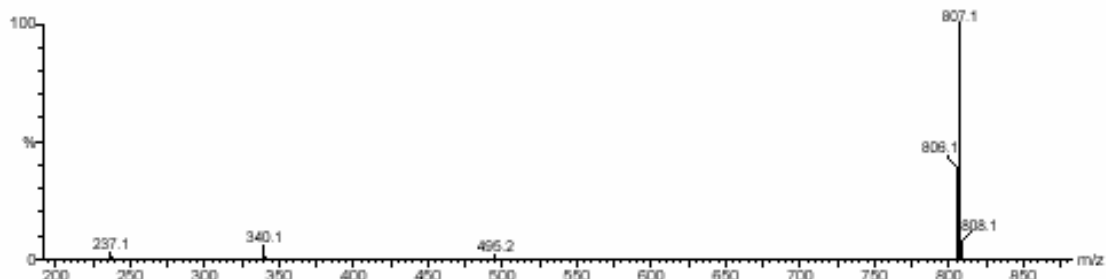


Figure 4-48. ESI⁺-MS of $2.2_B.2_B \cdot Pb^{2+} \cdot NCS^-$ complex.

The experimental (bottom) and calculated (top) mass spectra for the peaks associated with $2.2_B.2_B \cdot Pb^{2+} \cdot I^-$ and $2.2_B.2_B \cdot Pb^{2+}$ are shown in Figures 4-49 and 4-50, respectively.

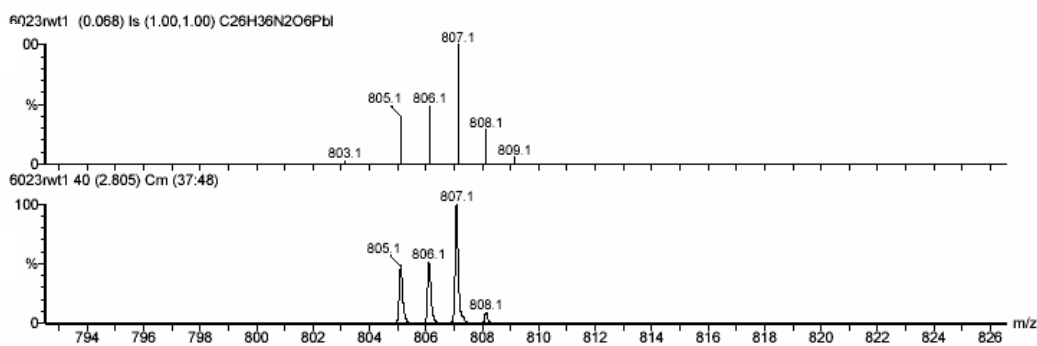


Figure 4-49. Calculated isotope distribution (top) and ESI⁺-MS of $[2.2_B.2_B \cdot Pb^{2+} \cdot I]^+$ (bottom).

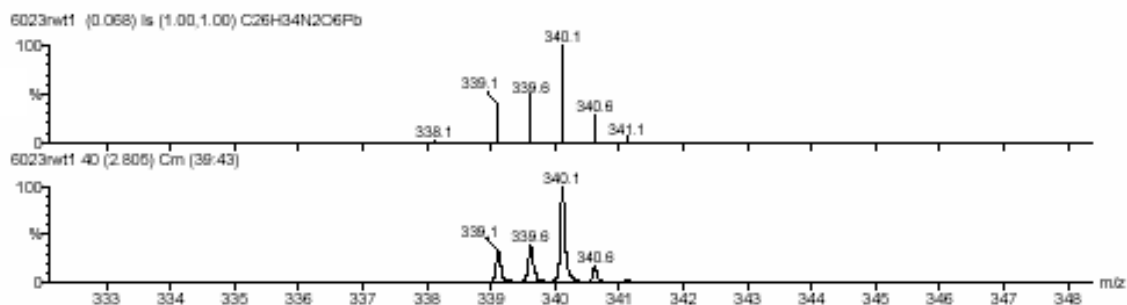


Figure 4-50. Calculated isotope distribution (top) and ESI⁺-MS of 2.2_B.2_B·Pb²⁺ (bottom).

The calculated isotope distribution patterns and the mass total are in good agreement with the mass total for the complexes. CsI is used to calibrate the mass spectra and residual iodide (I⁻, *m/z* = 127) present in the system complexed with the lead cryptate.

Comparison of the solid-state structures of the lead cryptates 2.2_B.2_B·Pb²⁺·NCS⁻, 2.2.2·Pb²⁺·NCS⁻·SCN⁻ and 2_N2_N2_N·Pb²⁺ will reveal if consistent trends exist for the metal complexes. The all nitrogen substituted cryptate 2_N2_N2_N·Pb²⁺ is coordinated to all 8 donor atoms and has four bonds with distances of 2.67-2.74 Å and four with contacts > 2.8 Å, including the two bridgehead nitrogens.³⁹ The three atom angle (∠N-M-N) between the nitrogen bridgeheads and the metal ion is 176.67°.³⁹ Table 4-14 shows the average lead-donor distances, N··N non-bonding distances, and three atom angle (∠N-M-N) between the nitrogen bridgeheads for 2_N2_N2_N·Pb²⁺ and the two lead cryptates previously discussed. The average Pb-O bonds for the oxygen containing cryptates were consistent with each other (~2.8 Å). The average lead to bridgehead nitrogen distance in cryptates 2.2.2·Pb²⁺·NCS⁻·SCN⁻ and 2_N2_N2_N·Pb²⁺ are very similar (2.88 Å, 2.85 Å), and 2.2_B.2_B·Pb²⁺·NCS⁻ is slightly shorter (2.77 Å). The comparisons show that the average lead-oxygen bonds are shorter than the average lead-nitrogen bonds. It also reveals that

lead has the shortest bonds between the nitrogens from the bridging strands in $2_N2_N2_N\cdot\text{Pb}^{2+}$ cryptate and the longest for the nitrogens in $2.2.2\cdot\text{Pb}^{2+}\cdot\text{NCS}^-\cdot\text{SCN}^-$ cryptate. The N \cdots N non-bonding distances for cryptates $2.2.2\cdot\text{Pb}^{2+}\cdot\text{NCS}^-\cdot\text{SCN}^-$ and $2_N2_N2_N\cdot\text{Pb}^{2+}$ are very similar (≤ 0.09 Å), but the distance in $2.2_{\text{B}}.2_{\text{B}}\cdot\text{Pb}^{2+}\cdot\text{NCS}^-$ is considerably (≥ 0.19 Å) shorter. The cryptand that contains benzene rings, $2.2_{\text{B}}.2_{\text{B}}$, results in a solid-state lead cryptate that has a three atom angle ($\angle\text{N-M-N}$) that differs more from linearity in comparison to the other lead cryptates.

Table 4-14. Average lead-donor distances and N \cdots N non-bonding distances for lead cryptates.

	$2.2_{\text{B}}.2_{\text{B}}\cdot\text{Pb}^{2+}$ CN = 9	$2.2.2\cdot\text{Pb}^{2+}$ CN = 10	$2_N2_N2_N\cdot\text{Pb}^{2+}$ CN = 8
Pb-O _{avg} ^a	2.76	2.80	--
Pb-N _{avg} ^a	2.77	2.88	2.70 ^c ; 2.82 ^d ; 2.85 ^e
N \cdots N ^a	5.52	5.76	5.71
$\angle\text{N-M-N}^{\text{b}}$	171.3	174.4	176.7

^aMeasurements are in Å. ^bMeasurements are in °. ^cShort Pb-N bridging strands. ^dLong Pb-N bridging strands. ^eBridgehead Pb-N.

Lead-containing crystal structures from the Cambridge Structural Database (CSD) can be classified as either holodirected (donor atoms distributed evenly) or hemidirected (donor atoms bunched to one side).⁴⁰ The cryptates $2.2_{\text{B}}.2_{\text{B}}\cdot\text{Pb}^{2+}\cdot\text{NCS}^-$, $2.2.2\cdot\text{Pb}^{2+}\cdot\text{NCS}^-\cdot\text{SCN}^-$, and $2_N2_N2_N\cdot\text{Pb}^{2+}$ are all holodirected structures. The Pb-O and Pb-N average bond distances for cryptate $2.2_{\text{B}}.2_{\text{B}}\cdot\text{Pb}^{2+}\cdot\text{NCS}^-$ is longer (≥ 0.15 Å) than the average values of 2.53 (15) Å and 2.62 (11) Å, respectively found in all holodirected divalent lead complexes.⁴¹ However, only 10% of all divalent lead compounds in the CSD have coordination numbers > 8 and bond lengths are likely to increase as the coordination number increases.⁴⁰

IV. Protonation and Metal Complexation Constants for An2.2.1 and An2.2.2

The solution properties of cryptands An2.2.1 and An2.2.2 were investigated to determine the effects of the benzo-substitution on the protonation and metal formation constants. Figure 4-51 shows the changes in absorbance with pH for cryptand An2.2.2. The diprotonated ligand has a peak of maximum absorbance, λ_{max} at 272 nm. As the pH increases, the λ_{max} shifts to a longer wavelength at 278 nm. Two isosbestic points are present from pH 3.0 - 3.4 at 264 nm and 276 nm as shown in Figure 4-52. The presence of an isosbestic point is evidence that only two absorbing components are present. As the pH is increased above 3.4, the isosbestic points are lost. Figure 4-53 is a semi-log plot of the measured absorbance at 284 nm versus a_{H} for An2.2.2. The data were fit to eq 4.1 and the calculated parameters used to construct the solid line are listed in the inset table. The Kaleidagraph data results listed in the tables throughout this work are the output of the data fitting program and are not representative of the correct number of significant figures. The observed absorbance (A_i) depends on the protonation constants K_{H1} and K_{H2} , parameters A_0 , A_1 , and A_2 which are the limiting absorbance values for the unprotonated, monoprotated, and diprotonated species of the ligand, respectively, and the hydrogen ion activity, a_{H} .

$$A_i = \frac{A_2 K_{\text{H1}} K_{\text{H2}} a_{\text{H}}^2 + A_1 K_{\text{H1}} a_{\text{H}} + A_0}{K_{\text{H1}} K_{\text{H2}} a_{\text{H}}^2 + K_{\text{H1}} a_{\text{H}} + 1} \quad (4.1)$$

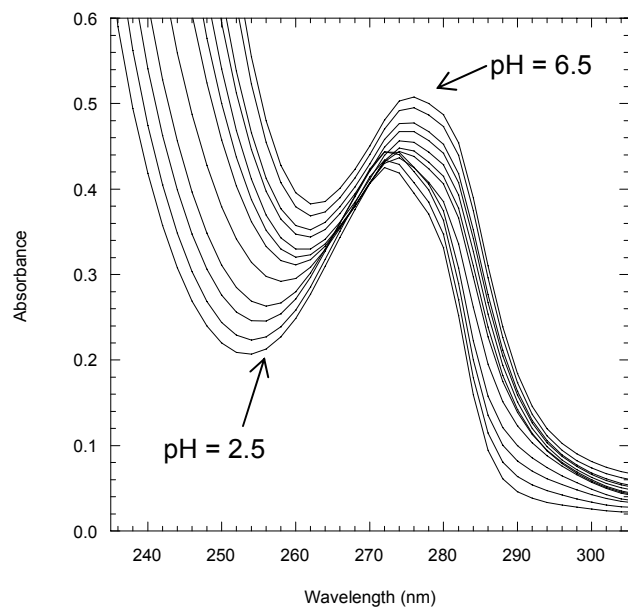


Figure 4-51. Spectra from the titration of 0.13 mM An2.2.2, (**19**), from pH 2.5-6.5. Some spectra have been omitted for clarity.

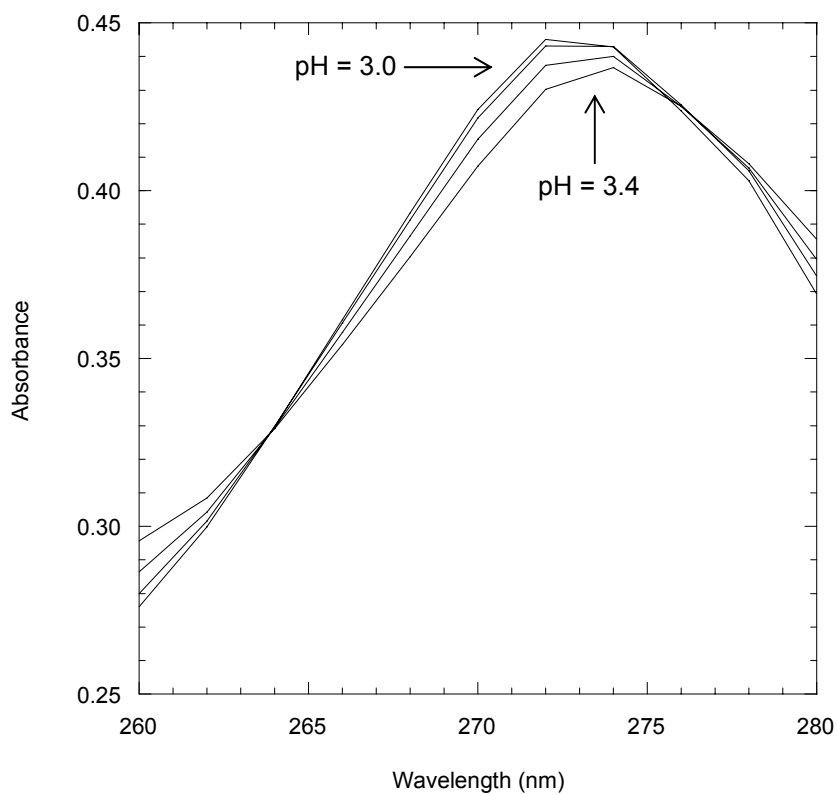


Figure 4-52. Isobestic points for cryptand An2.2.2, (**19**), at 264 nm and 276 nm.

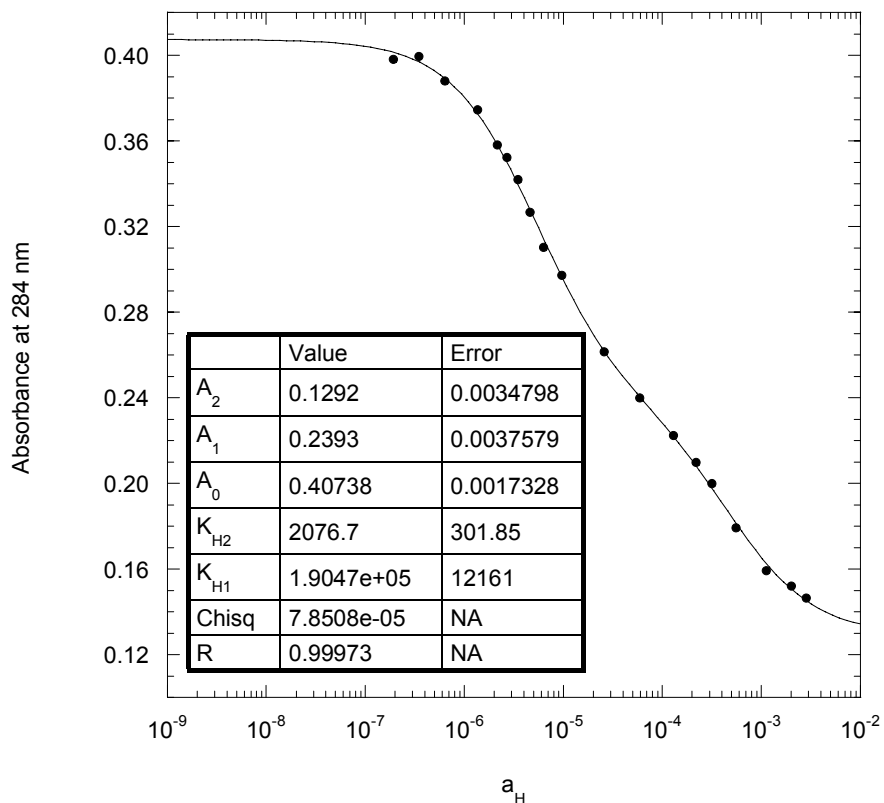


Figure 4-53. Plot of absorbance at 284 nm versus a_H for the titration of An2.2.2, (19), shown in Figure 4-51.

The calculated values for the protonation constants ($\log K_{Hi}$) are listed in Table 4-15. The values obtained using Kaleidagraph are at a specific wavelength listed in the table. Specfit utilizes multi-wavelength data sets to calculate K_{H1} and K_{H2} from a specified portion of the spectrum. For titration data analysis using Specfit in this project, the wavelength range will be 200-400 nm. This 200 nm range is where the absorbing species occur and 100 discrete wavelengths will be measured for this range. Both data fitting programs report error as standard error.

Table 4-15. Protonation constants ($\log K_{\text{Hi}}$) for An2.2.2, (19) in H₂O.

Exp. No.	Method ^a	λ , nm (range)	$\log K_{\text{H1}}$	Error	$\log K_{\text{H2}}$	Error
1	K	284	5.28	0.03	3.32	0.06
1	S	200-400	5.56	0.03	3.41	0.07
2	K	284	5.20	0.05	3.2	0.2
2	S	200-400	5.28	0.04	3.7	0.1
Avg.			5.33	0.16	3.41	0.21

^aK = Kaleidagraph, S = Specfit.

The protonation constants ($\log K_{\text{Hi}}$) for cryptand An2.2.2 are 5.3 ± 0.2 and 3.4 ± 0.2 . A species distribution plot showing the relative concentration (%) of each form of the ligand versus pH, shown in Figure 4-54, was constructed using the program SolEq⁴² and the values of K_{H1} and K_{H2} . The isosbestic points previously discussed are present when $\text{pH} \sim 3.5$, because the solution is made up primarily of the di- and monoprotonated ligand. The isosbestic points are lost as the pH increases because of the presence of the unprotonated ligand. At physiological pH (~ 7), cryptand An2.2.2 is present predominantly (>95%) in the unprotonated form. In contrast, the parent cryptand 2.2.2 is present as a mixture of the di- and monoprotonated species at physiological pH due to the larger values of $\log K_{\text{H1}}$ (9.60) and $\log K_{\text{H2}}$ (7.28).⁴³

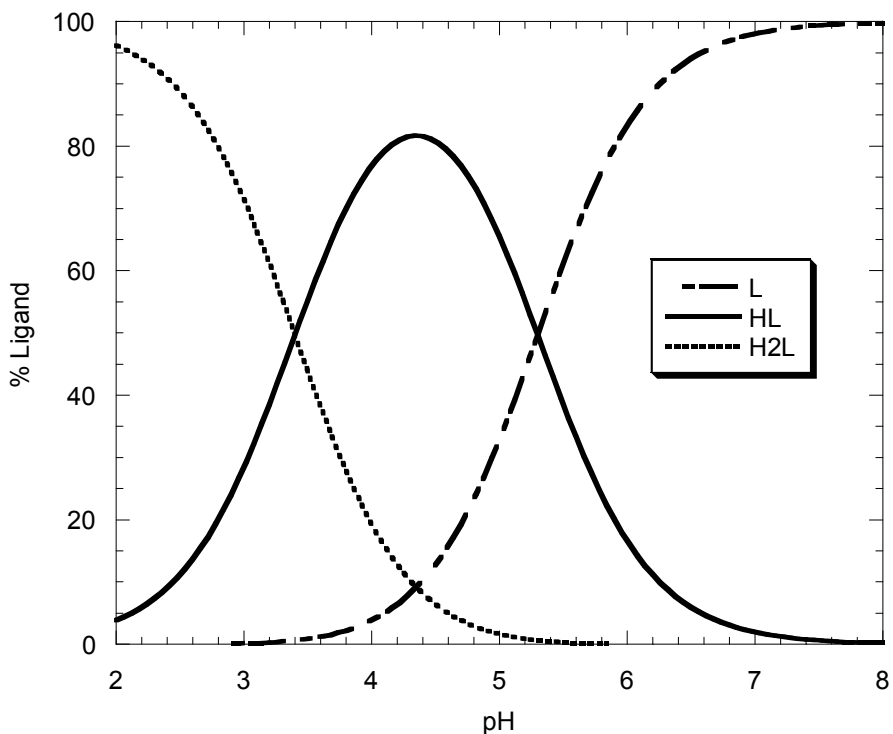


Figure 4-54. Species distribution for An2.2.2, (19).

Figure 4-55 shows the changes in absorbance with pH for cryptand An2.2.1. The diprotonated ligand has a peak of maximum absorbance, λ_{max} , at 272 nm. As the pH increases, λ_{max} shifts to a longer wavelength at 280 nm. Figure 4-56 is a semi-log plot of the measured absorbance at 240 nm versus a_{H} for An2.2.1. The data was fit using eq 4.1 and the calculated values used to construct the solid line are listed in the table (inset).

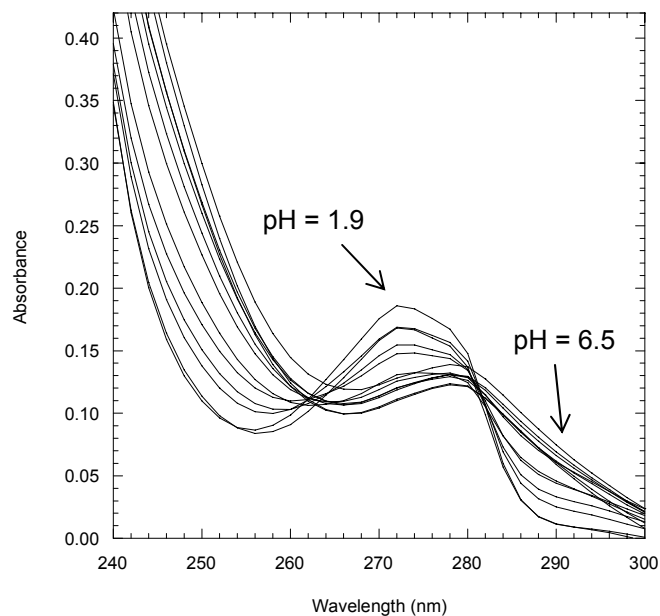


Figure 4-55. Spectra from the titration of 0.072 mM An2.2.1, (16), from pH 1.9-6.5. Some spectra have been omitted for clarity.

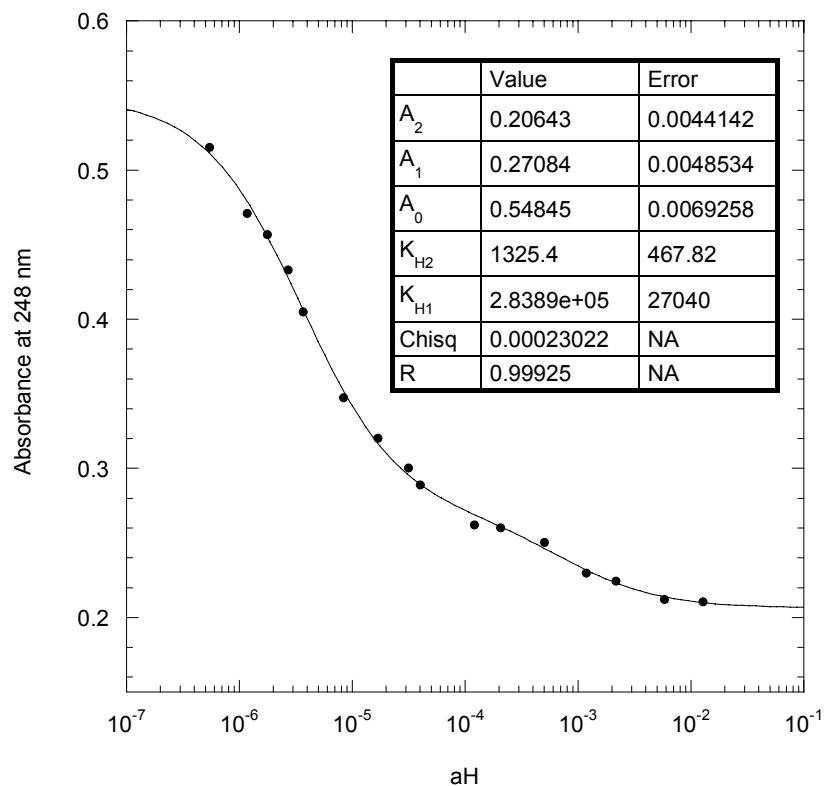


Figure 4-56. Plot of absorbance at 240 nm versus a_H for the titration of An2.2.1, (16), shown in Figure 4-55.

The calculated values for the protonation constants ($\log K_{Hi}$) are listed in Table 4-16. The Kaleidagraph fits are at a specific wavelength listed in the table. A value for K_{H2} was not determined from experiment 1 using Kaleidagraph. Specfit analysis of experiment 1 using the entire spectrum made it possible to obtain K_{H2} .

Table 4-16. Protonation constants ($\log K_{Hi}$) for An2.2.1, (16) in H₂O.

Exp. No.	Method ^a	λ , nm (range)	$\log K_{H1}$	Error	$\log K_{H2}$	Error
1	K	248	5.22	0.02	--	--
1	S	200-400	5.43	0.06	2.8	0.1
2	K	242	5.45	0.04	3.1	0.2
2	S	200-400	5.37	0.09	3.3	0.2
Avg.			5.40	0.10	3.1	0.3

^aK = Kaleidagraph, S = Specfit.

The protonation constants ($\log K_{Hi}$) for cryptand An2.2.1 are 5.4 ± 0.1 and 3.1 ± 0.3 . A species distribution plot of percent ligand versus pH is shown in Figure 4-57. Cryptand An2.2.1 is similar to cryptand An2.2.2 in that the only species present in an appreciable amount at physiological pH is the unprotonated ligand (>95%). The parent cryptand 2.2.1 has $\log K_{H1}$ and K_{H2} values of 10.53 and 7.50, respectively, and is present at physiological pH as a mixture of di- and monoprotonated species.⁴³

The addition of benzene rings in cryptands An2.2.1 and An2.2.2 lowers both K_{Hi} values by ≥ 4 orders of magnitude and also results in protonation constants that are closer together. The protonation constants K_{H1} and K_{H2} for 2.2.1 and 2.2.2 have a difference in magnitude of 3.1 and 2.4 log units, respectively, whereas cryptands An2.2.1 and An2.2.2 differ by 2.3 and 1.9 log units, respectively.

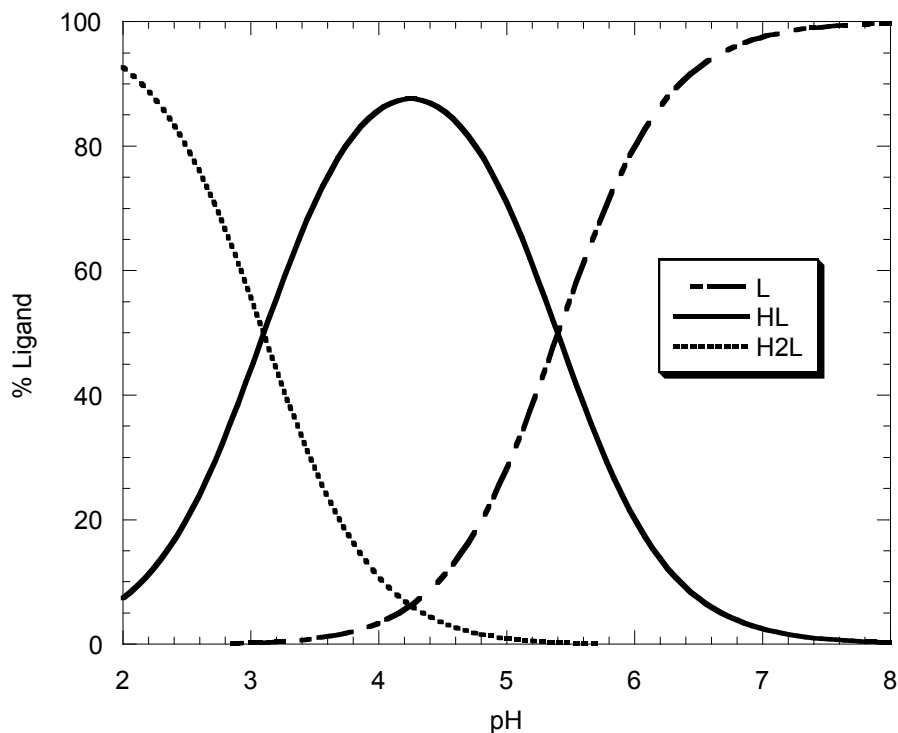


Figure 4-57. Species distribution of An2.2.1, (16).

The spectral properties of cryptand An2.2.2 with sodium, potassium, calcium, strontium, barium, cadmium, and lead were investigated initially at $\text{pH} \geq 7$. The pH was neutral or greater so that the ligand was only present in the unprotonated form. The concentration of metal needed to completely complex the ligand is an indication of how strong of an affinity the ligand has for the metal ions. Plots of the fraction of total absorbance change versus the ratio of metal to ligand concentrations indicate the binding stoichiometry.⁴⁴ The absorbance change (ΔA_i) is the difference between that of the original solution of ligand and a solution containing ligand plus metal ion. The fraction of absorbance change (f) is calculated as the change (ΔA_i) for a given amount of added metal ion divided by the maximum spectral change (ΔA_{tot}). The latter is defined as the difference in absorbance between the ligand solution with no metal ion present (A_L) and

the ligand solution containing the completely formed metal-ligand complex (A_{ML}). These parameters are defined by the following equations:

$$\Delta A_i = |A_L - A_i| \quad (4.2)$$

$$f = \frac{|\Delta A_i|}{|\Delta A_{tot}|} \quad (4.3)$$

$$\Delta A_{tot} = |A_L - A_{ML}| \quad (4.4)$$

The results of these plots will either show a scenario where the fraction of absorbance change stops at 1:1 metal to ligand mole ratio or continues to increase. If no change occurs, then the metal and ligand are completely or nearly completely complexed at 1:1 concentration ratio. If the fraction of absorbance change continues to increase then the metal is bound more weakly and not fully complexed. The spectra for titrations of cryptand An2.2.2 with $Pb(ClO_4)_2$ at pH = 7.0, $BaCl_2$ at pH = 8.2, and $SrCl_2$ at pH = 9.5 in H_2O are shown in Figures 4-58, 4-60, and 4-62, respectively. The plots of the fractional absorbance change at a specific wavelength versus the ratio of metal ion to An2.2.2 for these titrations are shown in Figures 4-59, 4-61, and 4-63, respectively. The plots of fractional absorbance change for each titration indicate that cryptand An2.2.2 binds almost quantitatively with Pb^{2+} , Ba^{2+} , and Sr^{2+} with 1:1 stoichiometry. The formation constants for these metal ligand complexes can be estimated from these plots if the fraction (f) of absorbance change at 1:1 metal to ligand ratio is less than 1.

The fraction (f) of absorbance change at 1:1 metal to ligand ratio is used to estimate the concentration of the metal-ligand complex and then used to estimate the formation constant by using the following equations.

$$ML = f \cdot C_L \quad (4.5)$$

$$M = M_0 - ML \quad (4.6)$$

$$L = L_0 - ML \quad (4.7)$$

$$K_{ML} = \frac{ML}{M \cdot L} \quad (4.8)$$

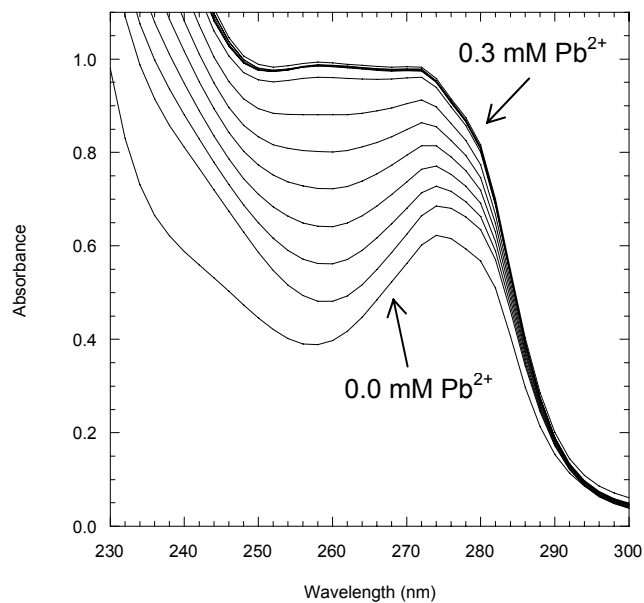


Figure 4-58. Spectra from the titration of 0.15 mM An2.2.2, (19), with lead at pH = 7.0.

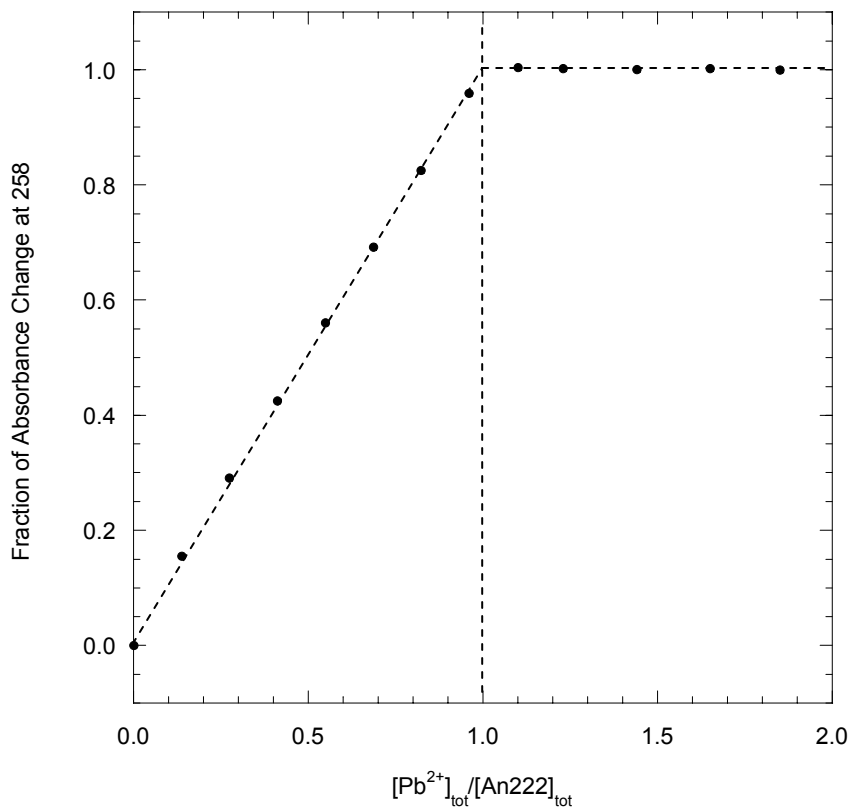


Figure 4-59. Plot of fraction of the absorbance change versus the ratio of total lead to total An2.2.2, (19), concentrations from the titration shown in Figure 4-58.

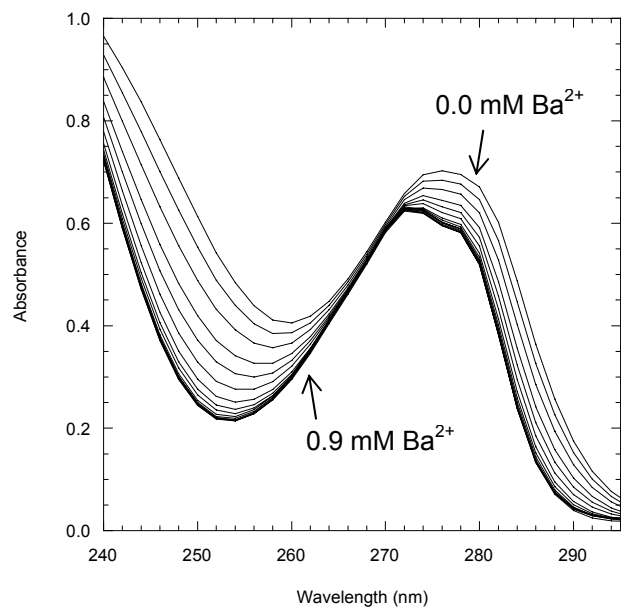


Figure 4-60. Spectra from the titration of 0.18 mM An2.2.2, (19), with barium at pH = 8.2.

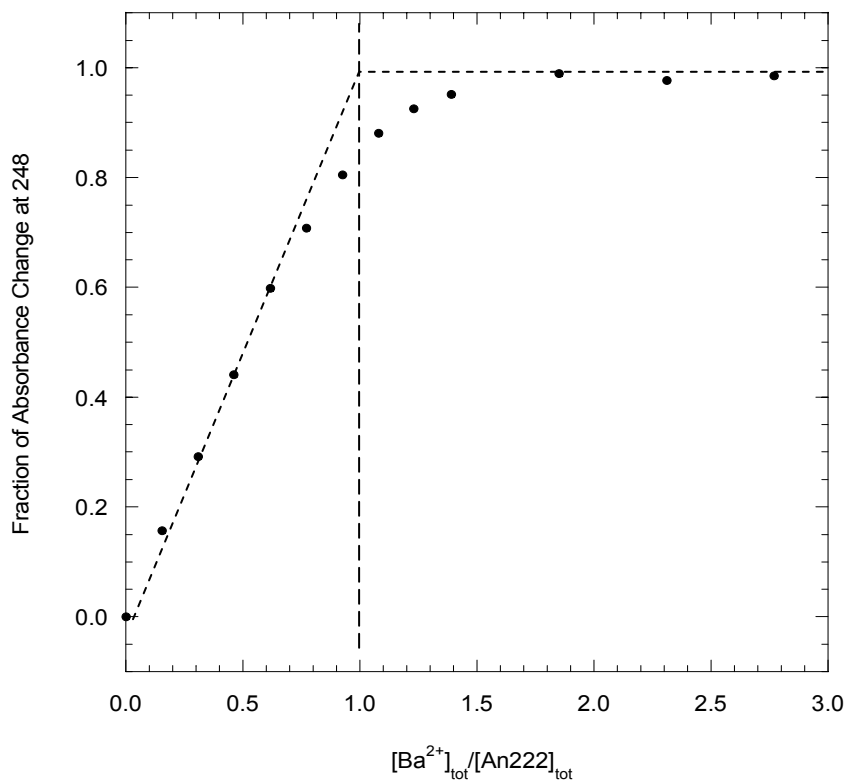


Figure 4-61. Plot of fraction of the absorbance change versus the ratio of total barium to total An2.2.2, (19), concentrations from the titration shown in Figure 4-60.

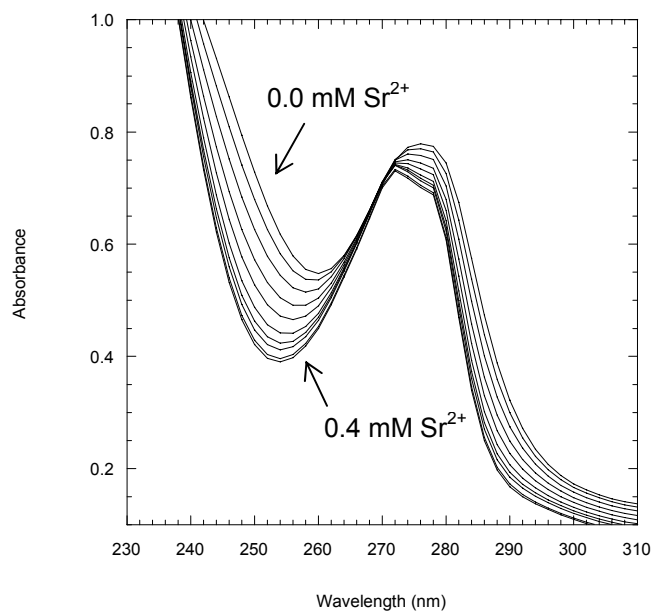


Figure 4-62. Spectra from the titration of 0.17 mM An2.2.2, (19), with strontium at pH = 9.5.

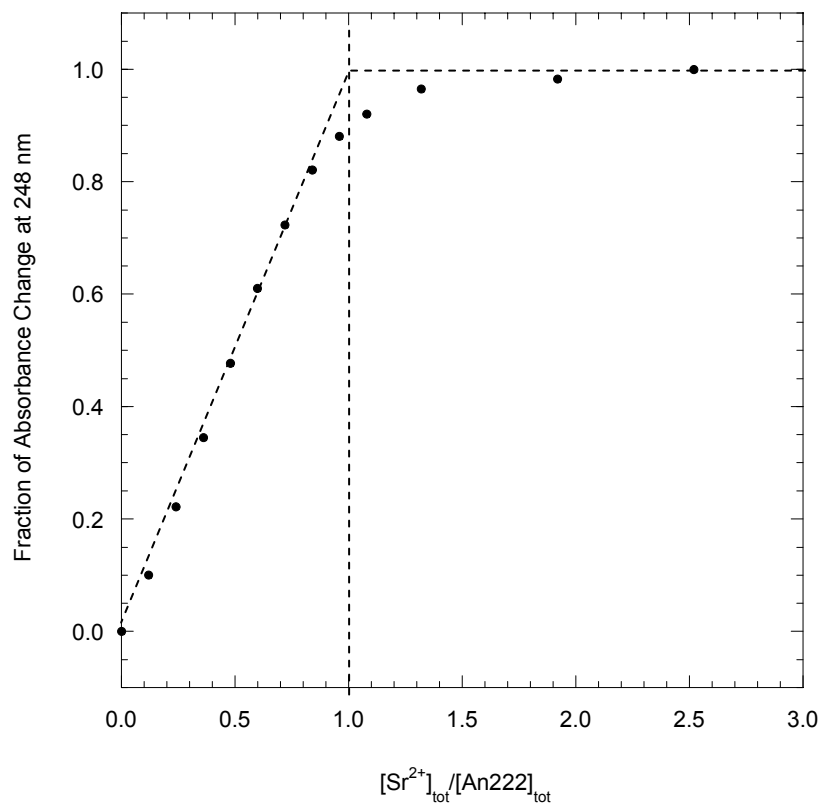


Figure 4-63. Plot of fraction of the absorbance change versus the ratio of total strontium to total An2.2.2, (19), concentrations from the titration shown in Figure 4-62.

The estimated formation constants are used to calculate a pH where cryptand An2.2.2 will not be fully complexed when the concentrations of the metal and ligand are equal. The conditional formation constants can be more accurately measured at this pH by increasing the competition between the metal and protons.

The spectra for titrations of cryptand An2.2.2 with BaCl₂ at pH = 3.7 and SrCl₂ at pH = 4.2 are shown in Figures 4-64 and 4-66, respectively. Plots of absorbance versus free metal ion concentration can be fit using eq 4.9. These fits are shown in Figures 4-65 and 4-67 for barium and strontium, respectively, and the calculated values used to construct the solid lines are listed in the table (inset). The absorbance measured (A_i) at an individual wavelength is dependent upon the conditional stability constant, K'_{ML} , concentration of the uncomplexed metal ion $[M]$, and the limiting absorbance values A_1 and A_0 for the metal ion-ligand complex and the uncomplexed ligand, respectively, as shown in the following equation:

$$A_i = \frac{A_1 K'_{ML} [M] + A_0}{K'_{ML} [M] + 1} \quad (4.9)$$

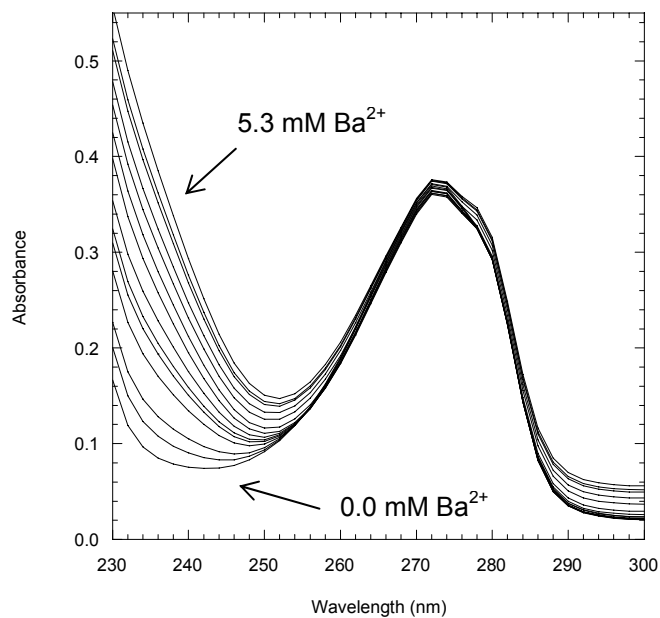


Figure 4-64. Spectra from the titration of 0.091 mM An2.2.2, (19), with barium at pH = 3.7. Some spectra have been omitted for clarity.

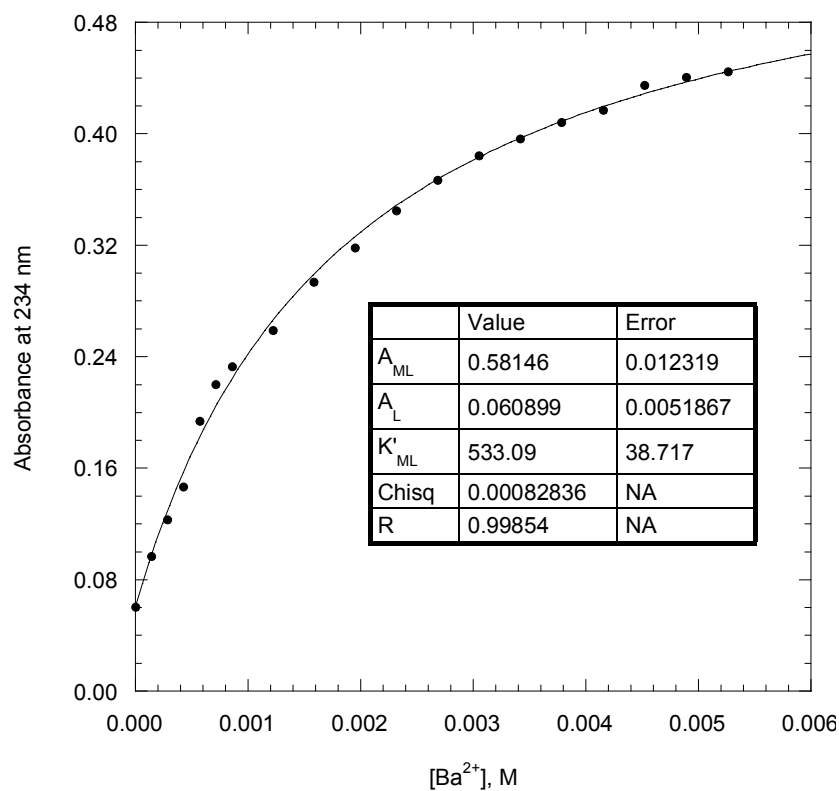


Figure 4-65. Plot of absorbance at 234 nm versus $[Ba^{2+}]$ for the titration of An2.2.2, (19), shown in Figure 4-64. The data were fit to eq 4.9 and the calculated values used to construct the solid line are listed in the table.

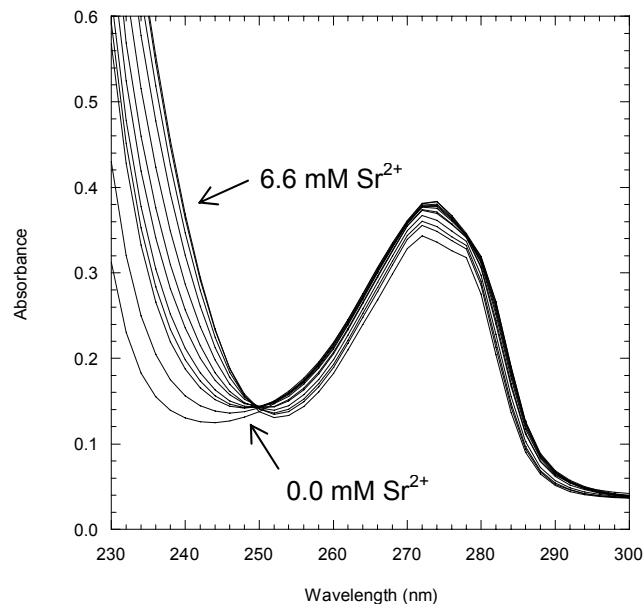


Figure 4-66. Spectra from the titration of 0.091 mM An2.2.2, (19), with strontium at pH = 4.2. Some spectra have been omitted for clarity.

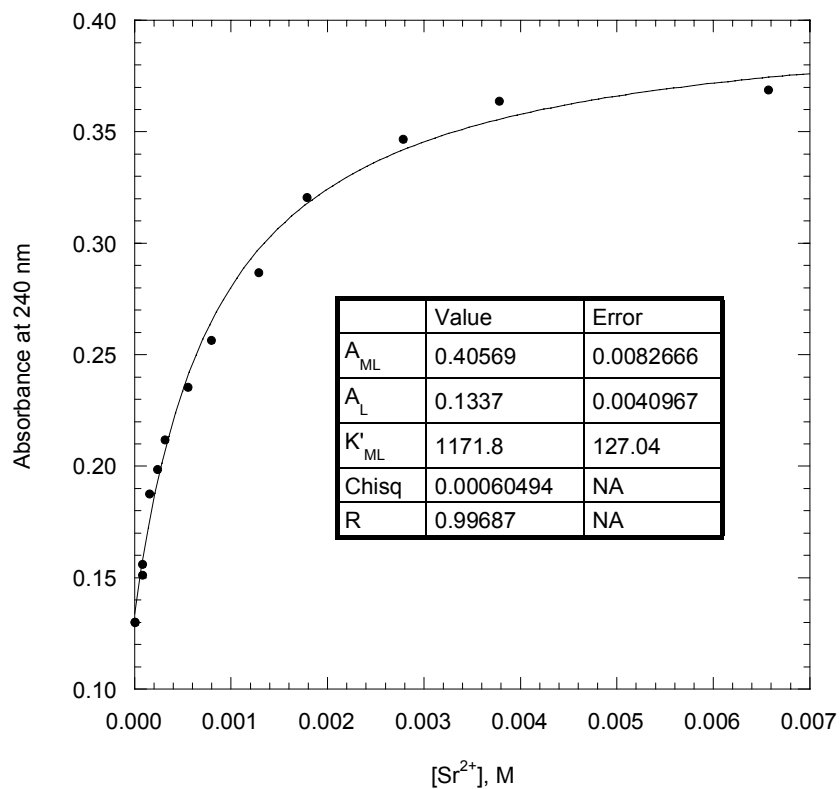


Figure 4-67. Plot of absorbance at 240 nm versus $[Sr^{2+}]$ for the titration of An2.2.2, (19), shown in Figure 4-66. The data were fit to eq 4.9 and the calculated values used to construct the solid line are listed in the table.

The conditional formation constants ($\log K'_{ML}$) for barium were determined at several pH values and the results are listed in Table 4-17. The formation constant for barium can be calculated using eq 4.10 using the previously determined protonation constants for An2.2.2. Cryptand An2.2.2 has a formation constant ($\log K_{ML}$) for barium of 4.7 ± 0.2 .

$$K_{ML} = \frac{K'_{ML}}{(1 + K_{H1}a_H + K_{H1}K_{H2}a_H^2)} = \frac{K'_{ML}}{\alpha_L} \quad (4.10)$$

Table 4-17. Formation constants ($\log K_{ML}$) for An2.2.2, (19) with barium in H₂O at 25°C.

Exp. No.	pH	$\log K'_{ML}$	Error	$\log K_{ML}$
1	4.7	4.14	0.05	4.86
2	4.3	3.80	0.01	4.91
3	9.3	4.84	0.03	4.84
4	4.1	3.48	0.04	4.78
5	4.1	3.47	0.04	4.87
6	3.9	3.03	0.03	4.64
7	3.7	2.73	0.03	4.62

The conditional stability constants for barium were also used to calculate the protonation constants of An2.2.2 in order to compare them with the values obtained from pH titrations. The plot of K'_{ML} versus a_H is shown in Figure 4-68 and the data was fit to eq 4.10 and the calculated values used to construct the solid line are listed in the table. The protonation constants $\log K_{H1}$ and $\log K_{H2}$ were calculated to be 3.9 ± 0.2 and 5.18 ± 0.04 , respectively. These K_{H1} and K_{H2} values are in agreement with the values previously determined by pH titrations without added metal ion.

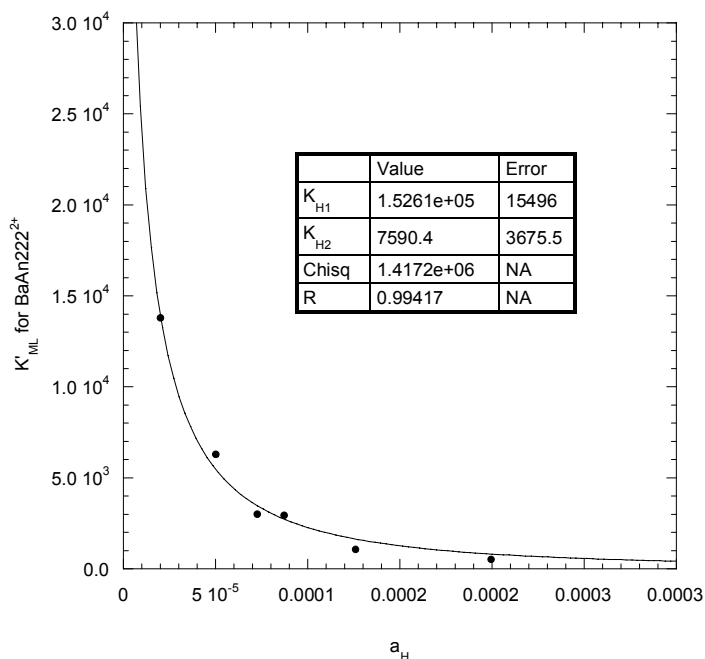


Figure 4-68. Plot of K'_{ML} vs. a_H for $BaAn2.2.2^{2+}$ using values from Table 4-17. The solid line is fit using eq 4-10 and the calculated K_H values are listed in the table (inset).

The conditional formation constants ($\log K'_{ML}$) for strontium were determined from duplicate experiments at two different pH values and the results are listed in Table 4-18.

The formation constant for strontium can be calculated using eq 4.10 using the previously determined protonation constants for $An2.2.2$. Cryptand $An2.2.2$ has a formation constant ($\log K_{ML}$) for strontium of 4.1 ± 0.6 .

Table 4-18. Formation constants ($\log K_{ML}$) for $An2.2.2$, (**19**) with strontium in H_2O at $25^\circ C$.

Exp. No.	Method ^a	λ , nm (range)	pH	$\log K'_{ML}$	Error	$\log K_{ML}$
1	K	240	3.8	3.07	0.05	4.75
1	K	276	3.8	2.38	0.07	4.06
1	S	200-400	3.8	2.97	0.07	4.65
2	K	240	4.2	3.07	0.05	4.29
2	K	274	4.2	2.19	0.06	3.41
2	S	200-400	4.2	2.0	0.1	3.22

^aK = Kaleidagraph, S = Specfit.

The very large (≥ 6) formation constant ($\log K_{ML}$) for cryptand An2.2.2 with $Pb(ClO_4)_2$ requires that this parameter be measured at a very low pH (~ 2) where the ligand is predominantly ($\geq 95\%$) present as the diprotonated species. The kinetics of the ligand and metal interaction at this pH are slowed down considerably so the titrations are accomplished by a batch method. The spectra for a batch titration of cryptand An2.2.2 with $Pb(ClO_4)_2$ at pH = 2.1 is shown in Figure 4-69. Plots of absorbance versus free metal ion concentration and absorbance versus the product of free metal ion concentration and alpha are shown in Figures 4-70 and 4-71, respectively. The plot of absorbance versus free metal concentration is fit using eq 4.9 and the plot of absorbance versus the product of free metal concentration and alpha is fit using the equation below. The alpha value is included in the calculations at every point to account for the variation in pH among individual solutions.

$$A_i = \frac{A_1 K_{ML} [M] \alpha_L + A_0}{K_{ML} [M] \alpha_L + 1} \quad (4.11)$$

$$\alpha_L = \frac{[L]}{[L]'} = (1 + K_{H1} a_H + K_{H1} K_{H2} a_H^2)^{-1} \quad (4.12)$$

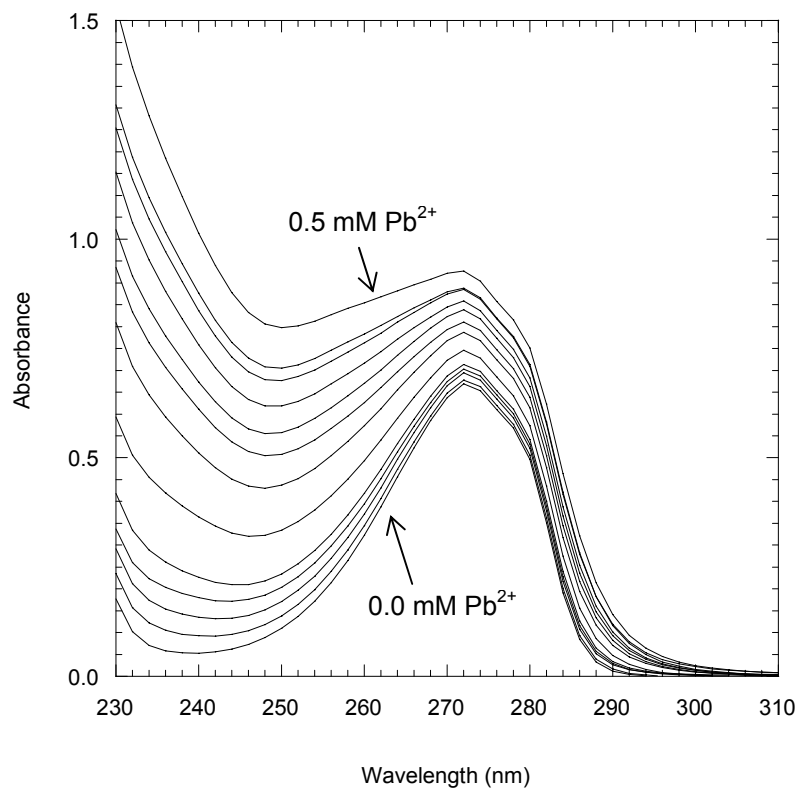


Figure 4-69. Spectra from the batch titration of 0.18 mM An2.2.2, (19), with lead at pH = 2.1.

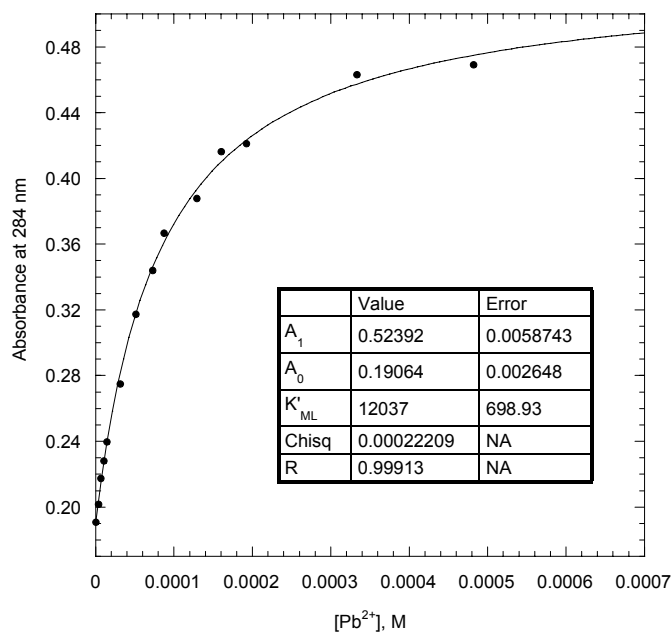


Figure 4-70. Plot of absorbance at 284 nm versus $[Pb^{2+}]$ for the titration of An2.2.2, (19), shown in Figure 4-69. The data were fit to eq 4.9 and the calculated values used to construct the solid line are listed in the table.

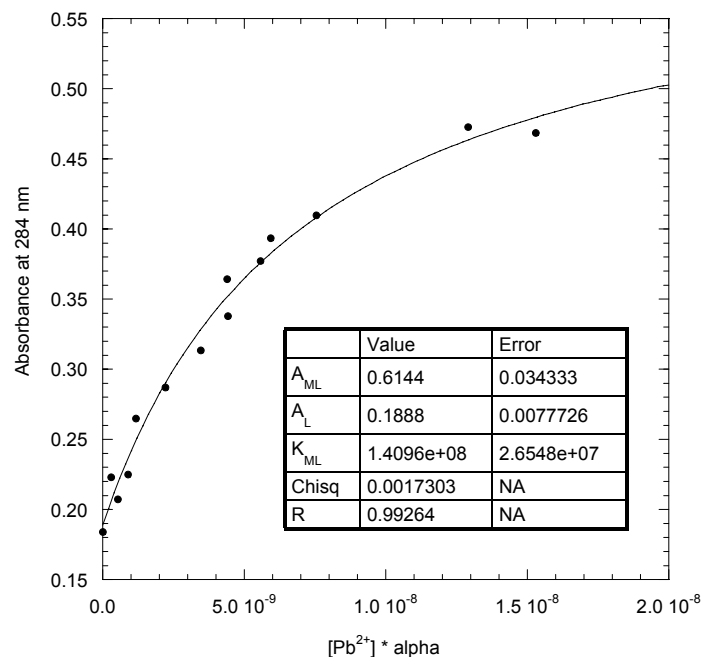


Figure 4-71. Plot of absorbance at 284 nm versus $[Pb^{2+}] * \alpha$ for a batch titration of An2.2.2, (19), and lead. The data were fit to eq 4.11 and the calculated values used to construct the solid line are listed in the table.

The formation constants for lead were determined by several batch titrations and the values are listed in Table 4-19. The calculations using the alpha factor among the individual solutions (eq 4.11) are identified with the letter a. Cryptand An2.2.2 has a formation constant ($\log K_{ML}$) for lead of 8.5 ± 0.3 .

Table 4-19. Formation constants ($\log K_{ML}$) for An2.2.2, (19) with lead in H₂O at 25°C.

Exp. No.	pH	$\log K'_{ML}$	$\log K_{ML}$	Error
1	2.25	3.99	8.2	0.08
1a	--	--	8.1	0.08
2	2.10	4.01	8.5	0.09
2a	--	--	8.9	0.1
3	2.15	4.08	8.5	0.03
3a	--	--	8.1	0.1
4	2.02	4.11	8.8	0.06
4a	--	--	9.0	0.07

The spectra for titrations of cryptand An2.2.2 with NaCl at pH = 9.0, Cd(ClO₄)₂ at pH = 7.7, CaCl₂ at pH = 9.4, and KCl at pH = 9.0 are shown in Figures 4-72, 4-74, 4-76, and 4-78, respectively. The plots of fraction of absorbance change versus the ratio of metal ion to An2.2.2 concentrations for these titrations indicate that cryptand An2.2.2 does not bind quantitatively at 1:1 metal ion to ligand concentration. Complete complexation of the ligand by the metal is not achieved at pH \geq 7 when the concentrations are equal. Therefore, the plots of absorbance versus free metal concentration shown in Figures 4-73, 4-75, 4-77, and 4-79 can be fit using eq 4.9 to determine the formation constants ($\log K_{ML}$) of each metal.

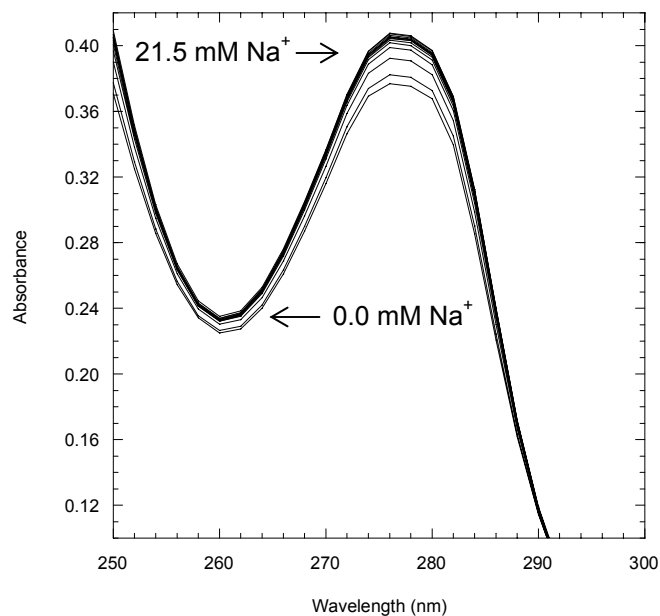


Figure 4-72. Spectra from the titration of 0.091 mM An2.2.2, (19), with sodium at pH = 9.0. Some spectra have been omitted for clarity.

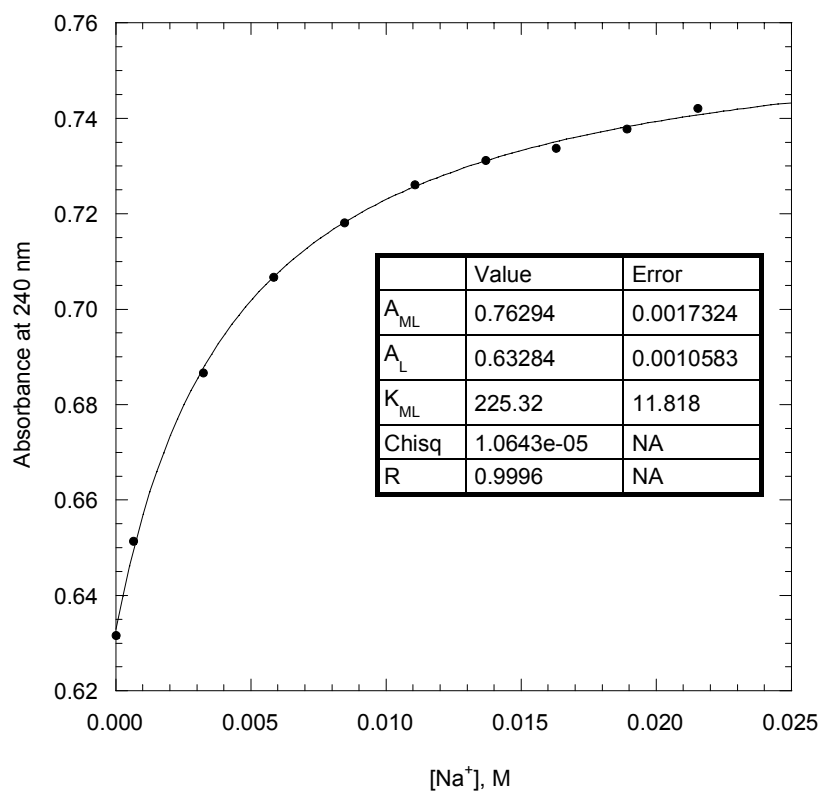


Figure 4-73. Plot of absorbance at 240 nm versus $[Na^+]$ for the titration of An2.2.2, (19), shown in Figure 4-72. The data were fit to eq 4.9 and the calculated values used to construct the solid line are listed in the table.

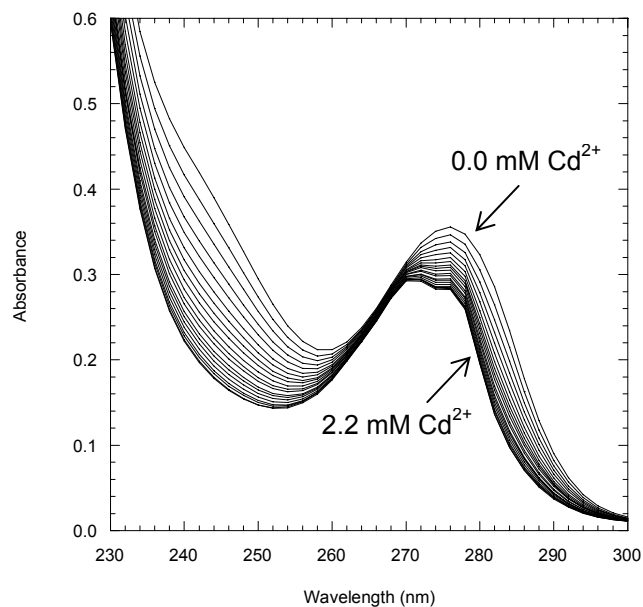


Figure 4-74. Spectra from the titration of 0.091 mM An2.2.2, (19), with cadmium at pH = 7.7. Some spectra have been omitted for clarity.

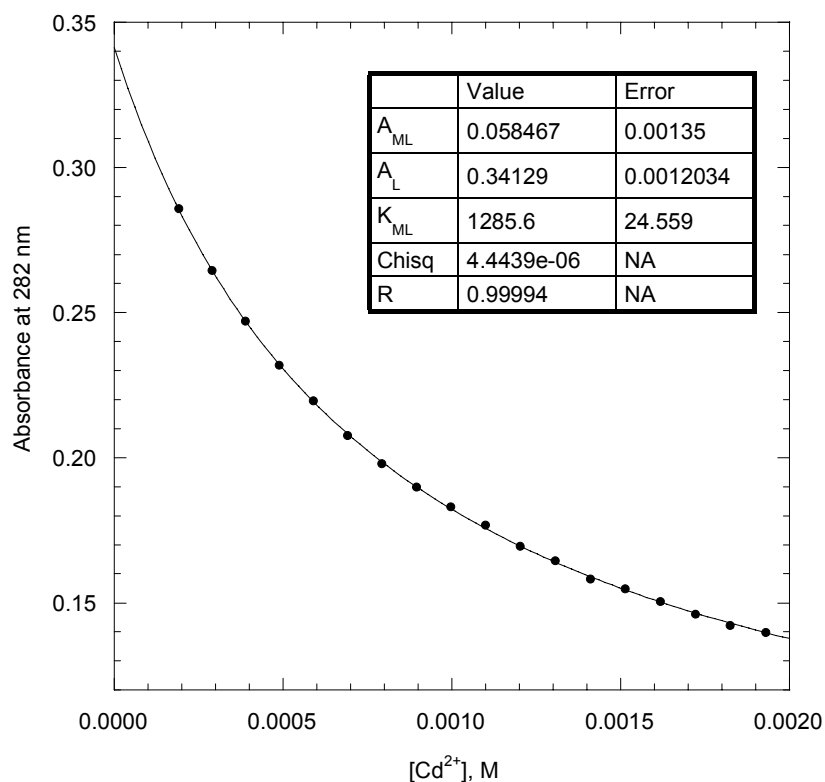


Figure 4-75. Plot of absorbance at 282 nm versus $[Cd^{2+}]$ for the titration of An2.2.2, (19), shown in Figure 4-74. The data were fit to eq 4.9 and the calculated values used to construct the solid line are listed in the table.

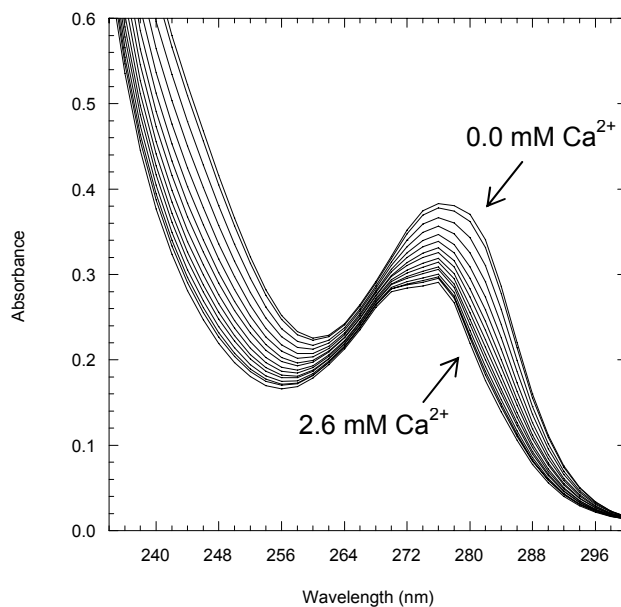


Figure 4-76. Spectra from the titration of 0.091 mM An2.2.2, (19), with calcium at pH = 9.4. Some spectra have been omitted for clarity.

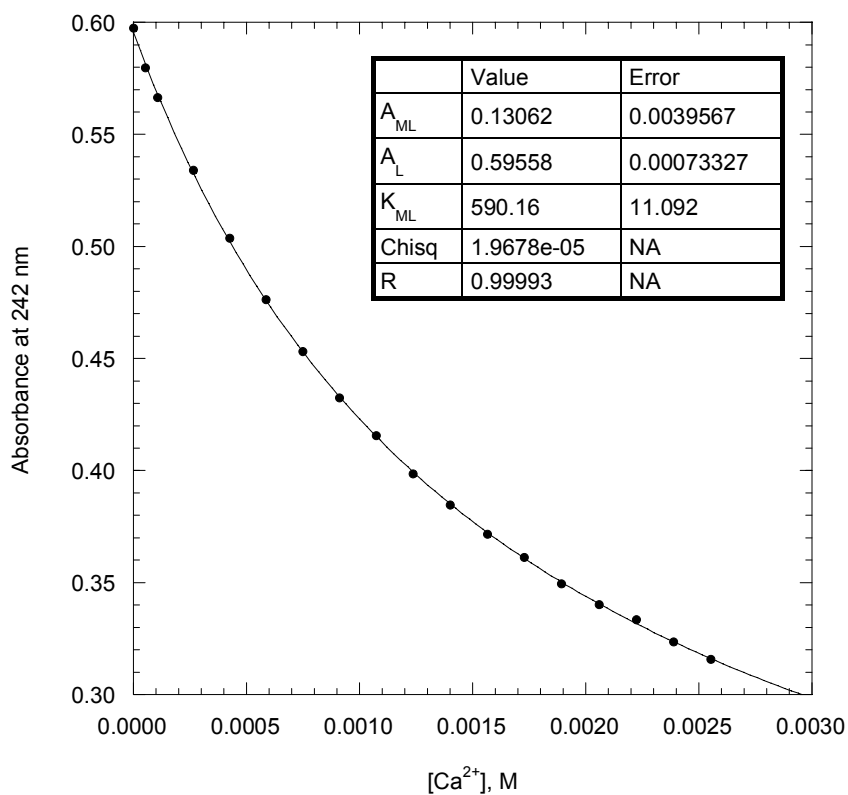


Figure 4-77. Plot of absorbance at 242 nm versus $[Ca^{2+}]$ for the titration of An2.2.2, (19), shown in Figure 4-76. The data were fit to eq 4.9 and the calculated values used to construct the solid line are listed in the table.

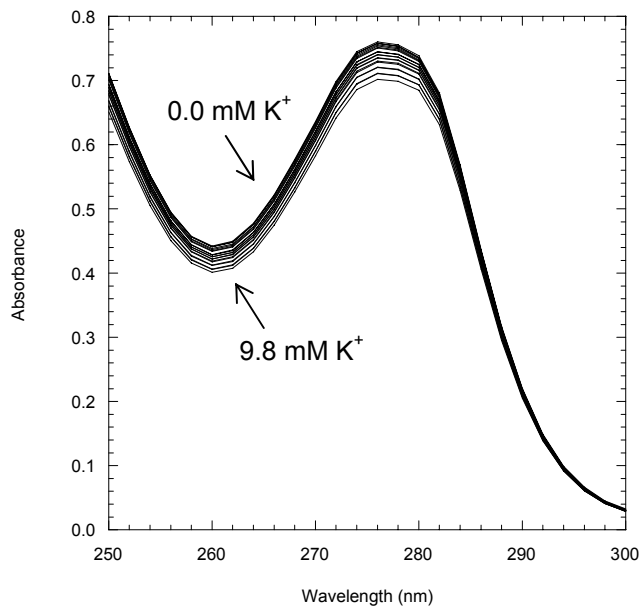


Figure 4-78. Spectra from the titration of 0.18 mM An2.2.2, (19), with potassium at pH = 9.0. Some spectra have been omitted for clarity.

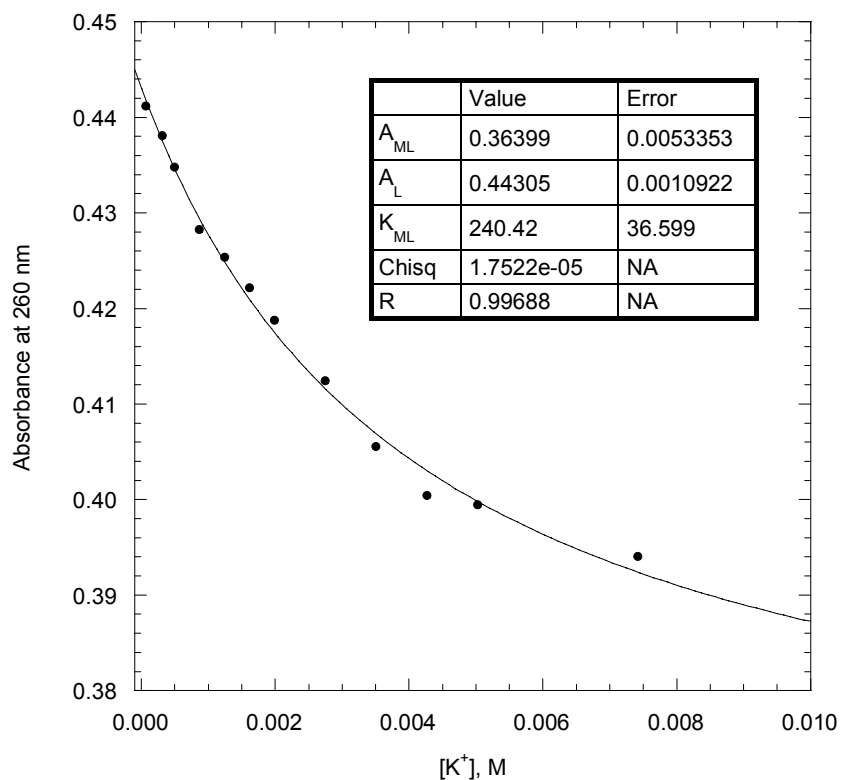


Figure 4-79. Plot of absorbance at 260 nm versus $[K^+]$ for the titration of An2.2.2, (19), shown in Figure 4-78. The data were fit to eq 4.9 and the calculated values used to construct the solid line are listed in the table.

The calculated values for the formation constants ($\log K_{ML}$) are listed in Table 4-20. The fits using Kaleidagraph are at a specific wavelength listed in the table. The Specfit analysis of the same experiments is located in the second $\log K_{ML}$ column with the corresponding error and these values were determined the wavelength region from 200 to 400 nm. The average formation constants ($\log K_{ML}$) for An2.2.2 with Na^+ , Ca^{2+} , Cd^{2+} , and K^+ are 2.4 ± 0.1 , 2.7 ± 0.1 , 3.0 ± 0.2 , and 2.0 ± 0.3 , respectively.

Table 4-20. Formation constants ($\log K_{ML}$) for An2.2.2, (19) in H_2O at 25°C .

Exp. No.	Metal	λ	$\log K_{ML}^a$	Error	$\log K_{ML}^b$	Error
1	Na	240	2.35	0.02		
1	Na	276	2.38	0.02	2.32	0.08
2	Na	250	2.47	0.09		
2	Na	284	2.5	0.10	2.33	0.09
1	Ca	242	2.79	0.01		
1	Ca	282	2.82	0.01	2.67	0.05
2	Ca	242	2.77	0.01		
2	Ca	282	2.80	0.01	2.61	0.08
3	Ca	242	2.68	0.01		
3	Ca	282	2.72	0.01	2.64	0.04
1	Cd	242	2.85	0.03		
1	Cd	282	2.87	0.03	3.0	0.1
2	Cd	242	3.11	0.01		
2	Cd	282	3.11	0.01	2.8	0.1
3	Cd	242	3.15	0.03		
3	Cd	282	3.14	0.03	3.27	0.06
1	K	262	2.03	0.08		
1	K	276	2.06	0.05	1.6	0.2
2	K	260	2.42	0.04		
2	K	274	2.30	0.06	1.7	0.8

^aFrom Kaleidagraph. ^bFrom Specfit.

Cryptand An2.2.2 differs from 2.2.2 because of the addition of benzene rings and is also differs from 2.2_B.2_B because of the location of the benzene rings. The difference in location of the benzene rings also transforms the nitrogens from alkyl to aryl in An2.2.2. Table 4-21 lists the formation constants ($\log K_{ML}$) of the metals studied in this

project for all three ligands. The structural changes clearly have an effect on the metal formation constants. The $\log K_{ML}$ values determined for cryptand An2.2.2 are ≥ 1.5 orders of magnitude lower in comparison to cryptand 2.2.2. The smaller cations sodium (0.97 Å) and calcium (0.99 Å) are less affected ($\Delta\log K = 1.6$ and 1.8, respectively) in comparison to the decrease by 4.9, 4.0, and 3.9 log units for the larger cations barium (1.34 Å), strontium (1.12 Å), and lead (1.20 Å), respectively.²³ The trend in formation constant values among the divalent cations for 2.2.2 ($Pb^{2+} > Ba^{2+} > Sr^{2+} > Cd^{2+} > Ca^{2+}$) is still present for cryptand An2.2.2. This behavior does not hold for the monovalent cations, where cryptand An2.2.2 has a larger K_{ML} value for sodium than for potassium while the opposite order is found with cryptand 2.2.2.

Table 4-21. Formation constants ($\log K_{ML}$) for 2.2.2, 2.2_B.2_B, and An2.2.2, (19) in H₂O at 25°C.

	2.2.2 ^a	2.2 _B .2 _B	An2.2.2
Na ⁺	4	3.4 ^b	2.4 ± 0.1
K ⁺	5.5	4.4 ^b	2.0 ± 0.3
Ca ²⁺	4.5	3.5 ^c	2.7 ± 0.1
Sr ²⁺	8.1	6.4 ^c	4.1 ± 0.6
Ba ²⁺	9.6	5.7 ^c	4.7 ± 0.2
Cd ²⁺	6.8	--	3.0 ± 0.2
Pb ²⁺	12.4	11.4 ^d	8.5 ± 0.3

^a Ref. ⁴⁵. ^b Ref. ⁴⁶. ^c Ref. ⁴⁷. ^d Ref. ⁴⁸.

The $\log K_{ML}$ values for cryptand An2.2.2 are lower in magnitude in comparison to 2.2_B.2_B by 0.8 - 2.9 orders of magnitude. The trend in binding constants changes from $Pb^{2+} > Sr^{2+} > Ba^{2+} > Ca^{2+}$ and $K^+ > Na^+$ for 2.2_B.2_B to $Pb^{2+} > Ba^{2+} > Sr^{2+} > Ca^{2+}$ and $Na^+ > K^+$ for An2.2.2. The K_{ML} values for 2.2_B.2_B and An2.2.2 show that the addition of benzene rings decreases the value of K_{ML} compared to 2.2.2. Cryptand An2.2.2 also shows that changing from alkyl to aryl nitrogens results in lower K_{ML} values. The

inherent selectivity ($K_S = K_{M^*L}/K_{ML}$) for lead over the biological cations sodium, potassium, and calcium is present in all three cryptands but slightly lower for An2.2.2.

The spectral properties of cryptand An2.2.1 with sodium, potassium, calcium, strontium, barium, cadmium, and lead were investigated initially at $\text{pH} \geq 7$ similarly to An2.2.2. The spectra for titrations of cryptand An2.2.1 with $\text{Pb}(\text{ClO}_4)_2$ at $\text{pH} = 6.9$ and $\text{Cd}(\text{ClO}_4)_2$ at $\text{pH} = 7.0$ are shown in Figures 4-80 and 4-82, respectively. The plots of fraction of absorbance change at a specific wavelength versus the ratio of metal ion to An2.2.1 concentration for these titrations are shown in Figures 4-81 and 4-83, respectively. The plots of fraction of absorbance change for Pb^{2+} and Cd^{2+} indicate $\geq 80\%$ complexation at 1:1 metal to ligand ratio. This percentage of complexation is not as high as the values found for An2.2.2 with Pb^{2+} , Ba^{2+} , and Sr^{2+} . The formation constants were estimated from these plots and metal titrations were performed at a lower pH as described for An2.2.2.

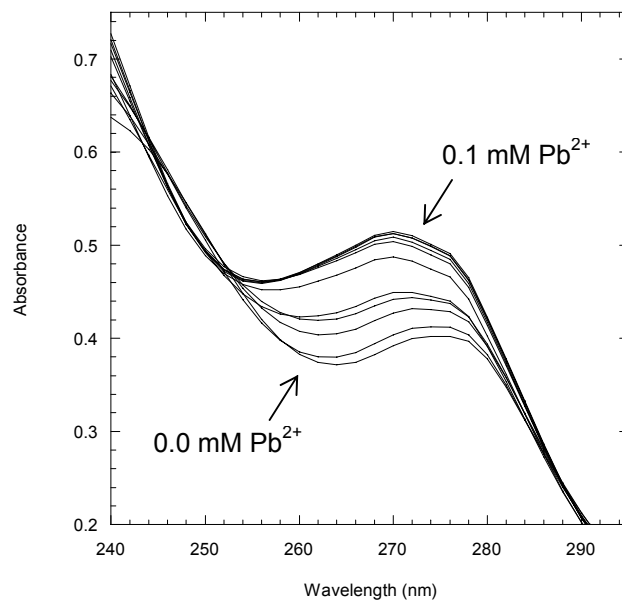


Figure 4-80. Spectra from the titration of 0.061 mM An2.2.1, (16), with lead at pH = 6.9. Some spectra have been omitted for clarity.

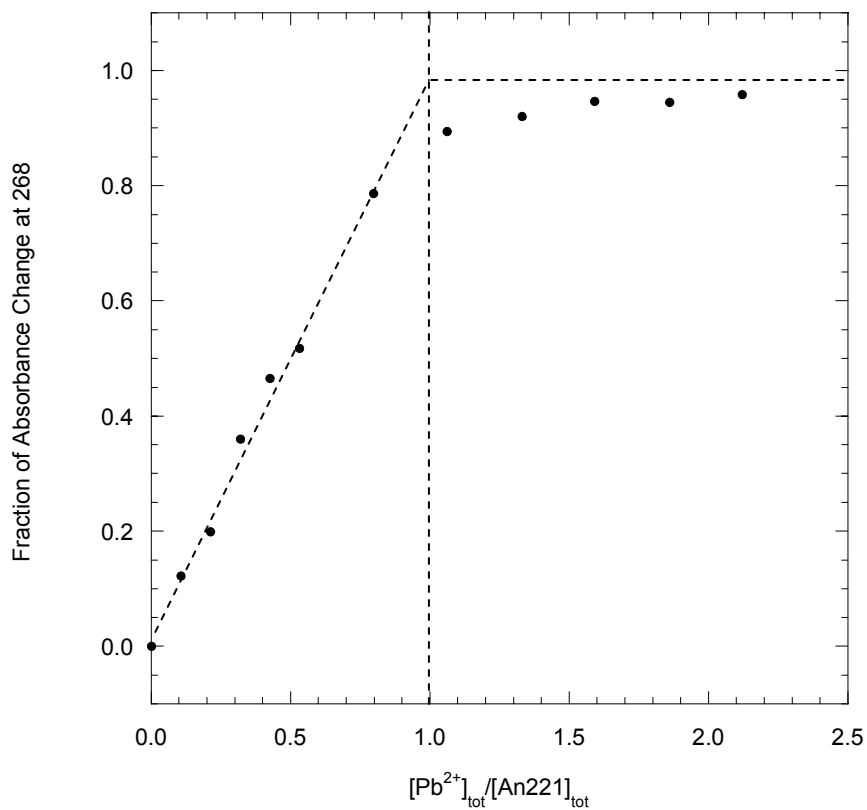


Figure 4-81. Plot of fraction of the absorbance change versus the ratio of total lead to total An2.2.1, (16), concentrations from the titration shown in Figure 4-80.

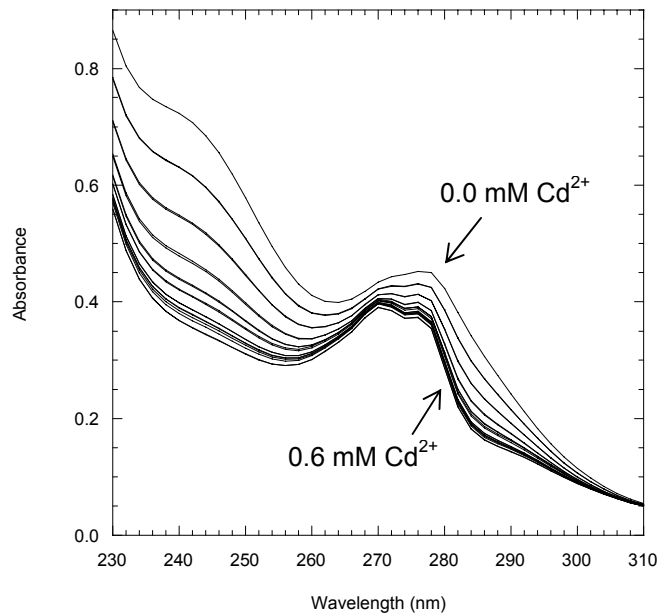


Figure 4-82. Spectra from the titration of 0.091 mM An2.2.1, (16), with cadmium at pH = 7.0. Some spectra have been omitted for clarity.

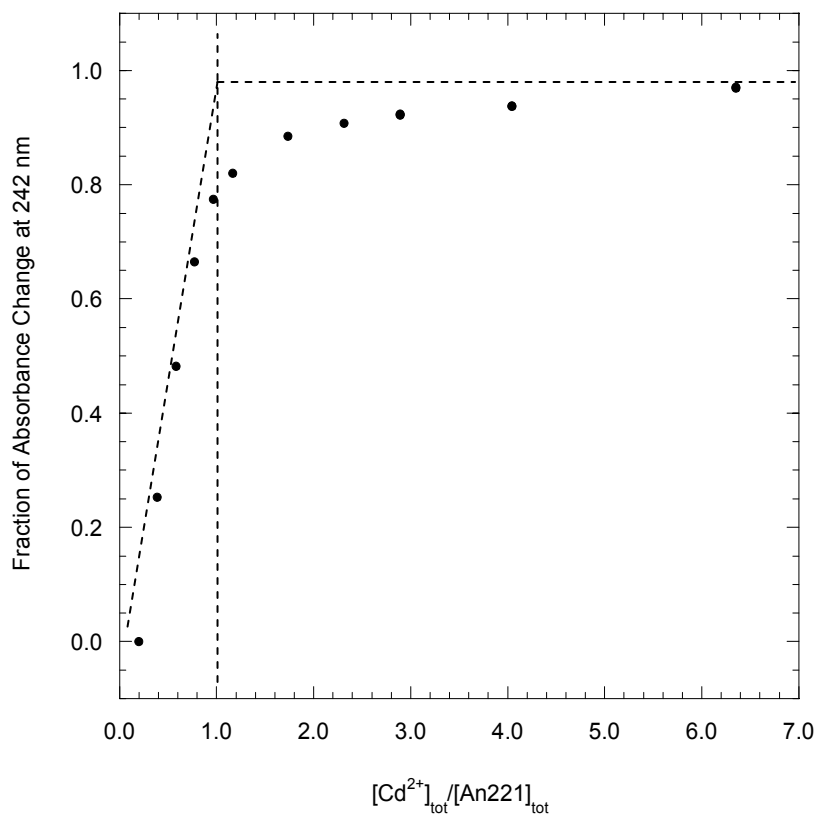


Figure 4-83. Plot of fraction of the absorbance change versus the ratio of total cadmium to total An2.2.1, (16), concentrations from the titration shown in Figure 4-82.

The spectra for titrations of cryptand An2.2.1 with $\text{Pb}(\text{ClO}_4)_2$ at $\text{pH} = 3.6$ and with $\text{Cd}(\text{ClO}_4)_2$ at $\text{pH} = 4.3$ are shown in Figures 4-84 and 4-86, respectively. Plots of absorbance versus free metal ion concentration are fit using eq 4.9. These fits are shown in Figures 4-85 and 4-87 for lead and cadmium, respectively and the calculated values used to construct the solid line are listed in the table.

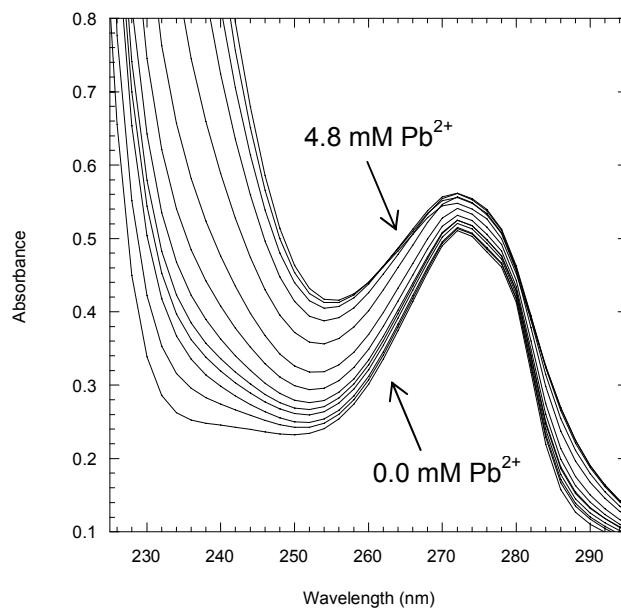


Figure 4-84. Spectra from the titration of 0.091 mM An2.2.1, (16), with lead at pH = 3.6. Some spectra have been omitted for clarity.

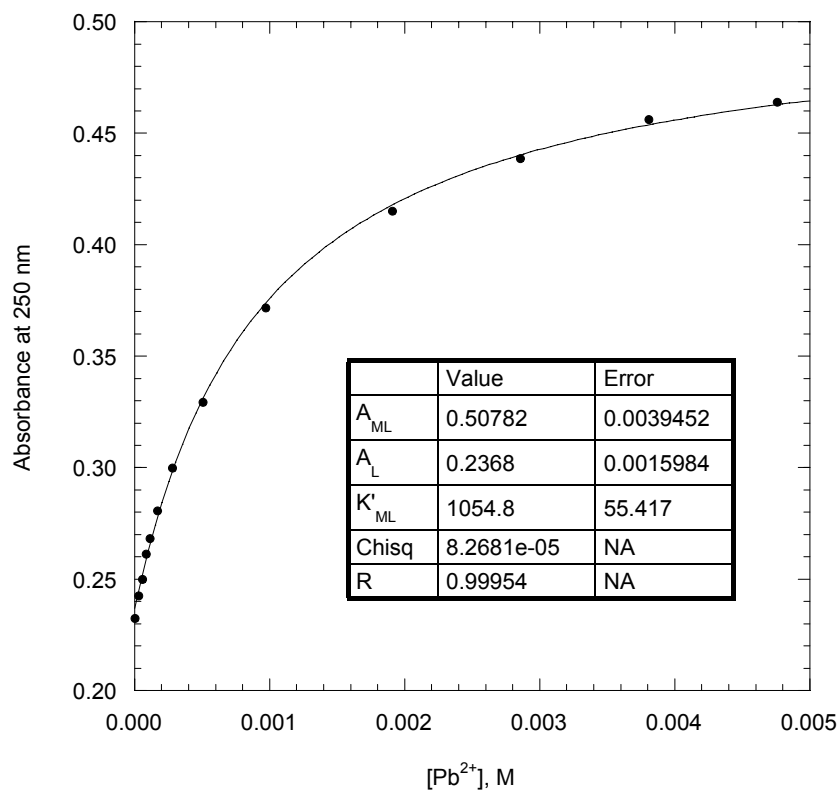


Figure 4-85. Plot of absorbance at 250 nm versus $[Pb^{2+}]$ for the titration of An2.2.1, (16), shown in Figure 4-84. The data were fit to eq 4.9 and the calculated values used to construct the solid line are listed in the table.

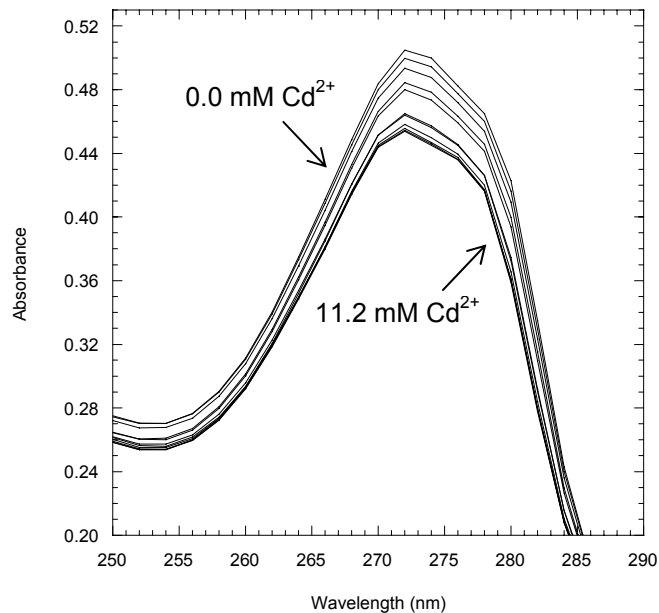


Figure 4-86. Spectra from the titration of 0.091 mM An2.2.1, (16), with cadmium at pH = 4.3. Some spectra have been omitted for clarity.

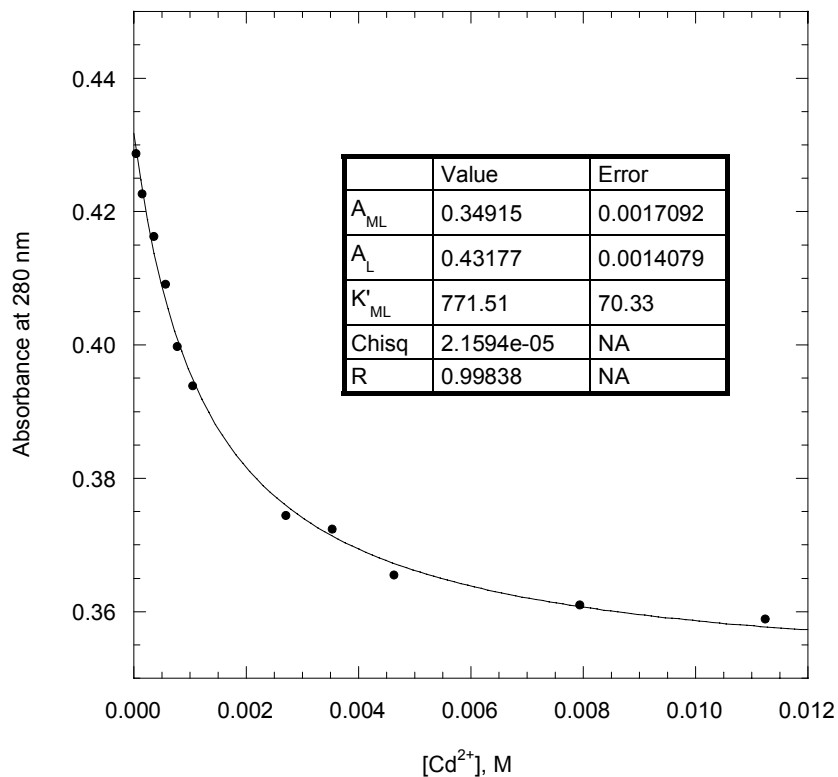


Figure 4-87. Plot of absorbance at 280 nm versus $[Cd^{2+}]$ for the titration of An2.2.1, (16), shown in Figure 4-86. The data were fit to eq 4.9 and the calculated values used to construct the solid line are listed in the table.

The conditional formation constants ($\log K'_{ML}$) for lead and cadmium were determined from duplicate experiments and the results are listed in Table 4-22. The analysis of the experiments using Specfit was determined for the wavelength region from 200 to 400 nm. The average formation constants ($\log K_{ML}$) for An2.2.1 with Pb^{2+} and Cd^{2+} are 5.0 ± 0.1 and 4.0 ± 0.1 , respectively.

Table 4-22. Formation constants ($\log K_{ML}$) for An2.2.1, (16) in H_2O at $25^\circ C$.

Exp. No.	Metal	Method ^a	λ , nm (range)	pH	$\log K'_{ML}$	Error	$\log K_{ML}$
1	Pb	K	250	3.6	3.02	0.02	4.91
1	Pb	S	200-400	3.6	3.19	0.07	5.08
2	Pb	K	250	3.5	2.91	0.01	4.93
2	Pb	S	200-400	3.5	2.90	0.06	4.92
1	Cd	K	280	4.3	2.83	0.06	3.96
1	Cd	S	200-400	4.3	2.63	0.08	3.76
2	Cd	K	280	4.3	2.89	0.04	4.02
2	Cd	S	200-400	4.3	3.0	0.2	4.13

^aK = Kaleidagraph, S = Specfit.

The spectra for titrations of cryptand An2.2.1 with $BaCl_2$ at $pH = 8.4$, $NaCl$ at $pH = 8.3$, $SrCl_2$ at $pH = 8.6$, $CaCl_2$ at $pH = 8.7$, and KCl at $pH = 9.1$ are shown in Figures 4-88, 4-90, 4-92, 4-94, and 4-96, respectively. The plots of fraction of absorbance change versus the ratio of metal ion to An2.2.1 concentration for these titrations indicate that cryptand An2.2.1 does not bind quantitatively at 1:1 metal to ligand concentration. Full complexation of the ligand by the metal is not achieved at a $pH \geq 7$ when the concentrations are equal. Therefore, the plots of absorbance versus free metal concentration shown in Figures 4-89, 4-91, 4-93, 4-95, and 4-97 for barium, sodium, strontium, calcium, and potassium, respectively can be fit using eq 4.9 to determine the formation constants of each metal.

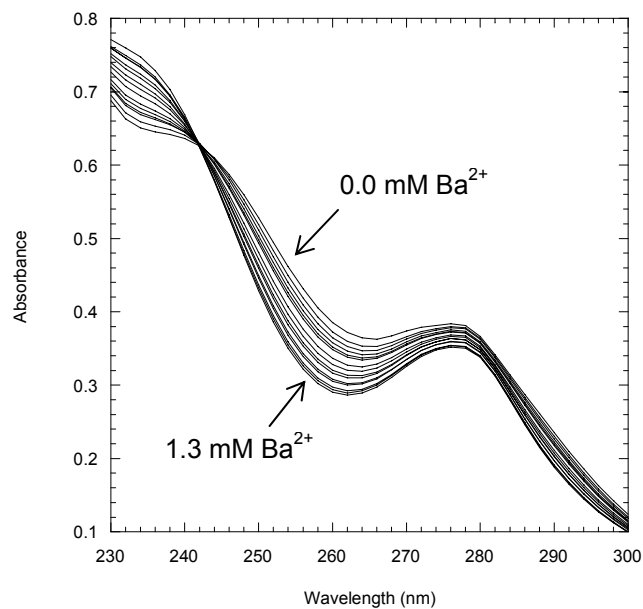


Figure 4-88. Spectra from the titration of 0.070 mM An2.2.1, (16), with barium at pH = 8.4. Some spectra have been omitted for clarity.

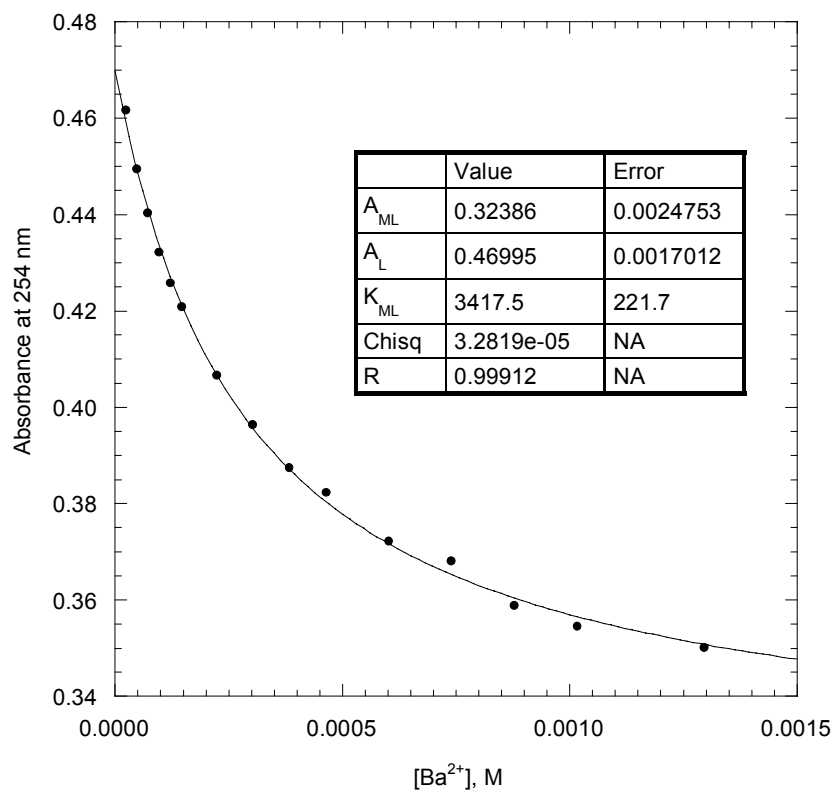


Figure 4-89. Plot of absorbance at 254 nm versus $[Ba^{2+}]$ for the titration of An2.2.1, (16), shown in Figure 4-88. The data were fit to eq 4.9 and the calculated values used to construct the solid line are listed in the table.

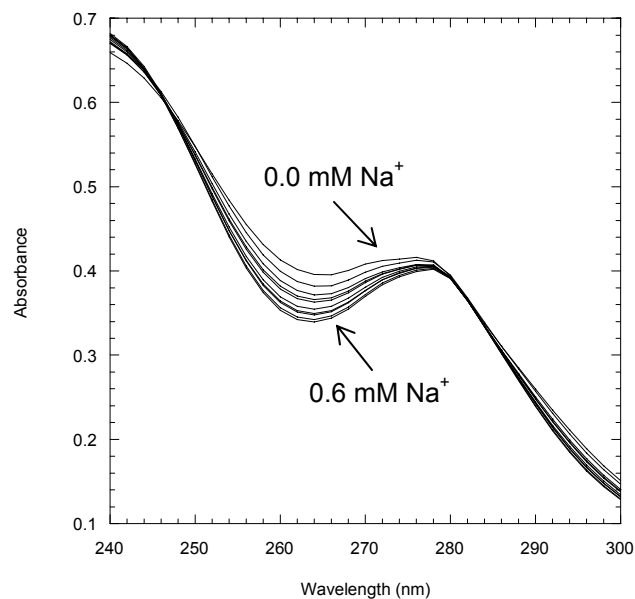


Figure 4-90. Spectra from the titration of 0.070 mM An2.2.1, (16), with sodium at pH = 8.3. Some spectra have been omitted for clarity.

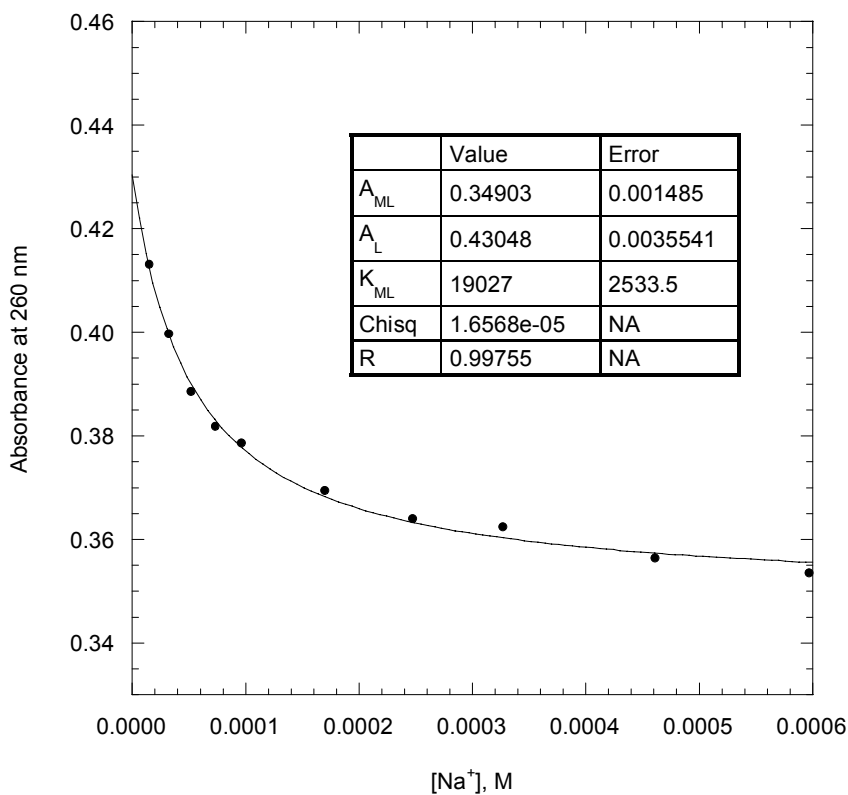


Figure 4-91. Plot of absorbance at 260 nm versus $[Na^+]$ for the titration of An2.2.1, (16), shown in Figure 4-90. The data were fit to eq 4.9 and the calculated values used to construct the solid line are listed in the table.

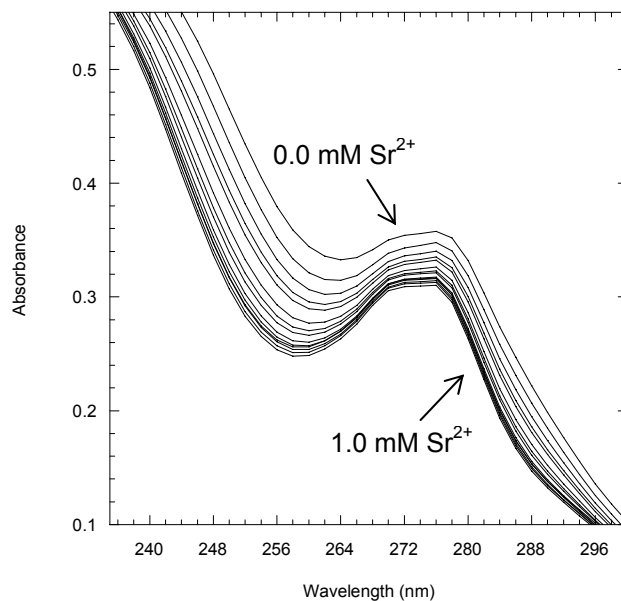


Figure 4-92. Spectra from the titration of 0.070 mM An2.2.1, (16), with strontium at pH = 8.6. Some spectra have been omitted for clarity.

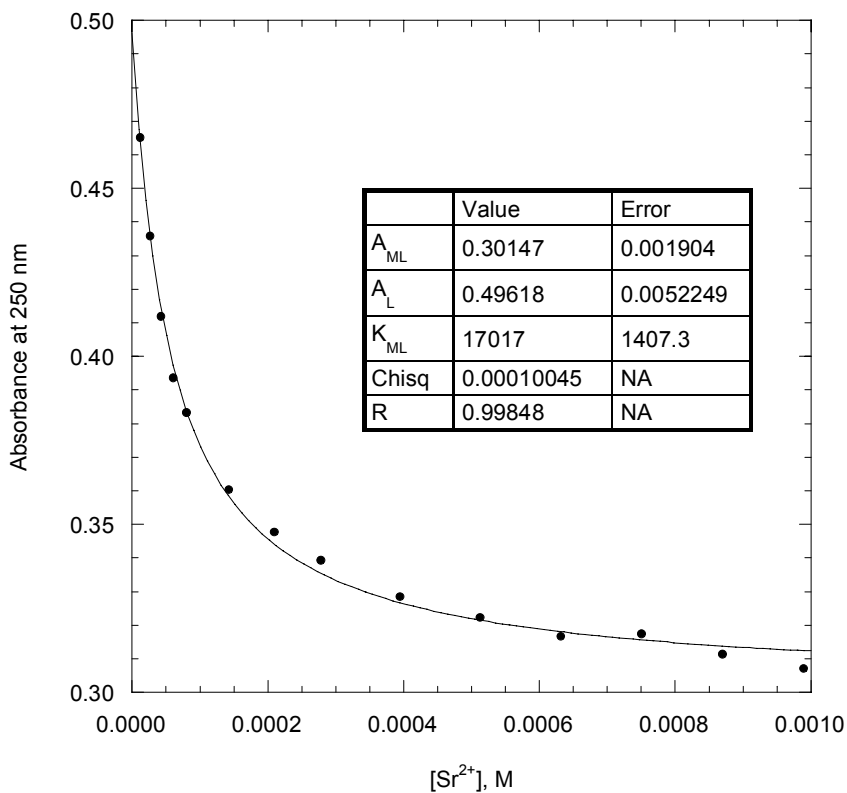


Figure 4-93. Plot of absorbance at 250 nm versus $[Sr^{2+}]$ for the titration of An2.2.1, (16), shown in Figure 4-92. The data were fit to eq 4.9 and the calculated values used to construct the solid line are listed in the table.

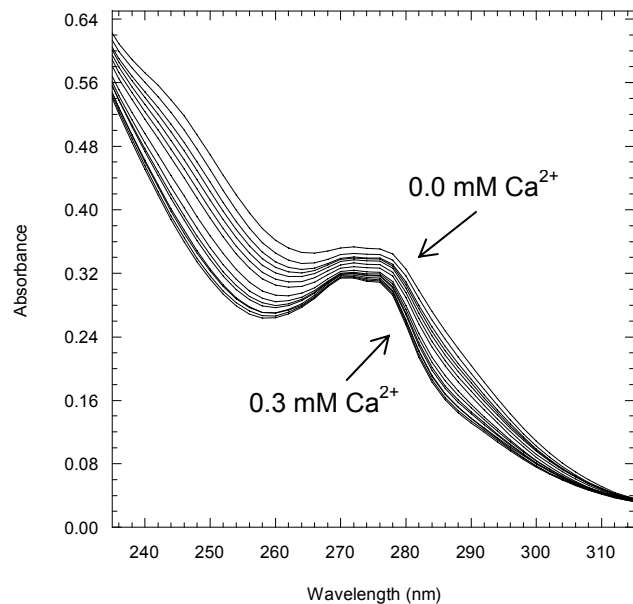


Figure 4-94. Spectra from the titration of 0.070 mM An2.2.1, (16), with calcium at pH = 8.7. Some spectra have been omitted for clarity.

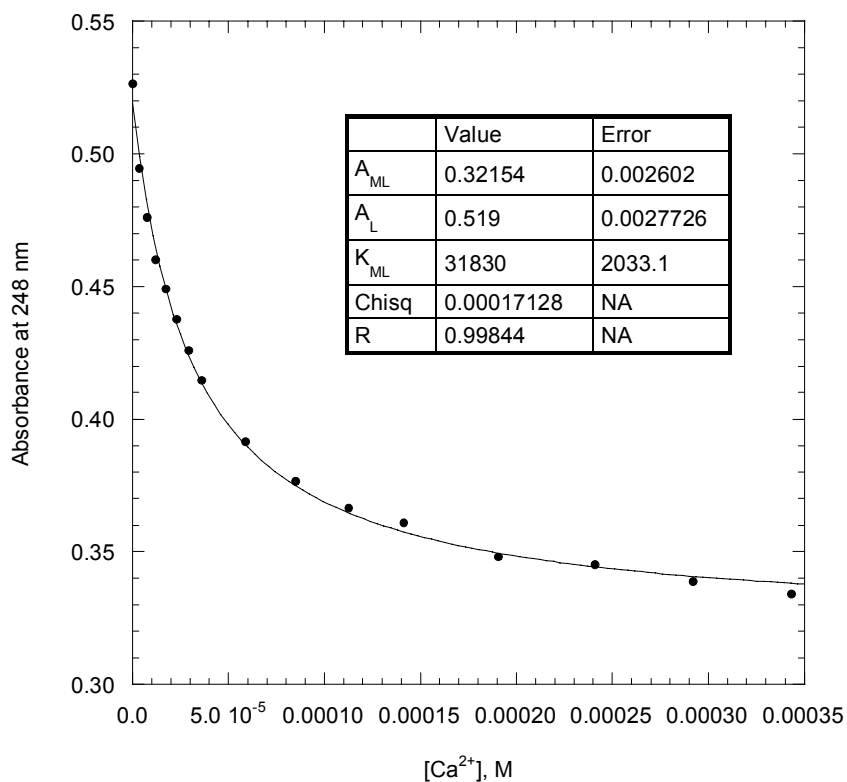


Figure 4-95. Plot of absorbance at 248 nm versus $[Ca^{2+}]$ for the titration of An2.2.1, (16), shown in Figure 4-94. The data were fit to eq 4.9 and the calculated values used to construct the solid line are listed in the table.

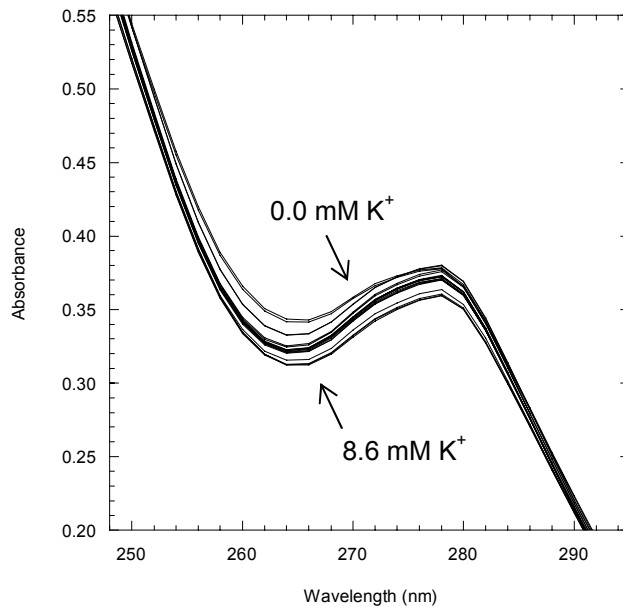


Figure 4-96. Spectra from the titration of 0.070 mM An2.2.1, (16), with potassium at pH = 9.1. Some spectra have been omitted for clarity.

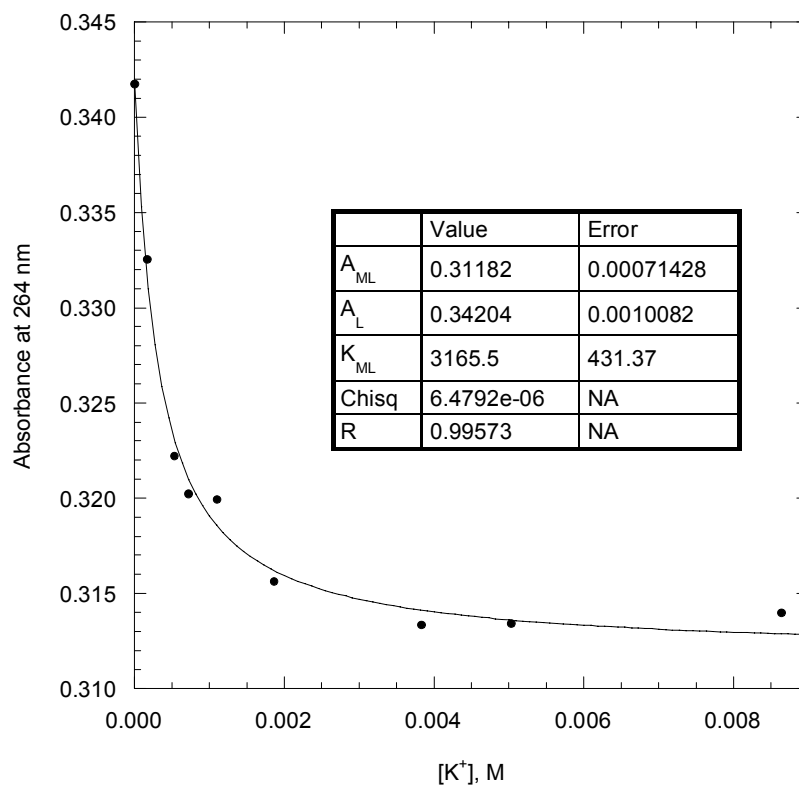


Figure 4-97. Plot of absorbance at 264 nm versus $[K^+]$ for the titration of An2.2.1, (16), shown in Figure 4-96. The data were fit to eq 4.9 and the calculated values used to construct the solid line are listed in the table.

The formation constants ($\log K_{ML}$) were determined from multiple experiments and a number of the results are listed in Table 4-23. The average formation constants ($\log K_{ML}$) for An2.2.1 with Ba^{2+} , Na^+ , Sr^{2+} , Ca^{2+} , and K^+ are 3.6 ± 0.4 , 4.1 ± 0.4 , 4.2 ± 0.4 , 4.3 ± 0.3 , and 3.7 ± 0.5 , respectively.

Table 4-23. Formation constants ($\log K_{ML}$) for An2.2.1, (16) in H_2O at $25^\circ C$.

Exp. No.	Metal	Method ^a	λ , nm (range)	$\log K_{ML}$	Error
1	Ba	K	254	3.53	0.03
1	Ba	S	200-400	3.70	0.07
2	Ba	K	256	3.68	0.06
2	Ba	S	200-400	4.2	0.2
3	Ba	K	252	3.04	0.02
3	Ba	S	200-400	3.19	0.09
1	Na	K	262	3.77	0.09
1	Na	S	200-400	3.9	0.2
2	Na	K	260	4.29	0.06
2	Na	S	200-400	4.6	0.2
1	Sr	K	250	4.23	0.04
1	Sr	S	200-400	4.56	0.07
2	Sr	K	284	3.69	0.04
2	Sr	S	200-400	4.19	0.03
1	Ca	K	284	4.38	0.02
1	Ca	S	200-400	4.56	0.07
2	Ca	K	284	3.94	0.05
2	Ca	S	200-400	4.3	0.1
1	K	K	258	4.15	0.07
1	K	K	264	4.20	0.07
2	K	K	264	3.50	0.06
2	K	K	270	3.09	0.07

^aK = Kaleidagraph, S = Specfit.

Cryptand An2.2.1 is different from 2.2.1 because of the addition of benzene rings and is also different from An2.2.2 because of the smaller cavity size and one less oxygen donor atom. Table 4-24 lists the formation constants ($\log K_{ML}$) with various metals for all three ligands as well as cryptand 2.1.1. The $\log K_{ML}$ values determined for cryptand An2.2.1 are lower than 2.2.1. The value for potassium is only slightly lower (0.2 log units) while

the other metals are significantly lower ranging from 1.3 (Na⁺) to 7.4 (Pb²⁺) log units. The alkali cations sodium and potassium are the least affected by the structural changes, with slightly larger changes observed for alkaline earth cations (2.6-3.1 log units). K_{ML} values for the heavy metal cations decrease by the greatest magnitude (5.5 and 7.4 log units for Cd²⁺ and Pb²⁺, respectively). The formation constants (log K_{ML}) of An2.2.1 for the heavy metal cations are similar in magnitude to those reported for cryptand 2.1.1. Cryptands An2.2.1 and 2.2.1 both have formation constant values higher for sodium compared to potassium. The K_{ML} value pattern for 2.2.1 is Pb²⁺ > Cd²⁺ > Sr²⁺ > Ca²⁺ > Ba²⁺ and is similar to that found for An2.2.1 which is Pb²⁺ ≥ Ca²⁺ ≥ Sr²⁺ ≥ Cd²⁺ > Ba²⁺.

Table 4-24. Formation constants (log K) for 2.1.1, 2.2.1, An2.2.2, (19) and An2.2.1, (16) in H₂O at 25°C.

	2.1.1 ^a	2.2.1 ^a	An2.2.1	An2.2.2
H ⁺ (1)	10.6 ^b	10.5	5.4 ± 0.1	5.3 ± 0.2
H ⁺ (2)	7.9 ^b	7.4	3.1 ± 0.3	3.4 ± 0.2
Na ⁺	3.1	5.4	4.1 ± 0.4	2.4 ± 0.1
K ⁺	<2 ^b	3.9	3.7 ± 0.5	2.0 ± 0.3
Ca ²⁺	2.5	6.9	4.3 ± 0.3	2.7 ± 0.1
Sr ²⁺	<2 ^b	7.3	4.2 ± 0.4	4.1 ± 0.6
Ba ²⁺	<2 ^b	6.3	3.6 ± 0.4	4.7 ± 0.2
Cd ²⁺	5.2	9.5	4.0 ± 0.1	3.0 ± 0.2
Pb ²⁺	7.3	12.4	5.0 ± 0.1	8.5 ± 0.3

^a Ref. ⁴⁵. ^b Ref. ⁴³.

The log K_{ML} values for cryptand An2.2.1 and An2.2.2 are all within 2 orders of magnitude of each other except for lead (Δlog K = 3.5 log units). Both cryptands have a similar formation constant value for strontium and both have greater values for sodium in comparison to potassium. The smaller cryptand An2.2.1 generally has a larger K_{ML} value for the smaller cations sodium (0.97 Å), calcium (0.99 Å), and cadmium (0.97 Å) while the larger cations barium (1.34 Å) and lead (1.20 Å) have higher K_{ML} values for

An2.2.2.²³ Potassium (1.33 Å) does not fit this behavior. Figure 4-98 presents the log K_{ML} values for An2.2.1 and An2.2.2 versus ionic radius.

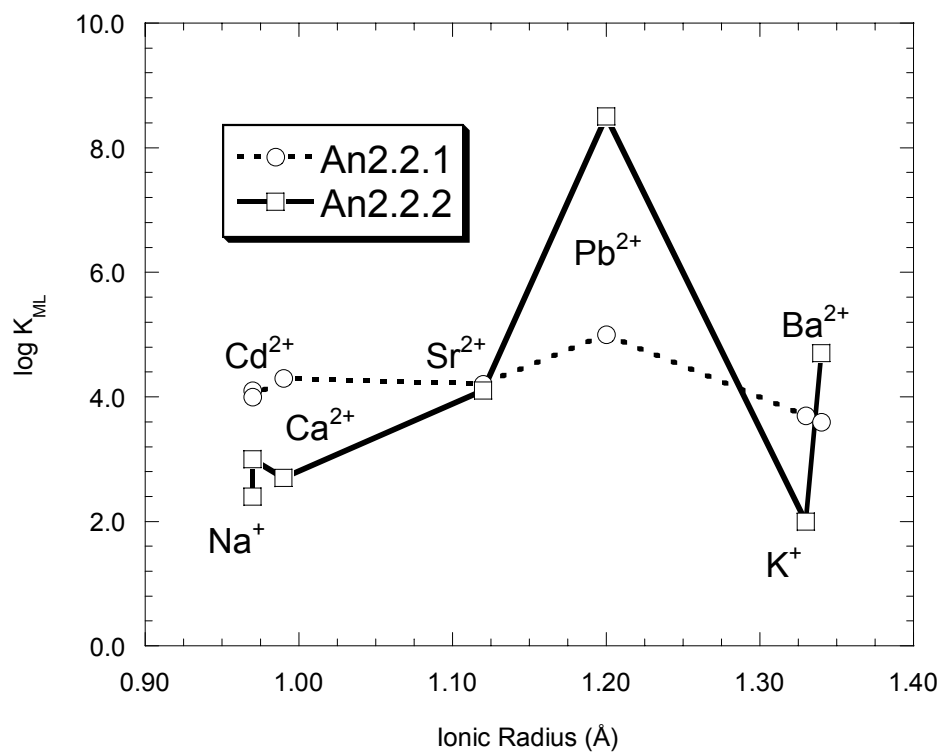


Figure 4-98. Complexation selectivity patterns of An2.2.1, (16), and An2.2.2, (19).

V. Summary

Cryptands An2.2.1, An2.2.2, An3.1.1, and An3.1.1.3 were synthesized by high dilution techniques. Solid-state structures were determined for cryptands An2.2.1, An2.2.2, and An3.1.1.3; cryptates An2.2.2·K⁺·ClO₄⁻, An2.2.2·Pb²⁺·(NCS⁻)₂, and 2.2_B.2_B·Pb²⁺·NCS⁻; and mono- and bicyclic intermediates An2.1*, An2.2*, An3.1*, An2.1, An2.2, An3.1, An2.2.1*, An2.1.2*, An2.2.2*, and An3.1.1*. The solid-state structures of two additional 18-membered macrocyclic diamides, 2.2* and 2.2_S*, were determined to evaluate trends in structural modifications. All 18-membered macrocyclic amides mentioned had intermolecular H-bonds except An2.2* and compound 2.2* has only intermolecular H-bonds. Conformational constraints imposed by the -SCCS-subunit and benzo groups result in a mixture of intra- and intermolecular H-bonds. NMR techniques were used to characterize the synthesized compounds and to confirm intramolecular hydrogen-bonding occurred in the macrocyclic amides An2.1*, An2.2*, and An3.1* in solution. The solid-state structures of cryptates An2.2.2·K⁺, An2.2.2·Pb²⁺, and 2.2_B.2_B·Pb²⁺ were determined and confirmed that the metal ions were located inside the cavity of the macrobicyclic ligand. These cryptates differed in coordination number (An2.2.2·K⁺ and An2.2.2·Pb²⁺ (CN = 10) vs. 2.2_B.2_B·Pb²⁺ (CN = 9)) and coordination sphere geometry (An2.2.2·K⁺ vs. 2.2_B.2_B·Pb²⁺). The potassium cryptate of An2.2.2 had average M-O and M-N distances slightly longer than the averages for 2.2_B.2_B·Pb²⁺. The average M-O and M-N distances were consistent with the distances found in other cryptate complexes containing lead and potassium from the literature. The cryptates containing benzo rings (An2.2.2·K⁺ and 2.2_B.2_B·Pb²⁺) had three atom angles (∠N-M-N) between the nitrogen bridgeheads and metal ion that differed more from linearity in

comparison to cryptates of ligands without benzene rings. The benzoannelated cryptate (An2.2.2·K⁺) showed a greater deviation from linearity in comparison to 2.2_B.2_B·Pb²⁺. Protonation constants for An2.2.1 and An2.2.2 are ≥ 2.5 pH units below the parent compounds 2.2.1, 2.2.2, and 2.2_B.2_B. The metal formation constants for cryptands An2.2.1 and An2.2.2 are all weaker in comparison to the parent cryptands 2.2.1, 2.2.2, and 2.2_B.2_B. The formation constants for the divalent cations are more affected by the structural changes in An2.2.1 and An2.2.2 in comparison to the monovalent cations. This is a result of an increase in ligand thickness (benzene rings) which decreases the interaction of the complexed cation with water and destabilizes the complex.⁴⁹ The inherent selectivity of the parent cryptands for lead over the biological cations sodium, potassium, and calcium is present for An2.2.2, but not for An2.2.1. Cryptand An2.2.1 shows very little selectivity for the cations studied in this project because of the decrease in basicity of the oxygens and nitrogens adjacent to the benzene rings, a small cavity size imposed by the conformational restrictions of the benzene rings, and an increase of ligand thickness.

References

- (1) Lehn, J. M. *Struct. Bonding* **1973**, *16*, 1-69.
- (2) Bowman-James, K. *Acc. Chem. Res.* **2005**, *38*, 671-678.
- (3) Szumna, A.; Jurczak, J. *Eur. J. Org. Chem.* **2001**, 4031-4039.
- (4) Jurczak, J.; Lipkowski, P.; Stankiewicz, T.; Urbanczyk-Lipkowska, Z. *Supramol. Chem.* **1995**, *6*, 87-94.
- (5) Taylor, R. W.; Khan, M. A.; Lehn, J.-M.; Dietrich, B. *Acta Crystallogr., Sect. C* **1988**, *44*, 1928-1931.
- (6) DeSimone, R. E.; Glick, M. D. *J. Am. Chem. Soc.* **1976**, *98*, 762-767.
- (7) Gluzinski, P.; Jurczak, J.; Krajewski, J. W.; Salanski, P.; Stankiewicz, T.; Urbanczyk-Lipkowska, Z.; Armbruster, T.; Burgi, H.-B. *Helv. Chim. Acta* **1992**, *75*, 1313-1319.
- (8) Brown, R. F. C.; Radom, L.; Sternhell, S.; Rae, I. D. *Can. J. Chem.* **1968**, *46*, 2577-2587.
- (9) Gribble, G. W.; Bousquet, F. P. *Tetrahedron.* **1971**, *27*, 3785-3794.
- (10) Hibbert, F.; Mills, J. F.; Nyburg, S. C.; Parkins, A. W. *J. Chem. Soc., Perkin Trans. 2* **1998**, 629-634.
- (11) Kilic, Z.; Gunduz, N. *Synth. React. Inorg. Met.-Org. Chem.* **1986**, *16*, 457-474.
- (12) Aguilar, J. C.; Rodriguez de San Miguel, E.; de Gyves, J.; Bartsch, R. A.; Kim, M. *Talanta* **2001**, *54*, 1195-1204.
- (13a) Biernat, J. F.; Jereczek, E.; Bujewski, A. *Pol. J. Chem.* **1979**, *53*, 2367-2371.
- (13b) NMR shift reagent tris-(dipivalomethanato) europium.
- (14) Formanovskii, A. A.; Mikhura, I. V.; Sokolovskii, S. A.; Murakhovskaya, A. S.; Terent'ev, P. B.; Sharbatyan, P. A. *Khim. Geterotsykl. Soedin.* **1988**, 1128-1135.
- (15) Sharghi, H.; Eshghi, H. *J. Sci. I. R. Iran* **1998**, *9*, 238-244.
- (16) Markovich, I. S.; Filyagina, N. A.; Dziomko, V. M.; Ryabokobylko, Y. S.; Adamova, G. M.; Zelichenok, S. L. *Khim. Geterotsykl. Soedin.* **1983**, 185-188.
- (17) Silverstein, R. M.; Webster, F. X. *Spectrometric Identification of Organic Compounds*, 6th ed.; John Wiley & Sons, Inc.: New York, 1998.
- (18) Formanovskii, A. A.; Murakhovskaya, A. S. *Khim. Geterotsykl. Soedin.* **1985**, 267-271.
- (19) Weiss, R.; Samuel, G. *Chem. Commun.* **1970**, 1654-1655.
- (20) Weiss, R.; Mathieu, F. *J. Chem. Soc., Chem. Commun.* **1973**, 816.
- (21) Weiss, R.; Metz, B.; Moras, D.; Mathieu, F. *J. Am. Chem. Soc.* **1978**, *100*, 4412-4416.
- (22) Dietrich, B. In *Comprehensive Supramolecular Chemistry*; Gokel, G. W., Ed.; Elsevier Science Inc.: New York, 1996; Vol. 1, pp 153-212.
- (23) *CRC Handbook of Chemistry and Physics*, 71st ed.; CRC Press inc.: Boca Raton, 1990-1991.
- (24) Pavia, D. L.; Lampman, G. M.; Kriz, G. S. J. *Introduction to Spectroscopy: A Guide for Students of Organic Chemistry*; W. B. Saunders Company: Philadelphia, PA, 1979.
- (25) Metz, B.; Moras, D.; Weiss, R. *J. Chem. Soc. Perkin Trans. 2* **1976**, 423-429.
- (26) Prasanna de Silva, A.; Nimal Gunaratne, H. Q.; Samankumara Sarchanayake, K. R. A. *Tetrahedron Lett.* **1990**, *31*, 5193-5196.

- (27) Lehn, J.-M.; Simon, J.; Wagner, J. *Nouv. J. Chim.* **1977**, *1*, 77-84.
- (28) Quici, S.; Manfred, A.; Raimondi, L.; Sironi, A. *J. Org. Chem.* **1995**, *60*, 6379-6388.
- (29) Wilson, S. R.; Tulchinsky, M. L. *J. Org. Chem.* **1993**, *58*, 1407-1408.
- (30) Lehn, J.-M.; Pagelot, A.; Saigo, K.; Kotzyba-Hibert, F.; Kintzinger, J.-P. *J. Chem. Soc., Chem. Commun.* **1981**, 833-836.
- (31) Lehn, J. M.; Pine, S. H.; Watanabe, E.-i.; Willard, A. K. *J. Am. Chem. Soc.* **1977**, *99*, 6766-6768.
- (32) Amendola, V.; Bastianello, E.; Fabbrizzi, L.; Mangano, C.; Pallavicini, P.; Perotti, A.; Lanfredi, A. M.; Ugozzoli, F. *Angew. Chem. Int. Ed.* **2000**, *39*, 2917-2920.
- (33) Jurczak, J.; Jarosz, M.; Tarnowska, A. *Synthesis* **2004**, 369-372.
- (34) Cathala, B.; Raouf-Benchekroun, K.; Galaup, C.; Picard, C.; Cazaux, L.; Tisnes, P. *Tetrahedron* **1996**, *52*, 9793-9804.
- (35) Metz, B.; Weiss, R.; Moras, P. D. *Acta Crystallogr., Sect. B* **1973**, *B29*, 383-388.
- (36) Weiss, R.; Metz, B. *Inorg. Chem.* **1974**, *13*, 2094-2098.
- (37) Informatics, W. L., 4.0 ed.: Milford, MA, 2003.
- (38) Taylor, R. W.; Ott, N. L.; Barnes, C. L.; Van Der Helm, D. *Acta Crystallogr. Sect. B* **1982**, *B38*, 2277-2280.
- (39) McKee, V.; Nelson, J.; Martin, N. *Inorg. Chim. Acta* **1994**, *218*, 5-8.
- (40) Claudio, E. S.; Goodwin, H. A.; Magyar, J. S. *Prog. Inorg. Chem.* **2003**, *51*, Chapter 1.
- (41) Shimoni-Livny, L.; Glusker, J. P.; Bock, C. W. *Inorg. Chem.* **1998**, *37*, 1853.
- (42) Powell, K. J.; Academic Software, 1999.
- (43) Lehn, J. M.; Sauvage, J. P. *J. Am. Chem. Soc.* **1975**, *97*, 6700-6707.
- (44) Ingle, J. D. J.; Crouch, S. R. *Spectrochemical Analysis*; Prentice-Hall, Inc.: Upper Saddle River, 1988.
- (45) Smith, R. M.; Martell, A. E., 6.0 ed., 2001.
- (46) Chantooni, M. K. J.; Kolthoff, I. M. *Proc. Natl. Acad. Sci.* **1981**, *78*, 7245-7247.
- (47) Cox, B. G.; Schneider, H.; Truong, N. v. *J. Am. Chem. Soc.* **1984**, *106*, 1273-1280.
- (48) Craig, M. E. Ph. D. Thesis. University of Oklahoma, Norman, OK, 1990.
- (49) Lehn, J. M.; Dietrich, B.; Sauvage, J. P. *J. Chem. Soc., Chem. Commun.* **1973**, 15-16.